Altering Physical Properties of Particles with Surface Roughness – Anomalous Properties of ‘Hedgehog’ Particles

by

Joong Hwan Bahng

A dissertation submitted in partial fulfillment
of the requirements for the degree of
Doctor of Philosophy
(Biomedical Engineering)
at the University of Michigan
2016

Doctoral Committee

Professor Nicholas Kotov, Chair

Professor Somin Lee

Professor Michael Solomon

Professor Scott VanEpps

DEDICATION

To my wife Hee Jeong, son Sungjo, parents, parents in law for everything

ACKNOWLEDGEMENTS

This dissertation is a cumulative supports and friendship from many brilliant individuals. I would like to express my sincere thanks and appreciations to every one of them.

First and foremost, I would like to express my sincere appreciation to my dear advisor Professor Nicholas Kotov. He has been my biggest proponent with his warmth, understanding and endless supports. He has been all inspiration with his unfathomable creativity and knowledge. He has never ceased to infuse a handful of encouragements when in need. I will always cherish countless discussion I had with him which enabled me to tackle tough problems. Also, I will never forget countless mornings I had spent in his office having a hot cup of coffee while enjoying his take on current opinion in the scientific communities.

I would like to also express sincere appreciation to the Department of Biomedical Engineering here at the University of Michigan. I had been generously granted scholarships and humility to endure periods of financial difficulties, of which I am forever grateful. In addition, I would like to also point out my committee members who had provided me with motivation and sincerity; Dr. Somin Lee, Dr. Michael Solomon, Dr. Scott VanEpps.

There are many colleagues, both present and past, of the Kotov group who have offered me both scientific motivation and unmatched hospitality. I

would like to especially thank Yi Chun Wang and Terry Shyu, with whom I have spent 6 years in the same office. I would like to further extend my gratitude to Siu On Tung, Gleiciani Silveira, Naomi Ramesar, Jian Zhu, Sudhanshu Srivastava, Ahmet Emre, Michelle Gonzalez, Dasha Bukharina, Douglas Montjoy, Kenji Hirai, Bongjun Yeom, Paul Podsiadlo, and countless others who have enriched my Ph.D. experience.

Most Importantly, I owe my whole-hearted appreciation and infinite gratitude to my wife, Hee Jeong Kim. None of my accomplishment would have been possible without her support, care and her loving heart.

Table of Contents

List of Figures

List of Tables

ABSTRACT

Particles are ubiquitous and are integral components of modern technology. Sensitive to any alterations or even a small perturbation in its constitutive properties, sizes and shapes, particles have been utilized as a versatile means in a compact platform with which to manipulate, enhance or transform any physico-chemical properties in its environment. Amongst the variety, procedural and synthetic diversities and accompanying investigation of the physical and chemical properties of micron-scale particles having highly rough surfaces is barren in previous studies. Yet, most of the particles found in nature are "rough" particles. Therefore, a thorough survey that maps the deviation in properties from what is expected of standard predictions from analytically "smooth" particles, accompanied by systematic analysis protocols, is expected bring a broad impact to multiple scientific and practical disciplines. A further understanding of the nature and physico-chemical properties of "rough" particles will enable better understanding of our environment, with which or around which to attain our engineering objectives.

In the early phase of the research as a precursor to the construction of "rough" particles, the focus was on the synthesis of smooth polymeric micro-spheres (μ-spheres). As μ-spheres had been extensively characterized, the focus was on the development and streamlining of large-scale fabrication process based

on microfluidics setup. Furthermore, its utility in biomedical applications supportive of pharmaceutical industries had been identified in the form of three-dimensional cell-culture scaffolds. Stacked layers of ordered arrays, or colloidal crystals, of polymeric μ-spheres were used as templates for inversion into hydrogel based 3D cell culture scaffolds.

The second phase of the research involved the synthesis and characterization of "rough" particles having orthogonal orientation of high aspect ratio ZnO nanospikes on polymeric μ-spheres, which we called the 'hedgehog' particles to reflect its morphology. In this phase, we studied the 'hedgehog' particles in a colloidal system and report an anomalous colloidal dispersion behavior; the 'hedgehog' particles stably disperse in 'phobic' solvents without polarity matching chemical modifications, thereby breaking the well-known 'similarity' rule.

Lastly, owing to unique geometrical and material configurations, the 'hedgehog' particles enabled us to study electromagnetic response of "rough" particles, where all of its photonic compartments are dielectric and lie within the Mie scattering regime. Here, we showed that the presence of surface roughness alters the electromagnetic responses from what would have been expected of typical micron-scale dielectric particles, which are as follows: 1) broadband scattering, 2) suppression of resonance, 3) suppression of higher-order modes, and 4) broadband suppression of backscattering.

These studies are only a small subset of synthetic and property diversities possible with “rough” particle configurations. We believe that continued investigation and further expansion in the knowledge of “rough”, as well as particles of other configurations, may enable us a spectrum of design possibilities for realizing high performance substrates and devices.

Chapter I

Introduction

1.1 Motivation

Definition of a particle various amongst disciplines. For this thesis, the following best fit the description of a particle. Particle is defined as a discrete and localized matter 1) that is distinguishable from its environment through physical boundaries (interface) and 2) to which physico-chemical properties may be ascribed within and around the boundary

Particles are classified according to sizes, its constituents, geometrical anisotropies and its dimensions, and compartmental arrangements in the case of composite particles (**Figure 1.1**) [3–11]. Particles in the nano-scale regime exhibits deviations in physical and chemical properties from its macroscale counterpart.

For example, optical properties and bandgap changes due to quantum effect, mechanical properties such as toughness and diffusion rates changes. Chemical properties also change due to high reactivity stemming from high surface volume/weight ratio.

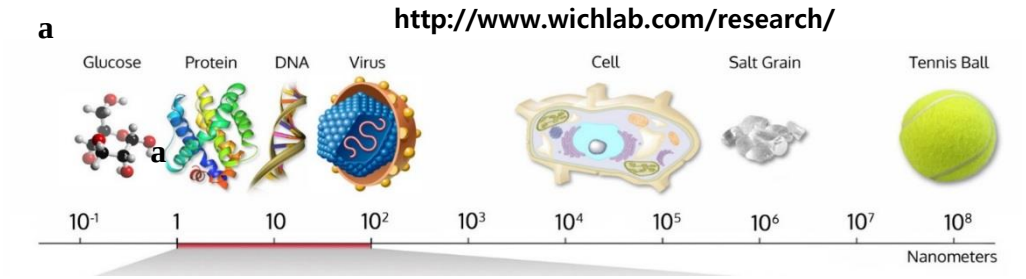

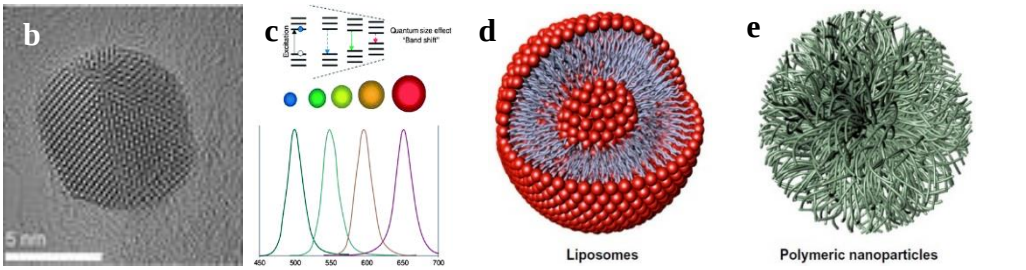

Scholl, Nature, 483, 421-427 | Mirzaei, J. Mater.Chem., 2012, 22, 22350-22365 | Sanna, International J. Nanomedicine, 2014, 9, 467-483

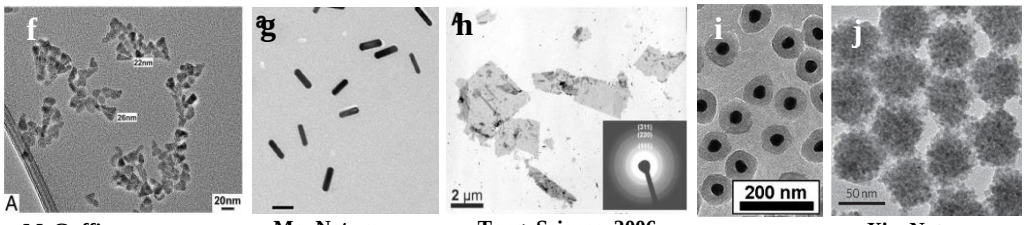

McGuffie, Nanomedicine, 2016, 12, 33-42 | Ma, Nature Communications, 2013, 4, 2689 | Tang, Science, 2006, 314, 274-247 | Perez, J. Mater. Chem, 2010, 20, 61-64 | Xia, Nature Nanotechnology, 2011, 6, 580-587

Figure 1.1. (**a**) Size-scale representations; (**b-j**) Types of particles in nanoscale regime

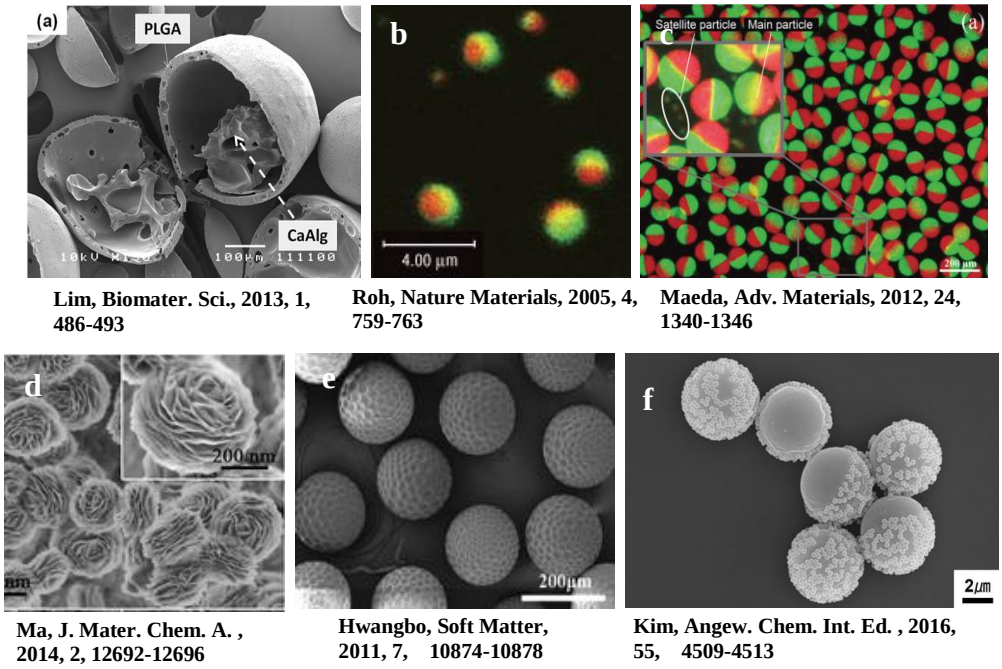

Lim, Biomater. Sci., 2013, 1, 486-493

Roh, Nature Materials, 2005, 4, 759-763

Maeda, Adv. Materials, 2012, 24, 1340-1346

Ma, J. Mater. Chem. A. , 2014, 2, 12692-12696

Hwangbo, Soft Matter, 2011, 7, 10874-10878

Kim, Angew. Chem. Int. Ed. , 2016, 55, 4509-4513

Figure 1.2. (**a-f**) Types of particles in micro-scale regime

Micro-particles are also categorized in the same manner (**Figure 1.2**) [12–17]. Particles are ubiquitous and plays an important role in a wide array of current technologies owing to flurries of advanced research devoted to 1) elucidating unique properties in all aspects scientific disciplines and 2) identification of practical utilities in current technology. Great accomplishments notwithstanding, there still remains procedural complications, incomplete understanding of empirical observations as well as not yet recognized distinguishing properties of particulate matters that may overcome the current

technological hurdles. Diversities of particle types and yet to be realized material and geometrical configurations may ascribe the current whereabouts.

In order to further increase the impact of particle technology to societal benefit, we expanded our research interest to understanding physico-chemical properties of particle types that are barren in previous ventures. In particular, we focused on synthesis, characterization and exclusive properties of all dielectric micro-particles having rough surfaces.

In the early phase of the research as a precursor to the construction of "rough" particles, the focus was on the synthesis of smooth polymeric micro-spheres (μ-spheres) using simple, cost-effective and readily accessible microfluidics system. Analytically smooth μ-spheres have been extensively characterized. Therefore, the research focus by-passed the scientific investigation and directly emphasized streamlining of large-scale fabrication and its utility where biomedical applications supportive to pharmaceutical industries were identified. The second phase of the research involved the synthesis and in depth characterization of all dielectric "rough" particles having orthogonal orientation of high aspect ratio ZnO nanospikes on polymeric μ-spheres, which we called the 'hedgehog' particles to reflect its morphology. In this phase, we studied the 'hedgehog' particles in a colloidal system and report alterations from the standard colloidal behavior in association with the surface roughness. Lastly, the 'hedgehog' particles feature unique geometrical and material configurations. This enabled us to study electromagnetic response of "rough" particles with photonic

compartments that are all dielectric and lie within the Mie scattering regime. Here, we studied the roles of wavelength comparable surface roughness that bring about deviations in the electromagnetic responses that are expected of a typical smooth dielectric μ-sphere.

A wide spectrum of colloidal sciences stem from our ability to control the behavior colloidal systems, such as dispersion and controlled aggregation, known as self-assembly process. This requires the knowledge of different types of forces that govern the particle-particle interaction in fluid. In depth research on colloidal systems began as early as 1860 by Thomas Graham. A milestone that quantitatively describe the interplay of forces that determine the stability of colloidal system was achieved through The Derjaguin-Landau-Verwey-Overbeek (DLVO) theory during 20^{th} century [18]. This chapter will first introduce some of the forces governing the colloidal behavior, followed by brief reviews on the properties and synthesis of the materials used in this endeavor. Next, current state-of-the art research on the construction of particles with rough surfaces will be overviewed.

1.2 Forces governing particle interactions

The forces that govern the physical behavior of the particulate matters are dependent on its size regime. The interaction between the microparticles are typically governed by the classical laws of physics and their behavior typically depends on the size and the constitutive properties of their volumetric and

interfacial constituents that determine the attractive and repulsive interactions. The evaluation of nano-scale colloidal systems require quantum mechanical effects, most of which are beyond the scope of this thesis.

The DLVO theory stands as one of the single most important the milestone in the field of colloidal science and has quantitatively described a large portion of the experimental observation of the colloidal stability. The DLVO theory is summarized as follows,

$$V_{DLVO} = V_{VdW} + V_{DL} \quad \text{Eq. 1.1}$$

, where the sum of van der Waals (V_{VdW}) and the electrical double layer approximates the total interaction potential between the particles in suspension. Full understanding of the interaction between the nanoparticles require quantum mechanical effects which is mostly beyond the scope of this thesis.

1.2.1 Van der Waals interactions

The volumetric forces that governs the attractive interaction between the microparticles are called en masse the van der Waal (vdW) forces and includes the Debye force, the Keesom force, and the London dispersion forces. The simplest approximations in the form of the 'pairwise' potential, where the interaction is non-retarded and also additive, the energies of all the atoms encompassed in a particle are summed with all the atoms in the other particle. The pairwise potential is described with the Hamaker constant, $A_H = \pi^2 C \rho_1 \rho_2$. Typical values of the Hamaker constants for condensed phases range between 10^{-20} and 10^{-19}J in

vacuum, and an order magnitude lower in water[19,20]. Analytical expression for interactions between various geometries have been derived using A_H. The vdW energy, in its simplest form, between two interacting spherical particles are given by the following:

$$V_{vdW} = \frac{-A_H}{12\pi d^2} \qquad \text{Eq. 1.2}$$

, where *d* is the minimum interaction distance between the spheres.

The validity of the pairwise additivity, which disregards the influence of the neighboring atoms, may come into question in many-atom systems due to changes in the effective polarizability, direct and indirect reflective influences on the surrounding atoms. Furthermore, the additive approach may also break down for interacting bodies in a medium. The issues with the additivity has been circumvented with the Lifshitz theory and the coupled diple method (CDM). In Lifshitz theory, the individual particles are considered as a continuous media rather than the atomic constructs. Their interaction is evaluated as bulk properties in terms of their constitutive properties such dielectric constants and refractive indices which also incorporates the effects of the intermediate substance[21–24]. The non-retarded Hamaker constant between two identical particles, in terms of their constitutive, in a medium having different absorption frequencies, obtained through Lifshitz approximation is given as follows[24,25]:

$$A_{131} = 3h\frac{\sqrt{\omega_1\omega_3}}{128\pi\bar{\varepsilon}^{7/4}}\frac{(X^2\bar{\varepsilon} + 2X\Delta\varepsilon\bar{\varepsilon}^{1/2} + \Delta\varepsilon^2(3+2Y)}{[(Y-\sqrt{Y^2-1})^{1/2} + (Y+\sqrt{Y^2-1})^{1/2}]^3}$$

$$\bar{\varepsilon} = 0.5(n_1^2 + n_3^2)$$

$$\Delta\varepsilon = n_1^2 - n_3^2$$

$$X = \frac{\omega_1}{\omega_3}(n_1^2 - 1) - \frac{\omega_3}{\omega_1}(n_3^2 - 1)$$

$$Y = \frac{1}{4\bar{\varepsilon}^{1/2}}[\frac{\omega_1}{\omega_3}(n_1^2 + 1) + \frac{\omega_3}{\omega_1}(n_3^2 + 1)] \qquad \text{Eq. 1.3}$$

, where ω_1, ω_3, n_1, n_3 are the absorption frequencies and refractive indices of the particle and the media, respectively.

The CDM, or the discrete dipole approximation, also includes the many-body interactions where each atom is modeled as a harmonic oscillator that responds to the local electric field[26]. Its dynamic polarizability is obtained with Drude atomic model,

$$\alpha(i\omega) = \frac{\alpha_o\omega_o^2}{\omega_o^2 + \omega^2} \qquad \text{Eq. 1.4}$$

, where α is the dynamic polarizability, α_o is the static polarizability, ω_o is characteristic frequency estimated from the ionization energy[27]. The local electric field is calculated by the superposition of the electric fields due to instantaneous induced dipole moments from the neighboring atoms. The vdW energy (V_{vdW}) between the interacting particles is obtained by subtracting the V_{vdW} self-energy of each of the particles from total V_{vdW} of the system.

1.2.2 Double Layer electrostatic interactions

Stability of colloidal dispersion requires repulsive forces that counter-balances and over triumphs the ubiquitous vdW attraction. If only the vdW type were present, the particles in liquid will agglomerate and eventually precipitate out of the solution. In a high dielectric constant liquid, particles are typically associated with interfacial charges that emanate electrostatic repulsion towards the particles with same charge polarity, thereby preventing their aggregation. There are two main mechanisms that impart surface charges to particle dispersion in liquids[20]: 1) ionization or dissociation of surface groups and 2) interfacial adsorption or binding of ions. The surface charges, co-ions, attracts oppositely charged layer of counter-ions equal in magnitude. The counter-ions in the Stern (or Helmholtz) layer are transiently bound to the surface, above which a mobile cloud of ions envelop through thermal motion, forming a diffuse layer known as the electric double layer (DL)[28–30], as depicted in **Figure 1**[31]. The electrostatic potential due to the interfacial charge distribution around the particles plays in the colloidal stability and its distribution is best modeled with the Poisson-Boltzmann equation. Details of the mathematical basis and derivation of analytical expression for potential distribution around charged particles and expressions relating surface potential to

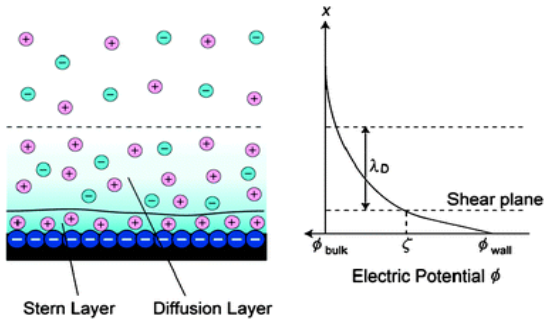

Figure 1.3: Graphic representation of EDL and the potential profile

surface charge density can be found in literature[32,33]. Analytical expression for EDL energies between the particles in liquid will be presented in **Chapter 4**.

1.2.3 Hydrophobic interactions

The DLVO theory closely approximates the behavior of hydrophilic particles in aqueous suspension. However, the DLVO theory fails to account for aggregation of hydrophobic colloids in similar dispersion media, despite some particles having high zeta (ζ)-potential[34,35]. This unusually strong attraction between the hydrophobic surfaces in aqueous environment is called the "hydrophobic interaction". The hydrophobic interactions, combined with the hydrophobic effects, is responsible for important biological structures such as assembly and folding of proteins, micelles and cell membranes[36–38]. Hydrophobic interaction also plays an important role in forming particle-bubble aggregates in the flotation process for water purification, mineral processing and particle separations [39,40]. Some of the theories that have been proposed to explain the hydrophobic interactions include 1) entropic origin due to configurational rearrangement of water molecules proximal to the hydrophobic surfaces[41–45], 2) phase changes that occurs in between the hydrophobic surfaces at close proximities due to meta-stability of the liquid layer[46,47], 3) bridging of the nanobubbles that forms on such surfaces[48,49], and 4) anomalous polarization of water molecules[50–52]. The origin and the mechanism of the hydrophobic interaction still remains a source of debate.

Israelachvili and Pashley were the first to notice the non-DLVO hydrophobic forces and found that its attractive strength was order of magnitude higher than that of the vdW energies[53]. Since then, vast amount of research has been devoted to the force measurements in relations to the surfaces of different hydrophobicities, characterized by the contact angle θ^o [54,55]. Typically, the hydrophobic forces are measured using the surface force apparatus (SFA)[56,57] or the atomic force microscopy (AFM)[58] and the analysis with the DLVO theory applies to surfaces that exhibit with a small range of contact angles, $20^o < \theta^o < 40^o$ [59]. In the DLVO evaluation, Surfaces with higher θ^o requires additional hydrophobic term, expressed by exponential functions and power laws[55,58,60–62].

1.3 Microparticles

Particles in the micron-scale size regime (1-1000μm) are generally referred to as microparticles. Other definition refines the microparticle dimension to finer limits (100nm – 100μm). Due to its size, microparticles have higher surface-to-volume ratio and surface energy compared to its macro-scale counterpart. In this thesis, the focus will be limited to the polymeric microparticles.

1.3.1 Synthesis

Emulsification is the most common methods employed to synthesize colloidal polymeric particles. There are two approaches to this method which is analogous to top-down and bottom-up fabrication process in the construction of micro-/nanostructures: 1) disintegration of large polymer droplet into smaller emulsions or 2) condensation of molecules/polymerization of precursor monomers within small droplets in the presence of appropriate initiator. The first approach requires large amount of emulsifying agents and mechanical energy to shear the bulk material. Moreover, the resulting particle sizes are on the upper-limit of the micron-scale with high poly-dispersity. Nonetheless, simplicity and rapidity is the main advantage of the first approach, which rendered adaptation towards industrial applications where mono-dispersity and the size of the particle is not a critical factor, automotive primer paint for example[63].

The latter approach, also known as emulsion polymerization, is widely used in industrial settings as well as academic benchtops due to excellent synthetic controls allowing versatility, finer sizes and mono-dispersity. In a typical emulsion polymerization process, the monomer precursors that includes a double bond moiety capable of undergoing free-radical polymerization, initiators and ligand stabilizers are mixed as aqueous dispersions. Upon energy input such as light or heat, the nucleation occurs followed by growth towards a specified diameter.

Formation of mono-disperse droplet emulsion via microfluidic devices subsequently inspired the creation of solid micro-particles through variety of

microfluidic platform. The Nakajima group reported controlled formation of emulsion droplets by forcing pressurized dispersed phase into a reservoir containing micron-scale slits of the silicon microchannel. The dispersed phase was extruded in the continuous phase as micro-droplets whose size was approximately 3 to 4 times larger than the length of the slits[64]. The Quake group succeeded in forming controlled emulsion through T-junction microchannel made of polydimethylsiloxane (PDMS). Whereas the breaking of the droplet was aided by surface tension effect in the slit silicon microchannel, here the droplets are detached through a combination of shear forces and squeezing effect exerted by the continuous phase upon satiation of the continuous phase in the channel. The advantage of the T-junction method includes control of the droplet sizes by both the channel width and the flow rates of the continuous phase[65,66]. Later, flow-focusing device (FFD) type in microfluidic platform was used for controlled droplet formation by the Stone group, where the dispersed phase is coaxially flanked by the continuous phase fluid flow[67,68]. While the FFD device offers advantage in potential scale-up production, it requires careful optimization of the flow conditions so as to yield highly controlled droplet formation. Focusing of the dispersed phase flow sheathed by the continuous phase in a co-flowing geometry was implemented onto the microfluidic device. Here, glass pipette inserted into a PDMS platform functioned as hollow channel for the continuous phase flow[69].

Typically, 3 mechanisms have been used in the conversion of droplet formation from the microfluidic devices into solid polymeric particles[70]. The heat-

based mechanism involves thermal polymerization of the droplet and subsequent cooling at room temperature[71,72]. The light-based mechanism involves energy input from the UV radiation onto the droplet containing the photo-sensitive type monomers[73]. The chemical reaction based method requires chemical species, added separately to the droplets, which could instigate the polymerization process[74,75]. The advantage of this method is that no input energy is required.

1.3.2 Applications

The use of polymeric microparticles can be traced back to the ancient Mayans[70]. Polymeric microparticles are ubiquitous in current technology and are deployed in a wide spectrum of applications ranging from analytical applications such as column supports in chromatography[76] and flow cytometry[77], biomedical applications such as carriers for drug delivery [78,79] and as fillers and bulking agents for tissue replacement[80] as well as various other tissue engineering applications[81–85] , to biological applications such as protein, nucleic acid and DNA capture and extractions[86–88]. The polymeric particles are important constituents for a wide variety of materials chemistry research and industries such as coatings and paints[89], in tire and tough plastic manufacturing[90] and in adhesives[91].

Assemblies of individual polymeric microparticles into higher order periodic structures have been shown to exhibit exotic optical properties and opened up a promising field of photonic crystals. Photonic crystals, owing to periodic structures of alternating high contrast refractive indices, could

theoretically possess a photonic bandgap, in which propagation of light of certain wavelengths is prohibited[92–94]. Such would occur with destructive interference of light, of a certain range of wavelengths determined by the size, geometry and arrangements of the periodic constituents, propagation at all directions. Several groups have created photonic crystals composed of self-assembled silica microspheres whose photonic bandgap resides in the near infrared range[95,96]. Latex particles close to the nano-scale regime have been self-assembled into photonic crystal film[97–99]. Polymeric microspheres have been used as a sacrificial template for construction of diamond-lattice crystals from silica microparticles with the aid of SEM attached nano-robots[100]. Further use of polymer microparticles as the transient support template could be envisioned in creating photonic crystals of diamond or pyrochlore crystal lattices via self-assembly route proposed by Hynninen[101]. Significance of this approach is the possibility of photonic bandgap material at visible wavelengths with suitable selection of high refractive index particulate units that constitutes the lattice.

Self-assemblies of polymer microspheres, especially into opal types, have led to another interesting biomedical applications. The colloidal crystals of polymeric microparticles were used as templates to created inverted colloidal crystal (ICC) scaffolds for 3-dimensional cell culture platform. Initially constructed with silicate materials by Kotov et. al using[102], the scaffolding materials were later further expanded to PLGA (here, glass microspheres were used as the assembling units for colloidal crystal template)[103] and hydrogels[104–106]

that closely mimics the mechanical properties of non-osseous tissues. The surface chemistry of the scaffolding materials determined the behavior of tissue formation; adhesive interface rendered by layer-by-layer film deposition promoted cell attachment and spreading while non-adhesive interface endorsed spheroid formation. The ICC scaffolds were further deployed as 3D platforms to create functional in vitro organs modeling bone marrow[107,108].

1.4 Zinc oxide nano-rods/wires

1.4.1 Properties and applications

Zinc oxide (ZnO) nanowires (NWs) have useful physical properties that are tied to a number of potential applications ranging from photo-catalysis, photonics, piezoelectric actuators, photovoltaics and optoelectronics. Due to its nano-scale geometry, ZnO NWs exert quantum confinement effects on the photons and carriers. In addition, due to high break-down fields, large electron saturation rates, high radiation resistances and efficient luminescence, the ZnO nanomaterials are suitable for high power optoelectronics at high temperature and frequency[109,110].

ZnO is a low cost and environmentally friendly group II-IV *n*-type semiconductor with a wide bandgap (~3.3 eV) and large exciton binding energy (60 meV at RT)[111,112]. ZnO exhibits efficient radiative process through excitonic recombination that can support stimulated emission at low threshold[113,114]. Together with large exciton binding energy (60 meV, RT) that

allows efficient emission at room temperature, ZnO possesses good material properties for room temperature mediated UV lasing devices such as blue LEDs[115–118].

Nano-scale ZnO structures, such as ZnO NWs, could potentially further lower the lasing threshold due to the quantum effects, where the density of states at the band gap edges are significantly increased, leading to enhanced radiative recombination[119]. In addition to the excitonic emission devices, the ZnO NWs have been used to improve the efficiency of excitonic photovoltaics. For example, the ZnO NW constructs have been incorporated in dye-sensitized solar cells (DSC) as anode scaffolds for dye and quantum dot (QD) loading[120,121]. The single crystalline (quasi)-1D structure of the ZnO NWs increase the electron transport rate, faster by several orders of magnitude compared to percolation through a random polycrystalline network. Other device applications include field emission devices owing to high melting point and stability under oxygen environment[122,123], piezoelectric-field effect transistors[124–126] and gas- and bio-sensors[127,128].

The nano-scale ZnO naturally features high surface-to-volume ratio. Combined with high reactive surfaces owing to wide band-gap and large exciton binding energy, ZnO is a promising candidate for photocatalysts. It currently plays a significant role in environmental remediation[129–132] due to its exceptional pollution mineralization rate. Various reports suggest higher photocatalytic

behavior of ZnO compared to TiO_2[133–135]. ZnO has been used as catalysts in various organic reactions[136,137].

In particular, optoelectronic properties of 1D ZnO NWs are well suited for efficient photo-catalysis, such as increased delocalization of the carriers and reduced surface trapping states resulting from movement confinement along the *c*-axis, rendering efficient charge separation[129,138]. Such attributes led to a variety of photocatalytic platforms comprising 1D ZnO nanostructures. For example, ZnO NWs arranged in a flower-like format[139,140], photocatalytic paper with ZnO NWs [141], Orthogonal ZnO Nws on inorganic flat surfaces [142], ZnO NWs as tetrapods[143], and an array of ZnO NWs on an optical disk[144] have all shown enhanced photocatalytic activities.

1.4.2 Synthesis

Advantages of ZnO NWs over other types such as GaN NWs include low cost and simple to fabricate in an environmentally benign process, hence suitable for industrial and large-scale photovoltaic and optoelectronic components[109,145]. ZnO NWs have been synthesized as free-standing colloids. However its useful properties are magnified when associated with a variety of substrates in a vertically aligned format, manifested by 1D anisotropic and quantum effects. Various methods to construct vertically aligned ZnO NWs is reviewed in the following sections.

Vapor phase synthesis is the most prevalent methods to create 1D metal oxide nanostructures[146]. Vapor phase synthesis produces high quality nanowires and the reactions typically take place in a closed chamber at high temperatures between 500^{o}C to 1500^{o}C under gaseous environment and a typical protocol begins with production of vapor species via evaporation, chemical reduction and gaseous reaction after which the vapor precursors are condensed onto a substrate of interest[147]. The methods include vapor liquid solid (VLS)[148] growth, chemical vapor deposition (CVD)[149], metal organic chemical deposition (MOCVD)[150], physical vapor deposition (PVD)[151], molecular beam epitaxy (MBE)[152], pulsed laser deposition (PLD)[153] and metal organic vapor phase epitaxy (MOVPE)[154]. VLS, due to simplicity and low-cost compared to other vapor phase methods, and MOCVD[155], due to catalyst-free and lower temperature growth[156], are widely employed in the ZnO NW synthesis.

Solution phase synthesis has numerous procedural advantages over the vapor phase methods, which includes low-cost, low temperature (<200^{o}C). The reaction condition allows flexibility in the choice of substrates and the growth media, both of which could include the organic variety, and also facile scale-up on large substrates[147,157]. In particular, the hydrothermal method, in which the solution method is carried in aqueous environment, has been widely used for ZnO NWs. Hydrothermally grown ZnO NWs have more defects than the other types due to the presence of oxygen vacancies, which enables visible light photo-catalysis without the transition metal doping[158,159].

The procedural sequences of hydrothermal growth of vertically aligned ZnO NWs are as follows: 1) adsorption of ZnO nanoparticles as seeds on substrates of interest – the seeding layers lowers the thermodynamic barrier for nucleation that leads to the NW growth[160], 2) preparation of the growth solution that includes the Zn^{2+} salts, such as zinc nitrate and zinc chloride, and alkaline agents, such as sodium hydroxide or hexamethylenetetramine, 3) hydrothermal growth of ZnO NWs from ZnO seeded substrates in the presence of the growth precursors. The reaction process in the presence of zinc nitrate as the source of the Zn^{2+} salts and hexamethylenetetramine as the reducing agent are as follows: 1) decomposition of reducing agent: $(CH_2)_6N_4 + 6H_2O \rightarrow 6HCHO + 4NH_3$, 2) hydroxyl formation: $NH_3 + H_2O \rightarrow NH_4^+ + OH^-$, 3) supersaturation: $2OH^- + Zn^{2+} \rightarrow Zn(OH)_2$, 4) ZnO NW growth: $Zn(OH)2 \rightarrow ZnO + H2O$.

1.5 Interfacial features

1.5.1 Composition and assembly

Unit micro-colloids have the potential to be a versatile building blocks with which one can create complex structures for a wide spectrum of applications and scientific endeavors. In addition, vast amount of materials and procedural knowledge accumulated in the field of nano-materials have added tools with which one can further tailor the properties of the micro-colloids that will govern its behavior. In fact, high quality research efforts have been dedicated in recent decades to develop strategies to tailor colloidal properties through interfacial

nano-engineering[161]. Examples include polymer, inorganic and biomolecule coated particles.

Polymer coated colloids are currently applied as catalysts, found in cosmetics, inks and paints[161]. Two main fabrication pathways have been developed to achieve colloids comprising a solid core and a polymeric shell; interfacial polymerization and adsorption at particle surface. The polymerization methods include monomer adsorption followed by its polymerization on microparticles[162–165] and nano-scale particles[166–168], hetero-coagulation and polymerization[169] and nano-scale emulsion polymerization[170,171]. The adsorption method takes procedural similarity to self-assembly technique in an LBL manner, where single or multilayer polyelectrolyte layers of thin shell are self-assembled through sequential electrostatic adsorptions on the colloids[172–176].

Interfacial decoration with inorganic materials offer versatility to engineer colloids with diverse physical and chemical properties. Two main synthetic pathways have been utilized to achieve the solid-core inorganic-shell particles; 1) precipitation and surface reactions, 2) deposition of preformed inorganic nanoparticles[161]. In the first synthetic routes, polymeric or inorganic cores as colloids are coated with inorganic layers via wither precipitation or by direct surface reaction with the aid of functional groups that facilitates the coating[177–187]. The predominant method that exemplifies the second method consists of LBL-like self-assembly of preformed inorganic nanoparticles on to the interface of the solid core of interest mediated by electrostatic adsorption[188–195], in

a manner similar to the sequential adsorption of polymeric layers described in the previous paragraph. One can easily notice the procedural simplicity and versatility of the colloidal template methods, with which one can employ to create a large variety of multi-composite colloids. Such creates opportunities engineer physical and chemical properties so as to meet the ever-demanding materials needs to meet the performance requirement for current technology.

1.5.2 Surface roughness

Amongst various manifests resulting from nano-scale processing on the particle surfaces, interfacial roughness is of particular interest. Surface roughness brings about changes in various types of physical properties of colloids and consequently effectuate deviation from expected colloidal behavior. For example, the presence of surface roughness have shown to affect coercivity of magnetic nanoparticles[196]. Furthermore, there have been reports of interesting plasmonic properties with gold multi-branched nanoparticles that display sharp tips[197–199]. In the micro-scale size regime, surface corrugation improves its capture efficiency on a flat plate[200], accredited to alteration of the force balance between the vdW and electrostatic interactions, and improves aerosol performances[201].

1.6 Light scattering [202–204]

Light scattering by particles is depicted as redirection of incident radiation due to interaction with particles. Refraction, reflection and diffraction all fall under the category of light scattering. There are 3 types of scattering. In an elastic scattering process, wavelength of the scattered light is the same as that of the incident light; energy of the light is conserved. Examples include Rayleigh scattering and Mie scattering. In an inelastic scattering process, emitted radiation has a different wavelength from that of the incident radiation, Examples include Raman scattering and fluorescence. Quasi-elastic scattering occurs in a moving scattering centers in which there is shift in the wave frequency in observer's perspectives (Doppler effect).

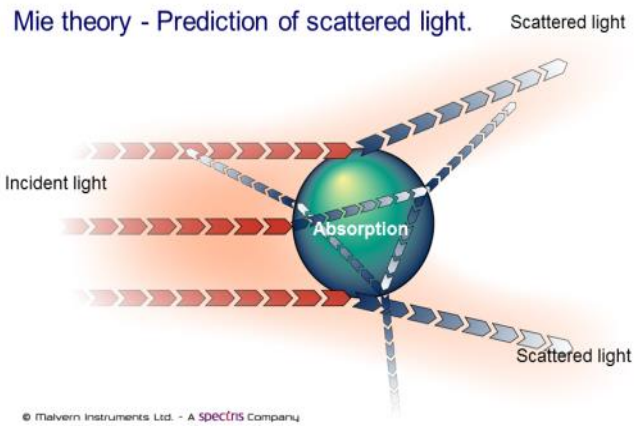

Figure 1.4: Scattered light (image from Malvern Instruments Ltd.)

The elastic scattering is categorized into 3 different scattering regimes. Geometrical scattering applies when the size of the particle is substantially larger than the incident wavelength ($d >> \lambda$), in which Snell's law and Fresnel equations apply. Rayleigh scattering is process in which electromagnetic (EM) radiation is scattered by particles much smaller than the wavelength of the incident light ($d << \lambda$). Typically, the upper limit is taken to be about 1/10 the incident light

wavelength. In this scattering regime, there is no local intensity maxima in the scattering phase function and non-polarized light is scattered in a spatially isotropic fashion. However, as the particle diameter increases, local intensity maxima appears in the scattering phase function accompanied by increase in the forward scattering represented by narrower angle widths. Other features include the following: 1) scattered intensity depends on the wavelength of the incident light and is inversely proportional to λ^4 [205]

$$I = I_o \frac{1 + cos^2\theta}{2R^2}\left(\frac{2\pi}{\lambda}\right)^4 \left(\frac{n^2 - 1}{n^2 + 2}\right)^2 \left(\frac{d}{2}\right)^6 \qquad \text{Eq. 1.5}$$

, 2) polarization remains unchanged between the incident and scattered wave, and 3) the exact shape of the scattering object is usually not very significant and are often treated as a sphere of equivalent volume (with few exceptions [206]). In the Mie scattering regime, the size of the light scattering particles are comparable to that of the incident light wavelengths ($d \sim \lambda$). The scattering phase function has local maxima that is dependent on the EM modes that the cavity supports. Here, the scattering intensity depends on the size, shape and the constitutive properties of the particles. Further complexities are added due to resonant cavity modes within the particles. Furthermore, polarization of light is not conserved between the incident and the scattered wave.

1.7 Mie theory [202,207–210]

Theory of light scattering by a sphere is referred to as Mie theory [211,212]. Mie theory has been utilized to characterize various microparticles [213–218] and aerosols [219–224]. The exact solution to the Mie theory is based on spherical, homogeneous, isotropic, non-magnetic and optically linear particles irradiated by infinite plane wave.

Taking the curl of the following two Maxwell's equation

$$\nabla \times \vec{E} = -i\omega\mu\vec{H} \quad \text{Eq. 1.6}$$

$$\nabla \times \vec{H} = i\omega\varepsilon\vec{E} \quad \text{Eq. 1.7}$$

, results in time dependent vector wave equations

$$\nabla^2\vec{E} + k^2\vec{E} = 0 \quad \text{Eq. 1.8}$$

$$\nabla^2\vec{H} + k^2 H = 0 \quad \text{Eq. 1.9}$$

, where $k^2 = \omega^2\varepsilon\mu$ is the wave vector, ε is the permittivity, μ is the permeability. Multipole expansion of the incident ($\vec{E}_{inc}$) electromagnetic wave in spherical vector harmonics form yields

$$\vec{E}_{inc} = E_o \sum_{n=1}^{\infty} i^{n-1} \frac{2n+1}{n(n+1)} (\vec{N}_{en}^{inc} + i\vec{M}_{on}^{inc}) \quad \text{Eq. 1.10}$$

, where

$$\vec{M} = \nabla \times (\vec{r}\psi) \quad \text{Eq. 1.11}$$

$$\vec{N} = \frac{\nabla \times \vec{M}}{k}$$ Eq. 1.12

, where ψ is a scalar function that satisfies the Helmholtz equation, leading to the vector spherical harmonics $\vec{M}$ and $\vec{N}$ solution to the Helmholtz equation,

$$\nabla^2\vec{M} + k^2\vec{M} = \nabla \times [\vec{r}(\nabla^2\psi + k^2\psi)]$$ Eq. 1.13

, thereby encompassing the properties of the time harmonic electromagnetic field ($\vec{E}(r,t),\ \vec{H}(r,t)$) . Within the expression, *e* denotes even number, *o* denotes odd number and *n* denotes mode number. Only the electric field component is mentioned in this section, as the magnetic component is simply $\vec{H} = -\frac{1}{i\omega\mu}\nabla \times \vec{E}$, or $\vec{H} = \frac{1}{\eta}\vec{k} \times \vec{E},\ \eta = \sqrt{\mu/\varepsilon}$. Hence, solving for $\vec{E}(r,t)$ reduces to solving the Helmholtz scalar wave equation $\nabla^2\psi + k^2\psi = 0$.

Converting the wave equation to spherical coordinates (*r, θ, ϕ*),

$$\frac{1}{r^2}\frac{\partial}{\partial r}\left(r^2\frac{\partial\psi}{\partial r}\right) + \frac{1}{r^2 sin\theta}\frac{\partial}{\partial\theta}\left(sin\vartheta\frac{\partial\psi}{\partial\vartheta}\right) + \frac{1}{r^2 sin\theta}\frac{\partial}{\partial\theta}\left(sin\vartheta\frac{\partial^2\psi}{\partial\phi^2}\right) + k^2\psi = 0$$ Eq. 1.14

, and solving for $\psi(r,\theta,\phi) = R(r)\Theta(\theta)\Phi(\phi)$ by the separation variables leads to

$$\psi_{eln}(r,\theta,\phi) = \cos(l\phi)\, P_n^l(cos\theta) z_n(kr),$$ Eq. 1.15

$$\psi_{oln}(r,\theta,\phi) = \sin(l\phi)\, P_n^l(cos\theta) z_n(kr)$$ Eq. 1.16

, where P_n^l is the associated Legendre functions of the first kind of degree *n* (mode number) and order *l* (order number), z_n represents any of the spherical Bessel functions, j_n (first kind), y_n (second kind), $h_n^{(1)} = j_n(kr) + iy_n(kr)$, $h_n^{(2)} = j_n(kr) - iy_n(kr)$. Any solution of the Helmholtz equation may be expressed as an infinite series of the vector spherical harmonic functions given below:

$$\vec{M}_{eln} = \nabla \times (\vec{r}\psi_{eln}) \quad \text{Eq. 1.17}$$

$$\vec{M}_{oln} = \nabla \times (\vec{r}\psi_{oln}) \quad \text{Eq. 1.18}$$

$$\vec{N}_{eln} = \frac{\nabla \times (\vec{r}\psi_{eln})}{k} \quad \text{Eq. 1.19}$$

$$\vec{N}_{oln} = \frac{\nabla \times (\vec{r}\psi_{oln})}{k} \quad \text{Eq. 1.20}$$

If $\vec{E}_{inc}$ is linearly polarized in the *x* direction and propagating in the *z* direction, the scattered ($\vec{E}_{sca}$) and transmitted ($\vec{E}_{tran}$) electric field is expressed as follows:

$$\vec{E}_{sca} = E_o \sum_{n=1}^{\infty} i^{n-1} \frac{2n+1}{n(n+1)} (a_n \vec{N}_{en}^{sca} + ib_n \vec{M}_{on}^{sca}) \quad \text{Eq. 1.21}$$

$$\vec{E}_{tran} = E_o \sum_{n=1}^{\infty} i^{n-1} \frac{2n+1}{n(n+1)} (c_n \vec{N}_{en}^{tran} + id_n \vec{M}_{on}^{tran}) \quad \text{Eq. 1.22}$$

, where a_n, b_n, c_n and d_n are Mie coefficients. In order to simplify the final expression, Riccati-Bessel functions are introduced (where $\rho = kr$):

$$\psi_n(\rho) = \rho j_n(\rho) \quad \text{Eq. 1.23}$$

$$\chi_n(\rho) = \rho y_n(\rho) \quad \text{Eq. 1.24}$$

$$\xi_n(\rho) = \rho h_n(\rho) \quad \text{Eq. 1.25}$$

The Mie coefficients are obtained by resolving the boundary conditions for the angular components at the surface – tangential components of $\vec{E}$ and $\vec{H}$ is continuous across the spherical boundary of the particle.

$$E_{\theta,inc} + E_{\theta,sca} = E_{\theta,tran} \quad \text{Eq. 1.26}$$

$$E_{\phi,inc} + E_{\phi,sca} = E_{\phi,tran} \quad \text{Eq. 1.27}$$

$$H_{\theta,inc} + H_{\theta,sca} = H_{\theta,tran} \quad \text{Eq. 1.28}$$

$$H_{\phi,inc} + H_{\phi,sca} = H_{\phi,tran} \quad \text{Eq. 1.29}$$

, or in terms of Riccati-Bessel functions,

$$\psi_n(mx)c_n + m\xi_n(x)b_n = m\psi_n(x) \quad \text{Eq. 1.30}$$

$$\psi_n{}'(mx)c_n + \xi_n{}'(x)b_n = \psi_n{}'(x) \quad \text{Eq. 1.31}$$

$$\psi_n(mx)d_n + \xi_n(x)a_n = \psi_n(x) \quad \text{Eq. 1.32}$$

$$\psi_n{}'(mx)d_n + m\xi_n{}'(x)a_n = m\psi_n{}'(x) \quad \text{Eq. 1.33}$$

The expression for the Mie coefficients a_n, b_n, c_n and d_n then becomes

$$a_n = \frac{m\psi_n(mx)\psi_n{}'(x) - \psi_n(x)\psi_n{}'(mx)}{m\psi_n(mx)\xi_n{}'(x) - \xi_n(x)\psi_n{}'(mx)} \quad \text{Eq. 1.34}$$

$$b_n = \frac{\psi_n(mx)\psi_n{}'(x) - m\psi_n(x)\psi_n{}'(mx)}{\psi_n(mx)\xi_n{}'(x) - m\xi_n(x)\psi_n{}'(mx)} \quad \text{Eq. 1.35}$$

$$c_n = \frac{-im}{\psi_n(mx)\xi_n{}'(x) - m\xi_n(x)\psi_n{}'(mx)} \quad \text{Eq. 1.36}$$

$$d_n = \frac{-im}{m\psi_n(mx)\xi_n{}'(x) - \xi_n(x)\psi_n{}'(mx)} \quad \text{Eq. 1.37}$$

, where $x = \frac{2\pi a}{\lambda}$ is the size parameter and *m* is the relative refractive index between the sphere and the propagating medium. The characteristic electromagnetic modes supported within the spherical cavity are called morphology dependent modes and its resonance locations could be determined by computing the poles of the Mie coefficients a_n and b_n.

Expressing the scattered field using the vector spherical harmonic solutions to the vector wave equations ($\vec{M}$ and $\vec{N}$) and the angular functions π_n and τ_n,

$$\vec{E}_{r,sca} = E_o \frac{cos\phi}{(kr)^2} \sum_{n=1}^{\infty} i^{n-1} (2n+1) a_n \xi_n(kr) \pi_n sin\theta \quad \text{Eq. 1.38}$$

$$\vec{E}_{\theta,sca} = E_o \frac{cos\phi}{kr} \sum_{n=1}^{\infty} i^{n-1} \frac{2n+1}{n(n+1)} (a_n \xi_n{}'(kr)\tau_n + ib_n \xi_n(kr)\pi_n) \quad \text{Eq. 1.39}$$

$$\vec{E}_{\phi,sca} = -E_o \frac{sin\phi}{kr} \sum_{n=1}^{\infty} i^{n-1} \frac{2n+1}{n(n+1)} (a_n \xi_n{}'(kr)\pi_n + ib_n \xi_n(kr)\tau_n) \quad \text{Eq. 1.40}$$

, where

$$\pi_n = \frac{P_n^1(cos\theta)}{sin\theta} \quad \text{Eq. 1.41}$$

$$\tau_n = \frac{dP_n^1(cos\theta)}{d\theta}$$ Eq. 1.42

If the observation (detector) of the scattered light is positioned such that

$$kr \gg (\frac{d}{\lambda})^2$$

, where *r* is the distance between the observation point and the scattering center and λ is the wavelength of light, the Ricatti-Bessel function describing the scattered field reduces to

$$\xi_n(kr) = i^{n+1}e^{-ikr}$$ Eq. 1.43

$$\xi_n{}'(kr) = i^n e^{-ikr}$$ Eq. 1.44

One can note that only $\vec{E}_{\theta,sca}$ and $\vec{E}_{\phi,sca}$ contributes to the far-field scattering pattern as the angular components are proportional to kr^{-1} while the radial component $\vec{E}_{r,sca}$ is proportional to kr^{-2}.

$$\vec{E}_{\theta,sca} = E_o \frac{e^{-ikr}cos\phi}{ikr}\sum_{n=1}^{\infty} i^{n-1}\frac{2n+1}{n(n+1)}(a_n\tau_n + b_n\pi_n)$$ Eq. 1.45

$$\vec{E}_{\phi,sca} = -E_o \frac{e^{-ikr}sin\phi}{kr}\sum_{n=1}^{\infty} i^{n-1}\frac{2n+1}{n(n+1)}(a_n\pi_n + b_n\tau_n)$$ Eq. 1.46

, from which scattered intensity normalized to the incident intensity can be obtained

$$I_\theta = I_\parallel = \left| \sum_{n=1}^{\infty} \frac{2n+1}{n(n+1)} (a_n \tau_n + b_n \pi_n) \right|^2 cos^2\phi \qquad \text{Eq. 1.47}$$

$$I_\phi = I_\perp = \left| \sum_{n=1}^{\infty} \frac{2n+1}{n(n+1)} (a_n \pi_n + b_n \tau_n) \right|^2 sin^2\phi \qquad \text{Eq. 1.48}$$

, where $\parallel$ and $\perp$ represents the polarization of the scattered field in relations to the scattering plane. Here, it could be noted that for $\theta = 0^o$ and $\theta = 90^o$ detection angles relative to the polarization of $\vec{E}_{inc}$, polarization of the scattered field is the same as the incident field. For all other angles, combined contribution of I_θ and I_ϕ is required.

Chapter II

Scale-up Production of Inverted Colloidal Crystal (ICC) CellCulture Scaffolds in Well-plate Format for Early Stage Organ Mimetic Drug Testing Platform

2.1 Background

Advancement in pharmaceutical science and technology has seen a rapid growth in the drug development. Despite the current knowledge from scientific research and multi-disciplinary engineering, it still takes an average of 15 years and $1.2 billion for a new drug to reach the market. In addition, approximately 2.2 million people suffer from pharmacological toxicities in the U.S. annually, of which approximately 100,000 is fatal.

The modern drug discovery and development process consists of several major stages. However, there are pitfalls stemming from the early-stage *in vitro*

testing. One reason for poor translation of early stage and preclinical data to the human trials (clinical phases) is the lack of effective *in vitro* assay platforms. The 2D substrates, such as micro-well plates and Petri-dishes, dominate the early stage *in vitro* culture platforms. However, over 30 years of research have shown distinct cell behaviors and responses in 3D culture systems which are not observed in 2D monolayer cultures. Moreover, cell phenotypes from the *in vitro* 3D cultures have shown close relevance to *in vivo* physiology. Absence of such complex mechanical and biochemical interplay in 2D cultures often lead to disoriented biological properties and distorted cell responses. With lack of appropriate contextual background environments observed *in vivo*, it is not surprising that over 90% of drugs that were approved in the early stage and the preclinical testing fail in human clinical phases. In fact, 75% of the cost of new drug development is spent on failures concentrated on early stages.

Aiming to minimize both duration and the cost of the development, we propose to develop high-throughput drug testing systems with 3D scaffolds. The 3D scaffolds will be intended for compatibility with well-plates, the standard substrate for high-throughput system. It will have porous inverted colloidal crystal (ICC) structure mimicking several organs *in vivo*. It will be transparent for amenable for optical instrumentation, the predominant mode of analysis for high-throughput system. The 3D ICC scaffolds will be standardized with consistencies in material properties and highly ordered and uniform geometry. Lastly, large number of scaffolds is required to have a meaningful transition to high-throughput

format. New manufacture process will be developed that will have a significant impact on the production of the scaffolds in terms of rate and cost.

2.2 Introduction

In the United States cancer is the second leading cause of mortality accountable for 25% of all deaths, killing approximately 590,000 people[225]. Despite such heavy toll in human mortality, death rates from cancer have been falling since the early 90's. Such notable decline in cancer death rates may be attributed to significant progresses in the anticancer drug development.

Despite increasing success rates, most of the common chemotherapeutic drugs practiced today cause adverse reaction-, dose-, or duration-dependent side-effects, termed pharmacological toxicity, due to non-specific toxicities of the drugs on healthy cells. Approximately 2.2 million people suffer from pharmacological toxicities in the U.S. annually, of which approximately 100,000 is fatal[226]. Inasmuch as their mechanisms of actions are to disrupt the cell cycle, the side effects are predominant on cells with rapid turnover including bone marrow cells, gastrointestinal cells and hair follicle(Newell 1964). Cardiac, hepatic, renal and lung toxicities have also been observed through such agents[227–230]. One very important question arises. How did such drugs make it to the clinical phases with misinterpreted margin of therapeutic safety profile?

A new drug discovery and development is a multi-stage process: early stage testing, preclinical phase, clinical phases (I, II, III) and approval phase

(IV)[231]. The early stage consists of large scale *in vitro* screening (target identification, validation, screening and lead optimization) where most of the work done is through cell-based assay. However, there are pitfalls stemming from the preclinical strategies. One reason for poor translation of preclinical data to the human trials (clinical phases) is the lack of effective *in vitro* assay platforms. The 2D substrates, such as micro-well plates and Petri-dishes, dominate the early stage *in vitro* culture platforms. 2D substrates are simple and convenient to use, are shown to exhibit high viability culture, and have served well to the biomedical and pharmaceutical sciences. However, over 30 years of research have shown distinct cell behaviors and responses in 3D culture systems which are not observed in 2D monolayer cultures. Moreover, cell phenotypes from the *in vitro* 3D cultures have shown closer relevance to *in vivo* physiology[232]. For example, normal breast epithelial cells cultured in 3D environment resulted in the formation of organized, growth-arrested acini structure. However, 2D monolayer cultures exhibited highly plastic behavior whose phenotype resembles its cancerous counterpart *in vivo* [233–236]. This results from loss of normal cell morphology due to alteration in mechanical and microenvironment cues -- by forcing cells to adjust to flat and rigid substrates. In another instance, etoposide, an inhibitor of the enzyme topoisomerase II used in chemotherapy, exhibit excellent suppression of melanoma in 2D cultures. However, it shows much reduced sensitivity in the more realistic 3D collagen-implanted spheroid culture[236].

Cells *in vivo* reciprocally interact with adjacent cells as well as to extracellular matrix (ECM) in 3D environment through integrins[237–240]. The ECM components, its mechanical properties and 3D topology are tissue specific and mediate a multitude of physiological responses, including growth, proliferation, migration and metabolism[241]. Absence of such complex mechanical and biochemical interplay in 2D cultures often lead to disoriented biological properties and distorted cell responses.

With lack of appropriate contextual background environments observed *in vivo*, it is not surprising that over 90% of drugs that were approved in the early stage and the preclinical testing fail in human clinical phases. In fact, 75% of the cost of new drug development is spent on failures concentrated on early stages[242,243]. It is estimated that a successful drug formulation can take up to $1.2 billion in capital and up to 15 years in time, one of the main components in increasing health care expenditure.

Evidences in academics as well as in industries indicate reasoned necessities to develop an enhanced high-throughput drug testing systems with 3D testing platform to minimize the development expenditure and duration. In this proposal, we aim to address this issue by developing and implementing 3D scaffolds into the current high throughput drug testing system on the basis of both standard well-plate readers and high content analysis (HCA) systems through integration into 2D well-plate formats.

An ideal substrate for *in vitro* drug testing should at least meet the following inherent and performance characteristics. First, the substrate should be biocompatible and recover original cell function to a certain degree. Second, the scaffolding material should have high degree of transparency as the current *in vitro* drug testing assays are characterized by optical-based instruments. Third, the manufacturing should be easy to bulk produce at low-cost as thousands of scaffolds are required for high throughput screening. And the last, lot-to-lot variability and xenogenic effects should be eliminated by avoiding heterogeneous materials selection and inconsistent topography in the design. In short, the scaffolds must be standardized.

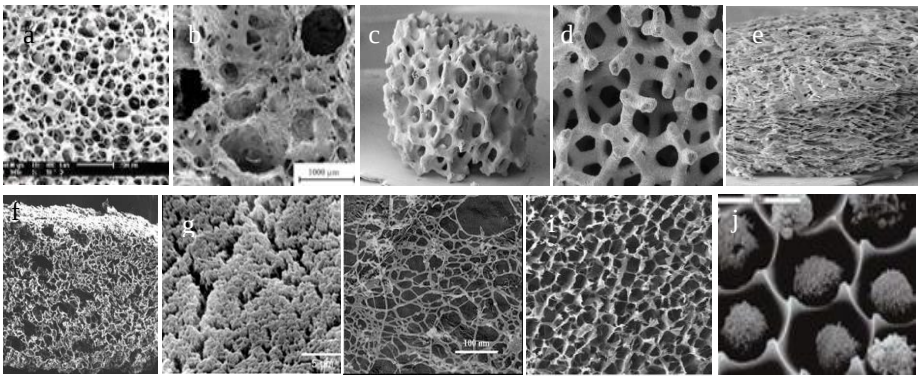

Figure 2.1. (a) PGA & PLA scaffolds (Synthecon), (b) Vitoss® (Orthovita), (c) BD™ 3D calcium phosphate (BD Biosciences), (d) Carbon fiber (Cytomatrix), (e) BD™ collagen compsite (BD Biosciences), (f) Open-celled PLA (BD Biosciences), (g) Matrigel ™ (BD Biosciences), (h) Puramatrix™ (3DM), (i) Algimatrix™ (Invitrogen), (j) Optical LiveCell® Array (Molecular Cytomics)

Diverse types of 3D scaffolds have been developed to date and are available commercially**, Figure 2.1**. Scaffolds shown in **Figure 2.1.a-f** are tissue engineering and therapeutics driven and the features they are not suitable to use in the early stage drug discovery platform. They lack transparency which renders

inaccessible to optical-based systems (for analysis) and inaccessible to UV light (for sterilization). In addition, the structural inconsistencies lead to scaffold-to-scaffold variability that may raise a question mark to the reproducibility of the assays. Moreover, most of these scaffolds are not cheap to fabricate. The scaffolds in **Figure 2.1.g-j** may have potentials in the in vitro assays. However, each possesses critical disadvantages. The components of Matrigel™ (**Figure 2.1.g**) are poorly characterized due to heterogeneity and are animal origin which may induce xenogenic effects. In addition, Matrigel™ is a gel encapsulating 3D scaffold, which will cause disadvantages in the inoculation and culture of non-adherent dispersion cells, motility of adherent cells, nutrient diffusion and cell retrieval for analysis. The AlgiMatrixl™ (**Figure 2.1.h**) is quite homogeneous and well characterized. The major disadvantage of AlgiMatrixl™ is its stochastic structure and the lack of control in its pore sizes. The PuraMatrix™ (**Figure 2.1.i**) is transparent with well-defined and homogenous material composition. However, it suffers the drawback of being a gel encapsulation matrix. The Optical LiveCell® (**Figure 2.1.j**) has excellent transparency and highly controlled micro-scale structure. However, it is expensive and it is not a true 3D structure. Summarizing, their inherent properties all lack standardization in 3D format and/or obstruct with post-culture analysis.

The ICC 3D hydrogel scaffolds for cell culture, developed in Kotov group, are born of unique manufacturing process whose inherent material and geometric

characteristics combine to possess exceptional substrate properties not observed in other 3D scaffolds. It has unique topology in the shape of an inverted replica of a colloidal crystal featuring spherical cavities with interconnected channels[102,104,106,244]. The substrate material is if a hydrogel variety made by free radical (co-)polymerization with acrylamide types, whose composition types and constitution percentages may vary depending on the intended culture types.

The unique ICC topology allows the following advantages as a 3D *in vitro* culture system: (1) high surface area (2) efficient nutrient delivery through the interconnecting channels (3) culture of both dispersion and adherent cell types (4) facile cell inoculation and extraction (5) structural (spherical cavities with interconnecting channels) resemblance of *in vivo* organs, such as bone marrow and thymus, pancreas. The synthetic hydrogel as the substrate material is a suitable substrate material due to the following: (i) can be well characterized (ii) homogenous material selection avoids lot-to-lot variability (iii) negates xenogenic effects due to synthetic material not being of animal origin (iv) provides tissue-like mechanical property (vi) high transparency allows for optical-based evaluation protocols and easy UV-sterilization.

Combination of unique manufacturing process with the unique material properties renders 3D ICC scaffolds suitable for *in vitro* early stage drug testing platform: (a) consistent geometric dimensions and material properties reduces experimental variability, (b) exceptional structural controllability allows

optimization of cellular microenvironment, (c) allows easy integration into well-plate, the most common format used in the pharmaceutical and biotech industries.

Currently, the implementation of the 3D ICC scaffolds to the high-throughput format requires a technique to mass-produce at a low cost and at higher rate. In terms of cost, fabrication of the colloidal crystals was identified to be one of the major hurdle, which requires purchase of highly mono-disperse solid polystyrene (PS) microparticles. In order to increase the production rate, a streamlined method to fabricate scaffolds in multiplicity per synthesis cycle - self-assembly of the microspheres into colloidal crystal and subsequent stages for conversion into ICC hydrogel scaffolds – needs development. The scaffold production rate from the current synthesis protocol, which was designed to fabricate each scaffolds one at time, is unrealistic to match the needs that is required for implementation towards high-throughput format. The majority of **chapter 2** will be devoted towards manufacture protocol that will enable a step closer to realizing the implementation and integration of 3D ICC scaffold platform towards high-throughput drug testing systems and infrastructures.

2.3 Microfluidics-based polystyrene microparticle synthesis

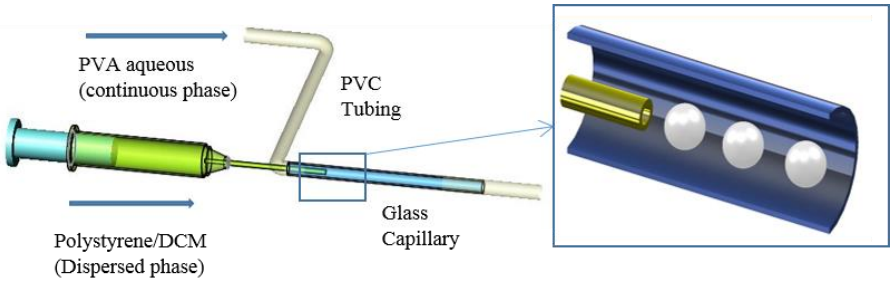

Figure 2.2. Schematics of fluidic devices and bead formation

Taking into account a large number of parallel experiments required for the drug testing, it was necessary to produce in vast quantity with minimal expense. One of the major obstacle to implement 3D ICC hydrogel scaffolds was the cost, of which, commercial mono-disperse PS microbeads are the single cost-limiting components in the fabrication of 3D ICC scaffolds. It was required to synthesize highly mono-disperse PS microbeads in-house at a low-cost. Developing a simple and very cost-effective method to synthesize highly mono-disperse PS microbeads was estimated to reduce the fabrication cost by more than 95%.

As such, the mono-disperse PS microbeads were synthesized via simple microfluidics-based emulsion[245,246]. The microfluidic device consisted of simply PVC tubing, syringe needles, and a glass micro-capillary tub. **Figure 2.2** shows the schematics of the microfluidic device. PS solution dissolved in

dichloromethane (DCM) served as the dispersed phase and aqueous solution of poly(vinyl alcohol) (PVA) served as stabilizer-containing continuous phase. The two phases were continuously introduced using two syringe pumps at two independently adjustable flow rates. The two phases formed a co-flow stream from the tip of the needle, where the dispersed phase was introduced, in the glass micro-capillary. A droplet formed and enlarged at the tip of the needle. When the droplet grew to a certain size, drag force due to the co-flowing continuous phase exceeds the interfacial tension and the droplet was pinched off. Since the continuous phase completely surrounds the dispersed phase, the drops were quickly adsorbed by the stabilizer to form stable emulsion and clogging due to polymer debris at the tubing wall can be avoided, **Figure 2.4**. The resultant droplets were collected and subsequently solidified by DCM evaporation in the oven at 37 °C.

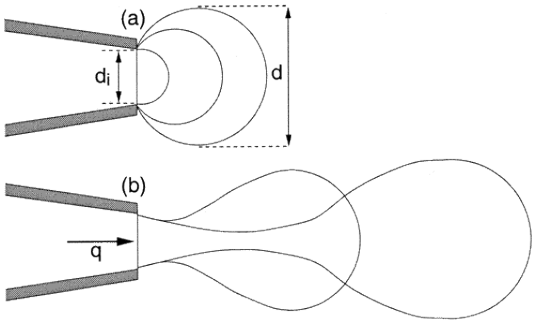

Figure 2.3. (a) Droplet growth, (b) Detachment[1]

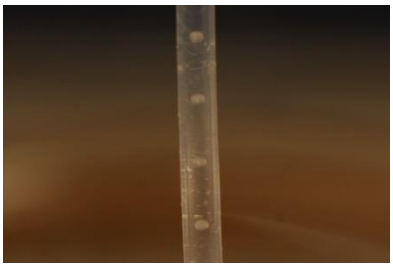

Figure 2.4. Stabilized droplets downstream

The diameter of the PS microbeads were controlled by adjusting the flow rate of each phase, as well as the PS concentration of the dispersed phase. The effect on the variation of the flow rate of each phase on the average diameter of

the PS microparticle was investigated by holding the flow rate of one of the phase constant.

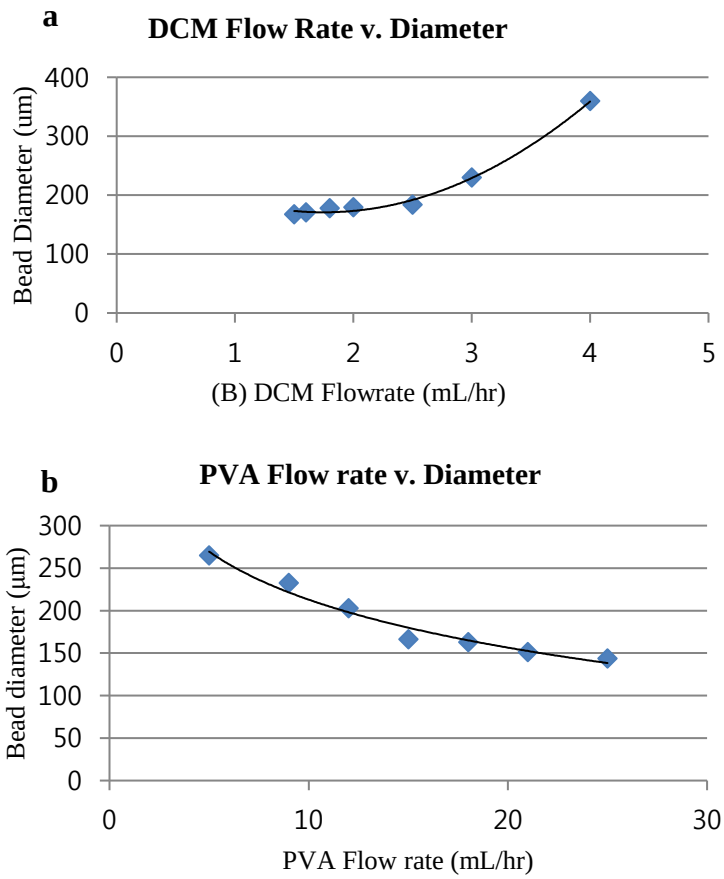

Figure 2.5. The effect of the flow rate of each phase on the diameter of the PS microbeads; (**a**) variation in the dispersed phase flow rate, (**b**) variation in the continuous phase flow rate

Figure 2.5.a shows the control of the bead diameter through variation in the dispersed phase flow rate; increase in the disperse phase flow rate resulted in increase in the bead diameter. This is expected as there is an increase in the polymeric content in the emulsion. **Figure2.5.b** shows bead diameter is control by varying the continuous phase flow rate; increase in the continuous phase flow rate resulted in decrease in the bead diameter. This is due to increase in the shear stress imposed on the droplet which shortened the growth time. We chose variation in continuous phase as the mode to control the bead diameter as production yield of PS microbeads was heavily dependent on the dispersed phase flow rate.

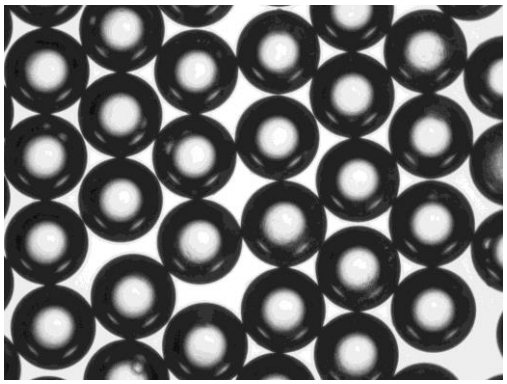

Figure 2.6. Mono-disperse PS

We initially aimed to synthesize PS microbeads ranging from 150 to 200 μm to resemble the dimensions of the inter-connecting cavities in the bone marrow. **Figure 2.6** shows images of PS microbeads synthesized with 10% PS/DCM at 3ml/hr co-flown with 10% aqueous PVA at 15ml/hr. The beads were highly mono-disperse with coefficient of variance of 1.2% and average diameter at 166.7 μm (taking out the occasional outliers).

2.4 Hydrogel as scaffolding materials

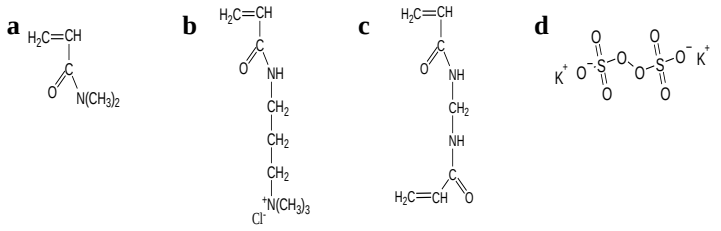

Figure 2.7. (a) N,N-Dimethylacrylamide (DMAA), **(b)** (3-Acrylamidopropyl)-trimethylammonium chloride (AMTAC) **(c)** N, N'-Methylene-bis-Acrylamide (NMBA), **(d)** Potassium Persulfate (KPS)

Hydrogel was employed as the substrate material for the ICC scaffold due to similar mechanical properties to tissues and ECM[247]. In particular, a cationic polyelectrolyte hydrogel, poly(DMAA-co-AMTAC), was developed as positively charged nature of the hydrogel surface was expected to promote cell-adhesion without further surface modification. Previously, surface modification via LBL with clay and oppositely charged polyelectrolyte was required to render the surface cell-adhesive[104]. In addition, from the previous studies, it was found that positively charged surfaces promoted cell adhesion due to protein absorption, either from the serum or from cell secretion, which in turn was anchored by cells through integrin. In addition, the electrostatic force between the negatively charged cell membrane also promotes cell adhesion[248–250].

The poly(DMAA-co-AMTAC) polyelectrolyte cationic hydrogel was synthesized by free radical initiated co-polymerization of DMAA and AMTAC, chemically cross-linked by NMBA in aqueous condition. The poly(DMAA-co-AMTAC) hydrogel, similar to typical polyelectrolyte hydrogel having charged

moieties embedded in to the backbone network, showed sensitivity to external factors such as pH, ionic strength and electrical fields[251,252]. The DMAA was chosen due to its hydrophilicity and biocompatibility, as evidenced by its uses as one of the main polymeric ingredients in contact lenses[253].

2.5 Biocompatibility of cell-adhesive polyelectrolyte poly(DMAA-co-AMTAC) hydrogel

Biocompatibility-Cytotoxicity of the poly(DMAA-co-AMTAC) hydrogel was evaluated prior to its incorporation as substrates for the 3D ICC scaffolds. Slabs of hydrogel discs were cut and sterilized, and HS5 human marrow stromal cell lines were initially cultured on the top of the slabs. The gels were pre-immersed in the culture medium, 90% Dulbecco's Modified Eagle's Medium (DMEM) supplemented with 10% Fetal Bovine Serum (FBS) and 1% penicillin-streptomycin, for 3 hours prior to culture. The result was positive showing cell viability, **Figure 2.8**. Currently available numerous selection of hydrogels, while non-toxic, require post-operative treatment to facilitate cell

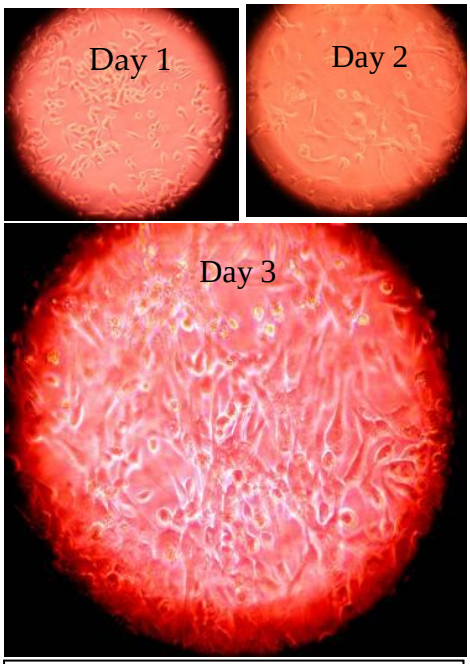

Figure 2.8 The HS5 stromal cell lines were cultured on 2D disc-like slabs of poly(DMAA-co-AMTAC) for 3 days. Adherence to the gel was confirmed at day 1. Cells were seen to proliferate as can be seen at the third day of the culture.

adhesion[247]. This is due to lack of cell receptors to hydrogel forming polymers. However, poly(DMAA-co-AMTAC) gel promotes cell adhesion through electrostatic force between the anionic cellular membrane and the cationic gel surface. Hence poly(DMAA-co-AMTAC) hydrogel provides a suitable substratum to support adhesion and growth of anchorage-dependent cells without the introduction of other biological cues or chemical modifications.

2.6 Fabrication of ICC hydrogel scaffolds

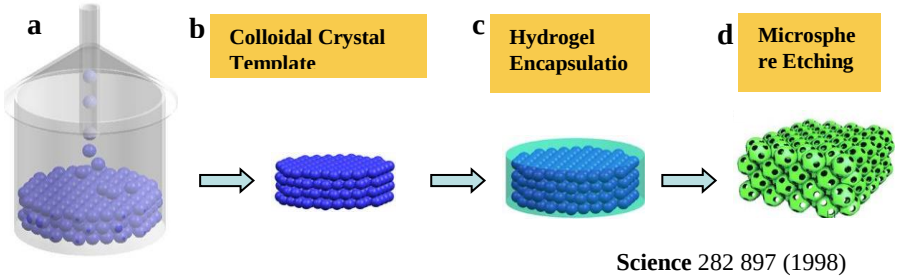

Figure 2.9. Fabrication Process: (**a**) sedimentation of colloidal crystal, (**b**) thermal annealing, (**c**) encapsulation with hydrogel, (**d**) etching of the microspheres[2]

Colloidal crystals were used as an invertible mold for the 3D cell culture scaffold. The fabrication process was based on "agitation while sedimentation", **Figure 2.9**. First, the plastic centrifuge tubes were fused with Pasteur glass pipettes. The centrifuge tube was used as the mold for the CC construction and the pipette was used to lower the sedimentation rate of the PS microspheres by forcing them through a narrow channel. The tube-pipette complex was filled with

isopropanol and was mounted on the top of an upside-turned glass beaker. The whole system was then placed on the ultrasonic bath. One drop of PS microsphere/isopropanol solution was discharged at the top of the complex once every 15-20 minutes while sonication. The sonication provided enough agitation that, upon reaching the bottom of the mold, the PS microspheres positioned themselves in the lowest energy spots and enabled highly packed ordered crystalline arrays. The sedimentation process took place in isopropanol so as to increase the buoyancy to the PS beads, resulting in a better crystalline structure and preventing large displacements

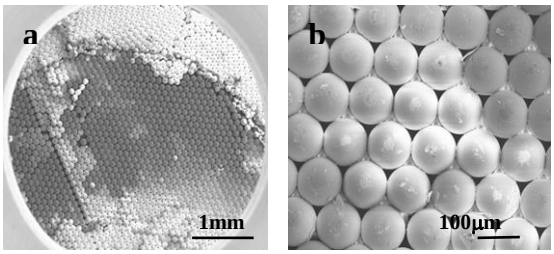

Figure 2.10. (**a,b**) SEM images of colloidal crystals made of 160µm polystyrene microspheres

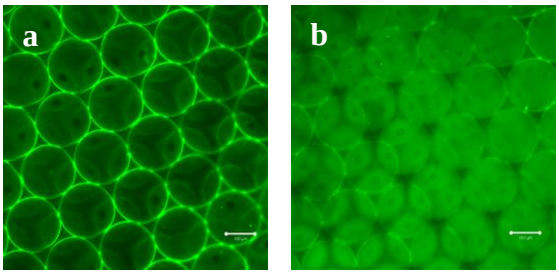

Figure 211. (**a**, **b**) 3D ICC poly(DMAA-so-AMTAC) scaffolds absorbed with FITC-BSA, taken with confocal microscopy (scale bar, 100µm)

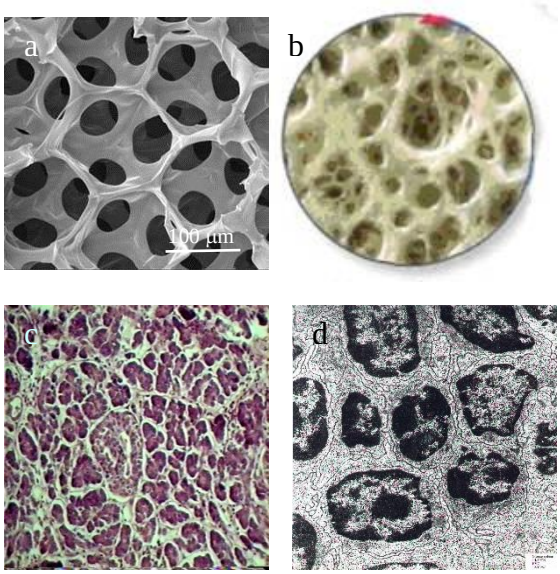

Figure 2.12. Morphological resemblance between (**a**) our ICC scaffold, (**b**) actual bone marrow, (**c**) Pancreas, **(d)** Spleen

which might shatter the ordered array. After the thickness of the CC grew to the desired height, the CC was dried at 60 °C overnight and heat treated for 4 hours at 120 °C while still in the tube mold. The heat treatment caused partial melting at the surfaces, which resulted in annealing of PS microspheres with their adjacent neighbors. The resulting CC was then easily extracted from the mold, **Figure 2.10**. Upon the fabrication of colloidal crystal, the poly(DMAA-co-AMTAC) precursor was infiltrated into the CC via centrifugation. Low viscosity of the precursor solution ensured complete infiltration in between the spherical units. The polymerization was initiated by adding aqueous KPS solution (3 w/v%) at a ratio of 1:10 by volume in an oxygen free environment and completed by further heat treatment at 75 °C for two hours and at 60°C overnight. After polymerization, excess hydrogel pieces were removed and the hydrogel encapsulated CC was then immersed in a THF bath for 48 hours to extract the internal PS microspheres resulting in a disc-shaped 3D ICC polyelectrolyte hydrogel tissue culture scaffold, **Figure 2.11**. Morphological resemblance of the 3D ICC scaffolds to the *in vivo* organs, **Figure 2.12**, makes such scaffolds suitable for structural supports in creating artificial organ *ex vivo*, thereby adding further adds significance.

2.7 Cell culture

Preliminary studies on the suitability of the scaffolds to several types of cells relevant to creating a niche in modeling artificial organs *ex vivo* was undertaken. Creating artificial organ *ex vivo* in well-plate format for the high-throughput analysis should further mimic actual physiological outcome in response to therapeutic compounds. This is expected to further reduce the development cost and duration. As an example, human bone marrow stromal cell lines, HS-5, and human erythroleukemia cell lines, K-562, were cultured in the 3D ICC poly(DMAA-co-AMTAC) scaffold for 3 weeks. The viability of the cells were evaluated by using calcein AM and ethidium homodimer staining. The outcome indicated good compatibility and cell viability, **Figure 2.13**, with excellent cell attachments visible along the walls of each cavity.

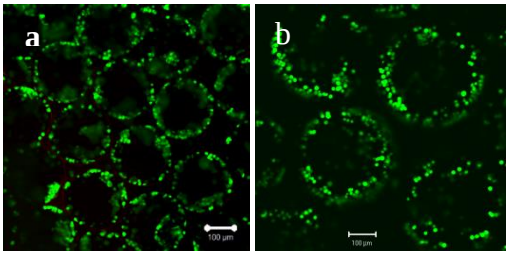

Figure 2.13 (**a**) HS-5, (**b**) K-562 in cell-adhesive 3D ICC poly(DMAA-co-AMTACC) hydrogel scaffolds

In addition, primary fetal human thymic epithelial cells (HUTEC) were in cultured in the poly(DMAA-co-AMTAC) ICC scaffolds to evaluate its suitability with primary cells. The culture duration of these samples was 4 weeks and the primary cells also exhibited good viability, **Figure 2.14a, b**. In order to further investigate the affinity of poly(DMAA-co-AMTAC) to cells, the scaffold was placed on the top of a confluent monolayer of HUTEC grown in a 48-well plate. The scaffold was then carefully removed and the side facing the cell layer was imaged. The cells migrated from the well plate into the scaffold, **Figure2.14.c**.

Moreover, the cells were found to migrate out of the scaffold onto the tissue culture multi-well. The fluorescence of the scaffold was a result of excitation from a Helium-Neon laser at 543nm at which the materials inherent auto-fluoresce. The settings of the confocal microscope were adjusted in order to enhance the scaffold's auto-fluorescence.

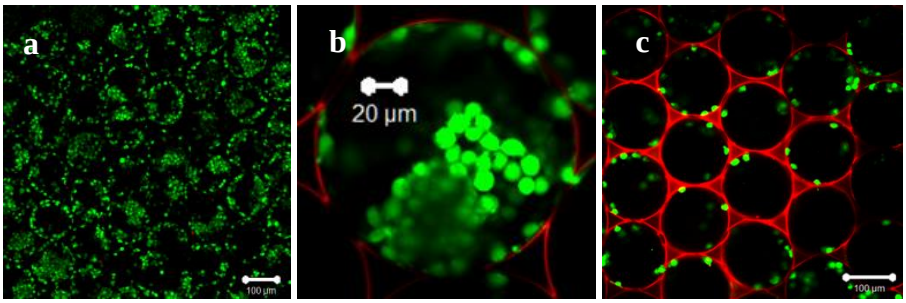

Figure 2.14 Confocal microscopy images of HUTEC cultured in a poly(DMAA-co-AMTAC) ICC hydrogel scaffold. (**a, b**) HUTEC cultured in %A=12.5%, %C=0.5% scaffold. The duration of culture for this sample was 4 weeks. (**c**) Migration of HUTEC from the bottom of the multi-well to the scaffold. The auto-fluorescence of the scaffold in addition to adjustment in the confocal microscopy settings enabled visualization of the scaffold.

When culturing epithelial cell types on ICC scaffolds made of non-adherent poly(acrylamide) hydrogels, formation of spheroids were noted, as was reported previously by Lee et. al[105]. The concept was further expanded towards co-culture of hepatocytes, HepG2, with prostate cancer stem cells, WPE-stem. **Figure 2.15.a, b** shows that individual cultures of both HepG2 and WPE-stem each yielded spheroid formation. Co-culture of WPE-stem and HepG2 at a 1:20 ratio yielded embedding of prostate cancer stem cells amidst spheroidal HepG2, **Figure 2.15.c-e**.

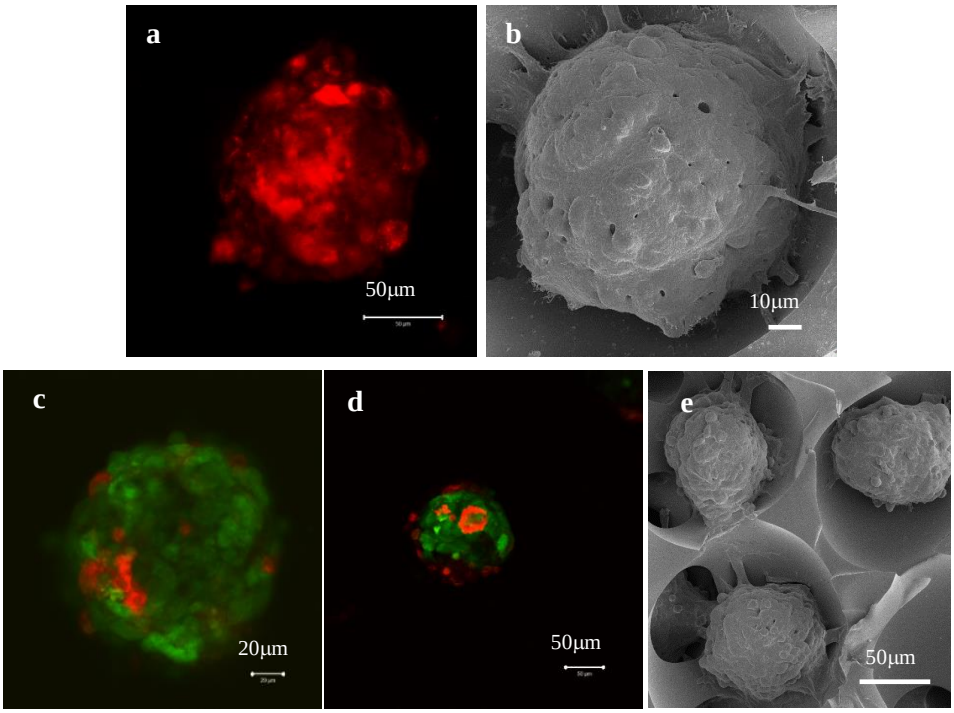

Figure 2.15 Spheroid formation on ICC scaffolds with non cell-adherent poly(acrylamide) hydrogels as substrate materials. Spheroid formation with (**a**) prostate cancer stem cells (WPE-stem), (**b**) hepatic epithelial cells (**c-e**) co-culture of WPE-stem with HepG2. The WPE-stem are embedded in the HepG2 spheroids, which could be used as model for cancer stem cell metastasis

Numerous seeding ratios between the WPE-stem and HepG2 cells were inoculated, and for all seeding ratio, the hetero-cellular interaction suppressed the growth of WPE-stem. Further evidence could be found in the confocal microscopy image, **Figure 2.15c, d**, where much higher stain intensity

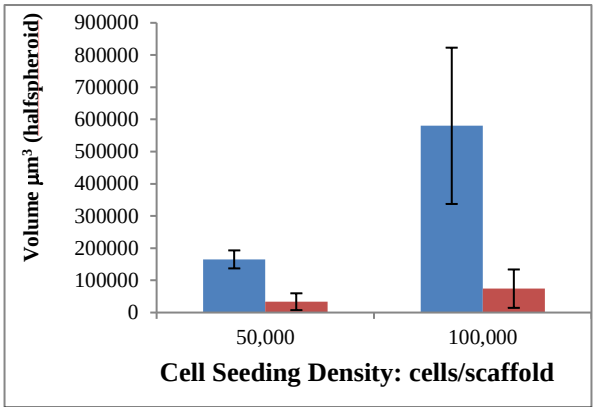

Figure 2.16. Heterocelluar interaction, represented by WPE-stem/HepG2 co-culture (red), suppresses growth potential of the WPE-stem, when compared to its mono-culture (blue)

indicates lack of proliferation. This may serve as a cancer stem-cell metastasis model in well-plate high-throughput format.

2.8 Scale-up production of colloidal crystals

The colloidal crystals were constructed individually in a single disposable mold. The excessive hydrogel was removed by hand and the template was etched one scaffold at time, requiring huge man-power and excessive manufacture time. Such necessitated new manufacture platforms and methods to streamline the fabrication process so as to eliminate intermediate stages and to produce scaffolds in multiplicities at a quicker rate.

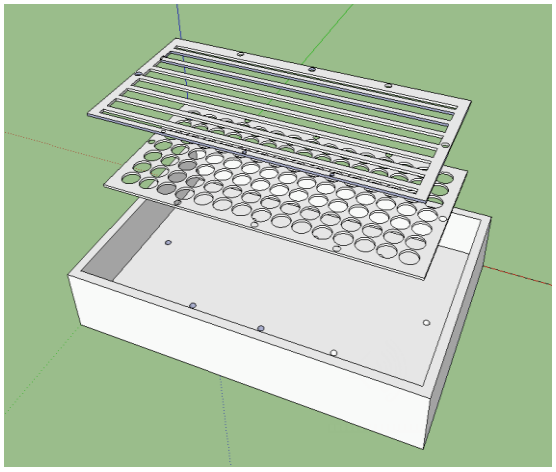

Figure 2.17. Schematics of the mold setup for fabrication 3D ICC scaffolds

The new manufacture protocol utilized a support dish, a perforated sheet as a mold for CC, a mesh and a lid, **Figure 2.17**. The support dish was designed to fit into a 1) microplate reader or Genie vortex for vibration assisted construction of CC and into a 2) swing bucket rotor for

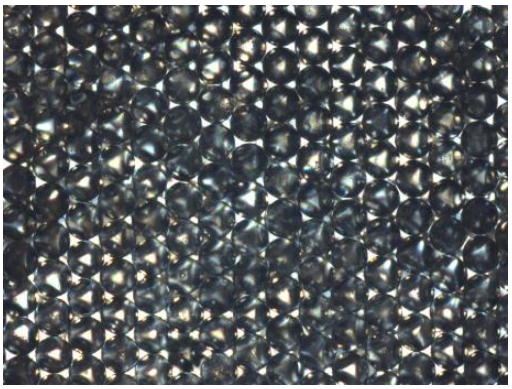

Figure 2.18. Optical images of CC constructed via vibration from microplate reader

centrifugation necessary for infiltration of hydrogel precursor. It was found that both the microplate reader microplate attached vortex Genie increased the ordering of the PS microbeads in the construction of the CC, **Figure 2.18**, with significantly less time. The support dish was made of delrin. Delrin was chosen due its light weight, easy to machine and resistance to harsh solvents such as THF. The mold for CC was made of perforated fiber glass sheet with 500μm in thickness. The mesh was made of fiberglass and this was fastened on top of the mold to secure the scaffolds in place during centrifuge and polymerization. Such design allowed entire manufacture processes, from the construction of the CC and subsequent conversion into the 3D ICC scaffolds, in a single setup.

Figure 2.19. Scale-up production of 3D ICC poly(DMAA-co-AMTAC) hydrogel scaffolds

In a typical demonstration, the fiberglass mold was fastened onto the Delrin support dish. The support dish was filled with isopropanol and mechanically agitated with well-plate reader or Genie vortex after each deposition of a monolayer of PS microbeads. After leveling the height with the mold, the isopropanol was completely dried and the beads were annealed in oven for 4 hours at 137 °C. Subsequently, the setup was filled with the hydrogel pre-polymer and the mesh were secured on the of the fiberglass mold. The whole setup was subjected to

centrifugation for thorough infiltration of hydrogel and heat treatment for polymerization. The setup was then disassembled and the excess hydrogel will removed by scraping the top of the fiberglass mold containing hydrogel infiltrated CC. The advantages of the aforementioned setup includes the following: 1) features re-usable mold, 2) significantly reduces hydrogel precursor-solution required per scaffold, 3) enables multiplicity in the scaffold production per manufacture cycle, thereby significantly reducing the required man-power.

2.9 Integration into micro well-plates

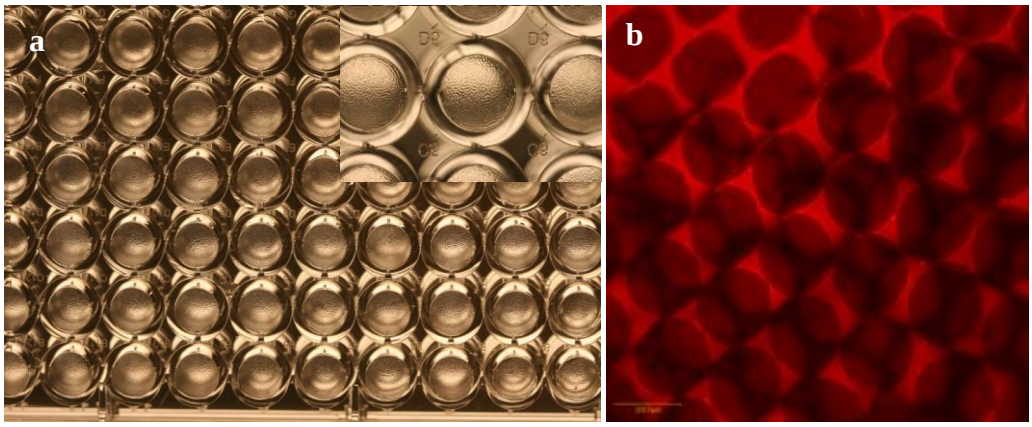

Figure 2.20. (a) Optical image of 3D ICC scaffolds tightly conformed into a 96 well plate, (b) confocal microscopy image of the scaffold stained with rhodamine B. The base framework is not affected by the restraint from the well-plate side walls.

Analytical instrumentations for early stage phases, such as those for automated high throughput screening (HTS), are designed around the micro well-plates. In order to render the 3D ICC scaffolds compatible with current drug testing procedures and fully integrated into current pharmaceutical infrastructure, the scaffolds are tightly morphed into the micro well-plates. The width of the CC

was designed in order to account for volume transition properties of poly(DMAA-co-AMTAC) hydrogel when immersed in cell culture media.

2.10 Outlook

Further work needs to be done to demonstrate the significance of introducing 3D ICC scaffolds in the early stages of drug development assays. Introducing the best possible physiological mimicry in high-throughput format during the early stage high-content analysis may bring about significant financial impact as well as expansion of resources for further therapeutics development for challenging diseases. For example, detection of compound associated non-specific toxicities, whose target may be the surrounding epithelial cells and ECM, and identification of false positives at early stages by monitoring the response of scaffolds as an organ unit could be envisioned.

As such, supplemental research could be devoted to modeling variety of artificial organs *ex vivo*. For example, bone marrow replicas *ex vivo* had been modeled with the 3D ICC scaffolds with aim to achieve continuous source of transplantable blood cells and to serve as laboratory model for investigation of immune diseases and drug toxicology[107]. In addition, comparison of the *ex vivo* bone marrow model, in terms of cell-stromal and cell-cell interactions, artificially recreated in 3 different types of 3D scaffolds have also been evaluated[108]. Expansion of currently existing bone marrow models into metastatic model, such as survival of prostate cancer stem cells, differentiation/proliferation and its

progenies, and their effect on the bone marrow niche, would provide holistic representation. Different models of human bone marrow could be constructed by simply tailoring appropriate ECM contexts in the scaffolds. This may produce outcomes with clinical relevance at the early stages, reduce the amount of currently required animal models and ultimately reduce high attrition rates.

Furthermore, due to physiological barriers imposed on the compounds in their free form, targeted drug delivery systems (DDS) based on nanotechnology have been employed to increase the therapeutic effects, whose development to market transition has been ineffective. Current knowledge achieved in biological principles indicates that such setbacks could be overcome with a suitable testing platform that is more representative of *in vivo* environment. Such model would also provide an opportunity to study intra-organ pharmacodynamics of the targeted DDS complex. Meeting the apparent need for a more effective platform for the targeted DDS research, thereby providing a versatile multi-purpose early stage platform, is expected to greatly enhance the progress in pharmaceutic discoveries.

Chapter III

Anomalous Dispersions of 'Hedgehog' Particles

- from *Nature* **517** 596-599

3.1 Introduction

Hydrophobic particles in water and hydrophilic particles in oil aggregate, but can form colloidal dispersions if their surfaces are chemically camouflaged with surfactants, organic tethers, adsorbed polymers or other particles that impart affinity for the solvent and increase inter-particle repulsion[20,254]. A different strategy for modulating the interaction between a solid and a liquid uses surface corrugation, which gives rise to unique wetting behaviour[255–257]. Here we show that this topographical effect can also be used to disperse particles in a wide range of solvents without recourse to chemicals to camouflage the particles' surfaces: we produce micrometre-sized particles that are coated with stiff, nanoscale spikes and exhibit long-term colloidal stability in both hydrophilic and hydrophobic

media. We find that these ‘hedgehog’ particles do not interpenetrate each other with their spikes, which markedly decreases the contact area between the particles and, therefore, the attractive forces between them. The trapping of air in aqueous dispersions, solvent auto-ionization at highly developed interfaces, and long-range electrostatic repulsion in organic media also contribute to the colloidal stability of our particles. The unusual dispersion behaviour of our hedgehog particles, overturning the notion that like dissolves like, might help to mitigate adverse environmental effects of the use of surfactants and volatile organic solvents, and deepens our understanding of inter-particle interactions and nanoscale colloidal chemistry.

3.2 Fabrication of ‘hedgehog’ particles

We imparted strong corrugation onto the surface of carboxylated polystyrene microspheres (μPSs) by attaching rigid zinc oxide (ZnO) nanoscale spikes (‘nanospikes’). This involves initial absorption of positively charged ZnO nanoparticles (NPs) onto the negatively charged μPSs and subsequent growth of ZnO nanowires using established protocols[258]. The resultant hedgehog particles combine micro- and nanoscale structural features (**Figure 3.1.a**), and their geometrical and topographical specifications can be adjusted by changing the growth conditions to modify the surface densities, lengths and diameters of nanospikes and the μPS diameters (**Figure 3.1.b-e**, **Figure 3.6-9**).

As-made hedgehog particles, with their polar ZnO surfaces, are highly hydrophilic. They form excellent dispersions in water (**Figure 3.1.f, l**) and other hydrophilic solvents. When rendering the hedgehog particles hydrophobic by silanization of the ZnO nanospikes with (7-octen-1-yl) trimethoxysilane (OTMS) or 1*H*,1*H*,2*H*,2*H*-perfluorooctyltriethoxysilane (PFTS) (spectroscopic evidence of silanization is shown in **Figure 3.14.c**), they form stable dispersions in heptane and hexane (**Figure 3.10.a, b**).

3.3 Dispersion stability of hydrophobic 'hedgehog' particles in aqueous media

Surprisingly, highly corrugated OTMS-modified hydrophobic hedgehog particles (OTMS-HPs) also form dispersions in water (**Figure 3.1.g, h, l**), and hydrophilic hedgehog particles disperse in representative hydrophobic solvents such as heptane, hexane and toluene (**Figure 3.4.a-h**). This illustrates that surface topography can be used to modulate the interaction between microscale particles and disperse them in phobic solvents.

Immediately on sonicating various hydrophobic OTMS-HP and PFTS-modified hydrophobic hedgehog particle (PFTS-HP) formulations in water (**Figure 3.11**), we observed the formation of a precipitate on the bottom of the vial, floating aggregates on top of the liquid, and a stable opalescent dispersion. Dispersions remain stable and free of aggregation for a subset of particles for at least five days, as verified by scanning electron microscopy (SEM) (**Figure 3.1.i**)

and dynamic light scattering (**Table 1**). The percentage of hydrophobic hedgehog particle aggregates floating on the surface of the dispersions increased with elongation of the nanospikes (**Figure 3.12**), but the colloidal stability of the particles dispersed in water was also enhanced (**Figure 3.2.k-m**).

To exclude the possibility that the observed behaviour arises because our samples contain a subpopulation of hydrophilic OTMS-HPs or PFTS-HPs or represent a special case of Janus colloids, that is, colloids consisting of distinct hydrophobic and hydrophilic interfacial sectors[259–261], we directly probed the hydrophobic nature of the particles after processing them into dried thin films. The filtrate of suspended OTMS-HPs exhibited high water repellency causing the droplets to roll off (the 'lotus effect'; **Figure 3.13**). Further evidence is obtained by injecting hydrophobic cadmium selenide (CdSe) nanoparticles into an aqueous dispersion of OTMS-HPs: confocal and transmission electron microscopy (TEM) images show the expected anchoring of hydrophobic nanoparticles on the spikes (**Figure 3.1.j, k**, **Figure 3.14.d**), thus confirming their hydrophobicity and the uniformity of surface derivatization. The stability of the hydrophobic hedgehog particles in aqueous dispersion did not change on CdSe adsorption.

The wetting of corrugated surfaces[256,262–264] is often attributed to a Cassie–Baxter wetting mode[265,266] and in our case could include formation of an air shell in the vicinity of the μPS core. Such trapped air bubbles[267] might provide buoyancy to the hedgehog particles, but are known to be thermodynamically unstable[268,269]. The presence of trapped air is verified by adding ethanol and

observing gas evolving from the dispersion, and by observing, in high-resolution confocal microscopy images of the particles, concentric shells with markedly different refractive indices as would be expected if an air shell is present (**Figure 3.2.a, b**, **Figure 3.15**). Hydrophilic hedgehog particles in water have no air shells, and they appear under the same conditions as uniformly lit particles (**Figure 3.2.c**, **Figure 3.16**).

When adding fluorescent cadmium telluride (CdTe) nanoparticles, stabilized with hydrophilic thioglycolic acid (TGA), to an aqueous dispersion of the hydrophobic hedgehog particles, a dark zone devoid of emission around the hedgehog particles confirms the presence of a layer of air. The dimensions of the emission exclusion zones closely match the diameter of hedgehog particles (**Figure 3.2.e**). The fact that similar images were obtained after five days of storage in the dark without agitation (**Figure 3.2.g**) attests to the long-term stability of dispersions of our hydrophobic hedgehog particles in water, consistent with long-term trapping of air at macroscale corrugated surfaces[270] (**Figure 3.18**). Hydrophilic hedgehog particles in identical luminescent media appear as bright spots with CdTe nanoparticles localized on and between the nanospikes (**Figure 3.2.f, h**).

Strong scattering of photons and electrons by ZnO nanospikes prevents successful optical or cryogenic TEM imaging of the air–water interface within hedgehog particles, but we can locate it by taking advantage of the fact that CdTe nanoparticles can self-assemble into nanowires[271] and nanosheets[9] at interfaces[272]:

a thin layer of CdTe nanoparticles that assembles more than 200 nm in from the ends of the ZnO nanospikes (**Figure 3.2.i**, **Figure 3.19**) pinpoints the water meniscus (**Figure 3.2.j**). This allows us to calculate an average hedgehog particle density of 0.92 g cm^{-3}, which closely matches the density of water and explains the buoyancy of the particles.

3.4 Interaction potential (EDLVO) between two hydrophobic 'hedgehog' particles in aqueous media

We must also explain why two individual hydrophobic hedgehog particles do not coalesce on collision. To do so, we refer to the extended Derjaguin–Landau–Verwey–Overbeek (E_DLVO) theory, according to which the sum of potentials associated with van der Waals (V_{vdW}), electrical double layer (V_{DL}) and hydrophobic (V_{HB}) interactions approximate the total interaction potential (V_{E_DLVO}) between the hydrophobic hedgehog particles: $V_{E\_DLVO} = V_{vdW} + V_{DL} + V_{HB}$. Evaluating interparticle interactions in different configurations (**Figure 3.3.a-c**, **Figure 4.2**), we find that hedgehog-particle/hedgehog-particle pair potentials display high repulsive energy barriers of at least $14k_BT$ (k_B, Boltzmann's constant) for the outer contour of spikes (x = 0; **Figure 3.3.d**). Penetration of the nanospikes into the interstitial spaces of another hedgehog particle ($x < 0$) is energetically unfavourable (**Figure 3.3.d**).

Comparison of the V_{E_DLVO} for hydrophobic hedgehog particles with that for hydrophobic μPSs (**Figure 4.7.d**) shows that the interfacial corrugations

transform the overall attractive potential into a repulsive one. For hedgehog particles with short nanospikes, V_{E_DLVO} reverses such that the interaction becomes attractive (**Figure 3.3.e**), matching the experimental results in **Figure 3.2.k**. The key reason for the anomalous stability of hedgehog particle dispersions is that V_{vdW} and V_{HB} are greatly decreased for corrugated particles compared with the smooth spheres (**Figure 3.3.f, g**), owing to the drastic reduction in the contact area in the former case. The total contour area of tapered spikes represents <3% of the surface area of the smooth particles (**Figure 3.1.a**).

The colloidal stability of hydrophobic hedgehog particles in water is also enhanced by the presence of the double electric layer at the air–water interface, increasing V_{DL}. The zeta-potential (ζ) of air bubbles, which affects their electrostatic repulsion, is known to be between −35 mV[273] and −65 mV[274]. Such high ζ is attributed to autoionization of water[275] that may also occur at the hydrophobic interfaces[275,276]. However, the fact that the hedgehog particle dispersion remains stable in the presence of 0.01–1.0 M NaCl, which leads to screening of electrostatic interactions and coagulation of 'normal' dispersions (**Figure 3.1.m, n**), shows that any increased electrostatic repulsion has a secondary role and that the anomalous colloidal behaviour of hedgehog particles is dominated by the reduction of attractive interactions between the particles. But limitations of Derjaguin–Landau–Verwey–Overbeek theory for high ionic strengths and nanoscale corrugated surfaces[277] may need to be considered for a more complete mechanistic explanation.

3.5 Dispersion stability of hydrophilic 'hedgehog' particles in apolar solvents

If the drastic reduction in attractive components of the pair-potential is the reason for the unusual stability of hedgehog particle dispersions, the same effect should occur in dispersions of hydrophilic colloids in hydrophobic solvents. Stable dispersions of hydrophilic hedgehog particles were obtained in heptane, hexane and toluene (**Figure 3.4.a**, **Figure 3.23**). SEM and confocal microscopy images (**Figure 3.4.b-e**) demonstrated non-agglomerated particles in the bulk of these dispersions and physical integrity of hedgehog particles (**Figure 3.4.f-h**). The μPS core of the hedgehog particles was dissolved in toluene, thus yielding a dispersion of hydrophilic hedgehog particle shells. As expected, ZnO nanoparticles and ZnO nanowires (**Figure 3.24**) do not disperse in the same solvents.

Calculations show that V_{vdW} for this type of dispersion is much reduced compared with smooth spheres, and that the overall pair potential of hydrophilic hedgehog particles in heptane is indeed repulsive with $V_{DLVO,HPs} = 1.4k_BT$ at $x = 0$ nm (**Figure 3.4.i, j**, **Figure 4.9**). Notably, dispersion in organic solvents lack the air layer between the spikes, and electrostatic interactions in organic solvents are not screened as in aqueous solutions and are therefore longer ranged.

3.6 Conclusion

The stability of our surfactant-free hedgehog particles in ‘phobic’ solvents offers a different perspective on scientific and technological problems related to colloidal interactions and might even enable new strategies for processing and dealing with colloids, for developing new drug delivery systems[278], and for colloidal self-assembly[261,279,280]. We also believe that the unusual solvation behaviour of hedgehog particles (contrary to the traditional expectations of particle dispersion stability in hydrophobic/hydrophilic solvents) could be used to develop efficient adsorbers, absorbers, scatterers or catalysts that need to function in both organic and aqueous media.

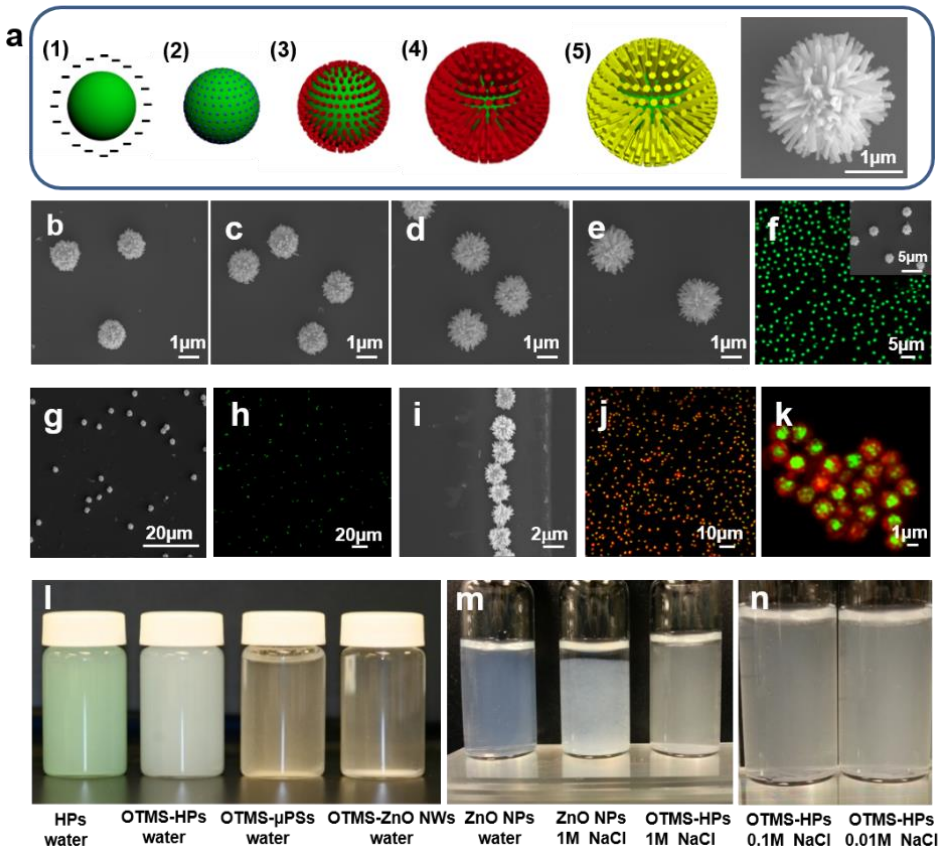

Figure 3.1. a, Negatively charged, carboxylate-terminated μPSs are used as core templates (1) on which positively charged ZnO NPs are adsorbed (2). ZnO nanospikes are grown from ZnO nanoparticles (3) to a designed length (4, 6). Hedgehog particles are rendered hydrophobic by exposure to OTMS or PFTS (5). **b–e**, SEM images of hedgehog particles with different ZnO nanospike lengths: 0.19 μm (**b**), 0.27 μm (**c**), 0.4 μm (**d**), 0.6 μm (**e**). **f**, Confocal microscopy of an aqueous dispersion of hydrophilic hedgehog particles with fluorescently labelled μPSs. Inset, SEM image for the same hedgehog particles. **g**, **h**, SEM (**g**) and confocal microscopy (**h**) of an aqueous dispersion of OTMS-HPs. **i**, SEM image of particles from the bulk of an aqueous OTMS-HP dispersion collected five days after initial preparation. **j**, **k**, Confocal microscopy images of fluorescent OTMS-HPs (green, λ_{max} = 486 nm) with adsorbed hydrophobic CdSe nanoparticles (red, λ_{max} = 655 nm) in an aqueous dispersion (**j**) and in the dried state (**k**). **l**, Photographs of aqueous dispersions of (left to right) hydrophilic hedgehog particles (HPs) with green-dyed μPSs, OTMS-HPs, OTMS-μPSs and OTMS-ZnO nanowires (NWs). **m**, Photographs of (left to right) ZnO nanoparticles (NPs) in water, ZnO nanoparticles in 1 M NaCl, and OTMS-HPs in 1 M NaCl. **n**, Photographs of OTMS-HPs in (left to right) 0.1 M NaCl and 0.01 M NaCl.

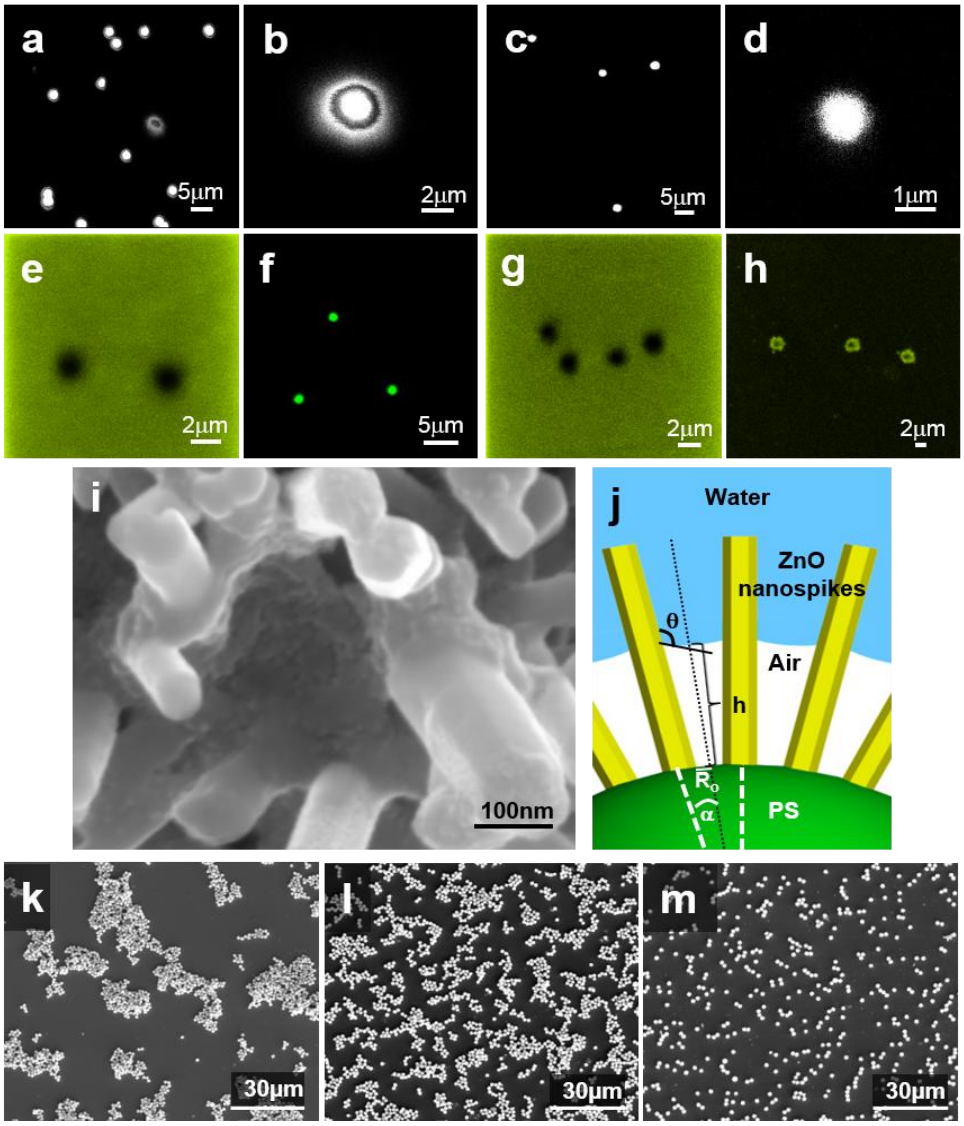

Figure 3.2. a–**h**, Confocal microscopy images of hydrophobic hedgehog particles labelled with hydrophobic CdSe NPs in aqueous dispersions (**a**, **b**) and hydrophilic hedgehog particles labelled with hydrophilic CdTe NPs in aqueous dispersions (**c**, **d**); hydrophobic hedgehog particles in an aqueous solution containing hydrophilic TGA-stabilized CdTe nanoparticles with green (λ_{max} = 540 nm) emission (**e**); hydrophilic hedgehog particles in an aqueous solution containing hydrophilic TGA-stabilized CdTe nanoparticles (**f**); the same sample from image **e** after five days of storage in dark (**g**); and the same sample from image **f**after five days of storage in dark (**h**). **i**, SEM image of a hydrophobic hedgehog particle with a self-assembled film of TGA-depleted CdTe nanoparticles between the ZnO nanospikes, indicating the location of the air–water interface. The hydrophobic hedgehog particles were immersed in an aqueous solution of CdTe nanoparticles for 72 h. **j**, Schematic diagram of the air–water interface, showing the experimental parameters (definitions in Supplementary Information). **k**–**m**, SEM images of aqueous dispersions of hydrophobic hedgehog particles with ZnO nanospike lengths of 0.19 μm (**k**), 0.40 μm (**l**) and 0.57 μm (**m**)

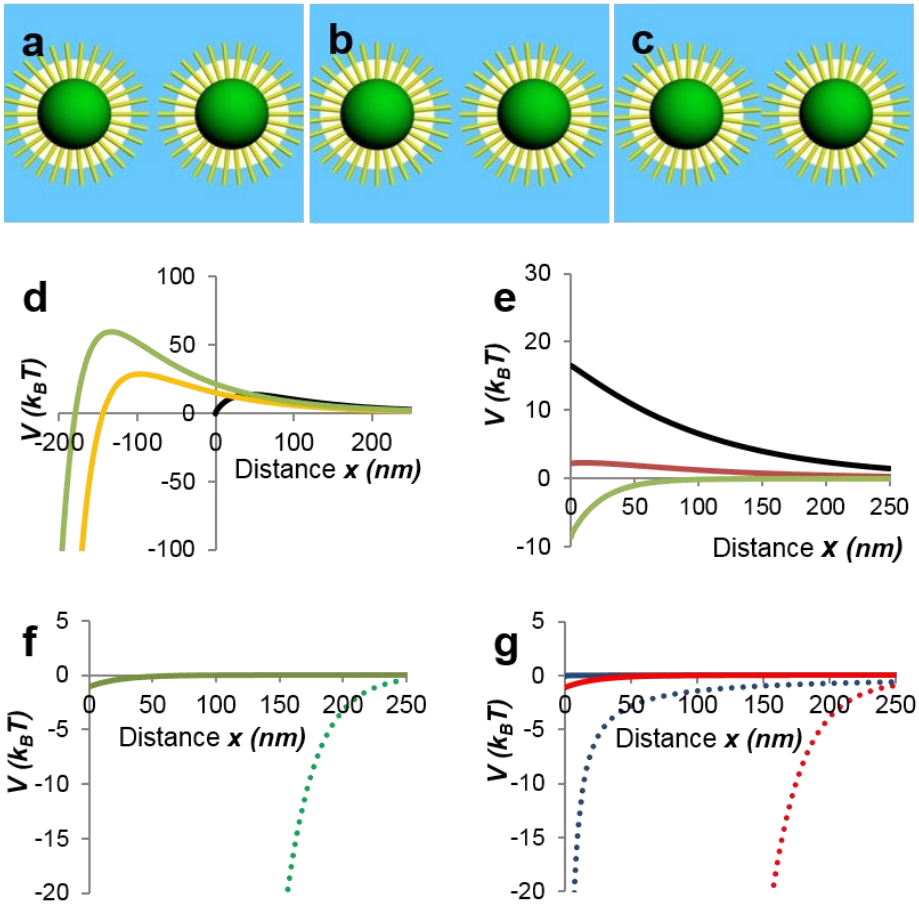

Figure 3.3. a–c, Two general configurations, spike-to-spike (S–S; **a**) and spike-to-gap (S–G; **b**), are considered, along with the intermediate case in which the ZnO nanospikes face the side walls of opposing particles (ZS–G;**c**). **d–g**, Interaction potentials between hydrophobic hedgehog particles. **d**, Pair potentials for hydrophobic hedgehog particles in S–S ($V_{E\_DLVO,S–S}$, black), S–G ($V_{E\_DLVO,S–G}$, orange) and ZS–G ($V_{E\_DLVO,ZS–G}$, green) configurations. The negative values of x correspond to the penetration of ZnO nanospikes into the interstitial spaces of another hedgehog particle; $x = 0$ corresponds to the outer contour around the spike tips. **e**, Pair potentials ($V_{E\_DLVO,HP}$) of hydrophobic hedgehog particles in an aqueous dispersion calculated according to the E_DLVO theory for the zeta-potentials at the air–water interface with $\zeta = -65$ mV (black line) and $\zeta = -35$ mV (red line), and for hydrophobic hedgehog particles with short nanospikes from Fig. 3.2.k (green line). **f**, Hydrophobic interaction potentials of OTMS-HPs ($V_{HB,HP}$, green) and OTMS-µPSs ($V_{HB,PS}$, dotted green). **g**, Van der Waals interaction potentials of OTMS-HPs ($V_{vdW,HP}$, blue) and OTMS-µPSs ($V_{vdW,PS}$, dotted blue) and total attractive potentials of OTMS-HPs ($V_{vdW+HB,HP}$, red) and hydrophobic OTMS-µPS ($V_{vdW+HB,PS}$, dotted red) in water.

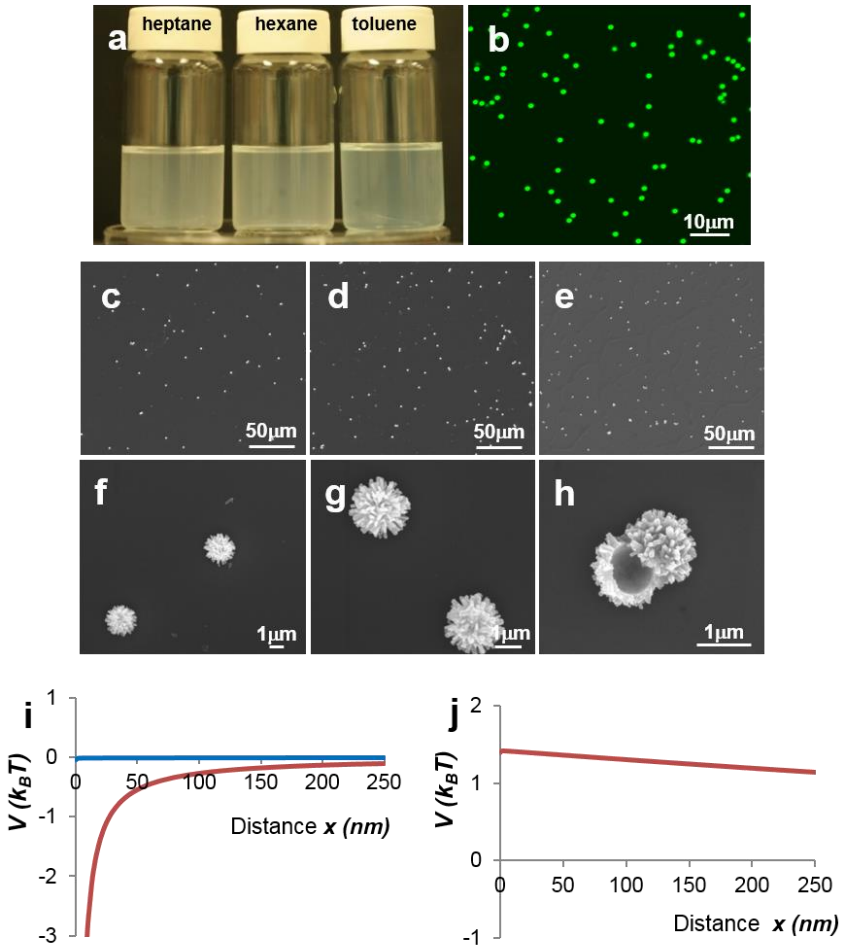

Figure 3.4. a, Dispersions of hydrophilic hedgehog particles in (left to right) heptane, hexane and toluene. As in the case of dispersion of hydrophobic hedgehog particles in water, after sonication of hydrophilic hedgehog particles in organic solvent there was always a small amount of precipitate in the bottom of the vial. **b**, Confocal microscopy image of hydrophilic hedgehog particles in heptane. **c**–**e**, SEM images of hydrophilic hedgehog particles from dispersions in heptane (**c**), hexane (**d**) and toluene (**e**). **f**–**h**, SEM images of individual hedgehog particles in heptane (**f**), hexane (**g**) and toluene (**h**). Toluene dissolves the μPS core in the hedgehog particles, rendering dispersions of hydrophilic spiky shells. **i**, Van der Waals interaction potentials V_{vdW} of hydrophilic hedgehog particles (blue) and μPS (red) in heptane. **j**, Total pair potential V_{E_DLVO} of hydrophilic hedgehog particles in heptane.

3.7 Supplementary Information

3.7.1 'Hedgehog' particles – geometry and topology

3.7.1.1 Nanospikes.

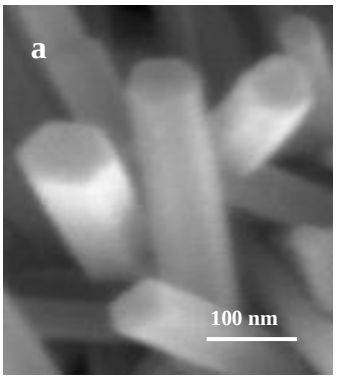

Figure 3.5. (**a**) SEM image of ZnO nanospikes with hexagonal cross-section grown on the μPS cores

3.7.1.2 Variation of nanospike density on HPs

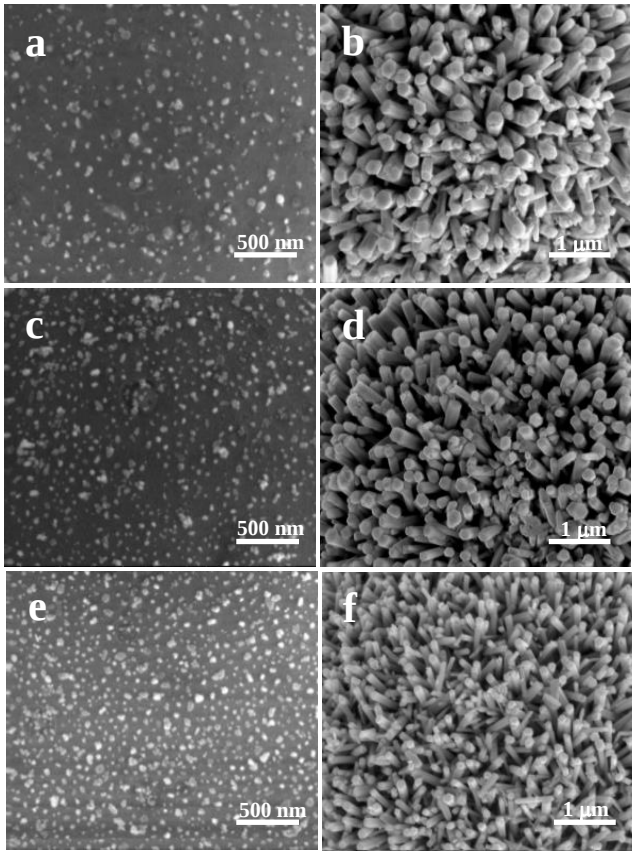

Figure 3.6. SEM images of the surface of (**a, c, e**) µPS with adsorbed ZnO NPs and (**b, d, f**) HPs made from the same after the growth of ZnO nanospikes. Variable density of adsorbed ZnO NPs and grown ZnO nanospikes should be noted. The concentrations of ZnO seed solutions are (**a, b**) 0.001wt%, (**c, d**) 0.01wt%, (**e, f**) 0.1wt %.

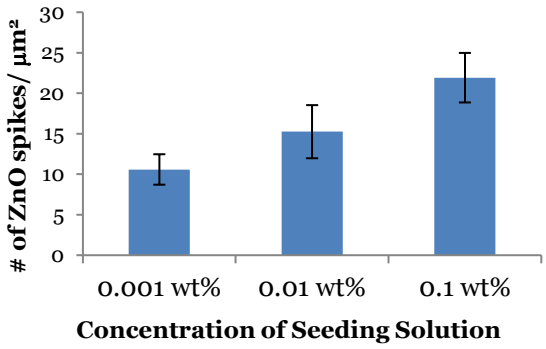

Figure 3.7. Statistical analysis of nanospike densities for different coverage densities of ZnO NPs on μPS cores (*n*=12). The error bar shows s.d.

Comment 1: The nanospike densities were varied by adjusting the ZnO NP concentration during the seeding process. As expected, ZnO nanospike densities decrease with decreasing seeding concentrations. Enumeration of spikes per μm^2 (**Figure 3.7**) confirms the visual observations (**Figure 3.6.a-f**). The spike densities were obtained by taking the average of the total number of spikes counted from 12 randomly chosen square areas, 1 μm^2 per square. **Figure 3.6** also reveals that the diameter of the spikes decreases with increasing spike densities because the abundance of nucleation sites results in faster consumption of ZnO precursors[281–284].

3.7.1.3 Variation of nanospike wodth

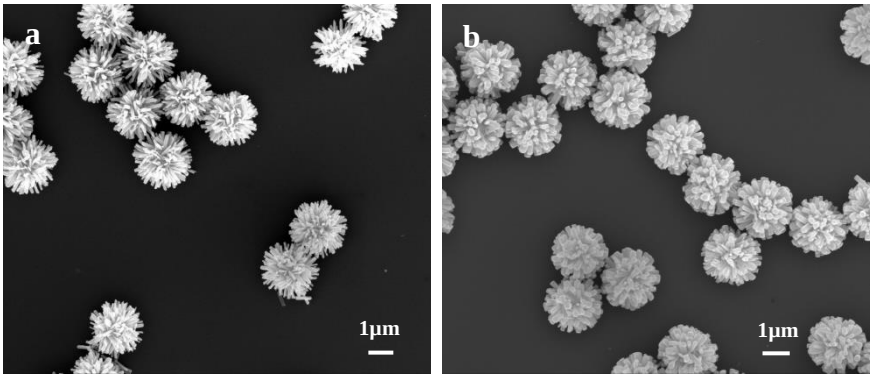

Figure 3.8. SEM images of (**a**) typical HPs used in the studies. (**b**) Increase in precursor concentrations and reaction time increases nanospike diameters. 1µm µPS was used as the cores in both cases.

3.7.1.4 Variation of µPS diameter

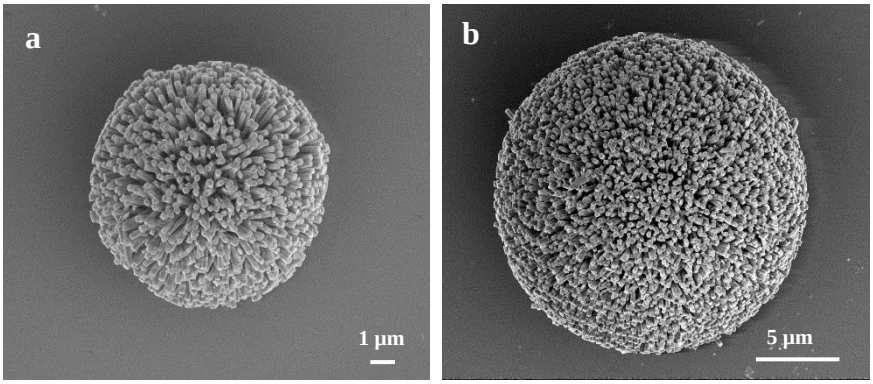

Figure 3.9. SEM images of HPs made from µPSs of different diameters: (**a**) 3 µm and (**b**) 10 µm.

3.7.2 Hydrophobic 'hedgehog' particles in aqueous media

3.7.2.1 Dispersion of hydrophobic HPs in both non-polar and polar media.

Organosilane moieties have been widely used as hydrophobic agents to lower the surface free energy of solids[285]. Numerous methods have been developed to tailor interfacial properties of metals/metal oxides, such as ZnO[286–288]. The resulting hydrophobic HPs disperse in both organic (**Figure 3.10.a, b**) and aqueous (**Figure 3.10.c**) media.

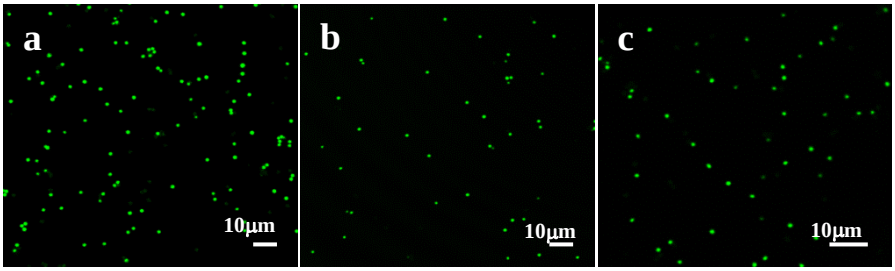

Figure 3.10. Hydrophobization of ZnO and HPs. (**a-c)** Confocal microscopy images of OTMS-modified HPs dispersed in **(a)** heptane, **(b)** hexane and **(c)** DI water

3.7.2.2 Long-term aqueous suspensions of hydrophobic HPs.

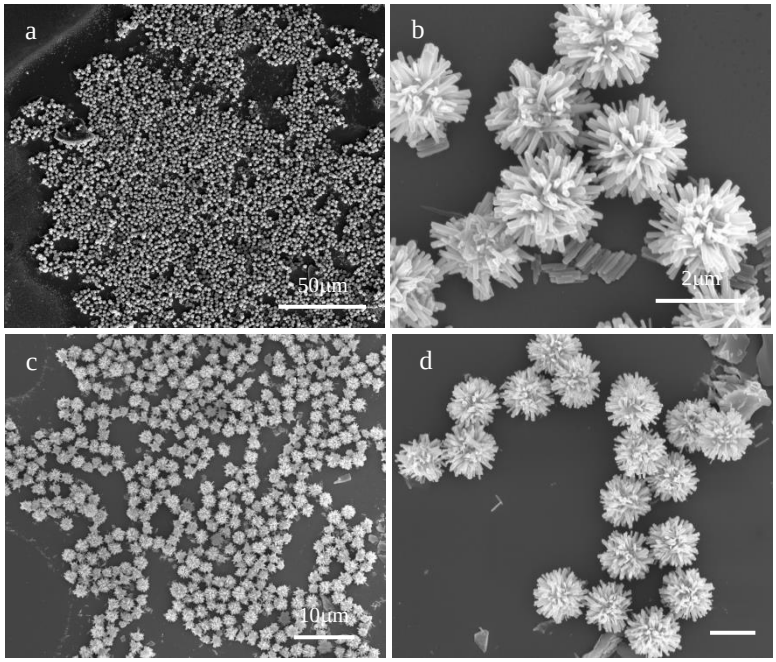

Figure 3.11. Long-term stability of aqueous dispersions of hydrophobic HPs. SEM images of hydrophobic HPs present in the bulk of the aqueous dispersion (a, b) six days and (c, d) seven days after the initial preparation. In all samples, the HPs are modified with 1*H*,1*H*,2*H*,2*H*-perfluorooctyltriethoxysilane (PFTS).

(a) DLS: hydrophobic HPs

Peak Size (nm)	1091	1054	1086	2327	1026	2101	1244	1570
Intensity (%)	75.2	100.0	14.2	68.1	39.5	52.8	53.7	43.6

(b) DLS: hydrophilic HPs

Peak Size (nm)	1032	1579	1518	1231	1319	1327	1217	1059
Intensity (%)	100.0	100.0	100.0	100.0	100.0	100.0	100.0	100.0

Table 3.1 Dynamic light scattering (DLS) study of the aqueous dispersions of OTMS-HPs. (a) DLS showing particle sizes found in the supernatant of aqueous dispersion of OTMS-HPs five days after initial dispersion and its relative proportions in the population. The values may be inconsistent due to high scattering of the HP interface; (b) DLS of particle sizes and their proportions found in the supernatant of aqueous dispersion of as-made hydrophilic HPs. The values shown are in geometric range of the HPs which confirms the presence and long-term stability of OTMS-HPs in water.

3.7.2.3 Influence of the length of nanospikes on dispersability

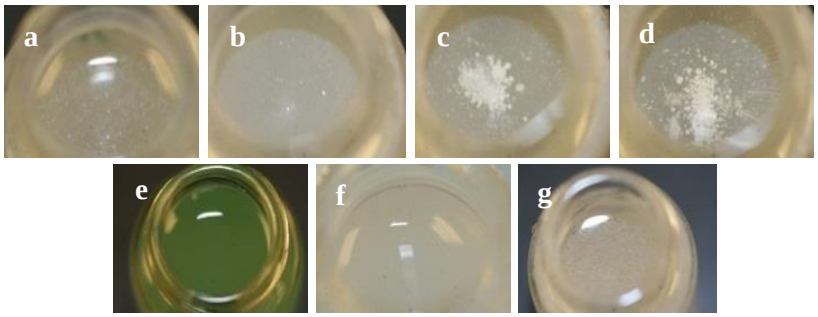

Figure 3.12. a-d, Photographs of surfaces of aqueous dispersions hydrophobic HPs with variable length of nanospikes **(a)** 0.19 μm, **(b)** 0.27 μm, **(c)** 0.4 μm, **(d)** 0.57 μm; **e-g**, photographs of surfaces of aqueous dispersions of **(e)** hydrophilic μPS, and **(f)** hydrophobic OTMS-modified μPS, **(g)** hydrophobic OTMS-modified ZnO nanowires identical to nanospikes on HPs.

3.7.2.4 Wetting properties of film and confirmation of surface hydrophobicity

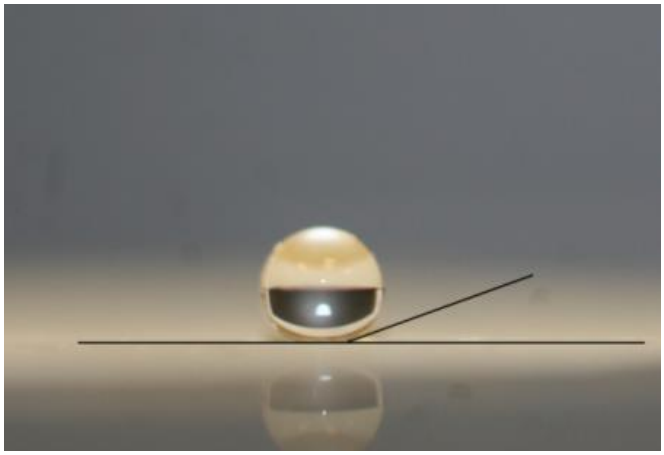

Figure 3.13. Microphotograph of a water droplet placed on a film of OTMS-HPs made after filtration of a OTMS-HP suspension through a polycarbonate membrane. The contact angle is indicative of the superhydrophobic properties of the dried film.

Comment 2: Enhancement of hydrophobicity with nano- and micro-scale surface roughness has been well documented[289]. A film of hydrophobic HPs made by

filtration exhibits superhydrophobic behavior (**Figure 3.13**). A similar hydrophobic surface was obtained after drying an OTMS-modified HP aqueous dispersion on a piece of Kevlar® fabric. Complete wetting is seen on a film of hydrophilic HPs. A hydrophilic film with a contact angle of 1-2° was observed when we used a dispersion of HPs without OTMS treatment.

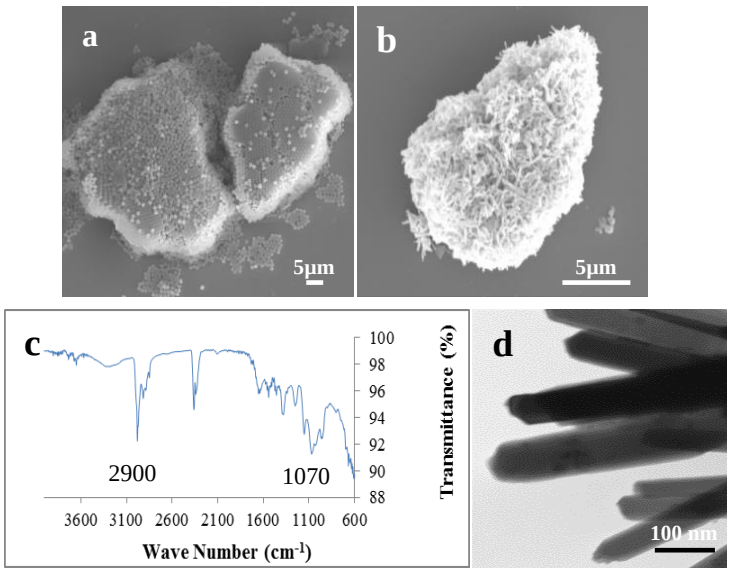

Figure 3.14. Confirmation of hydrophobicity. SEM images of typical agglomerates formed by OTMS-modified (**a**) hydrophobic µPS and (**b**) ZnO nanowires upon attempted dispersion in water; **(c)** FTIR measurements shows absorption peaks at ≈2900 cm^{-1} and ≈1070 cm^{-1}, assigned to methylene (-CH_2-) and Si-O stretching. The measurement also displays a broad band between 900 ~1000 cm^{-1} which is attributed to Zn-O-Si stretching vibration; (**d**) TEM image of OTMS-modified ZnO nanospikes on HPs with adsorbed hydrophobic CdSe NPs with red (λ_{max} = 655 nm) luminescence. 50 µL of a hexane solution of hydrophobic CdSe NPs was injected into 2 mL of a 0.15% (*w/v*) of OTMS-HPs in water.

Dispersions of OTMS-treated smooth hydrophobic µPSs and OTMS-treated hydrophobic ZnO nanowires as two separate dispersions had no colloidal stability

and precipitated within seconds (**Figure 3.14.a, b)**. Fourier transformation infrared spectroscopy (FTIR) (Jasco FT/IR 4100) was used to confirm the adsorption of silane groups onto the ZnO surface (**Figure 3.14.c**). Hydrophobicity is further confirmed by adsorption of hydrophobic CdSe quantum dots (QD) onto the hydrophobic modified ZnO nanospike surface (**Figure 3.14.d**)

3.7.3 Interfacial entrapment of air-pockets in hydrophobic 'hedgehog' particles

3.7.3.1 Confocal microscopy

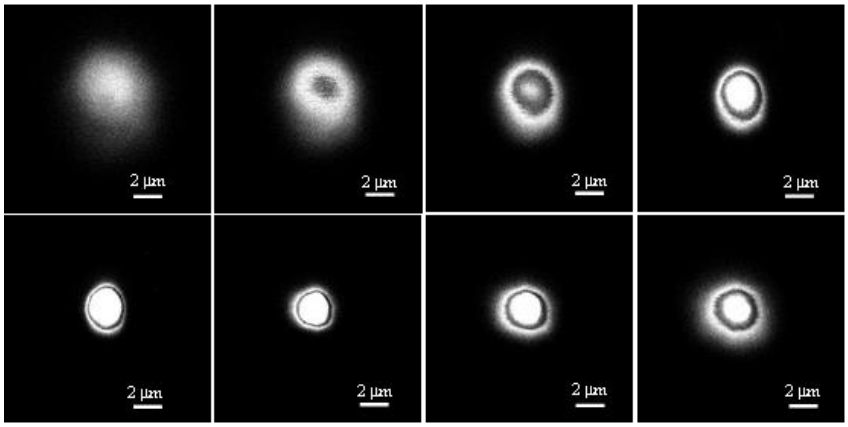

Figure 3.15. Z-stack series of OTMS-HPs dispersed in water.

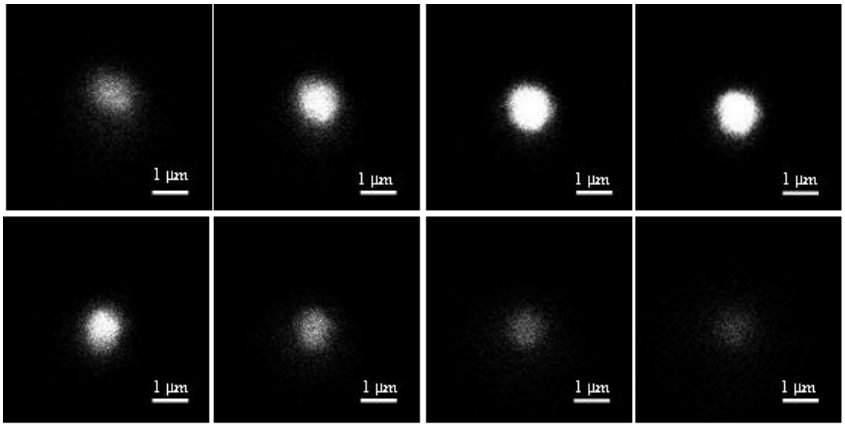

Figure 3.16. Z-stack series of as-made hydrophilic HPs dispersed in water.

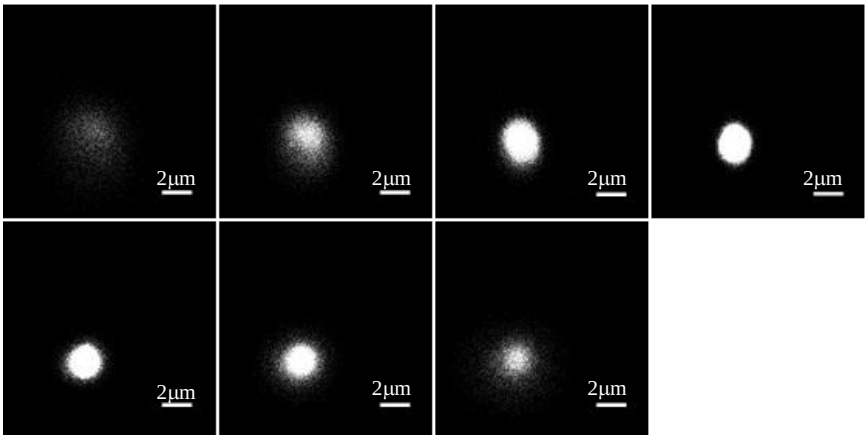

Figure 3.17. Z-stack series of hydrophobic HPs dispersed in 50-50 v/v water/ethanol mixture

Comment 3: The patterns in **Figure 3.15** obtained by excitation of hydrophobic CdSe NPs adsorbed on the hydrophobic ZnO nanospikes of HPs in aqueous solution are consistent with light scattering on single particles composed of concentric spheres of varying refractive indices.

In contrast, such patterns are not observed when fluorescent hydrophilic HPs with electrostatically adsorbed CdTe NPs are dispersed in aqueous solution (**Figure 3.16**) and when hydrophobic HPs are dispersed in a mixture of water/ethanol (**Figure 3.17**) where the air-water meniscus is expected to rupture due to lowering of the surface tension.

Comment 4: Long-term stability of air-pockets and plastrons on corrugated macroscale substrate with ZnO nanospikes.

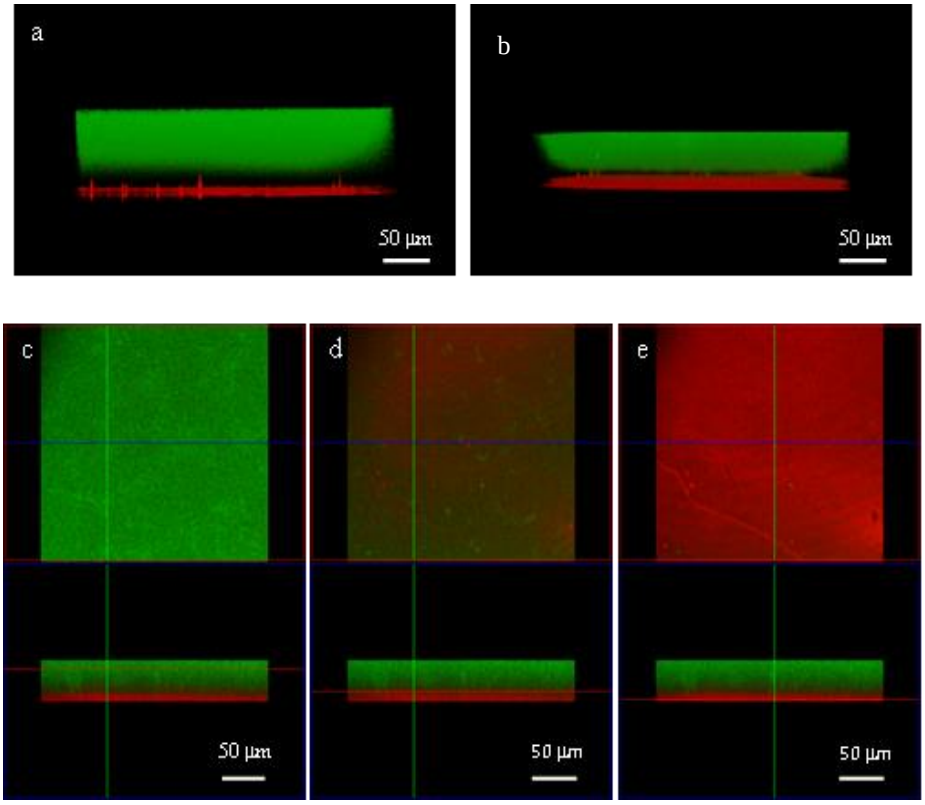

Figure 3.18. Long-term dynamics of plastrons on hydrophobic ZnO nanospikes surface. a-b, confocal microscopy images of plastrons (a) at day zero and (b) day five, taken from the same sample. c-d, *x-y* plane cross section at three different distances from glass surface (*z*-coordinates) corresponding to c. layers of water, d. outermost tips of ZnO nanospikes with the entrapped layer of air, and e. near the bottom of the layer of ZnO nanospikes

In addition to the calculations of the Laplace pressure, the stability of the air layer on OTMS-HPs in water can be further confirmed experimentally. In the work by Poetes et al.[270], they observed so called plastrons on corrugated macroscale substrates by confocal microscopy. Poetes et al defined plastrons as a

thin layer of air supported by outstanding but sparse pinning points. Importantly, Poetes et al. also reported that the initial (thick) plastrons ultimately decayed to secondary plastrons defined as air entrapped in between the lower level surface asperities that exhibit long-term stability.

In addition to the literature data, we also sought to experimentally observe the long-term survival of air-pockets on spiky surfaces. Hydrophobic ZnO nanospikes were grown across a 2D glass surface and the stability of the layer of air was investigated by confocal microscopy. The ZnO particles were hydrophobized with OTMS and rendered fluorescent by coating them with hydrophobic CdSe NPs (655 nm, red). The aqueous layer above them was labeled with 20 μM fluorescein isothiocyanate (FITC) (520 nm, green). The dark space sandwiched between the red and green fluorescent phases corresponds to the entrapped air, i.e., plastrons. At day 0, we observed a continuous layer of air in accordance with Steiner et al. (**Figure 3.18.a**). At day 5, plastrons were still present, albeit with a notable decrease of thickness. We observed that the top part above the contour of ZnO nanospikes (**Figure 3.18.b**) disappeared. Importantly, the confocal microscopy images representing the cross-sections parallel to the ZnO-water interface (**Figure 3.18.c-e**) show (a) the presence of air entrapped between the ZnO spikes (**Figure 3.18.d**), and (b) an absence of water in the bottom of the ZnO layer (**Figure 3.18.e**). Overall, we believe that the calculations of Laplace pressure, literature data, and our own experimental data are indicative of long-term stability of air entrapped between the ZnO nanospikes.

3.7.3.2 CdTe NP assembly at the air-water interface.

Thioglycolic acid (TGA) capped hydrophilic CdTe NPs assemble at the interface between air and water to form a dense layer of interpenetrating CdTe nanowires between nanospikes at a depth of ≈200 nm from the outer contour of the nanospikes, indicating Cassie-Baxter wetting model. Additional images of the CdTe layer marking the interface are given in **Figure 3.19**.

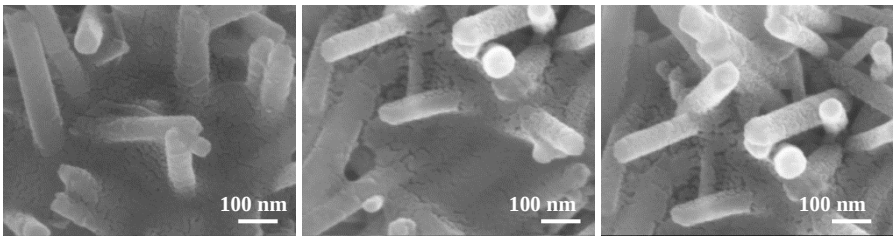

Figure 3.19. SEM images of the thin layer of CdTe NP film self-assembled at air-water interface between the ZnO nanospikes.

3.7.4 Nomenclature

Symb.	Definition
ρ_{HP}	Effective density of HP
ρ_{PS}	Density of μPS core
ρ_{ZnO}	Density of ZnO
ρ_{air}	Density of air
ρ_{water}	Density of water
V_{HP}	Total volume of HP
V_{PS}	Total Volume of μPS
V_{ZnO}	Total volume of all ZnO nanospikes on the surface of HPs
v_{ZnO}	Volume of individual ZnO nanospikes
V_{air}	Total volume of air entrapped
V_{water}	Total volume of water penetrated in the nanowire "shell"
R_{HP}	Average radius of HPs

R_{PS}	**Average radius of μPSs**
W	**2x apothem of hexagon (ZnO spikes)**
d	**Average length of ZnO nanospikes**
cA_{ZnO}	**Average cross-sectional area of ZnO nanospike**
SA_{PS}	**Surface area of μPS core**
η	**Nanospike coverage efficiency**
γ	**Dimensionless water penetration coefficient**

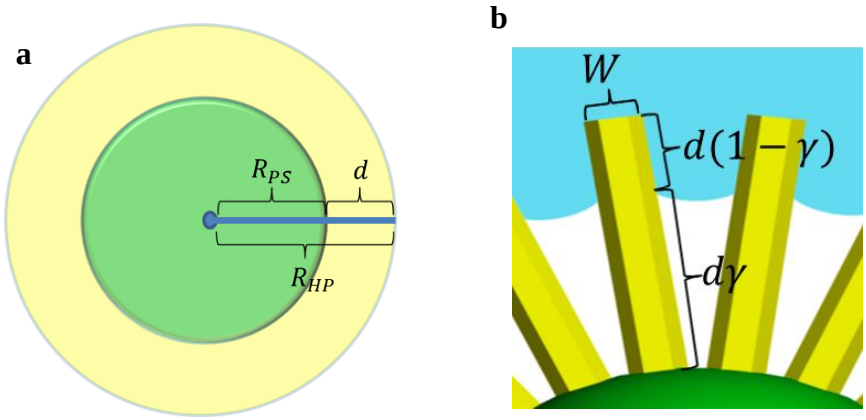

Figure 3.20. Schematics showing geometrical variables in describing the three-phase shell of HPs.

3.7.5 Physical manifests

3.7.5.1 Expression of Hydrophobic HP Density

The density of hydrophobic HPs, in general form, can be written as:

$$\rho_{HP} = \frac{V_{PS}}{V_{HP}}\rho_{PS} + \frac{V_{ZnO}}{V_{HP}}\rho_{ZnO} + \frac{V_{air}}{V_{HP}}\rho_{air} + \frac{V_{water}}{V_{HP}}\rho_{water} \quad \text{Eq. 3.1}$$

The following shows the expression for the geometrical components of the HPs:

The cross-sectional area of an individual ZnO spike: $cA_{ZnO} = \frac{\sqrt{3}}{2}W^2$ Eq. 3.2

The surface area of μPS core: $SA_{PS} = 4\pi {R_{PS}}^2$ Eq. 3.3

Number of spikes per ideal HP (perfect coverage):

$$N = \frac{4\pi {R_{PS}}^2}{\frac{\sqrt{3}}{2}W^2} \quad \text{Eq. 3.4}$$

Number of spikes per experimental HP (imperfect coverage):

$$N\eta = \frac{4\pi {R_{PS}}^2}{\frac{\sqrt{3}}{2}W^2}\eta \quad \text{Eq. 3.5}$$

Length of the ZnO spike: $d = R_{HP} - R_{PS}$ Eq. 3.6

The volume of an individual ZnO NW:

$$v_{ZnO} = \frac{\sqrt{3}}{2}W^2 d \quad \text{Eq. 3.7}$$

, where N is the number of spikes on HPs assuming perfect coverage, and η is the coverage efficiency, defined as the ratio of number of experimentally determined spikes over N. The water penetration coefficient, , was obtained by measuring the depth of air-water interfacial CdTe QDs films from the spike tips. The data are obtained from SEM images and **Image J**.

The total volume of ZnO spikes, V_{ZnO}, total volume of HP, V_{HP}, and the volume of the μPS core, V_{PS}, can be obtained from the following:

$$V_{ZnO} = v_{ZnO} N\eta = 4\pi\eta {R_{PS}}^2 R_{HP} - 4\pi\eta R_{PS}^3 \quad \text{Eq. 3.8}$$

$$V_{HP} = \frac{4}{3}\pi {R_{HP}}^3 \quad \text{Eq. 3.9}$$

$$V_{PS} = \frac{4}{3}\pi {R_{PS}}^3 \quad \text{Eq. 3.10}$$

The volume of entrapped air is calculated by subtracting the volume of ZnO nanospikes where length, $d\gamma$, is from the surface of the μPS to the air-water interface (V_{ZnO}^*), and the volume of the μPS (V_{PS}) is from the volume of a sphere that encloses the air-entrapment (V_{HHP}^*). The volume of water in the HP shell can be calculated by subtracting the volume of a sphere enclosing air-entrapment (V_{HHP}^*) and the volume of ZnO nanospikes (V_{ZnO}^{**}), where length, $d(1-\gamma)$, is from the air-liquid interface to the spike-tip, from the total volume of the HP (V_{HHP}).

$$V_{HP}^* = \frac{4}{3}\pi(R_{PS} + d\gamma)^3 = \frac{4}{3}\pi(\gamma R_{HP} + (1-\gamma)R_{PS})^3 \quad \text{Eq. 3.11}$$

$$V_{ZnO}^* = \mathrm{c}A_{ZnO} d\gamma N\eta = 4\pi\gamma\eta R_{PS}^2 R_{HP} - 4\pi\gamma\eta R_{PS}^3 \quad \text{Eq. 3.12}$$

$$V_{ZnO}^{**} = \mathrm{c}A_{ZnO} d\gamma N\eta = 4\pi(1-\gamma)\eta R_{PS}^2 R_{HP} - 4\pi(1-\gamma)\eta R_{PS}^3 \quad \text{Eq. 3.13}$$

$$V_{air} = V_{HP}^* - V_{ZnO}^* - V_{PS} = \frac{4}{3}\pi\gamma^3 R_{HP}^3 + \frac{4}{3}\pi((1-\eta)^3 - 1 + 3\gamma\eta)R_{PS}^3 + 4\pi\gamma((1-\gamma)^2 - \eta)R_{PS}^2 R_{HP} + 4\pi\gamma^2(1-\gamma)R_{HP}^2 R_{PS} \quad \text{Eq. 3.14}$$

$$V_{water} = V_{HP} - V_{HP}^* - V_{ZnO}^{**} = \frac{4}{3}\pi(1-\gamma^3)R_{HP}^3 - 4\pi(1-\gamma)(\gamma(1-\gamma) + \eta)R_{HP}R_{PS}^2 - 4\pi\gamma^2(1-\gamma)R_{PS}R_{HP}^2 + 4\pi(1-\gamma)\eta R_{PS}^3 \quad \text{Eq. 3.15}$$

Substituting **Eq.3.40-47** to **Eq.3.33** and after subsequent rearrangement, the density of the HPs, ρ_{HP}, can be found.

$$\begin{aligned}\rho_{HP} = (&\rho_{PS} + 3\eta(\rho_{water} - \rho_{ZnO}) + 3\gamma\eta(\rho_{air} - \rho_{water}) - \gamma^3\rho_{air} + 3\gamma^2\rho_{air} \\ &- 3\gamma\rho_{air})y^3 \\ &+ \big(3\eta(\rho_{ZnO} - \rho_{water}) + 3\gamma\eta(\rho_{water} - \rho_{air}) \\ &+ 3\gamma^3(\rho_{air} - \rho_{water}) + 6\gamma^2(\rho_{water} - \rho_{air}) \\ &+ 3\gamma(\rho_{air} - \rho_{water})\big)y^2 \\ &+ \big(3\gamma^2(\rho_{air} - \rho_{water}) + 3\gamma^3(\rho_{water} - \rho_{air})\big)y \\ &+ \gamma^3(\rho_{air} - \rho_{water}) + \rho_{water}\end{aligned} \quad \text{Eq. 3.16}$$

, where

$$y = \frac{R_{PS}}{R_{HP}}$$

Substitution of the geometrical specifications of freely suspended hydrophobic HPs ($\eta = 0.144, \gamma = 0.57,\ y = 0.47$), the density of hydrophobic HPs in free suspension is $\rho_{HP} = 0.92$ g/cm^3, which closely approximates that of water.

3.7.5.2 Solution to Free Suspension

Assuming $\rho_{air} = 0$ and $\rho_{water} = 1$, and solving for $\rho_{HP} = \rho_{water}$, we could solve for y, the ratio between the radius of μPS and HP, in terms of η and γ.

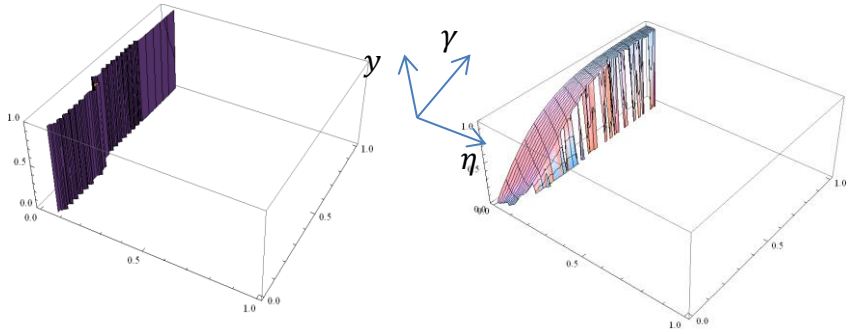

Figure 3.21. The graph shows range of possible values of y, η and γ to render free suspension of hydrophobic HPs in water. Being a cubic equation, three sets of solutions were expected. However, one of the solutions of y gives ranges of negative values, which does not make physical sense and, hence, is omitted. The coverage coefficient must be sufficiently low to increase the proportion of air-entrapment to reduce overall ρ_{HP} such that $\rho_{HP} \approx \rho_{water}$.

3.7.5.3 Physical manifest – zeta potential (ζ)

[NaCl]	Average ζ-potential (mV)
DI water	-36.6 ± 2.4 (n = 3)
0.01 M	-31.1 ± 4.5 (n = 9)
0.1 M	-19.3 ± 1.2 (n = 9)
1.0 M	-10.9 ± 3.2 (n = 9)

Table 3.2. ζ–potential of hydrophobic HPs in varying ionic strengths. NaCl is added to aqueous dispersion of hydrophobic HPs (0.46% (*w/v*), corresponding to 2.27×10^6/ml) to final concentrations listed in the table.

Comment 5: ζ–potential values of hydrophobic HPs vary with the ionic strength of the media. These values are similar to, and display comparable trends with, those of air-bubbles under the same conditions. Yang et al.[290] determined ζ–potential values of air-bubbles in water to be ≈ -25 mV for 0.01 M NaCl and ≈ -19 mV for 0.1 M NaCl at pH 7.

3.7.6. Laplace pressure in 'hedgehog' particles

Laplace pressure across the air-water meniscus in hydrophobic HPs was found to be ΔP = 5.5 kPa at 25°C. For "normal" air bubbles in water of comparable size, ΔP = 167.2 kPa at 25°C. The nanospikes, therefore, stabilize the layer of air around the HP which, in part, explains the longevity of these dispersions.

Comment 6: Geometry of the interface between HP and water is depicted in **Figure S17**. The Laplace pressure across the meniscus in this configuration is described by Eq. 3.17[291–293]

$$\Delta \mathrm{P} = P - P_o = -\frac{\gamma \cos(\theta - \alpha)}{R_o + h * \tan(\alpha)} \qquad \text{Eq. 3.17}$$

where P is the pressure in the liquid, P_o is the pressure in the entrapped air (equal to that of atmosphere), γ is the surface tension of water, θ is Young's contact angle of water on the OTMS-ZnO surface, R_o is half the width between the adjacent spikes on the μPS surface, h is the height of the meniscus, and α is the inclination angle (**Figure 3.22**). R_o and α are dependent on the nanospike density and can be easily obtained through trigonometry relations. Representative samples referenced for this study have $\approx 9 \sim 10$ spikes per circumference with $R_o = 129.6$ nm, and $\alpha = 15^{\circ}$. The contact angle of ZnO film treated with octadecyltrimethoxy silane (OTES), $\theta = 106^{\circ}$[294] was used in the calculations as

OTES is very similar to OTMS. Substituting in the parameters, the Laplace pressure across the meniscus is $\Delta P = 5.51$ kPa. Here, $\Delta P > 0$ discourages diffusion of air from the pockets into the bulk liquid. Concurrently, $> \alpha + 90^{\circ}$. This fact indicates that the transition from Cassie-Baxter to Wenzel wetting[293] has a substantial energy barrier and is hindered, which further stabilizes the interface structure depicted in **Figure 3.22**.

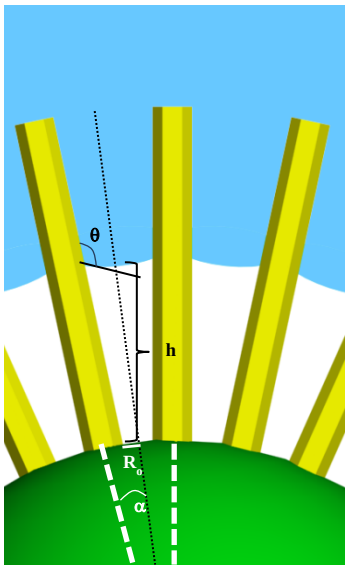

Figure 3.22. Air-water meniscus in between the ZnO spikes

3.7.7 Hydrophilic ‘hedgehog’ particles in apolar media

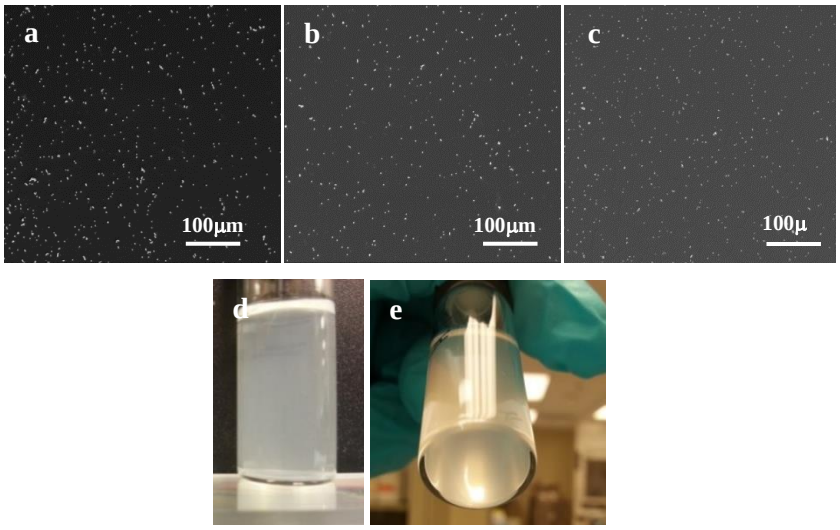

Figure 3.23. Low magnification SEM images of dispersion of hydrophilic HPs from organic solvents in (**a)** heptane, **(b)** hexane, and **(c)** toluene; (**d, e**) photographs of dispersion of hydrophilic HPs in heptane.

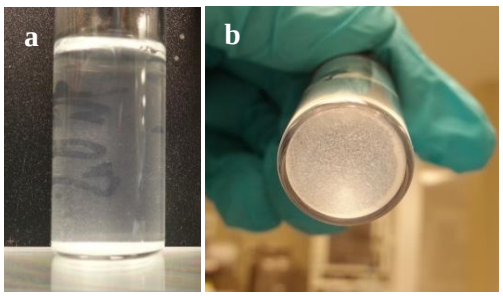

Figure 3.24. Photographs of attempted dispersions of (**a**) hydrophilic ZnO NPs and (**b**) hydrophilic ZnO nanowires in heptane.

3.8 Absence of steric repulsion

We find the concept of steric repulsion typically used in colloidal chemistry for polymer-modified particles as an additional source of stabilization mechanism between the HPs incompatible, for both hydrophobic HPs in water and hydrophilic HPs in non-polar organic solvent. The steric repulsion is typically present in colloids, whose external surface is either adsorbed or grafted with spatially diffuse polymer chains, which are immersed in "good solvent". The flexibility and redistribution of thermally mobile ("dynamic roughness")[20] chains elicits coordination of enthalpic and entropic responses required for steric repulsion. The steric stabilization arises from two major reasons when diffuse polymeric layers of colloids are overlapped at close distances; inter-digitation or compression of the steric layers resulting in increase in the polymer concentration (mixing or osmotic factor) and in entropic configuration loss due to volume restriction[295–299]. Let us first consider the case of hydrophilic HPs in heptane which represents incompressible and rigid ("static roughness") nanospikes immersed in "bad solvent". The total change in the free energy of steric interaction of mixing, ΔG_m, can be written as follows:

$$\Delta G_m = \Delta H_m - T\Delta S_m \qquad \text{Eq. 3.18}$$

Here, ΔH_s is the enthalpic contribution in desolvation of "bound" heptane solutes from the ZnO nanospikes, which can be neglected. On the other hand, relocation of heptane from the nanospike interstitials to the HP exterior increases the entropic configuration of the heptane solutes, collectively leading to $\Delta G_s \leq 0$ as $\Delta S_s \geq 0$, indicating attractive interaction potential. This is contrary to the original hypothesis of the relevance of steric stabilization. Furthermore, if we assume ZnO nanospikes to be rigid macroscopic polymer chains, quantitative osmotic effect of the interaction, described by[296]

$$V_p(H) = \frac{4\pi R}{\nu}(\phi)^2 \left(\frac{1}{2} - \chi\right)\left(d - \frac{x}{2}\right)^2 < 0 \qquad (\mathrm{d} < x < 2d)$$

Eq. 3.19

, points to attractive potential ($V_p(H) < 0$) as $\left(\frac{1}{2} - \chi\right) < 0$, where χ is Flory-Huggins solvency parameter and ν is the molecular volume of the solvent. At the same time, ZnO nanospikes are fixed to the core surface and rigid along its length. Under such conditions, the loss of entropy due to compression of ZnO nanospikes seems to be too little to affect their behavior. The same sets of considerations also applies to aqueous dispersion of hydrophobic HPs; incompressible "static roughness" immersed in "bad solvent".

Chapter IV

EDLVO Calculation of Anomalous Dispersions of 'Hedgehog' Particles

- Excerpt from *Nature* **517** 596-599

4.1. Theoretical framework

In this section, we investigated the interaction potential between the hydrophobic HPs to account for their aqueous dispersions. We assumed that the μPS core makes a negligible contribution to the total interactions of HPs with the exception of the special cases described below. The interactions between HPs are dominated by the shell of nanospikes[300], with the structure depicted in **Figure 3.22**. The sum of van der Waals (V_{VdW}), the electrical double layer (V_{DL}), and the

hydrophobic energies (V_{HB}), termed the extended DLVO energies (V_{E_DLVO}), approximates the total interaction potential between the HPs.

$$V_{E\_DLVO} = V_{VdW} + V_{DL} + V_{HB}$$

Eq. 4.1

Note that ZnO nanospikes are stiff and thus entropic effects and other repulsive contributions from steric interactions originating from compression of long surface ligands typical for polymer-modified colloids, do not contribute to the stabilization of HPs.

4.1.1 Van der Waal interactions.

4.1.1.1 Calculations of van der Waal interactions based on the Hamaker model.

In the framework of colloidal chemistry London dispersion force are considered to make the greatest contribution to van der Waals interactions. This is not correct for anisotropic nanoscale colloids with characteristic sizes in the range of 2-20 nm for which the presence of permanent dipoles[301] increases considerably the contribution of Keesom and Debye forces to interparticle forces. In the context of this study we shall adhere to traditional view of van der Waals interaction as primarily dispersion forces between two induced transient dipoles because the diameter of ZnO nanospikes and the μPS particles are substantially larger than ZnO NPs for which the components associated with dipoles become significant[302].

Considering the distance between the μPS cores, the van der Waals interaction potential, V_{VdW}, between the HPs can by approximated by the interaction between the ZnO nanospikes,

$$V_{VdW} = -\frac{AR}{12}\left(\frac{1}{x+2d} - \frac{2}{x+d} + \frac{1}{x}\right) - \frac{A}{6}\ln\left(\frac{x(x+2d)}{(x+d)^2}\right)$$

$$(R \gg x, d)$$

Eq. 4.2

, where R (m) is the radius of the HPs, d is the thickness of the shell, and x (m) is the closest distance between the nanospike shells, i.e., the gap between HPs. The V_{VdW} interaction energy between two dissimilar shells takes the general form given by[303],

$$V_{VdW} = -\frac{A(R_1R_2)}{6(R_1+R_2)}\left(\frac{1}{x+d_1+d_2} - \frac{1}{x+d_1} - \frac{1}{x+d_2} + \frac{1}{x}\right) - \frac{A}{6}\ln\left(\frac{x(x+d_1+d_2)}{(x+d_1)(x+d_2}\right)$$

Eq. 4.3

The Hamaker's constant A(J) could be estimated by the Tabor-Winterton representation with the assumption that ν_e, the electronic absorption frequency, is the same for all media[20],

$$A_{132} \approx \frac{3}{4} k_B T \left(\frac{\varepsilon_1 - \varepsilon_3}{\varepsilon_1 + \varepsilon_3}\right)\left(\frac{\varepsilon_2 - \varepsilon_3}{\varepsilon_2 + \varepsilon_3}\right) + \frac{3h\nu_e}{8\sqrt{2}} \frac{(n_1^2 - n_3^2)(n_2^2 - n_3^2)}{\sqrt{(n_1^2 + \eta_3^2)}\sqrt{(n_2^2 + n_3^2)}\left\{\sqrt{(n_1^2 + n_3^2)} + \sqrt{(n_2^2 + n_3^2)}\right\}}$$

Eq. 4.4

, where k_B is Boltzmann's constant (1.381 x 10^{-23} J/K), *T* is temperature (293 K), *h* is Planck's constant (6.626 x 10^{-34} J•s), ν_e is the electronic absorption frequency, and ε_i (i = 1,2,3) and n_i (i = 1,2,3) are dielectric constants and refractive indices of ZnO, in air and water, respectively. The subscript number in A_{132} and similar constants describe the materials (first and third number) across the medium (second number). Theoretical approaches are available to evaluate these constants, however, because of their tendency to overestimate the values of the Hamaker constants[304], we used the experimental values of A_{131} obtained in the previous studies[305]. A_{232} was obtained with the following values using **Eq. 4.4**: $\varepsilon_2 = 1.00059,\ n_2 = 1.000293,\ \varepsilon_3 = 78.5,\ n_3 = 1.333$ and $\nu_e = 3 \times 10^{15}$ s^{-1}.

4.1.1.2 Calculation of van der Waal interactions using the Coupled Dipole Method (CDM).

The Hamaker's treatment of vdW forces[306] considers them to be additive. This means that vdW forces acting on adjacent elements of the interacting bodies, for instance two atoms of zinc or oxygen, are independent of each other. Thus, the overall vdW force between the interacting bodies can be calculated as a sum of

pairwise interactions between atoms constituting each body. However, this pairwise treatment is inconsistent with the physical nature of the London dispersion interactions making the primary contribution to the vdW forces within Hamaker's approach. Polarization of closely positioned atoms (or larger constitutive elements) of the interacting bodies must affect each other, and therefore the dispersion forces. Pairwise treatment of vdW interactions is, therefore, inherently inaccurate. Taking into account the validity of this concern, we decided to evaluate the discrepancy between the additive and non-additive treatment of the dispersion forces.

To make a comparison we decided to calculate the energy of London dispersion interactions for two identical ZnO nanorods following additive and non-additive treatment of these forces. As a research model we used ZnO nanorods with atomic structure depicted in **Figure 4.1.a**. These ZnO nanorods are thinner and smaller than nanospikes on HPs, but can give appropriate comparison between additive and non-additive treatment of dispersion forces for our system. Atoms of zinc and oxygen with characteristic atomic polarizabilities represent the interacting elements in these models. Their atomic coordinates were calculated by using standard atomic force-fields with SPARTAN quantum mechanical software suite.

The coupled dipole model (CDM)[307,308] can directly account for multibody polarization effects between atoms using the polarization tensor $\boldsymbol{T_{ij}}$ where the atomic polarizations are calculated using the Drude model. This model is directly

applicable to NPs with known atomic coordinates. We carried out CDM calculations adapting the standard system of interaction matrices for inorganic NPs with well-defined crystal lattice[26,309].

We found that the energy of vdW interactions of the model ZnO nanorods calculated using pairwise approximation is higher than that calculated using CDM for the same separations (**Figure 4.1**). From these calculations we also concluded that the estimates made using the Hamaker's approach provide an upper limit of vdW interactions in our case. Considering potential concerns about inaccuracy of the Hamaker's approach originating from non-additivity of dispersion interactions, one can see that the difference is relatively small and does not exceed 15% for the model used. This difference is likely to be smaller for mesoscale nanorods constituting the nanospikes. The knowledge of the upper limit of the energy of attractive interactions provides a suitable framework for comparison with repulsive interactions because the colloidal stability of the HPs may even be better than the estimates will show. Therefore, throughout this study we shall use the Hamaker's method to calculate the energy of vdW interactions.

A final note needs to be made regarding the generality of the comparative calculation of vdW interactions using CDM and Hamaker's method. Non-additivity of the dispersion forces does not necessarily lead to reduced energy of vdW interaction and is dependent on both structural and geometrical factors.

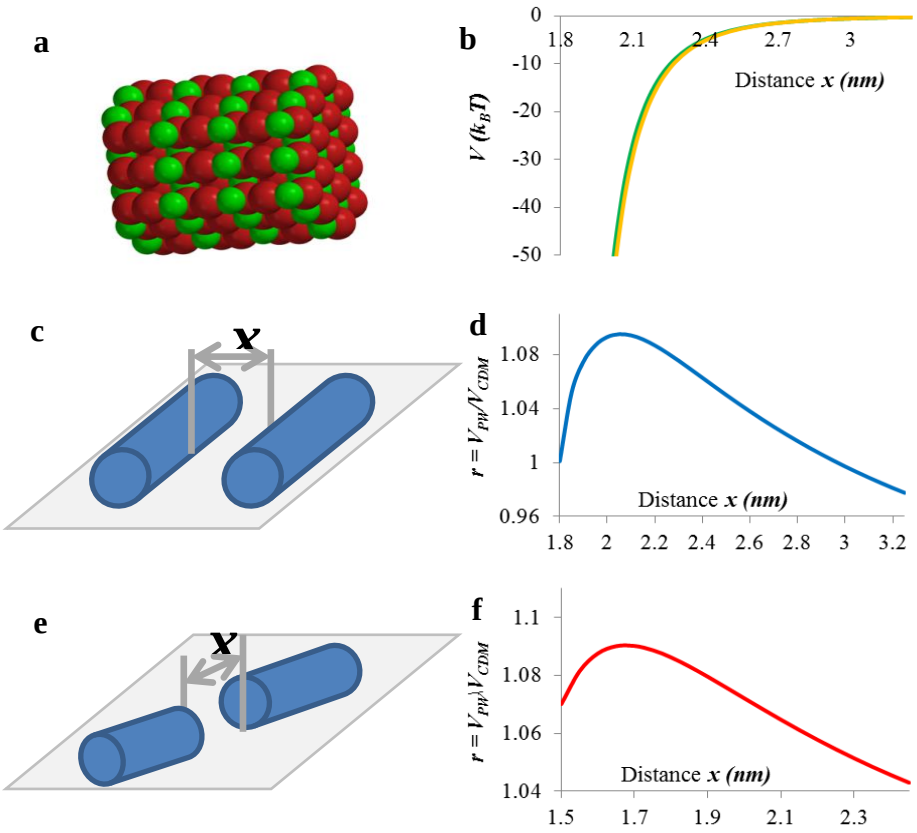

Figure 4.1. **(a)** model atomic structure of ZnO nanorods, **(b)** vdW energies between ZnO nanorods in end-to-end configuration evaluated with the pairwise Hamaker model (orange), $V_{PW,}$ and with the CDM model (green), $V_{PW,}$; **c-f,** the ratio, ***r***, of vdW energies assessed from the pairwise Hamaker model to the CDM model for interaction between ZnO nanorods in **(c, d)** parallel and in **(e, f)** end-to-end configurations.

4.1.2. Double Layer electrostatic interactions

The Poisson-Botzman formalism for two identical particles[310] was used to calculate the electrostatic repulsive potential associated with the ionic double layer, V_{DL}, between the hydrophobic HPs, given by,

$$V_{DL} = 2\pi\varepsilon_o\epsilon_r R\zeta^2 \ln(1 + e^{-\kappa x}) \quad \text{Eq. 4.5}$$

where $\varepsilon_0 = 8.85 \times 10^{-12}$(Farad m^{-1}) is the permittivity of vacuum, $\varepsilon_r = 78.5$ is the dielectric constant of water, R (m) is the radius of the HPs and ζ is the zeta potential of surface of interest. The reciprocal double layer thickness (κ, Debye length), is given by,

$$\kappa = \sqrt{\frac{1000 N_A e^2}{\varepsilon_r \varepsilon_0 k_B T} \sum_i M_i \times Z_i^2}$$

Eq. 4.6

where $e = 1.6 \times 10^{-19}$ (Coloumbs), $N_A = 6.023 \times 10^{23}$ (Avogadro's number), M_i and Z_i are the molar concentration and valency of ions, respectively. The ideal Debye length of pure water, κ^{-1}, is 962 nm. Under typical conditions where the presence of CO_2 converts to carbonic acid, κ^{-1} is reduced to 200 nm[311]. In this calculation we use the practical Debye length, $\kappa^{-1} \approx 100$ nm, of DI water that is in accord with previous studies[312–314]. The general form of the double layer electrostatic repulsion for interaction between dissimilar spheres is given by[315],

$$V_{DL} = \frac{\pi \varepsilon_0 \varepsilon_r R_1 R_2}{R_1 + R_2} (\zeta_1^2 + \zeta_2^2) \left\{ \frac{2\zeta_1 \zeta_2}{\zeta_1^2 + \zeta_2^2} ln\left(\frac{1 + e^{-\kappa x}}{1 - e^{-\kappa x}}\right) + \ln(1 - e^{-2\kappa x}) \right\}$$

Eq. 4.7

4.1.3. Hydrophobic interactions

Due to the lack of a theoretical expression that describes the hydrophobic interaction, only the empirical fits of experimental results are available. In our

studies, the hydrophobic interaction potential, V_{HB}, is represented by the single exponential function[53],

$$\frac{F_{HB}}{R} = Ce^{(-\frac{x}{\lambda})}$$

Eq. 4.8

where C is the hydrophobic amplitude, and λ (m) is the decay length generally accepted in the field of colloidal chemistry.

4.2. EDLVO calculations of pair-potentials between hydrophobic 'hedgehog' particles in aqueous media

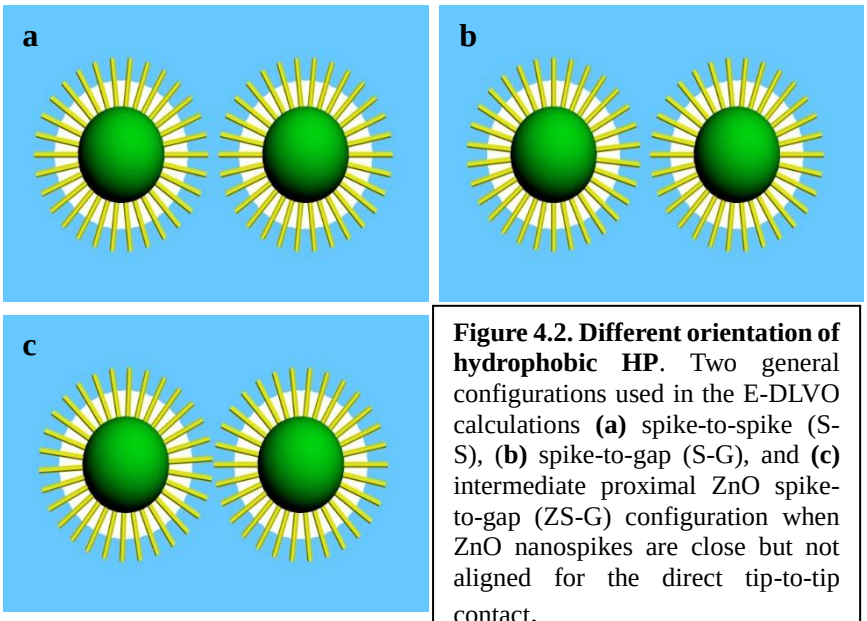

Figure 4.2. Different orientation of hydrophobic HP. Two general configurations used in the E-DLVO calculations **(a)** spike-to-spike (S-S), (**b)** spike-to-gap (S-G), and **(c)** intermediate proximal ZnO spike-to-gap (ZS-G) configuration when ZnO nanospikes are close but not aligned for the direct tip-to-tip contact.

Our studies have shown that aqueous suspensions of hydrophobic HPs have interface depicted in **Figure 3.20.b and Figure 4.2**. For brevity of

mathematical notations, ZnO nanospikes will be referred to in this section as "spikes." The interaction potential of the hydrophobic HPs depends on the orientation of nanospikes with respect to each other. We investigated two typical configurations, which are depicted in **Figure 4.2**, spike-to-spike (S-S) (**Figure 4.2.a**) and spike-to-gap (S-G) (**Figure 4.2.b**). An intermediate orientation between S-S and S-G configurations, where ZnO nanospikes are in the vicinity of each other but not in line for direct contact, is termed proximal ZnO spike-to-gap (ZS-G) configuration (**Figure 4.2.c**).

Total pair-interaction potential is calculated by summation of multiplication between the geometrical probability and $V_{E\_DLVO,}$ of each configuration

$$V_{E\_DLVO,HPs} = P_s V_{E\_DLVO,S-S} + P_a V_{E\_DLVO,S-G} + P_w V_{E_{DLVO},ZS-G}$$

Eq. 4.9

They are exemplified below for aqueous media. The calculations of pair potentials for HPs with and without the layer of entrapped air were carried out following similar protocol. The case with no air entrapment is applicable to HP interactions in organic solvents and for HP with short nanospikes. Albeit the difference in parameters such as dielectric constant, concentration of ions, Hamaker constants, etc., they followed the same template.

4.2.1. Spike-to-spike configuration (S-S)

HP-HP interactions in the S-S configuration (**Figure 4.2.a**) are comprised of spike-to-spike, air-to-air, and wall-to-wall interactions. Here, "wall" refers to proximal ZnO spikes and represents the inclined sidewalls of neighboring spikes, whose volume also contributes to the van der Waals interaction potential. Due to surface heterogeneity, we adopted an approach developed by Mishchuk et al.[316–319], and described the potentials between HPs with probabilities of interactions. Specifically, for example, an array of nanospikes is approximated as a ZnO shell with corresponding probability that describes its geometrical attributes such as thickness and density. Side walls of spikes are also approximated as a shell of ZnO whose circumferential area fraction is projected onto the shell that geometrically coincides with air-pockets.

The vdW interaction energy of each component is given by,

$$V_{vdW,ss} = -\frac{A_{131}R_{HP}}{12}\left(\frac{1}{x+2d} - \frac{2}{x+d} + \frac{1}{x}\right) - \frac{A_{131}}{6}\ln\left(\frac{x(x+2d)}{(x+d)^2}\right)$$

Eq. 4.10

$$V_{vdW,aa} = -\frac{A_{232}(R_{HP}-d+\gamma d)}{12}\left(\frac{1}{x+2d} - \frac{2}{x+2d-\gamma d} + \frac{1}{x+2d-2\gamma d}\right) - \frac{A_{232}}{6}\ln\left(\frac{(x+2d-2\gamma d)(x+2d)}{(x+2d-\gamma d)^2}\right)$$

Eq. 4.11

$$V_{vdW,ww} = -\frac{A_{131}(R_{HP}-d+\gamma d)}{12}\left(\frac{1}{x+2d} - \frac{2}{x+2d-\gamma d} + \frac{1}{x+2d-2\gamma d}\right) - \frac{A_{232}}{6}\ln\left(\frac{(x+2d-2\gamma d)(x+2d)}{(x+2d-\gamma d)^2}\right)$$

Eq. 4.12

, and the total vdW interaction energy is given by,

$$V_{vdW,S-S} = P_{ss}V_{vdW,ss} + \ P_{aa}V_{vdW,aa} + P_{ww}V_{vdW,ww}$$

Eq. 4.13

where $V_{vdW,ss}$, $V_{vdW,aa}$ and $V_{vdW,ww}$ are vdW interaction energies between the ZnO nanospikes, between air-pockets, and the ZnO sidewalls across water, respectively, and *x* is defined as the closest distance between the interacting surfaces. The depth of water penetration is described with γd and represents the shell thickness of the entrapped air layer (**Figure 3.20.b**). Correspondingly, $R_{HP} - (1-\gamma)d$ describes the radius of the air layer around the particle core. Also note that the closest distance between the tips of nanospikes and that between the air-entrapment is not the same and is adjusted in the equation according to the specific geometry. We used previously reported values of Hamaker's constants for ZnO interactions through water, $A_{131} = 1.89 \times 10^{-20}$ (J)[305], and for air interactions through water, $A_{232} = 3.72 \times 10^{-20}$ (J). P_{ss} , P_{aa} , and P_{ww} are the probabilities of mutual interaction between the ZnO nanospikes, between the air bubbles, and the ZnO sidewalls, given by,

$$P_{ss} = P_s^2 = (\frac{SA_{ZnO}}{SA_{HP}})^2$$

$$P_{aa} = P_a^2 = (\frac{SA_{air}}{SA_{HP}})^2$$

$$P_{ww} = P_w^2 = (\frac{SA_{wall}}{SA_{HP}})^2$$

Eq. 4.14

where $SA_{HP} = 4\pi {R_{HP}}^2$, $SA_{ZnO} = \frac{\sqrt{3}}{2} W^2 N\eta$, $SA_{air} = 4\pi[R_{HP} - (1-\gamma)d]^2 - \frac{\sqrt{3}}{2} W^2 N\eta$, and $SA_{wall} = 4\pi(1-\gamma)d(2R_{HP} - (1-\gamma)d)$ are surface areas of the HPs, ZnO tips, air bubbles, and ZnO sidewalls, respectively. Experimental geometric specifications of HPs are as follows: $R_{HP} = 1071$ nm, $d = 571$ nm, $\gamma = 0.647$, $P_{ss} = (0.0318)^2 = 0.00101$, $P_{aa} = (0.627)^2 = 0.393$, $P_{ww} = (0.341)^2 = 0.116$. Here, N is the number of spikes on HPs, assuming perfect coverage, and η is the coverage efficiency, defined as the ratio of the number of experimentally determined nanospikes over N.

The double layer electrostatic potential is calculated from **Eq. 4.5**. Here, we used the experimentally determined values of zeta-potential of air bubbles in aqueous solution: $\zeta_{air} = -65\text{mV}$[274] and -35mV[273]. Zeta potential of ZnO used in the calculations was $\zeta_{ZnO} = +26.3\text{ mV}$[320]. The double layer potential in this configuration is given by,

$$V_{DL,S-S} = P_{ss}V_{DL,ss} + P_{aa}V_{DL,aa} + P_{ww}V_{DL,ww}$$

Eq. 4.15

where

$$V_{DL,ss} = 2\pi\varepsilon_o\varepsilon_r R_{HP}\zeta_{ZnO}^2 \ln(1 + e^{-\kappa x})$$

Eq. 4.16

$$V_{DL,aa} = 2\pi\varepsilon_o\varepsilon_r (R_{HP} - (1-\gamma)d)\zeta_{air}^2 \ln(1 + e^{-\kappa(x+2(1-\gamma)d)})$$

Eq. 4.17

$$V_{DL,ww} = 2\pi\varepsilon_o\varepsilon_r (R_{HP} - (1-\gamma)d)\zeta_{ZnO}^2 \ln(1 + e^{-\kappa(x+2(1-\gamma)d)})$$

Eq. 4.18

The hydrophobic interaction potential is calculated according to **Eq. 4.8** by integrating over *x* and substituting in the effective radius reflective of interaction between spherical particles.

$$V_{HB,S-S} = P_{ss}V_{HB,ss} + P_{aa}V_{HB,aa} + P_{ww}V_{HB,ww}$$

Eq. 4.19

, where

$$V_{HB,ss} = \frac{1}{2}R_{HP}C\lambda e^{(-\frac{x}{\lambda})}$$

Eq. 4.20

$$V_{HB,aa} = \frac{1}{2}(R_{HP} - (1-\gamma)d)C\lambda e^{(-\frac{x+2(1-\gamma)d}{\lambda})}$$

Eq.4.21

$$V_{HB,ww} = \frac{1}{2}(R_{HP} - (1-\gamma)d)C\lambda e^{(-\frac{x+2(1-\gamma)d}{\lambda})}$$

Eq. 4.22

$V_{HB,ss}$, $V_{HB,aa}$, and $V_{HB,ww}$ are hydrophobic interaction energies between the ZnO nanospikes, between entrapped air, and between the ZnO sidewalls, respectively. The strength and the range of hydrophobic interaction depend on the hydrophobicity of the interacting substrates, quantified by the water contact angle (θ_c)[321].

The contact angle of OTMS-modified ZnO flat surface is found to be $\approx 106^{o}$[5,15]. Hydrophobicity of air bubbles is assumed to be equal to the hydrophobic OTMS-modified ZnO surface. Empirical values of $C = -9$ (mN/m) and $\lambda = 24$ (nm),

obtained from AFM force measurements between a glass sphere and a silica plate, were used; both of them are for hydrophobized surfaces with silane moieties and $\theta_c = 100^\circ$ [43].

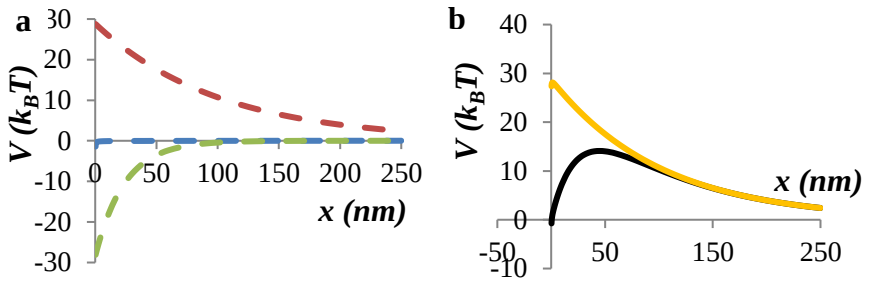

Figure 4.3. Interaction potential of hydrophobic HPs at S-S approach configuration. **(a)** $V_{vdW,S-S}$ (blue dashed line), $V_{DL,S-S}$ (red dashed line) and $V_{HB,S-S}$ (green dashed line). **(b)** $V_{E\_DLVO,S-S}$ (black solid line) and $V_{DLVO,S-S}$ (orange solid line)

Figure 4.3.a shows $V_{vdW,S-S}$ (blue dashed line), $V_{DL,S-S}$ (red dashed line) and $V_{HB,S-S}$ (green dashed line). The magnitude of each of the interaction potentials is much smaller than expected. Additionally, the vdW potential between the HPs are of non-contributing factor to overall interaction potential due to geometrical attributes. Small surface area fraction of the ZnO spikes (3%) and extensive minimum interaction distances between the air bubbles and the walls greatly reduce the vdW interactions between the HPs. **Figure 4.3.b** shows the extended DLVO potential, $V_{E\_DLVO,S-S}$ (black solid line), and the DLVO potential, $V_{DLVO,S-S}$ (orange solid line). It can be seen that the interaction potential of hydrophobic HPs

is repulsive over all distances even after the inclusion of the hydrophobic component, with maximum repulsive energy at $V_{E\_DLVO,Max,S-S} = 14.1k_BT$.

4.2.2. Spike-to-gap configuration (S-G)

HP-HP interactions in the S-G configuration (**Figure 4.2.b**) are comprised of interactions between nanospikes and air layer, between the air-pockets and between air and the ZnO sidewall of the nanospikes. The V_{vdW} interaction energies take the following form:

$$V_{vdW,S-G} = P_{sa}V_{vdW,sa} + P_{aa'}V_{vdW,aa'} + P_{wa'}V_{vdW,wa'}$$

Eq. 4.23

, where

$$V_{vdW,sa} = -\frac{A_{132}R_{HP}(R_{HP} - d + \gamma d)}{6(2R_{HP} - d + \gamma d)}\left(\frac{1}{x + d + \gamma d} - \frac{1}{x + d} - \frac{1}{x + \gamma d} + \frac{1}{x}\right) - \frac{A_{132}}{6}\ln\left(\frac{x(x + d + \gamma d)}{(x + d)(x + \gamma d)}\right)$$

Eq. 4.24

$$V_{vdW,aa'} = -\frac{A_{232}(R_{HP} - d + \gamma d)}{12}\left(\frac{1}{x + d + \gamma d} - \frac{2}{x + d} + \frac{1}{x + d - \gamma d}\right) - \frac{A_{232}}{6}\ln\left(\frac{(x + d - \gamma d)(x + d + \gamma d)}{(x + d)^2}\right)$$

Eq. 4.25

$$V_{vdW,wa'} = -\frac{A_{132}(R_{HP} - d + \gamma d)}{12}\left(\frac{1}{x + d + \gamma d} - \frac{2}{x + d} + \frac{1}{x + d - \gamma d}\right) - \frac{A_{132}}{6}\ln\left(\frac{(x + d - \gamma d)(x + d + \gamma d)}{(x + d)^2}\right)$$

Eq. 4.26

where $V_{vdW,sa}$, $V_{vdW,aa'}$ and $V_{vdW,wa'}$ are vdW energies of nanospike-air interactions, air-air interactions and sidewall-air interactions across water, respectively. Unlike the previous configuration, repulsive V is possible as $A_{22} < A_{33} < A_{11}$ leading to $A_{132} < 0$[19,322–325]. The Hamaker's constant relating ZnO and air through water, A_{132}, is approximated from the following relation[20,326]

$$A_{132} = (\sqrt{A_{11}} - \sqrt{A_{33}})(\sqrt{A_{22}} - \sqrt{A_{33}})$$

Eq. 4.27

Due to negligible molecule density of air layer in comparison to ZnO or water, $A_{22} \approx 0$. Therefore, **Eq. 4.27** becomes

$$A_{132} \approx -\sqrt{A_{33}}(\sqrt{A_{11}} - \sqrt{A_{33}})$$

Eq. 4.28

Using the previously reported experimental values ($A_{11} = 9.21 \times 10^{-20}$J[305], $A_{33} = 3.72 \times 10^{-20}$(J), $A_{132} = -2.14 \times 10^{-20}$(J) and is indeed negative.

P_{sa}, $P_{a,a'}$ and $P_{w,a'}$ is given by,

$$P_{sa} = P_s P_a = \left(\frac{SA_{ZnO}}{SA_{HP}}\right)\left(\frac{SA_{air}}{SA_{HP}}\right)$$

Eq. 4.29

$$P_{aa'} = P_a P_{a'} = \left(\frac{SA_{air}}{SA_{HP}}\right)\left(\frac{SA_{air} - SA_{ZnO}}{SA_{HP}}\right)$$

Eq. 4.30

$$P_{wa'} = P_w P_{a'} = \left(\frac{SA_{wall}}{SA_{HP}}\right)\left(\frac{SA_{air} - SA_{ZnO}}{SA_{HP}}\right)$$

Eq. 4.31

where P_{sa} is the probability of ZnO nanospikes facing the entrapped air, $P_{a,a'}$ is the probability of interaction between the air pockets and $P_{w,a'}$ is the probability of the sidewall facing the air-pocket in S-G orientation (**Figure 4.2**). The double layer electrostatic potential in this configuration is given by,

$$V_{DL,S-G} = P_{sa}V_{DL,sa} + P_{aa'}V_{DL,aa'} + P_{wa'}V_{DL,wa'}$$

Eq. 4.32

where

$$V_{DL,sa} = \frac{\pi\varepsilon_0\varepsilon_r R_{HP}(R_{HP} - d + \gamma d)}{2R_{HP} - d + \gamma d}(\zeta_{air}^2 + \zeta_{ZnO}^2)\left\{\frac{2\zeta_{air}\zeta_{ZnO}}{\zeta_{air}^2 + \zeta_{ZnO}^2} ln\left(\frac{1 + e^{-\kappa x}}{1 - e^{-\kappa x}}\right) + \ln(1 - e^{-2\kappa x})\right\}$$

Eq. 4.33

$$V_{DL,aa'} = 2\pi\varepsilon_o\varepsilon_r(R_{HP} - (1-\gamma)d)\zeta_{air}^2 \ln(1 + e^{-\kappa(x+(1-\gamma)d)})$$

Eq. 4.34

$$V_{DL,wa'} = \frac{1}{2}\pi\varepsilon_0\varepsilon_r(R_{HP} - d + \gamma d)(\zeta_{air}^2 + \zeta_{ZnO}^2)\left\{\frac{2\zeta_{air}\zeta_{ZnO}}{\zeta_{air}^2+\zeta_{ZnO}^2} ln\left(\frac{1+e^{-\kappa(x+(1-\gamma)d)}}{1-e^{-\kappa(x+(1-\gamma)d)}}\right) + \ln\left(1 - e^{-2\kappa(x+(1-\gamma)d)}\right)\right\}$$

Eq. 4.35

$V_{DL,sa}$, $V_{DL,aa'}$ and $V_{DL,wa'}$ are double layer electrostatic energies of nanospike-air interactions, air-air interactions and sidewall-air interactions across water, respectively. Similarly, the hydrophobic interaction potential is given by,

$$V_{HB,S-G} = P_{sa}V_{HB,sa} + P_{aa'}V_{HB,aa'} + P_{wa'}V_{HB,wa'}$$

Eq. 4.36

where

$$V_{HB,sa} = \frac{R_{HP}(R_{HP}-d+\gamma d)}{2R_{HP}-d+\gamma d} C\lambda e^{(-\frac{x}{\lambda})} \quad \text{Eq. 4.37}$$

$$V_{HB,aa'} = \frac{1}{2}(R_{HP} - (1-\gamma)d) C\lambda e^{(-\frac{x+(1-\gamma)d}{\lambda})} \quad \text{Eq. 4.38}$$

$$V_{HB,wa'} = \frac{1}{2}(R_{HP} - (1-\gamma)d) C\lambda e^{(-\frac{x+(1-\gamma)d}{\lambda})} \quad \text{Eq. 4.39}$$

The negative values of *x* in the S-G configuration represent a configuration when the nanospikes penetrate in the interstitial spaces. The point with $x = d(1-\gamma) \approx -200$nm represents the location of the air-water meniscus such that the coordinate origin coincides with the nanospike tip. Unlike the previous approach configuration, the overall vdW energy itself is repulsive for $x < -160$nm ($V_{vdW,S-G} > 0$) due to $A_{132} < 0$ and $\|P_{sa}V_{vdW,sa}\| + \|P_{wa'}V_{vdW,wa'}\| \gg \|P_{aa'}V_{vdW,aa'}\|$. Such interaction arises from proximity of entrapped air-pockets to the spikes; in this configuration, x is the closest distance between the meniscus and the ZnO spikes, while $x + d - \gamma d$ is the closest distance between the air pockets as well as between the wall and air-pockets. Moreover, one can note attractive well from double layer energies at close proximity, $V_{DL,S-G} < 0$ for $x < -196$ nm. This is due to electrostatic attraction between ZnO and air bubbles

($V_{DL,sa} < 0$, $V_{DL,wa'} < 0$) as $\zeta_{air}\zeta_{ZnO} < 0$. At $x > -196$ nm, $\|P_{aa'}V_{DL,aa'}\| \gg \|P_{sa}V_{DL,sa}\| + \|P_{wa'}V_{DL,wa'}\|$ and $V_{DL,S-G} > 0$.

Without the hydrophobic interaction, $V_{DLVO,S-G}$ is repulsive beyond $x \approx -196$ nm (**Figure S21.b**) with maximum repulsion at the energy barrier, $V_{DLVO,Max,S-G} \approx 51k_BT$ at $x \approx -160$ nm. Taking $V_{HB,S-G}$ into consideration, the attractive interaction potential shifts to a further distance away from the meniscus ($V_{E\_DLVO,S-G} < 0$ at $x < -145$ nm). Importantly, $V_{E\_DLVO,S-G} > 0$ at $x = 0$ nm, which correspond to repulsive potential at the contour around the ends/tips of nanospikes. Therefore, it is energetically unfavorable for the nanospikes to assume positions in between the nanospikes of other HPs as in **Figure S21.b**. The barrier at the HP interface is $V_{E_{DLVO},S-G} = 14.8k_BT$.

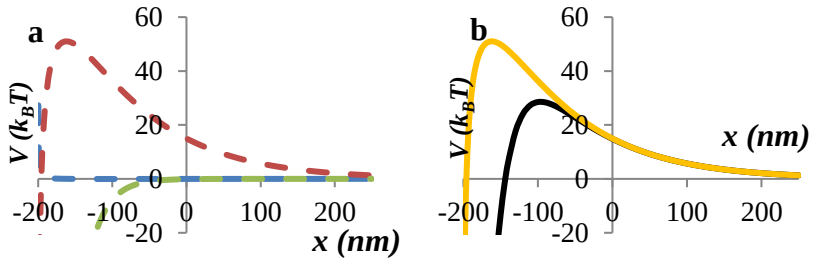

Figure 4.4. Interaction potential of hydrophobic HPs in the S-G configuration. **(a)** $V_{vdW,S-G}$ (blue dashed line), $V_{DL,S-G}$ (red dashed line) and $V_{HB,S-G}$ (green dashed line). **(b)** $V_{E\_DLVO,S-G}$ (black solid line) and $V_{DLVO,S-G}$ (orange solid line).

4.2.3 Proximal ZnO- spike-to-gap configuration (ZS-G)

As an intermediate between S-S and S-G configurations (**Figure 4.2.c**), one can consider a configuration where the ZnO nanospikes are not aligned to

engage in direct contact but close enough to interact. In this case, the particle experiences additional interactions from the side wall of ZnO nanospikes, especially for $x < 0$. These HP-HP interactions can be described as a sum of spike-to-sidewall, sidewall-to-air, and air-to-air interactions. The V_{vdW} interaction energies take the following form:

$$V_{vdW,ZS-G} = P_{sw}V_{vdW,sw} + P_{wa'}V_{vdW,wa'} + P_{aa'}V_{vdW,aa'}$$

Eq. 4.40

, where

$$V_{vdW,sw} = -\frac{A_{131}R_{HP}(R_{HP} - d + \gamma d)}{6(2R_{HP} - d + \gamma d)}\left(\frac{1}{x + d + \gamma d} - \frac{1}{x + d} - \frac{1}{x + \gamma d} + \frac{1}{x}\right) - \frac{A_{131}}{6}\ln\left(\frac{x(x + d + \gamma d)}{(x + d)(x + \gamma d)}\right)$$

Eq. 4.41

$$V_{vdW,wa'} = -\frac{A_{132}(R_{HP} - d + \gamma d)}{12}\left(\frac{1}{x + d + \gamma d} - \frac{2}{x + d} + \frac{1}{x + d - \gamma d}\right) - \frac{A_{132}}{6}\ln\left(\frac{(x + d - \gamma d)(x + d + \gamma d)}{(x + d)^2}\right)$$

Eq. 4.42

$$V_{vdW,aa'} = -\frac{A_{232}(R_{HP} - d + \gamma d)}{12}\left(\frac{1}{x + d + \gamma d} - \frac{2}{x + d} + \frac{1}{x + d - \gamma d}\right) - \frac{A_{232}}{6}\ln\left(\frac{(x + d - \gamma d)(x + d + \gamma d)}{(x + d)^2}\right)$$

Eq. 4.43

, where $V_{vdW,sw}$, $V_{vdW,wa'}$ and $V_{vdW,aa'}$ are vdW energies of nanospike-sidewall interactions, sidewall-air interactions, and air-air interactions across water,

respectively. Similarly, the double layer electrostatic potential in this configuration is given by,

$$V_{DL,ZS-G} = P_{sw}V_{DL,sw} + P_{wa'}V_{DL,wa'} + P_{aa'}V_{DL,aa'}$$

Eq. 4.44

where

$$V_{DL,sw} = \frac{2\pi\varepsilon_0\varepsilon_r R_{HP}(R_{HP}-d+\gamma d)\zeta_{ZnO}^2}{2R_{HP}-d+\gamma d}\left\{ln\left(\frac{1+e^{-\kappa x}}{1-e^{-\kappa x}}\right) + \ln(1-e^{-2\kappa x})\right\}$$

Eq. 4.45

$$V_{DL,wa'} = \frac{1}{2}\pi\varepsilon_0\varepsilon_r(R_{HP}-d+\gamma d)(\zeta_{air}^2+\zeta_{ZnO}^2)\left\{\frac{2\zeta_{air}\zeta_{ZnO}}{\zeta_{air}^2+\zeta_{ZnO}^2} ln\left(\frac{1+e^{-\kappa(x+(1-\gamma)d)}}{1-e^{-\kappa(x+(1-\gamma)d)}}\right) + \ln\left(1-e^{-2\kappa(x+(1-\gamma)d)}\right)\right\}$$

Eq. 4.46

$$V_{DL,aa'} = 2\pi\varepsilon_o\varepsilon_r(R_{HP}-(1-\gamma)d)\zeta_{air}^2\ln(1+e^{-\kappa(x+(1-\gamma)d)})$$

Eq. 4.47

$V_{DL,sw}$, $V_{DL,wa'}$, and $V_{DL,aa'}$ are double layer electrostatic energies of nanospike-sidewall interactions, sidewall-air interactions, and air-air interactions across water, respectively. The hydrophobic interaction potential is given by,

$$V_{HB,ZS-G} = P_{sw}V_{HB,sw} + P_{wa'}V_{HB,wa'} + P_{aa'}V_{HB,aa'}$$

Eq. 4.48

, where

$$V_{HB,sw} = \frac{RR_{HP}(R_{HP}-d+\gamma d)}{2R_{HP}-d+\gamma d}C\lambda e^{(-\frac{x}{\lambda})}$$

Eq. 4.49

$$V_{HB,wa'} = \frac{1}{2}(R_{HP} - (1-\gamma)d)C\lambda e^{(-\frac{x+(1-\gamma)d}{\lambda})} \quad \text{Eq. 4.50}$$

$$V_{HB,aa'} = \frac{1}{2}(R_{HP} - (1-\gamma)d)C\lambda e^{(-\frac{x+(1-\gamma)d}{\lambda})} \quad \text{Eq. 4.51}$$

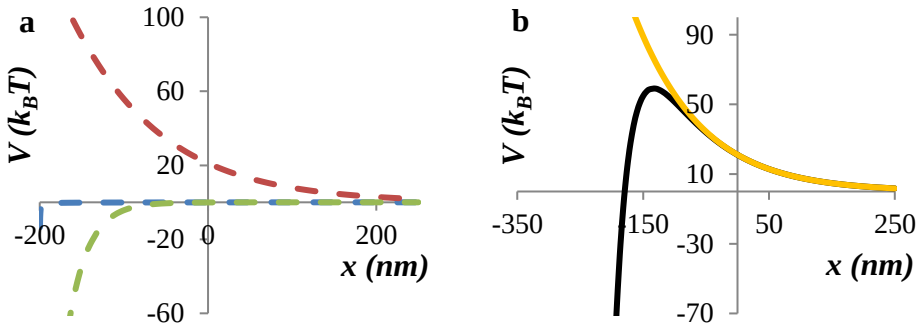

Figure 4.5. Interaction potential of hydrophobic HPs in the ZS-G configuration. **(a)** $V_{vdW,ZS-G}$ (blue dashed line), $V_{DL,ZS-G}$ (red dashed line) and $V_{HB,ZS-G}$ (green dashed line). **(b)** $V_{E_{DLVO},ZS-G}$ (black solid line) and $V_{DLVO,ZS-G}$ (orange solid

In this configuration, the magnitude of the double layer repulsive interaction potential is the highest among the three configurations depicted in **Figure 4.2**. As in the S-G configuration, it is energetically unfavorable for the spikes to assume positions in between the nanospikes of other HPs, as in **Figure 4.5.b**. The barrier at the HP interface is $V_{E_{DLVO},ZS-G} = 21\ k_BT$.

4.3 EDLVO calculations for hydrophobic polystyrene microspheres

In this section, we evaluated the interaction potential between "normal," smooth μPS particles identical to those used as HP cores. In particular, it is important in the context of this work to evaluate the interaction potential between OTMS-modified hydrophobic μPS in an aqueous environment. By comparing interaction potentials between the hydrophobic HPs and between colloids of hydrophobic and smooth surfaces, one would evaluate the effect of surface corrugation on the interaction potential between the particles. The interaction energy, $V_{E\_DLVO,PS}$, is given by

$$V_{E\_DLVO,PS} = -\frac{A_{434}R_{PS}}{12x} + 2\pi\varepsilon_o\epsilon_r R_{PS}\zeta_4^2 \ln(1+e^{-\kappa x}) + \frac{1}{2}R_{PS}C\lambda e^{(-\frac{x}{\lambda})}$$

Eq. 4.52

In the vdW component, A_{434} (1.37×10^{-20} J) is the Hamaker's constant of μPS across water layer[23] and R_{PS} (500 nm) is the radius of the μPS core. In the double layer component, ζ_4 (-12mV) is the zeta potential of uncharged non-functionalized μPS[327]. Equal hydrophobicity of μPS surfaces with other HP components enables us to assume the empirical values of $C = -9$ (mN/m) and $\lambda = 24$ (nm). The result shows that the attractive well ($x < 3$ nm) of $V_{DLVO,PS}$ is attributed to smaller ζ_4 (**Figure 4.6.b**). The magnitude and the range of attraction is considerably greater with addition of V_{HB}, $V_{E\_DLVO,PS} < 0$ at $x < 160$ nm.

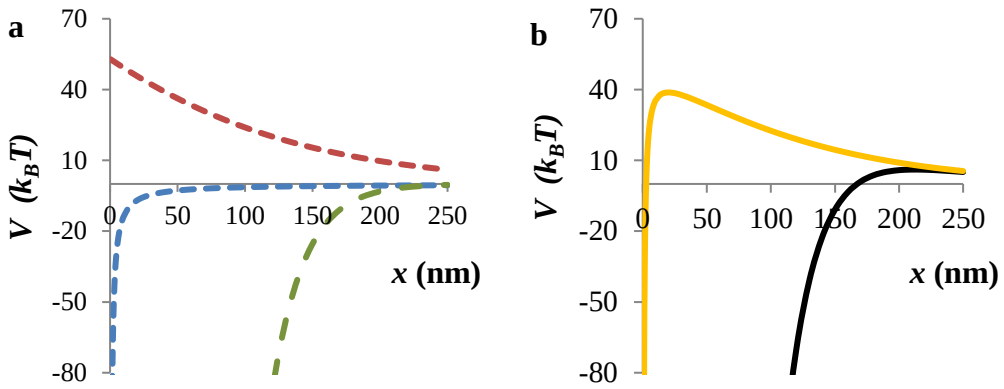

Figure 4.6. Interaction potential of OTMS-modified hydrophobic μPS. **(a)** $V_{vdW,PS}$ (blue dashed line), $V_{DL,PS}$ (red dashed line) and $V_{HB,PS}$ (green dashed line). **(b)** $V_{E\_DLVO,PS}$ (black solid line) and $V_{DLVO,PS}$ (orange solid line).

4.4 Discussion – orientation configuration and EDLVO

The interaction potential between the hydrophobic μPS, $V_{E\_DLVO,PS}$, shows strong attraction for all relevant distances and is superimposed on the plot.

Despite the absence of the air-pockets, $V_{DL,PS}$ is higher than the $V_{DL,S-S}$. This is due to a large interaction distance between air pockets in the S-S configuration. Irrespective of the approach configurations, the hydrophobic HPs are repulsive for $x > 0$ (**Figure 4.7.d**), while it is even more energetically unfavorable for nanospikes to interpenetrate (see evaluations of S-S, S-G, and ZS-G configurations).

Hydrophobic interaction potential between colloidal particles depends on the interacting surface area fraction and on the interaction distance from one another.

As such, $V_{HB,PS}$ (blue) and $V_{HB,ZnO}$ (red) indicate a significant level of hydrophobic attraction compared to $V_{HB,S-S}$ (black), $V_{HB,S-G}$ (orange) and $V_{HB,ZS-G}$ (**Figure 4.7.a**); between the interactions of smooth hydrophobic colloids, 100% of the surface area is available at minimum interaction distances. Here, $V_{HB,ZnO}$ represents hydrophobic attractive energy between two ZnO shells whose thickness corresponds to the length of the HP spike. Hence, should a ZnO shell be complete instead of being made from nanospikes, it would have the highest hydrophobic attraction potential. The S-S configuration has the lowest hydrophobic attraction potential amongst the three possible interaction configurations. In all cases, V_{vdW} is significantly smaller in comparison with V_{HB} (**Figure 4.7.b**). The main repulsive energies come from the DL electrostatic potential due to entrapped air-pockets attributed to large (in magnitude) ζ at the meniscus.

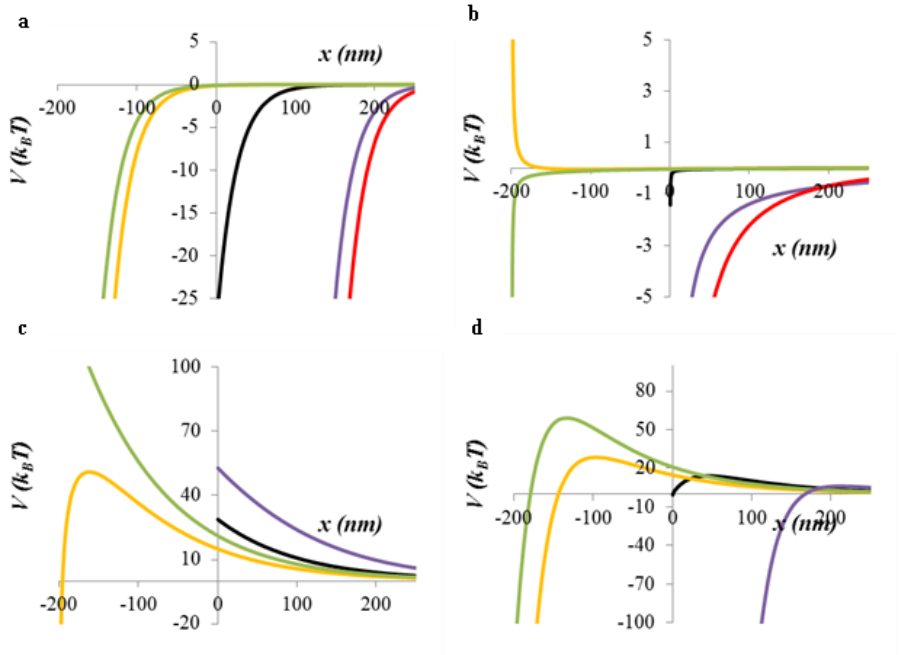

Figure 4.7. **(a) Hydrophobic potential**; $V_{HB,S-S}$ (black), $V_{HB,S-G}$ (orange), $V_{HB,ZS-G}$ (green), $V_{HB,PS}$ (blue), and $V_{HB,ZnO}$ (red) **(b) vdW potential**; $V_{vdW,S-S}$ (black), $V_{vdW,S-G}$ (orange), $V_{vdW,ZS-G}$ (green), $V_{vdW,PS}$ (blue), and $V_{vdW,ZnO}$ (red); **(c) double layer electrostatic potential**; $V_{DL,S-S}$ (black), $V_{DL,S-G}$ (orange), $V_{DL,ZS-G}$ (green) and $V_{DL,PS}$ (blue), **(d) total interaction potential** between hydrophobic HPs in S-S ($V_{E\_DLVO,S-S}$, black), S-G ($V_{E\_DLVO,S-G}$, orange) and ZS-G ($V_{E\_DLVO,ZS-G}$, green) configurations. The negative values of x in the S-G configuration describe the displacement of ZnO into the interstitial voids. The hydrophobic HPs are always repulsive from, and beyond, the ZnO tips. The total interaction potential between hydrophobic μPS ($V_{E\_DLVO,PS}$, blue) is superimposed onto the plot.

4.5 EDLVO for hydrophobic HPs at different ionic strengths

Interaction between colloids in the presence of ions typically leads to aggregation of particles due to screening of ionic interactions by ions. In this section, we look into the interaction potential of hydrophobic HPs in aqueous NaCl solutions of varying ionic strength. Trends and values of ζ of air bubbles with variation of the ionic strength are referenced to previous studies conducted by Yang et al.[11], and the Debye length, κ^{-1}, is obtained in accord with the ionic strength under investigation. E-DLVO potential calculations based on the above values indeed show instability of hydrophobic HPs in high ionic strength aqueous environment (**Figure 4.8**). This contradicts experimental observations because even at high ionic strength dispersions the HPs exhibit noticeable dispersion stability although with slightly increased flocculation. We attribute this discrepancy to the well-known deviations of DLVO theory at high ionic strengths (> 0.01 M of 1:1 electrolyte).

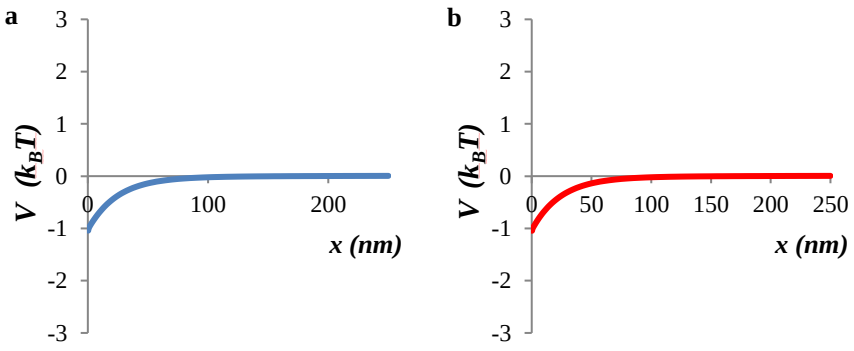

Figure 4.8. Pair potentials of hydrophobic HPs in NaCl solution calculated according to the E-DLVO theory for (a) 10^{-2} M (blue line) and (b) 10^{-1} M (red line).

4.6 DLVO for hydrophilic 'hedgehog' particles in apolar organic solvents

In this section, we evaluate the DLVO potential to elucidate the dispersion mechanism of hydrophilic HPs in organic solvents. The calculation approach is similar to the configurations in short hydrophobic HPs. Entrapment of air does not take place in this system due to low surface energy of organic solvent.

The calculations based on DLVO theory revealed that the stability of hydrophilic HP dispersion in, for instance, hexane is attributed to significant reduction in the interacting surface area at the outer edges of the HPs defined by the contour of ZnO spike tips similarly to the dispersions of hydrophobic HPs in water discussed above. vdW interaction potential is negligible for HP particles dispersed both in hexane (**Figure 3.4i**, main text) and ethanol (**Figure 4.9.)**. Note that vdW interactions of hydrophilic HPs in nonpolar organic solvents such as heptane and ethanol are similar due to similar Hamaker's constants $A_{ee} = 4.2 \times 10^{-20}$ J[20] and $A_{hh} = 4.1 - 4.3 \times 10^{-20}$ J[21,328,329] are Hamaker's constants for ethanol in air and heptane in air respectively.

We also calculated the total pair-potential of HPs in ethanol. These calculations bear relevance to evaluation of the stability of HP dispersions in ethanol after the rupture of the air-pockets described in the studies of the origin of the colloidal stability of OTMS-HP dispersions in water. They were carried out for $\kappa^{-1} = 38 \pm 5$ nm)[330,331] $\varepsilon_r = 24.5$[332], $\zeta_{ZnO} = -27$ mV[333], and $\zeta_{PS} = -31$ mV[276,334]. Note that DLVO has significant limitations when being applied to

mixed and amphiphilic solvents and the calculation results need to be considered as rough estimates valid within the theoretical framework described above. Nevertheless, we found that the pair potential is by no means indicative of strong attractive interactions (**Figure 4.9b)**. This means that the behavior of the particles will be governed predominantly by the Brownian motion. This is somewhat unusual of the particles of this size and is more characteristic of behavior of NPs.

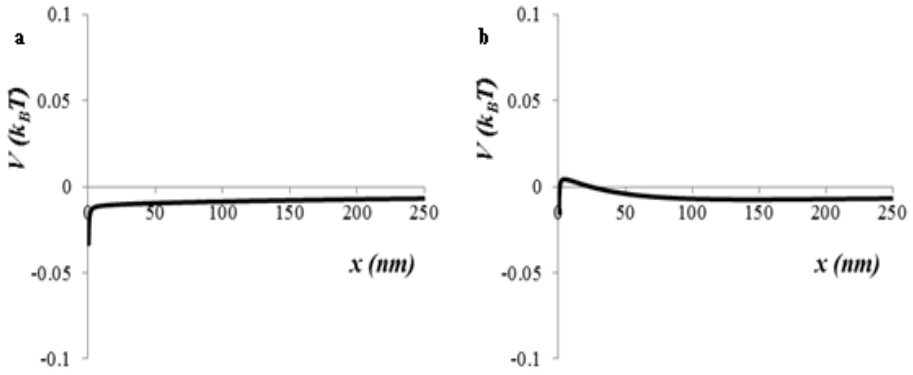

Figure 4.9. vdW interaction potential between HPs in ethanol, (b) pairwise potential of HPs in ethanol

Additional comments need to be made about DL potential of hydrophilic HPs in heptane. Since dielectric constant of heptane is $\varepsilon_r = 1.92$[335], one should expect a substantial increase in κ^{-1} due little concentration of ionic species in heptane. Previous studies indeed show that there is a dramatic increase in κ^{-1} for solvents with relative permittivity lower than 15[336,337].

Chapter V

Interaction Potential between Nanoparticles

5.1. EDLVO between DMAET stabilized CdTe quantum dots and Cytochrome C

The extended DLVO interaction energies between CdTe_DMAET and Cytc C are approximated by the following expression:

.

$$V_{EDLVO} = V_{vdW} + V_{DL} + V_{DP} + V_{Q-DP} + V_{HB} \quad \text{Eq. 5.1}$$

, where V_{vdW}, V_{DL}, V_{DP}, V_{Q-DP}, V_{HB} are van der Waals (vdW), double layer electrical repulsion (DL), dipole-dipole (DP), charge-dipole (Q-DP), and hydrophobic (HB) interaction potentials, respectively.

5.1.1 Van der Waals interactions

Total van der Waals potential between CdTe NPs capped with a shell of DMAET and Cytochrome C (CytC) can be evaluated as follows[300,338]:

$$V_{vdW} = V_{vdW,CdTe-CytC} + V_{vdW,DMAET-CytC} \quad \text{Eq. 5.2}$$

, where

$$V_{vdW,CdTe-CytC} = \frac{-(\sqrt{A_{11}}-\sqrt{A_{44}})(\sqrt{A_{33}}-\sqrt{A_{44}})H_{CdTe-CytC}(m,n)}{12} \quad :$$

$$m = \frac{x+d}{2R_{CdTe}} \quad , \; n = \frac{R_{CytC}}{R_{CdTe}} \quad \text{Eq. 5.3}$$

$$V_{vdW,DMAET-CytC} = \frac{-(\sqrt{A_{22}}-\sqrt{A_{44}})(\sqrt{A_{33}}-\sqrt{A_{44}})H_{DMAET-CytC}(m,n)}{12} \quad :$$

$$m = \frac{x}{2(R_{CdTe}+d)} \quad , \quad n = \frac{R_{CytC}}{R_{CdTe}+d} \quad \text{Eq. 5.4}$$

H(m,n), the Hamaker function, is given by

$$H(m,n) = \frac{n}{m^2+mn+n} + \frac{n}{m^2+mn+m+n} + 2\ln\left[\frac{m^2+mn+m}{m^2+mn+m+n}\right] \quad \text{Eq. 5.5}$$

Here, x is the closest distance between the DMAET-capped CdTe NPs and CytC. $A_{11}(11.4 \times 10^{-20}\text{J})$[24], $A_{22}(7 \times 10^{-20}\text{J})$[339], $A_{33}(9.63 \times 10^{-20}\text{J})$[340], $A_{11}(3.72 \times 10^{-20}\text{J})$ [20] are Hamaker constants for CdTe, hydrocarbons, proteins and water respectively. R_{CdTe} (1.9nm) is the radius of CdTe NPs, d (0.74nm) is the thickness of the DMAET shell around the NPs, R_{CytC} (1.55nm) is the radius of CytC approximated as a spherical entity.

5.1.2 Double Layer electrostatic interactions

Double layer repulsive potential between DMAET-capped CdTe NPs and Cytochrome C can be evaluated following references [341,342]:

$$V_{DL} = 4\pi\varepsilon_o\varepsilon_r(R_{CdTe} + d)R_{CytC}\Gamma_{CdTe\_DMAET}\Gamma_{CytC}\left(\frac{k_BT}{e}\right)^2\frac{\exp(-\kappa x)}{x + R_{CytC} + R_{CdTe} + d}$$

Eq. 5.6

,where

$$\Gamma_{CdTe-DMAET} = \frac{8 * \tanh(\frac{e\psi_{CdTe\_DMAET}}{4k_BT})}{1 + \sqrt{1 - \frac{2\kappa(R_{CdTe} + d) + 1}{(\kappa(R_{CdTe} + d) + 1)^2}\tanh^2(\frac{e\psi_{CdTe\_DMAET}}{4k_BT})}}$$

Eq. 5.7

$$\Gamma_{CytC} = \frac{8 * \tanh(\frac{e\psi_{CytC}}{4k_BT})}{1 + \sqrt{1 - \frac{2\kappa R_{CytC} + 1}{(\kappa R_{CytC} + 1)^2}\tanh^2(\frac{e\psi_{CytC}}{4k_BT})}}$$

Eq. 5.8

, where ε_0 is the permittivity of vacuum, ε_r is the dielectric constant of water, $\psi_{CdTe-DMAET}$ is the zeta potential of DMAET-capped CdTe NPs (+26mV), ψ_{CytC} is the zeta potential of CytC (+7mV). κ is the reciprocal double layer thickness (Debye length), is given by,

Eq. 5.9

$$\kappa = \sqrt{\frac{1000 N_A e^2}{\varepsilon_r \varepsilon_0 k_B T} \sum_i M_i \times Z_i^2}$$

where e is electric charge (Coloumbs), N_A is Avogadro's number, M_i and Z_i are the molar concentration and valency of ions, respectively. The Debye length of NaCl electrolytes specific to ionic strength of interest is calculated accordingly. The practical Debye length of water is taken to be $\kappa^{-1} \approx 100\text{nm}$ [312–314].

5.1.3 Dipole-Dipole interactions

Dipole-dipole energies is derived according to the interaction model and is approximated by the following:

$$V_{DP} = \frac{-\mu_{CdTe}\mu_{CytC}}{2\pi\varepsilon_o\varepsilon_r} * \frac{(x + R_{CdTe} + R_{CytC} + d)}{x(x + 2R_{CdTe} + 2d)(x + 2R_{CytC})(x + 2R_{CdTe} + 2R_{CytC} + 2d)}$$

Eq. 5.10

, where μ_{CdTe} (100D) [301,343] and μ_{CytC} (340D) [344] are dipole moment of CdTe NPs and CytC, respectively.

5.1.4 Charge-Dipole interactions

Charge-dipole energy according to our interaction model is evaluated from the following:

$$V_{Q-DP} = -\frac{\mu_{CytC} Q_{CdTe\_DMAET} - \mu_{CdTe\_DMAET} Q_{CytC}}{4\pi\varepsilon_o\varepsilon_r} * \frac{1}{(x + R_{CdTe} + R_{CytC} + d)^2}$$

Eq. 5.11

, where $Q_{CdTe-DMAET}$ and Q_{CytC} are the total surface charge of DMAET-capped CdTe and CytC respectively. We used previously reported surface charge of CdTe NPs (+3e) [345]. The surface charge of CytC is obtained from the following relations [346]:

$$\sigma_{CytC} = \frac{2\varepsilon_r\varepsilon_o\kappa k_B T}{ze}\sinh\left(\frac{ze\psi_{CytC}}{2k_B T}\right)\sqrt{\left[1 + \frac{1}{\kappa R_{CytC}}\frac{2}{\cosh^2(\frac{ze\psi_{CytC}}{4k_B T})} + \frac{1}{(\kappa R_{CytC})^2}\frac{8\ln[\cosh(\frac{ze\psi_{CytC}}{4k_B T})]}{\sinh^2(\frac{ze\psi_{CytC}}{2k_B T})}\right]}$$

$$Q_{CytC} = 4\pi R_{CytC}^2 * \sigma_{CytC}$$

Eq. 5.12

5.1.5 Hydrophobic interactions

Hydrophobic interaction is represented by the single exponential function [62],

$$\frac{F_{HB}}{R} = Ce^{(-\frac{x}{\lambda})}$$ Eq. 5.13

where C is the hydrophobic amplitude and λ (m) is the decay length. Integrating over *x* and substituting in the effective radius, we obtain hydrophobic interaction energy reflective of our interaction model:

$$V_{HB} = \frac{(R_{CdTe} + d)R_{CytC}}{R_{CdTe} + R_{CytC} + d} C\lambda e^{(-\frac{x}{\lambda})} \quad \text{Eq. 5.14}$$

The strength and the range of hydrophobic interaction were previously shown to depend on the contact angle of the interacting substrates (θ_c) [62]. Due to lack of literature data on the hydrophobicity of DMAET and CytC, we used data based on similar chemical moieties. The contact angle of 2-(diethyamino)ethanethiol (DEAET) on a gold coated substrate was found to be $\theta_c = 74^o$ [347]. Furthermore, interfacial reaction of polyimide film with ethanethiol induced reduction in polarity with water contact angle $64^o < \theta_c < 78^o$ [348]. A self-assembled monolayer (SAM) of porphyrin on a gold substrate showed contact angle $76^o < \theta_c < 78^o$ [349]. Based on the contact angle data, we used $C = -9$ (mN/m) and λ = 2 (nm), which are based on interacting surfaces with contact angle $\theta_c = 81^o$ [62].

5.1.5 Self-terminating self-assembly process of DMAET stabilized CdTe quantum dots and Cytchrome C towards spherical supraparticles

Mixture of DMAET stabilized CdTe and Cytochrome C leads to formation of self-terminating self-assemblies of spherical supraparticles with narrow size distributions[350]. The self-termination of the assembling process originates from competition between the electrostatic repulsion and assortments of attractive interactions. The classical and extended EDLVO calculations show that the overall interaction between the CdTe_DMAET and Cytc C is attractive (**Figure**

5.1). Despite the classical DLVO theory having multiple questionable points, it does layout a rough estimate of the scale of the force involved. In this system, the aggregation barrier is smaller than the k_BT. Extending the DLVO by adding various terms such as dipole–dipole, charge–dipole, and hydrophobic interactions, the pair potential becomes attractive for all distances. Furthermore, increase in size results in increase in the electrostatic repulsion and accounts for the self-terminating nature of the assembly process.

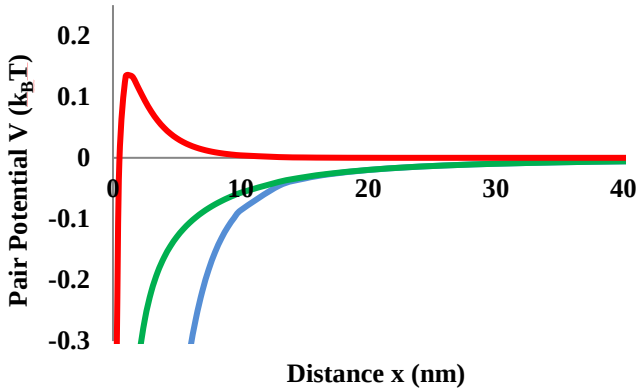

Figure 5.1. (Pair potential between CdTe NPs and CytC according to DLVO and E-DLVO theories: V_{DLVO} (red); V_{EDLVO1} (green); V_{EDLVO2} (blue), where $V_{DLVO} = V_{vdW} + V_{DL}$, $V_{EDLVO1} = V_{vdW} + V_{DL} + V_{DP} + V_{Q-DP}$, $V_{EDLVO2} = V_{vdW} + V_{DL} + V_{DP} + V_{Q-DP} + V_{HB}$

5.2. EDLVO between CdTe quantum dots

5.2.1 EDLVO between TGA stabilized CdTe quantum dots

The extended DLVO interaction energies between quantum dots are approximated by the following expression:

$$V_{EDLVO} = V_{VdW} + V_{DL} + V_{DP} + V_{Q-DP} \quad \text{Eq. 5.15}$$

, where V_{VdW} V_{DL} V_{DP} V_{Q-DP} are Van der Waals, DL electrical repulsion, dipole-dipole and charge-dipole interaction potentials, respectively.

5.2.1.1 Van der Waals interactions

Total Van der Waals potential between CdTe NPs capped with a shell of TGA can be evaluated as follows[300,338]:

$$V_{VdW} = V_{VdW,shell} + V_{VdW,core} + V_{VdW,core-shell} + V_{VdW,shell-core} \quad \text{Eq. 5.16}$$

, where

$$V_{VdW,shelll} = \frac{-A_{232}H_{shell}(m,n)}{12} \quad : \quad m = \frac{x}{2(R_{CdTe}+d)} \quad , \; n = 1$$

$$V_{VdW,core} = \frac{-A_{131}H_{core}(m,n)}{12} \quad : \quad m = \frac{x+2d}{2R_{CdTe}} \quad , \quad n = 1$$

$$V_{VdW,core-shell} = \frac{-A_{132}H_{core-shell}(m,n)}{12} \quad : \quad m = \frac{x+d}{2R_{CdTe}} \quad , \quad n = \frac{R_{CdTe}+d}{R_{CdTe}}$$

$$V_{VdW,shell-core} = \frac{-A_{132}H_{shell-core}(m,n)}{12} \quad : \quad m = \frac{x+d}{2(R_{CdTe}+d)} \quad , \quad n = \frac{R_{CdTe}}{R_{CdTe}+d}$$

Eq. 5.17-20

H(m,n), the Hamaker function, is given by

$$H(m,n) = \frac{n}{m^2+mn+n} + \frac{n}{m^2+mn+m+n} + 2\ln\left[\frac{m^2+mn+m}{m^2+mn+m+n}\right]$$

Eq. 5.21

Here, x is the closest distance between the TGA-capped CdTe NPs, A_{131} is Hamaker constant of CdTe interactions in water (4.85 x 10^{-20} J, value of closely CdS QD is used [351,352]), A_{232} is Hamaker constant of TGA interactions in water (5 x 10^{-21} J, which approximates interactions between hydrocarbon chains in water [20,339,353]), A_{132} relates CdTe and TGA in water. A_{132} is approximated from the following relation [20])

$$A_{132} = (\sqrt{A_{11}} - \sqrt{A_{33}})(\sqrt{A_{22}} - \sqrt{A_{33}})$$ Eq. 5.22

where $A_{11} = 11.4 \times 10^{-20}$J [24] (value of CdS in air), $A_{22} = 7 \times 10^{-20}$J [339], $A_{33} = 3.72 \times 10^{-20}$J [20]. R_{CdTe}(=5nm) is the radius of CdTe NPs, d(=0.76nm, maximum length of TGA [354]) is the thickness of the TGA shell around the NPs.

5.2.1.2 Double Layer electrostatic interactions

Total Van der Waals potential between CdTe NPs capped with a shell of TGA can be evaluated as follows [341,342,355,356]

$$V_{DL} = 4\pi\varepsilon_o\varepsilon_r(R_{CdTe} + d)^2\Gamma^2\left(\frac{k_BT}{e}\right)^2 \frac{\exp(-\kappa x)}{x + 2(R_{CdTe} + d)}$$

Eq. 5.23

Where

$$\Gamma = \frac{8 * \tanh(\frac{e\psi_{CdTe-TGA}}{4k_BT})}{1 + \sqrt{1 - \frac{2\kappa(R_{CdTe} + d) + 1}{(\kappa(R_{CdTe} + d) + 1)^2}\tanh^2(\frac{e\psi_{CdTe-TGA}}{4k_BT})}}$$

Eq. 5.24

where ε_0 is the permittivity of vacuum, ε_r is the dielectric constant of water andψ_{CdTe} is the zeta potential of CdTe-TGA(=-6mV) NPs . κ, the reciprocal double layer thickness (Debye length), is given by,

$$\kappa = \sqrt{\frac{1000N_Ae^2}{\varepsilon_r\varepsilon_0k_BT}\sum_i M_i \times Z_i^2}$$

Eq. 5.9

where e is electric charge (Coloumbs), N_A is Avogadro's number, M_i and Z_i are the molar concentration and valency of ions, respectively. The practical Debye length of water is taken to be $\kappa^{-1} \approx 100$ nm [312–314].

5.2.1.3 Dipole-dipole interactions

Dipole-dipole interaction potential is approximated by the following [342,355]:

$$V_{DP} = \frac{-\mu_{CdTe}^2}{2\pi\varepsilon_o\varepsilon_r} * \frac{1}{r(r^2 - 4R_{CdTe}^2)}$$

, where Eq. 5.25

$$r = x + 2d + 2R_{CdTe}$$

Here, μ_{CdTe} (dipole moment of CdTe NPs) is taken to be 100D [301,343].

5.2.1.4 Charge-dipole interactions

Charge-dipole interaction energy requires the knowledge of total surface charge on the particle (Q) which is related by ψ_{CdTe} with the following expressions [346]

$$\sigma = \frac{2\varepsilon_r\varepsilon_o\kappa k_B T}{ze}\sinh\left(\frac{ze\psi_{CdTe}}{2k_B T}\right)\sqrt{\left[1 + \frac{1}{\kappa a}\frac{2}{\cosh^2(\frac{ze\psi_{CdTe}}{4k_B T})} + \frac{1}{(\kappa a)^2}\frac{8\ln[\cosh(\frac{ze\psi_{CdTe}}{4k_B T})]}{\sinh^2(\frac{ze\psi_{CdTe}}{2k_B T})}\right]}$$

$$Q = 4\pi R_{CdTe}^2 * \sigma$$

Eq. 5.26

Charge-dipole interaction energy is evaluated from the following [355]

$$V_{Q-DP} = -\frac{Q_{CdTe}^2\mu_{CdTe}^2}{6(2\pi\varepsilon_o\varepsilon_r)^2 k_B T}\frac{1}{r^4}$$

Eq. 5.27

, where

$$r = x + 2d + 2R_{CdTe}$$

5.2.2 EDLVO between "bare" CdS quantum dots

Only the interactions between the CdS NP cores are required due to lack of stabilizers. The distance consideration corresponding to the shell thickness (in the CdTe-TGA NPs) is not required.

$$V_{VdW}(CdS, CdS) = -\frac{A_{131}}{6}\left(\frac{2R_{CdS}^2}{2R_{CdS}x + x^2} + \frac{2R_{CdS}^2}{4R_{CdS}^2 + 4R_{CdS}x + x^2} + ln\left[\frac{4R_{CdS}x + x^2}{4R_{CdS}^2 + 4R_{CdS}x + x^2}\right]\right) \quad \text{Eq. 5.28}$$

$$V_{DL} = 4\pi\varepsilon_o\varepsilon_r {R_{CdS}}^2 \Gamma^2 \left(\frac{k_B T}{e}\right)^2 \frac{\exp(-\kappa x)}{x + 2R_{CdS}} \quad \text{Eq. 5.29}$$

, where

$$\Gamma = \frac{8 * \tanh(\frac{e\psi_{CdS}}{4k_B T})}{1 + \sqrt{1 - \frac{2\kappa R_{CdS} + 1}{(\kappa R_{CdS} + 1)^2} \tanh^2(\frac{e\psi_{CdS}}{4k_B T})}}, \qquad \psi_{CdS} = -15\text{mV}$$

$$V_{DP} = \frac{-\mu_{CdS}^2}{2\pi\varepsilon_o\varepsilon_r} * \frac{1}{r(r^2 - 4R_{CdS}^2)} \quad \text{Eq. 5.30}$$

, where

$$r = x + 2R_{CdS} \ , \ \mu_{CdTe} = \mu_{CdS},$$

$$V_{Q-DP} = -\frac{Q_{CdS}^2 \mu_{CdS}^2}{6(2\pi\varepsilon_o\varepsilon_r)^2 k_B T}\frac{1}{r^4}$$

Eq. 5.31

, where

$$r = x + 2R_{CdS}$$

$$\sigma = \frac{2\varepsilon_r\varepsilon_o\kappa k_B T}{ze}\sinh\left(\frac{ze\psi_{CdS}}{2k_B T}\right)\sqrt{\left[1 + \frac{1}{\kappa R_{CdS}}\frac{2}{\cosh^2(\frac{ze\psi_{CdS}}{4k_B T})} + \frac{1}{(\kappa R_{CdS})^2}\frac{8\ln[\cosh(\frac{ze\psi_{CdS}}{4k_B T})]}{\sinh^2(\frac{ze\psi_{CdS}}{2k_B T})}\right]}$$

Eq. 5.32

5.3 Electrostatic forces and potential between gold nanorods with dihedral orientation

An expression for the electrostatic force between two gold nanorods at a separation distance *h* with a dihedral angle θ is derived in this section. In order to simplify the derivation, several assumptions are made which are as follows: 1) each of the gold nanorods are assumed a line of charges whose line charge density λ is approximated by charge density conversion from the experimentally obtained

ζ-potential. 2) The separation distance is defined along the orthogonal axis between two parallel planes, each plane encompassing the line charges. Therefore, the separation distance remains constant and the derivation simplifies to 2D geometry, as shown in **Figure 5.2**

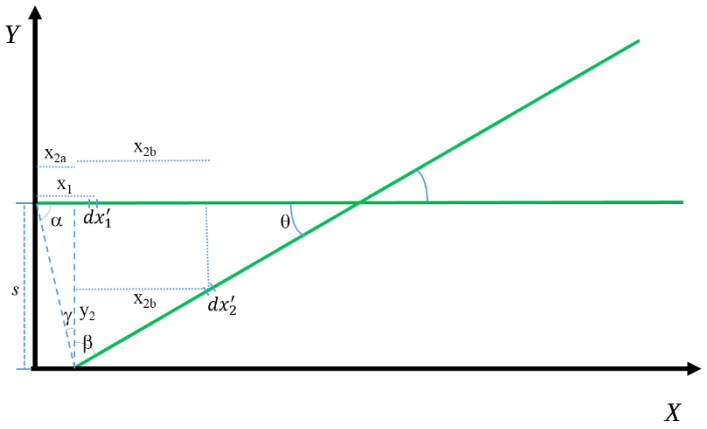

Figure 5.2. The x-y plane view of the gold nanorods with dihedral angle θ.

The line charge x_1' are set parallel to the x-axis and forms a dihedral angle θ with the line charge x_2'. Importantly, the initial point of the line charge x_1' contacts the *y*-axis and that of the line charge x_2' contacts the *x*-axis. The differential electrostatic force between the differential elements of each nanorods, dx_1' and dx_2', is evaluated as follows.

$$d\vec{F} = \frac{1}{4\pi\varepsilon_o\varepsilon_r}\int_0^l\int_0^l \frac{dq_1 dq_2}{r^3}\vec{r} \qquad \text{Eq. 5.33}$$

, where $\vec{r} = \overrightarrow{r_2} - \overrightarrow{r_1}$ is the displacement vector, $r = \|\vec{r}\|$, $\overrightarrow{r_1} = x_1\hat{x}$ and $\overrightarrow{r_2} = x_2\hat{x} + x_2\hat{y} + x_2\hat{z}$. The *x*-component of $\overrightarrow{r_2}$, $x_2 = x_{2a} + x_{2b}$, can be found by simple trigonometric relations. The constant x_{2a} represents the location where the initial tip of x_2' is projected onto the *x*-axis and x_{2b} represents the projection x_2' onto the *x*-axis, and are found as follows:

$$x_{2a} = s\tan\gamma$$
$$x_{2b} = x_2'\cos\theta \qquad \text{Eq. 5.34}$$

, where $= {}^{l}/_{2}\sin\theta$, $\gamma = {}^{\theta}/_{2}$ as $2\alpha + \theta = 180^o$ (equal lateral triangle), $\gamma = \alpha - \beta$ and $\beta = 90^o - \theta$. Hence, the projection of along the *x*-axis is expressed as

$$x_2 = x_{2a} + x_{2b} = \frac{l}{2}\sin\theta\tan\frac{\theta}{2} + x_2'\cos\theta \qquad \text{Eq. 5.35}$$

In addition, the *y*-component of $\overrightarrow{r_2}$ is expressed as follows via simple trigonometry:

$$y_2 = -s + x_2'\sin\theta = (x_2' - {}^{l}/_{2})\sin\theta \qquad \text{Eq. 5.36}$$

The z-component remains constant at all length along the nanorods at the experimentally found separation distances at $z_2 = h$. The displacement vector expressed in terms of the line charges, x_1' and x_2' is as follows:

$$\vec{r} = \left(\frac{l}{2}\sin\theta\tan\frac{\theta}{2} + x_2'\cos\theta - x_1'\right)\hat{x} + \left(\left(x_2' - \frac{l}{2}\right)\sin\theta\right)\hat{y} + h\hat{z}$$

Eq. 5.37

Substituting differential charge densities in terms of differential line charges, $dq_1' = \zeta dx_1'$ and $dq_2' = \zeta dx_2'$ and integrating over the length of each line charges, total electrostatic force between x_1' and x_2' is obtained as follows:

$$\vec{F} = A\int_0^l\int_0^l \frac{\left[\left(\frac{l}{2}\sin\theta\tan\frac{\theta}{2} + x_2'\cos\theta - x_1'\right)\hat{x} + \left(\left(x_2' - \frac{l}{2}\right)\sin\theta\right)\hat{y} + h\hat{z}\right]}{\left(\frac{l}{2}\sin\theta\tan\frac{\theta}{2} + x_2'\cos\theta - x_1')^2 + ((x_2' - \frac{l}{2})\sin\theta)^2 + h^2\right)^{3/2}} dx_2' dx_1'$$

, where

$$A = \frac{\sigma_{line}^2}{4\pi\varepsilon_0\varepsilon_r}$$

Eq. 5.38

The line charge density, σ_{line}, is obtained via zeta-potential measurement of the gold nanorods (ψ_{Au}). Due to aspect ratio of the gold nanorods being close to unity ($AR = l/w \approx 1.2$), where w is the width of the gold nanorods, surface charge density is calculated assuming a spherical particulate model [346],

$$\sigma_{surface} = \frac{2\varepsilon_r \varepsilon_o \kappa k_B T}{ze} \sinh\left(\frac{ze\psi_{Au}}{2k_B T}\right) \sqrt{\left[1 + \frac{1}{\kappa R_{Au}} \frac{2}{\cosh^2\left(\frac{ze\psi_{Au}}{4k_B T}\right)} + \frac{1}{(\kappa R_{Au})^2} \frac{8\ln[\cosh\left(\frac{ze\psi_{Au}}{4k_B T}\right)]}{\sinh^2\left(\frac{ze\psi_{Au}}{2k_B T}\right)}\right]}$$

$$R_{Au} = \frac{L+W}{2} \qquad \text{Eq. 5.39}$$

$$\sigma_{line} = \sigma_{surface} \times R_{Au}$$

, where R_{Au} is the effective diameter of the gold nanorods. For simplicity, 1-1 electrolytes are assumed in the surrounding media for charge density approximation from the z-potential measurements (Eq. 5.30). Additionally, ε_0 is permittivity of vacuum, ε_r is dielectric constant of water, k_B is Boltzmann constant and T is the absolute temperature. The Debye length, κ, is given by,

$$\kappa = \sqrt{\frac{1000 N_A e^2}{\varepsilon_r \varepsilon_0 k_B T} \sum_i M_i \times z_i^2} \qquad \text{Eq. 5.40}$$

where e is electric charge (Coloumbs), N_A is Avogadro's number, M_i and z_i are the molar concentration and valency of ions, respectively, where $z_i = 1$ is assumed.

Electrostatic Energy between two gold nanorods with dihedral orientation.

The electrostatic energy due to line charge density at the dihedral configuration can be found by the following:

$$U = \frac{1}{2}\int \frac{dq_1 dq_2}{4\pi\varepsilon_o\varepsilon_r r} = \frac{1}{2}\int \frac{\sigma^2}{4\pi\varepsilon_o\varepsilon_r r}\, dx_1 dx_2$$

$$= K\int_0^l \int_0^l \frac{dx_2 dx_1}{\left(\frac{l}{2}\sin\theta\tan\frac{\theta}{2} + x_2\cos\theta - x_1)^2 + ((x_2 - \frac{l}{2})\sin\theta)^2 + h^2\right)^{1/2}}$$

$$K = \frac{\sigma_{line}^2}{8\pi\varepsilon_0\varepsilon_r}$$

Eq. 5.41

Chapter VI

Light Scattered by 'Hedgehog' Particles

6.1 Introduction

Sensitive to even a small perturbation in its construct, particles provide versatile and compact platforms with which to design electromagnetic responses. With great advances in the nanofabrication, diverse particle types exhibiting unique and useful scattered radiation patterns have been realized or theoretically predicted[357–359]. In particular, particles exhibiting broadband scattering with flexibility to suppress backscattering and enhance forward scattering[360–363] hold promises in a diverse array of photonics devices servicing photodetectors, antennas and photovoltaics [364–367]. Recently, we have reported the 'hedgehog'

particles with anomalous dispersion behavior that breaks the well-known "similarity rule"[368]. The 'hedgehog' particles represent a novel class of "rough" particles comprised of all dielectric components that lies within the Mie scattering regime due to wavelength comparable dimensions. It should be noted that such types of particles are barren in previous endeavors both experimentally and theoretically. In this letter, we will show that the 'hedgehog' particles feature broadband light scattering in conjunction with broadband suppression of backscattering and enhanced transmission. Such far-field pattern stems from the presence of spiky interfaces that significantly suppresses resonant behavior within the particle and that reshapes the near-field profile in the form of simultaneous excitation of electric and magnetic fundamental modes. Addition to a library of electromagnetic responses of diverse particle types is expected further enrich scientific foundation and engineering of photonic devices.

6.2 Fabrication

We initially reasoned that the 'hedgehog' particle (HP) is an efficient broadband light scatterer due to embodiment of multiple electromagnetic interferences at the spiky interface. The HPs are constructed by electrostatic adsorption of ZnO NPs as seeds onto carboxylated PS μ-spheres and subsequent growth of ZnO nano-spikes through hydrothermal and sonochemical processes (**Figure 6.1.a-e**). The nano-topographical details, such as the length and thickness

of the spikes, could be easily tailored to specifications by adjusting the growth conditions (**Figure 6.1.f-l)).**

6.3 Extinction spectra of HPs in water

Unlike typical smooth and low refractive index dielectric micro-particles, the HPs exhibit atypical extinction features with two peaks, notably one broadband peak at ~ 730 nm (P_1) and another narrower peak at ~405nm (P_2) and does not correlate with the extinction features of either the ZnO NWs nor the PS μ-spheres (**Figure 6.2.a**). It should be noted that peak normalized (P.N.) spectra is discussed as the present work focuses on the spectral line shape rather than the scattering intensities and efficiencies. Spectral tuning is easily achieved by adjusting its corrugation geometry. Increase in the ZnO nanospike length (*l*) causes spectral redshift and broadening of both of the peaks. Similar trend is observed with increase in the nanospike width (*w*).

6.4 Origin of the broadband peak, FDTD solutions of far-field patterns in water

The uncharacteristic broadband peak P_1 that spans from the visible to the NIR range suggests electromagnetic coupling between the structural components within the HPs. Due to its high aspect ratio nano-topography, analytical Mie theory is not adequate to representatively compute the EM responses. Here, finite difference time domain (FDTD) method has been employed as its approach is

suitable to handle optical properties of geometrically complex particles[369]. Model HP (M-HP) was reconstructed to mirror imperfect orthogonalization of ZnO nanospikes to reflect the experimental construct (**Figure 6.11**). The FDTD based simulations (Lumerical FDTD Solutions) of extinction cross-section (σ_{ext}) by the M-HP illuminated with total field/scattered field (TFSF) plane wave approximates the spectral line-shape of spectroscopic measurement with excellent agreement (**Figure 6.3.c, Figure 6.12**). The FDTD simulation based on the M-HP also captures spike width dependent peak-shifts and additionally shows expected red-shift with increase in the spike density (**Figure 6.3.a, b**). As expected, the overall σ_{ext} of a HP is scattering dominant due to non-absorbing dielectric components (**Figure 6.13**).

The lack of spectral correlation between the HP and its components (**Figure 6.2.a**) suggest that the origin of P_1 points to particle architecture. Indeed, evolution of σ_{ext} from a PS μ-sphere and a ZnO nanospike to the M-HP construct shows that the ortho-spherical arrangement of ZnO nanospikes is the governing structural attribute that generates P_2 (**Figure 6.3.d**). In the presence of PS μ-sphere, linearly polarized plane wave irradiation (polarized in the *z*-direction, propagating along *x*-direction, λ = 1004 nm) shows redistribution of electric field (E-field) vector profile that spatially extends to the core. The presence of the PS μ-sphere increases the polarizability within the HP and induces electric field coupling with the core substrate, reminiscent of the "dressing"

effect[370]. Such leads to a further spectral redshift of the σ_{ext} line-hape (**Figure 6.3.e, f**).

It should be noted that the M-HP requires higher nanospike densities (*N*) to spectrally match with the experimental construct ($N_{experiment}$~$200 - 250$, $N_{M-HP} = 500$). This may be due to large mesh size employed in the FDTD simulations to remain within the computational budget; this may not sufficiently grasp the geometrical finesse and complexities at the interfacial corrugation. Hence, simplifying the empirical HP features to appropriate core-shell representation should yield extinction line-shape accordant with spectroscopic measurements. Due to orthogonalization of spikes in spherical format, the spiky volume of the HP is remodeled with gradient refractive index via three discretized shells at 1:1:1 or 3:2:1 (outer: middle: inner shell) thickness ratios, layered on the PS μ-sphere. Refractive indices of each shells are designated by effective medium approximation (EMA) using Maxwell Garnett mixing rule [371,372] for two-phase heterogeneous media. The triple-shell model representative of HPs having $N_{3-shell} = 250 \sim 275$ indeed shows extinction pattern with excellent agreement with the far-field experimental data (**Figure 6.15, 6.16**).

6.5 Broadband suppression of backscattering and enhancement of forward scattering

Triple-shell models with analytically smooth surfaces and EMA derived constitutive properties, however, are unable to accurately account for the near-

field profiles. This is more evident in air representing higher refractive index contrast. First, excellent agreement in the far-field pattern is achieved with the M-HP and the experimental construct suspended in mid-air, to prevent the "dressing" effect with surfaces (**Figure 6.4.a**). FDTD simulations of a PS μ–sphere of equivalent diameter to the HP in air exhibit resonant behavior, which eventually dissipates due to leaky nature of the low refractive index material. The resonant behavior is also seen in the far-field extinction data where ripples of sharp peaks are observed within the coarse oscillation [373,374] (**Figure 6.4.b**). The gradient refractive index triple-shell model also exhibits resonant behavior, but at much lower Q-factor (**Figure 6.4.b**). Meanwhile, the resonant feature is significantly suppressed in the lower wavelengths and non-existent at $\lambda > 650$ nm for the M-HP (**Figure 6.4.b**). Here, one can say that light undergoes, not completely but close to, a non-resonant form of Mie scattering. Despite the constitutive properties and size ranges that predicts resonance from the Mie theory, the suppression of resonance is reasoned by the inability of the core cavity to efficiently confine light due to its refraction towards optically more dense nanospikes, followed by the radiative decay.

The non-resonant form of scattering is further verified by coupling free effect at the near-fields (**Figure 6.4.c, d**, **Figure 6.19**) and by spectral overlap of σ_{ext} between a single M-HP and a pair of M-HPS with zero separation distance aligned perpendicular to the incident plane wave (**Figure 6.18**). It will be mentioned later that the non-resonant form of scattering, characterized by explicit

forward directionality and previously achieved with all polymer core-shell nanowires[375], plays an important role in shaping the scattering pattern by the HPs.

So far, it is observed, owing to the spiky interface, that M-HP exhibits significant suppression of resonant behavior. The FDTD-based simulation also shows a very useful scattering anisotropy in the form of suppression of backscattering. The M-HP exhibits broadband suppression of backscattering, and there are multiple regions (1490 nm < λ < 1744 nm, 1490 nm < λ < 1744 nm, 1490 nm < λ < 1744 nm) where zero-backscattering occurs (P<0.01) (**Figure 6.5a**). Zero-backscattering is defined as percentage of normalized power collected at a monitor located behind the radiation source that is less than 1% (**Figure 6.20.a**). At the same time, enhancement of forward scattering occurs at the spectral vicinity of zero-backscattering, aided by the forward directionality of the overall scattering pattern due to suppression of resonance. There are multiple regions where forward to backward scattering ratio (*F*/*B*) exceeds 200, 2075 nm < λ < 2690 nm denoted as *Region 1* and 1509 nm < λ < 1674 nm denoted as *Region 2* (**Figure 6.5.b**). The maximum *F*/*B* reaches as high as 680, at λ = 2423 nm. It should be noted that in the previous studies that demonstrated broadband suppression of backscattering and enhancement of forward scattering, the spectral range was limited to ~70nm, with *F*/*B* ~ 3 [363]. *F*/*B* ~8 was achieved with silicon nanoparticles [360].

The mechanism behind such scattering anisotropy could be elucidated with the near-field profiles within the particle. First looking at *Region 1* where

F/*B* > 200, magnetic dipole (MD) mode is excited within a PS μ-sphere of *r* = .5 μm, representing the core of the HP, when illuminated with a plane wave of λ = 2423 nm (**Figure 6.21**). Meanwhile, both MD and electric dipole (ED) modes are excited simultaneously within an M-HP at the same wavelength (**Figure 6.5.g, h**). The presence of ZnO nanospikes excites additional ED that undergoes spectra redshift due to the "dressing" effect towards spectral location of the MD that is present within the PS core cavity. Such simultaneous excitation of the two fundamental modes causes suppression of scattering in the backward direction. This is due to opposite parities of the angular functions τ_n and π_n in the scattering intensities *I*, leading to destructive interference in the backward direction [376]. In fact, the ED and MD fundamental modes are co-excited within the M-HP across the spectrum in *Region 1* (**Figure 6.22**), Meanwhile higher order modes are excited within a PS μ-sphere of equivalent diameter to the HPs (*r* = 1.1 μm), showing magnetic quadrupole (MQ) and electric quadrupole (EQ) modes when irradiated with λ = 2437 nm and 2192 nm, respectively (**Figure 6.5.c-d, Figure 6.23**).

In *Region 2*, where *F*/*B* > 200 occur at lower wavelengths, Mie theory predicts the presence of higher-order multipoles due to its sufficient sizes and refractive indices [202]. However, in place of higher modes, the fundamental ED and MD modes are co-excited within the M-HP (**Figure 6.5.i-j**) when illuminated with λ = 1575 nm, similar to the profiles in *Region 1*. Here the spiky features at the interface suppresses the higher-order modes which would occur if a smooth

and solid shell of equivalent thickness were present (**Figure 6.24**) in place of the nanospikes; in the HP, higher-order modes, characterized by peripheral concentration of E-field, become "lossy" due to radiative damping at the "leaky" periphery. On the other hand, higher order multipole is observed within a PS μ-sphere with equivalent diameter to the HP, in which the near-field profile suggests excitation of magnetic octupole (MO) modes when illuminated with λ = 1575 nm (**Figure 6.5.e-f, Figure 6.25**). Higher-order modal damping had also been previously reported with plasmonic "rough" nanoparticles [377,378]. Here, the "rough" plasmonic particles constitutes core diameter that falls at the border of the Rayleigh and the Mie regime, while the surface roughness features lie well within the Rayleigh scattering. Their differences lie in the preservation of resonant oscillation, accompanied by near-field enhancement.

6.6 Conclusion

In this letter, we have demonstrated that HP exhibits broadband suppression of backscattering and enhancement of forward scattering and elucidated the role of ZnO nanospikes in shaping the near-field profiles that leads to such useful scattering anisotropy. Due to scaling invariance in the Maxwell's equation, through proper size selections, the scattering anisotropy may be expanded to visible as well as millimeter wave regions where a large majority of current practical photovoltaic devices operate[365,379,380]. In addition to photonics

community, robust modeling and optical characterization of "rough" particles appeal to a diverse scientific and practical disciplines. For example, accurate description of aerial aerosols may enable better characterization of EM radiation through the atmosphere and better assessment of their climatic impact [381]. Its utility may span to precise characterization of biological entities that uses light scattering such as flow cytometry [382].

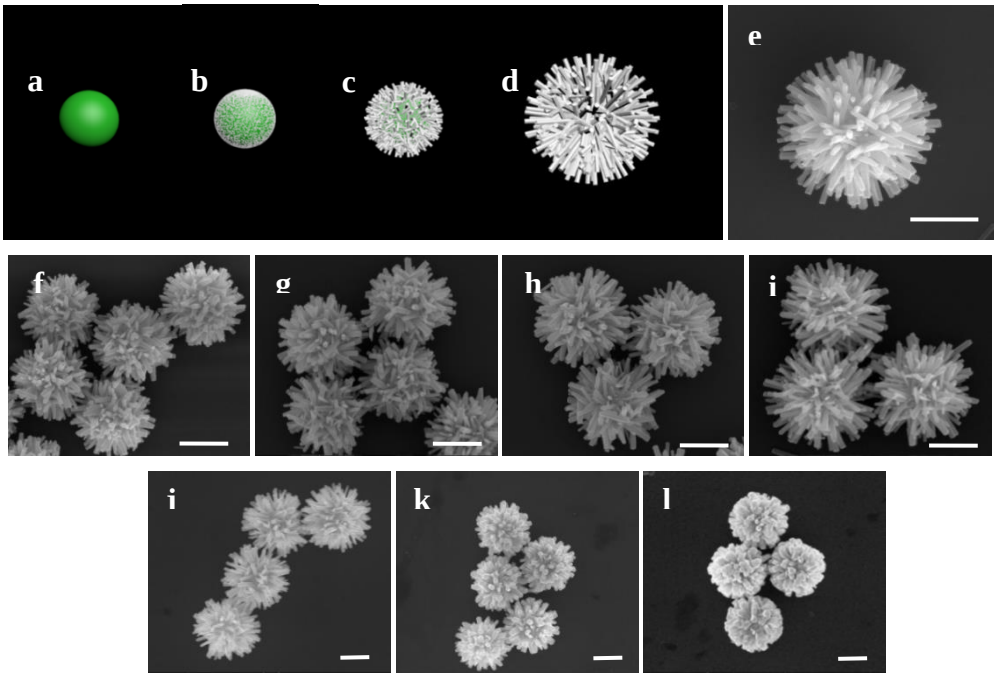

Figure 6.1 | Hedgehog particles; a-d, (**a**) carboxylated PS μ-spheres are used as templates (**b**) on which ZnO NPs are seeded through electrostatic adsorption, after which (**c-d**) ZnO nanospikes are grown to a specific length; (**e**) Scanning electron microscopy (SEM) image of HPs; **f-i**, SEM images of HPs with ZnO nanospikes of different lengths (*l*), **(f)** *l* = 0.19 μm, **(g)** *l* = 0.27 μm, **(h)** *l* = 0.4 μm, **(i)** *l* = 0.6 μm; **j-l**, SEM images of HPs with ZnO nanospikes of different widths (*w*), **(j)** *w* = 0.19 μm, **(k)** *w* = 0.27 μm, **(l)** *w* = 0.4 μm. Scale bar all 1 μm

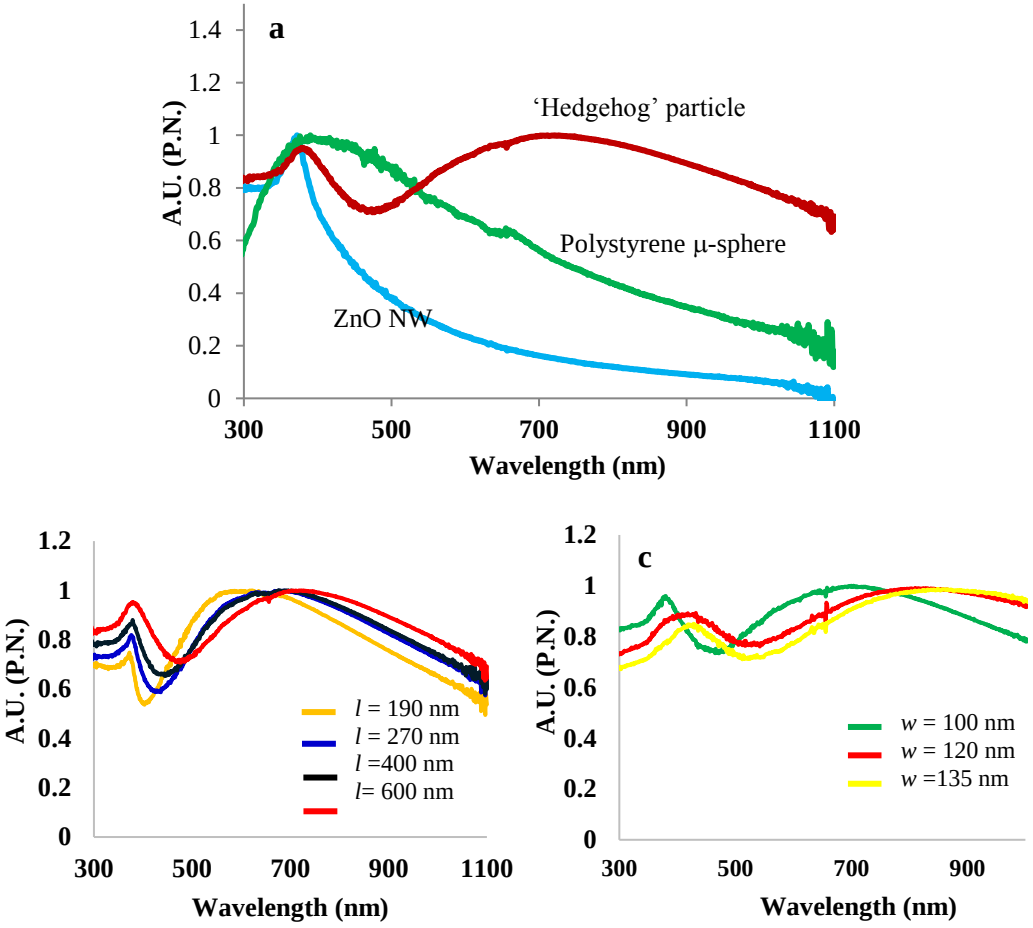

Figure 6.2 | Peak normalized (P.N.) UV-Vis extinction spectra of HPs in aqueous suspension; (**a**) P.N. extinction spectra (absorbance unit, A.U.) of ZnO NWs (light blue), PS μ-sphere (green) and HPs (red); **b-c**, P.N. extinction spectra of HPs with (**b**) varying spike lengths, l = 190 nm (orange), l = 270 nm (blue), l = 400 nm (black), l = 600 nm (red), and (**c**) varying spike widths, w = 100 nm (green), w = 120 nm (red), w = 135 nm (yellow), in aqueous suspensions.

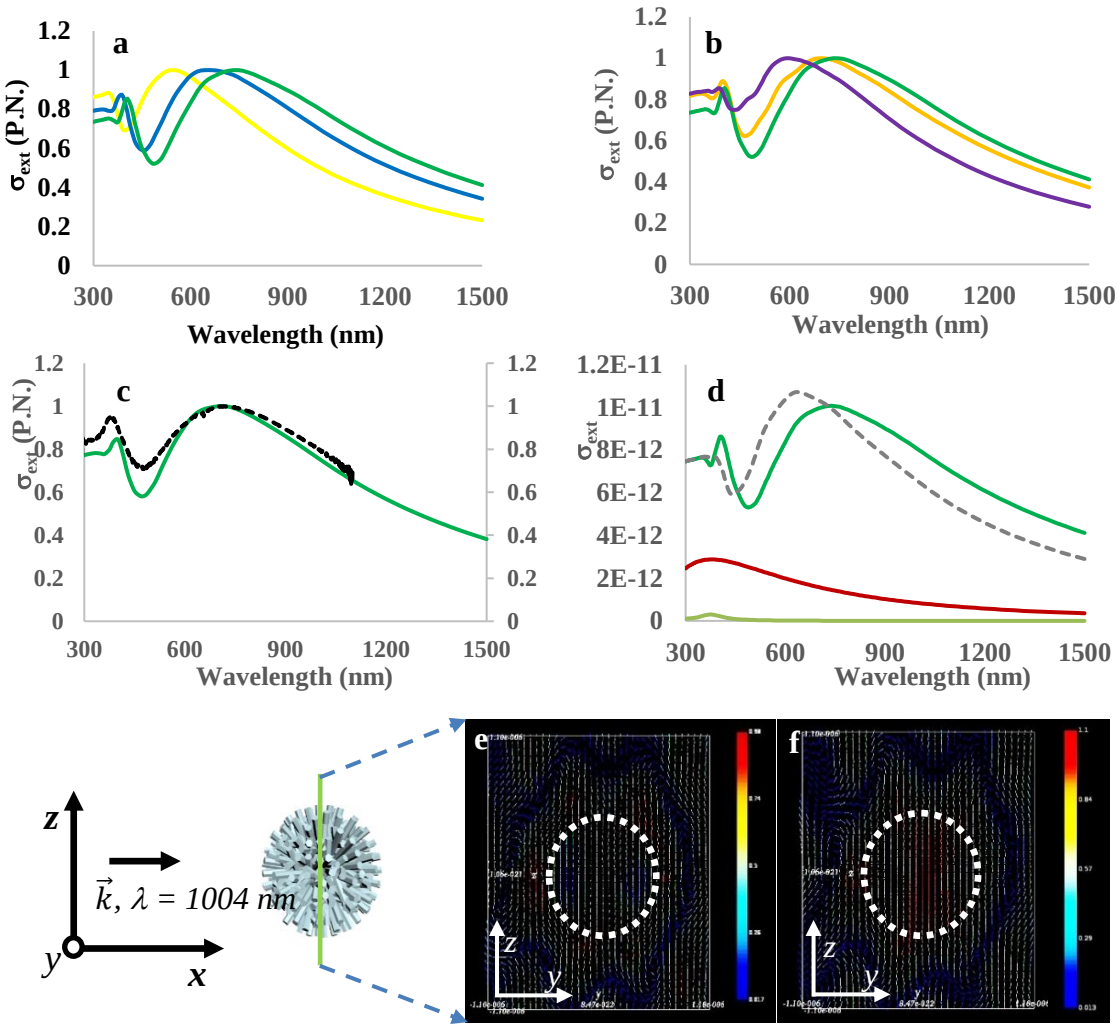

Figure 6.3 | Theoretical calculation of extinction cross-section (σ_{ext}) of HP in water using FDTD method; a-b, σ_{ext} (P.N.) of model HP (M-HP) having (**a**) variations in nanospike *w* (with constant *l* = 600 nm and *N* = 500), *w* = 120 nm (green), *w* = 100 nm (blue), *w* = 75 nm; (**b**) variations in nanospike density *N* (with constant *l* = 600 nm and *w* = 120 nm), *N* = 500 (green), *N* = 350 (orange), *N* = 250 (blue); **(c)** excellent agreement between theoretical (green) and experimental measurement (perforated black); (**d**) evolution of σ_{ext} starting from single nanospike (grey) and PS μ-sphere (red) to ZnO nanospikes (*N* = 500, *l* = 120 nm, *w* = 120 nm) in spherical array (perforated grey) to the HP (green); **e-f**, electric field profile at the center cross-section perpendicular to plane wave light propagation (λ = 1004 nm) through (**e**) ZnO nanospikes (*N* = 500, *l* = 600 nm, *w* = 120 nm) in spherical array format, (**f**) HP.

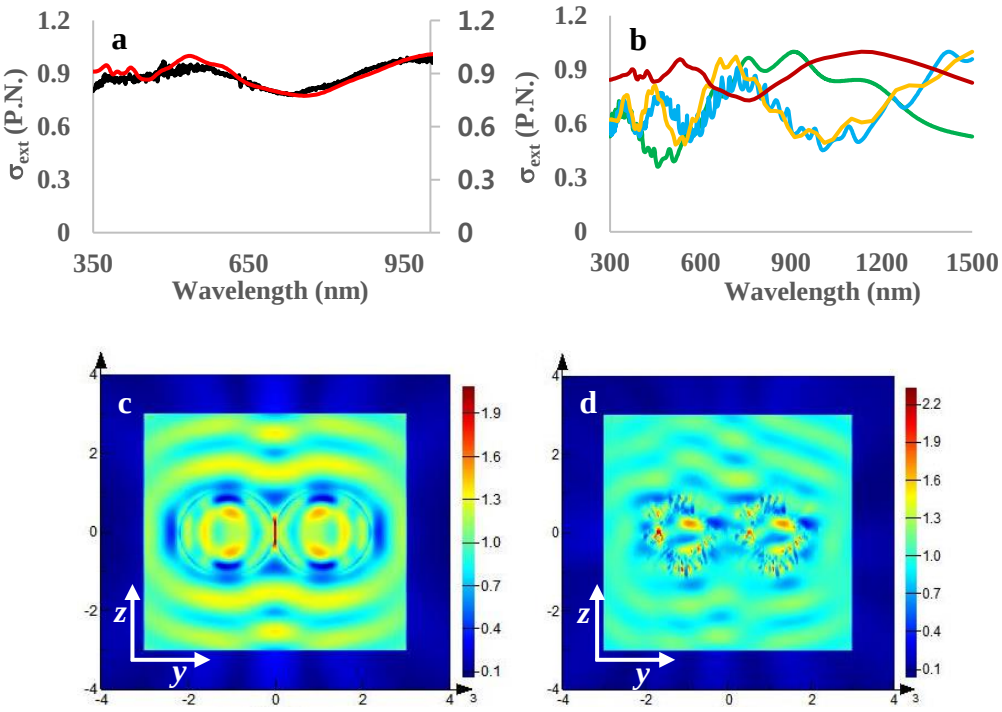

Figure 6.4 | FDTD solutions of M-HP in air; a, b, (**a**) excellent agreement in the extinction line shape between the M-HP (N = 300, l = 600 nm w = 120 nm (red)) and the experimental measurement (perforated black) in air; (**b**) FDTD solutions of σ_{ext} of PS μ-sphere of r = 0.5 μm (green) and r = 1.1 μm (light blue) in radius and the triple-shell model, r = 1.1 μm, (orange) showing a series of sharp resonant peaks within coarse oscillations; The M-HP (red) shows suppressed ripples indicative of non-resonant scattering; **c-d**, E-field intensity showing coupling effect (**c**) between a pair of PS μ-spheres and coupling-free effect (**d**) between a pair of M-HPs. The particles are aligned perpendicular to incident plane wave polarized in the z-direction and propagating along the x-direction and at zero separation distance (s = 0).

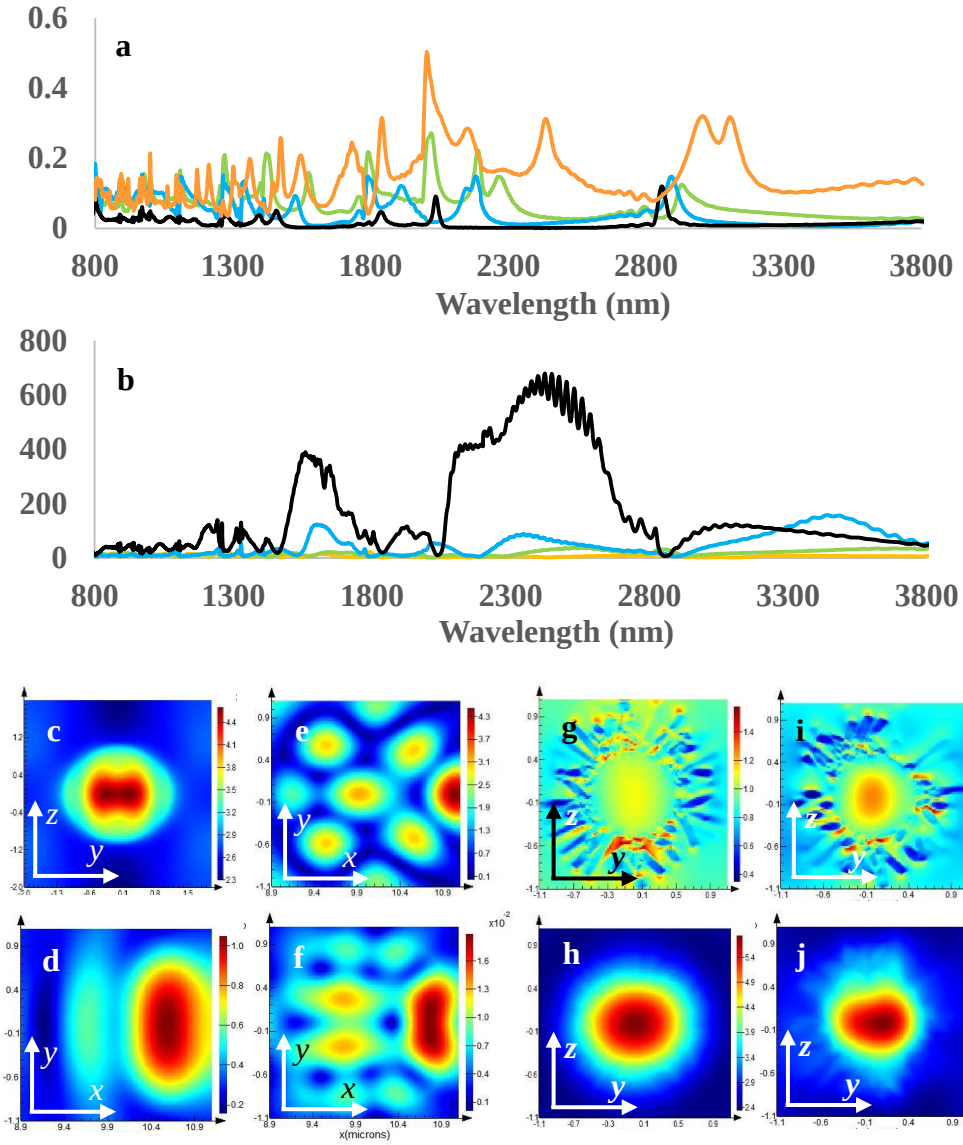
a
0.6
0.4
0.2
0
800
1300
1800
2300
2800
3300
3800
Wavelength (nm)
b
800
600
400
200
0
800
1300
1800
2300
2800
3300
3800
Wavelength (nm)
c
d
e
f
g
h
i
j
z
y
x
x(microns)

Figure 6.5 | Broadband suppression of backscattering and enhancement of forward scattering exhibited by M-HP through FDTD-based simulation; (**a**) normalized power transmission monitored behind the radiation source showing broadband suppression of backscattering and (**b**) high forward scattering to backward scattering ratio (F/B) exhibited by the M-HP, (r = 1.1 μm, black) compared with PS μ-sphere (r = 1.1 μm, green), ZnO μ-sphere (r = 1.1 μm, orange) and the triple-shell model (r = 1.1 μm, light blue); PS μ-sphere of equivalent diameter to HP exhibits **(c**, **d**) H-field intensity profiles that indicates excitation of magnetic quadrupole mode (MQ), (**e**) E-field and (**f**) H-field intensity profiles that indicates excitation of magnetic octupole mode (MO) when irradiated with plane wave at λ = 2437 nm and λ = 1575 nm, respectively. Meanwhile, (**g**, **i**) E-field intensity profiles and (**h**, **j**) H-field intensity profiles indicate co-excitation of ED and MD modes in an M-HP, at both λ = 2437 nm and λ = 1575 nm. All plane waves are polarized in the z-direction and propagates along the x-direction.

6.7 Supplementary Information

6.7.1 Spectroscopy measurement (absorbance unit, A.U.) and FDTD based calculations of extinction cross-section (σ_{ext}) for polystyrene μ-sphere and ZnO nanowire in water

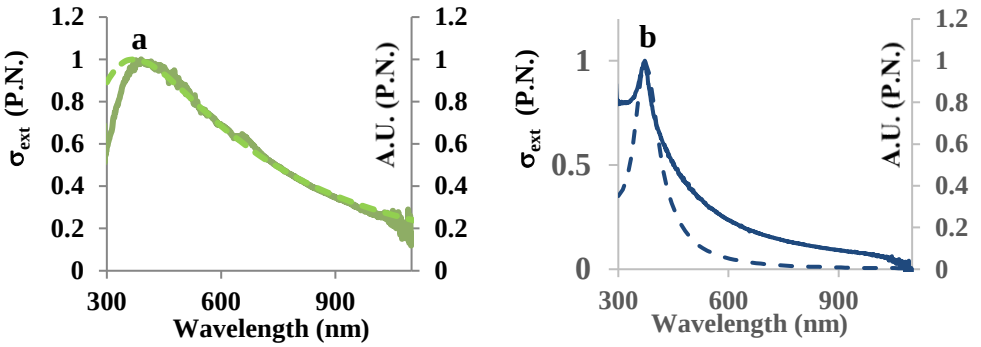

Figure 6.6 | Comparison of peak normalized (P.N.) extinction spectra in absorbance unit (A.U.) from UV-Vis spectroscopy, denoted as solid line, and extinction cross-section (σ_{ext}) from the FDTD-based calculations, denoted as perforated line; (**a**) PS μ-sphere, radius (*r*) = 500nm, (**b**) ZnO NWs, width (*w)* = 120 nm and length (*l*) = 600 nm.

6.7.2 FDTD simulation of ZnO nanowire in water

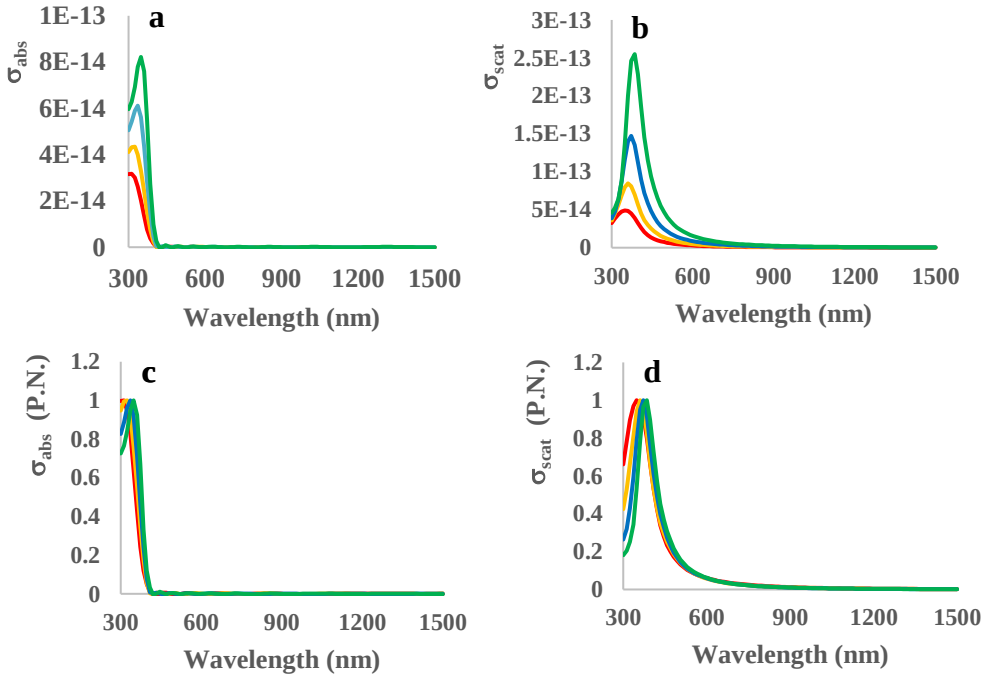

Figure 6.7 | Spectral contribution to σ_{ext} in a single ZnO nanospike in water; a-b, Single ZnO nanospike **a**) absorption cross-section (σ_{abs}) and **b**) scattering cross-section (σ_{scat}) for ***l*** = 190 nm (red), 270 nm (orange), 400 nm (blue), 600 nm (green); **c-d**, peak normalized **c**) σ_{abs} **d**) σ_{scat} from **a**) and **b**), respectively. The width of nanospikess are *w* = 120 nm for all the lengths considered

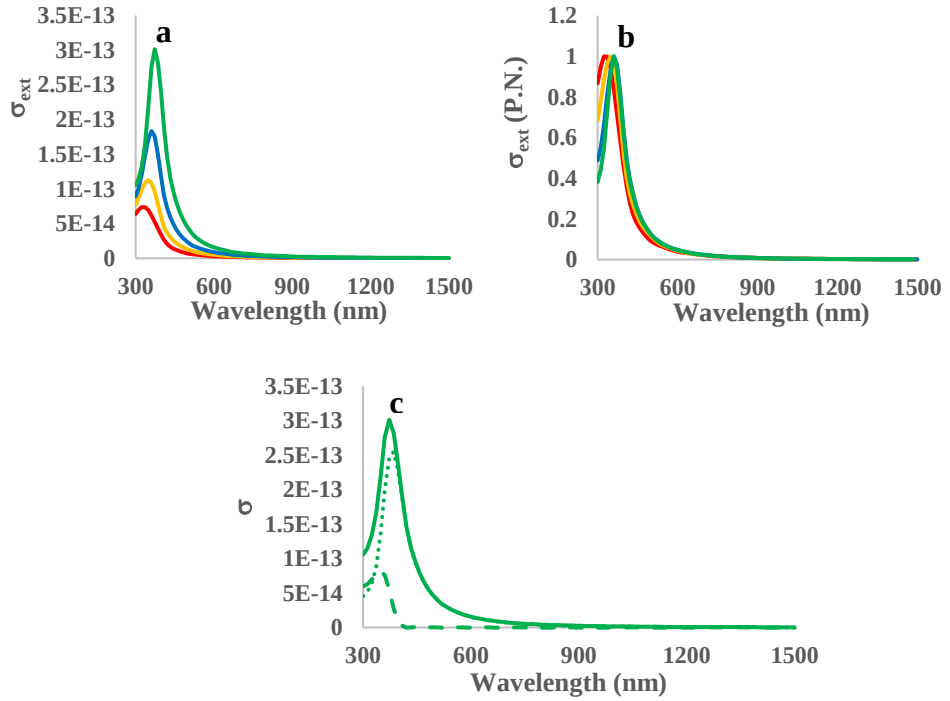

Figure 6.8 | σ_{ext} of a single ZnO nanospike (of different lengths) in water; a-b, (**a**) σ_{ext} and (b) P.N. σ_{ext} of a single ZnO nanospike of l = 190 nm (red), 270 nm (orange), 400 nm (blue), 600 nm (green) for constant $\boldsymbol{w}$ = 120 nm; (c) contribution of σ_{abs} (perforated line) and σ_{scat} (dots) to the total σ_{ext} for ZnO nanospike with w = 120 nm and l = 600nm

Comment: the extinction of ZnO NWs are also scattering dominant.

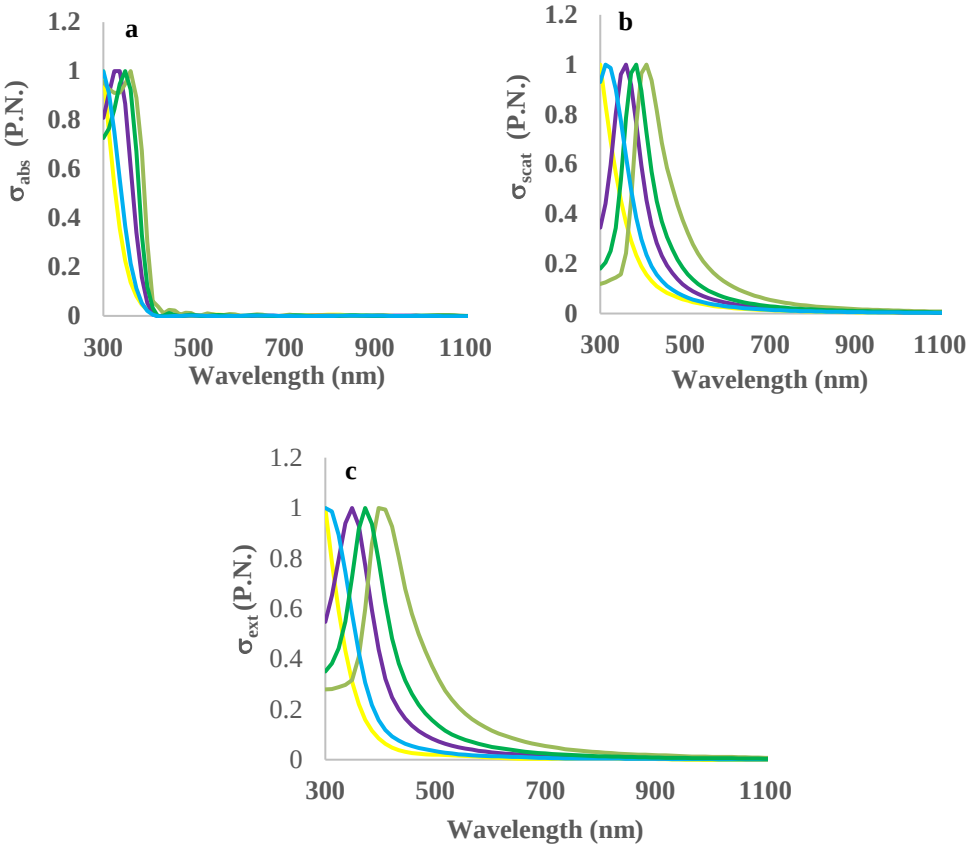

Figure 6.9 | Spectral contribution to σ_{ext} in a single ZnO nanospike (of different width); a-b, peak normalized **a**) σ_{abs} **b**) σ_{scat} and **c**) σ_{ext} of a ZnO nanospike with w = 50 nm (yellow), 75 nm (light blue), 100 nm (purple), 120 nm (green) 150 nm (grey) and 200 nm. The length of the ZnO nanospike is $\boldsymbol{l}$ = 600 nm for all widths considered.

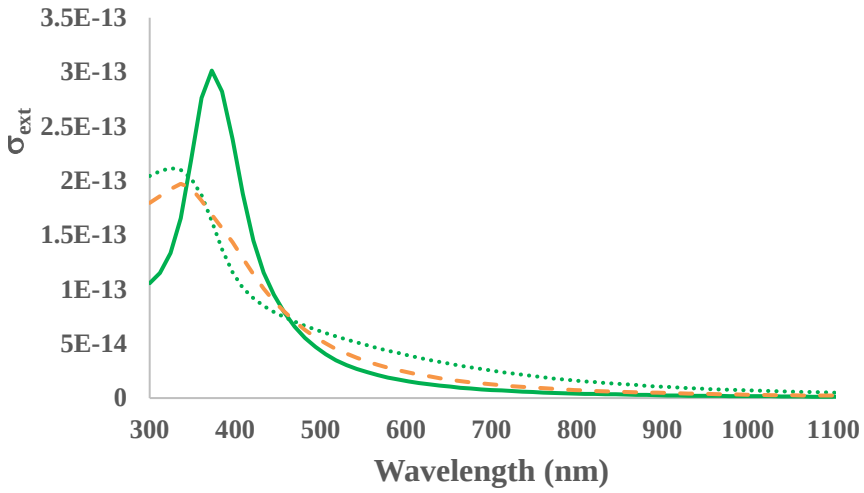

Figure 6.10 | σ_{ext} of a ZnO NW (*w* = 120nm, *l* = 600nm) in water at various orientations relative to the incident plane wave; parallel to the incident light (solid line), at 45^{o} angle of incidence (dotted line) and perpendicular to the incident light (perforated line)

6.7.3 FDTD Simulation of model 'hedgehog' particle in water

6.7.3.1 CAD of M-HP

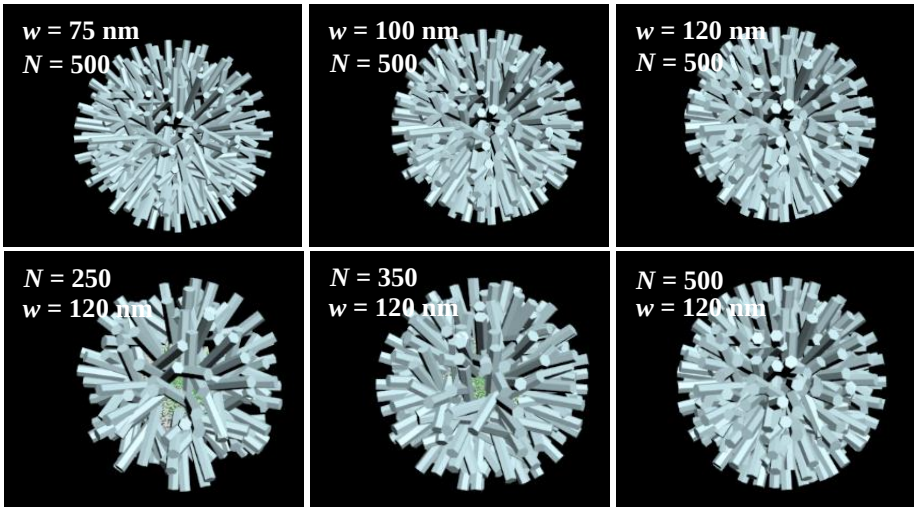

Figure 6.11 | Model HP (M-HP) constructed from computed aided design software (3D Max Studio). The model HP is constructed by layering ZnO nanopyramids on PS μ-sphere onto which the ZnO nanospikes are scattered to create imperfect orthogonalization that reflects the experimental construct. The spherical format of ZnO nanospikes only (without the nanopyramids) are exported to the FDTD based simulation software (FDTD Solutions, Lumerical Inc.) in which PS μ-sphere is inserted in a way that there is no void space between the spherical array of ZnO nanospikes and the μ-sphere.

6.7.3.2 FDTD simulation of M-HP with different nanospike configurations

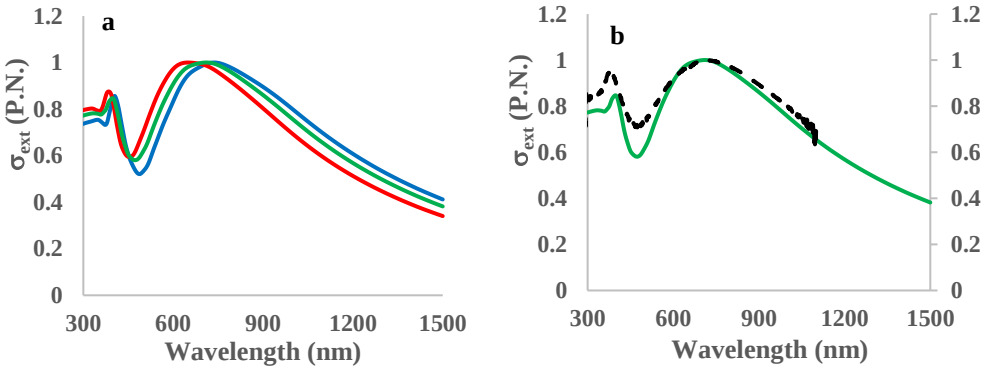

Figure 6.12 | FDTD based theoretical calculation of σ_{ext} of HP in water using FDTD method; (**a**) P.N. σ_{ext} of two HPs at a separation distance, d = 700 nm. The blue line corresponds to 2 HPs, each having N = 500, w = 120 nm, l = 600 nm. The red line corresponds to 2 HPs, each having N = 500, w = 100 nm, l = 600 nm. The green line corresponds to 2 HPs, where one HP is comprised of N = 500, w = 100 nm, l = 600 nm and the other HP is comprised of N = 500, w = 120 nm, l = 600 nm. The σ_{ext} of the heterogeneous mixture (green) lies in between that of the two homogenous mixtures (blue, red); (**b**) there is an excellent spectral overlap between the FDTD-based σ_{ext} of 2 HP mixture (green, (**a**)) and spectroscopic measurement of a collection of HPs in aqueous suspension (black perforated). The spectroscopic measurement is representative of average light extinction due to a collection of HPs having slight variations in overall interfacial geometry

6.7.3.3 Spectral contributions

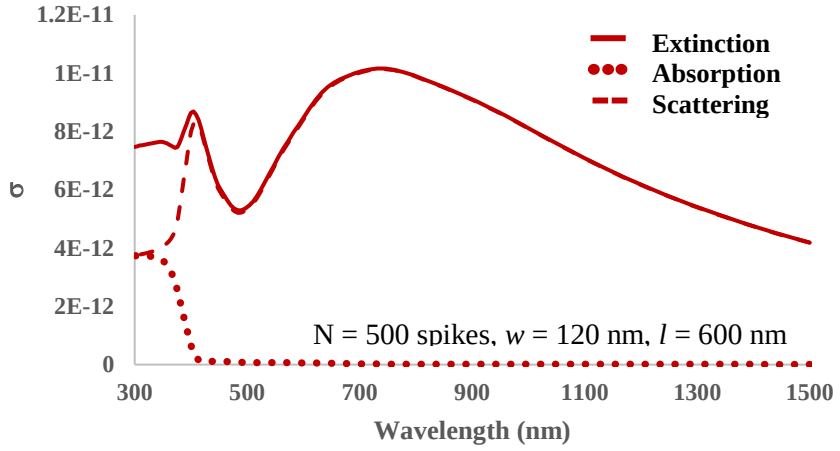

Figure 6.13 | Spectral contribution σ_{ext} in a single HP; contribution of σ_{abs} (dotted) and σ_{scat} (perforated) to the total σ_{ext} of a single HP (N = 500, $\boldsymbol{w}$ = 120 nm and $\boldsymbol{l}$ = 600 nm).

6.7.3.4 EM coupling between the spikes

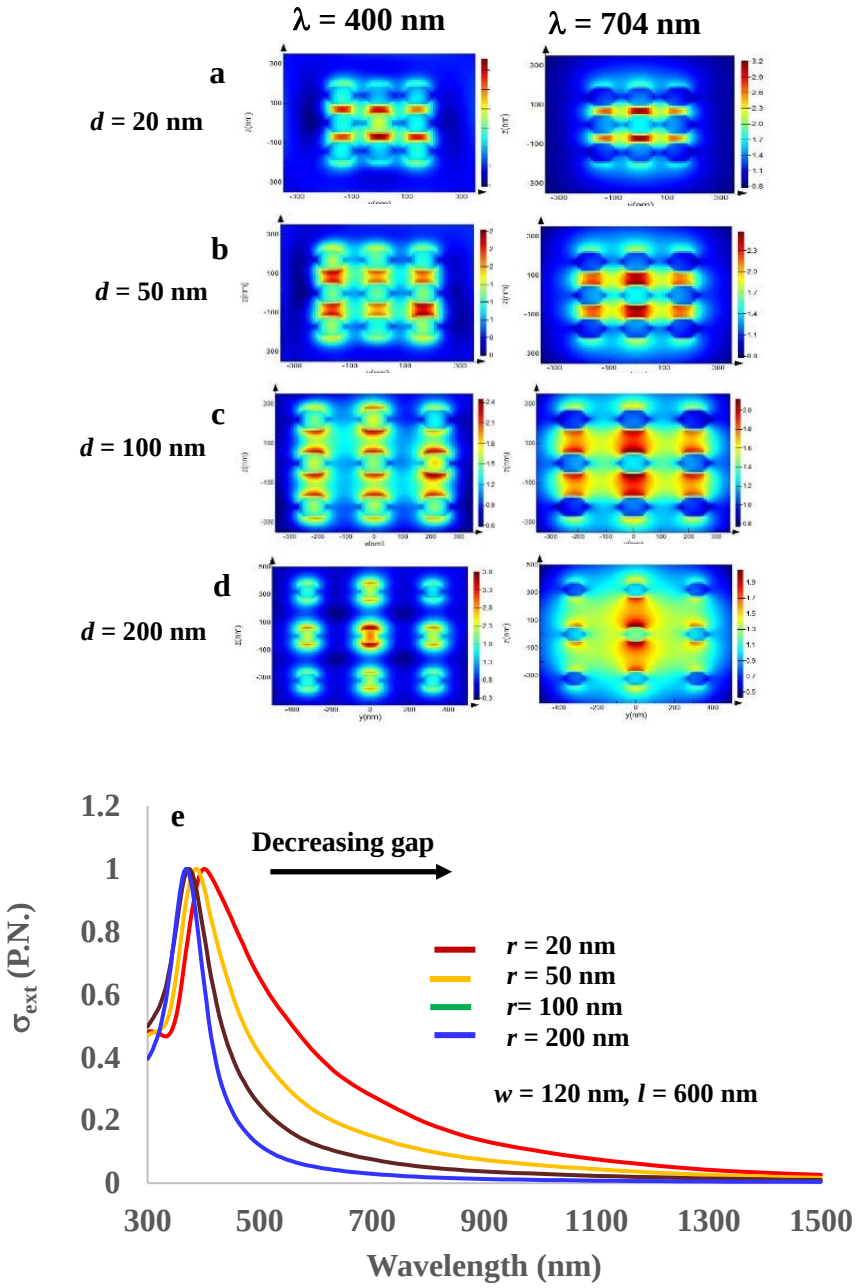

Figure 6.14 | Electric field (E-field) coupling between the ZnO nanospikes in a 3 x 3 array and its spectral shift; a-d, 3 x 3 array of parallel ZnO nanospikes (w = 120 nm , l = 600 nm) oriented parallel to the incident light (λ = 400 nm and λ = 704 nm) at separation distance (d) of (**a**) d = 20 nm, (**b**) d = 50 nm, (**c**) d = 100 nm, (**d**) d = 200 nm; (**e**) σ_{ext} of orientations (**a**) – (**d**).

6.7.4 FDTD simulations of triple-shell model in water

6.7.4.1 Excellent agreement between theory and experiment from the triple-shell model

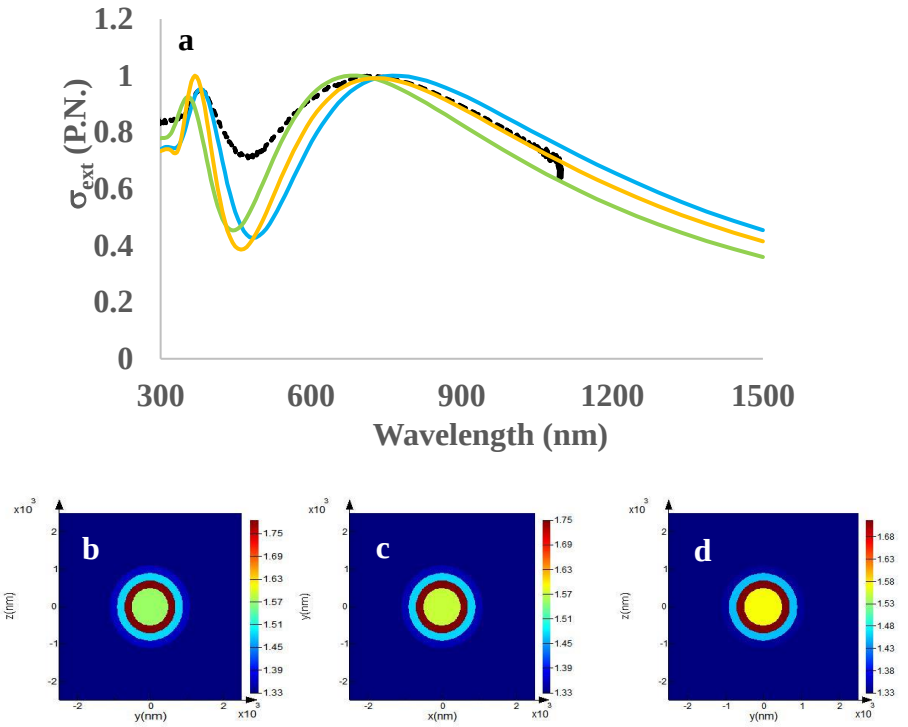

Figure 6.15 | Discretized gradient refractive index triple-shell model; triple-shell model having 1:1:1 thickness ratios with step-wise variations in refractive indices, where the refractive index of each shell layers are determined by Maxwell Garnett effective medium approximations; (**a**) FDTD simulations of σ_{ext} of the triple-shell model that corresponds to HPs having w = 120 m, l = 600 nm and N = 275 (**blue**), N = 265 (**orange**), N = 250 (**green**). The perforated black line represents the spectroscopic measurement (A.U.) of HPs in aqueous suspension. Refractive index representation of the 1:1:1 triple-shell that corresponds to (**b**) N = 275 (f_{outer} = 0.27 , f_{middle} = 0.42, f_{inner} = 0.75), (**c**) N = 275 (f_{outer} = 0.26 , f_{middle} = 0.41, f_{inner} = 0.72), (**d**) N = 250 (f_{outer} = 0.25 , f_{middle} = 0.39, f_{inner} = 0.68), where f is the volume fraction of ZnO.

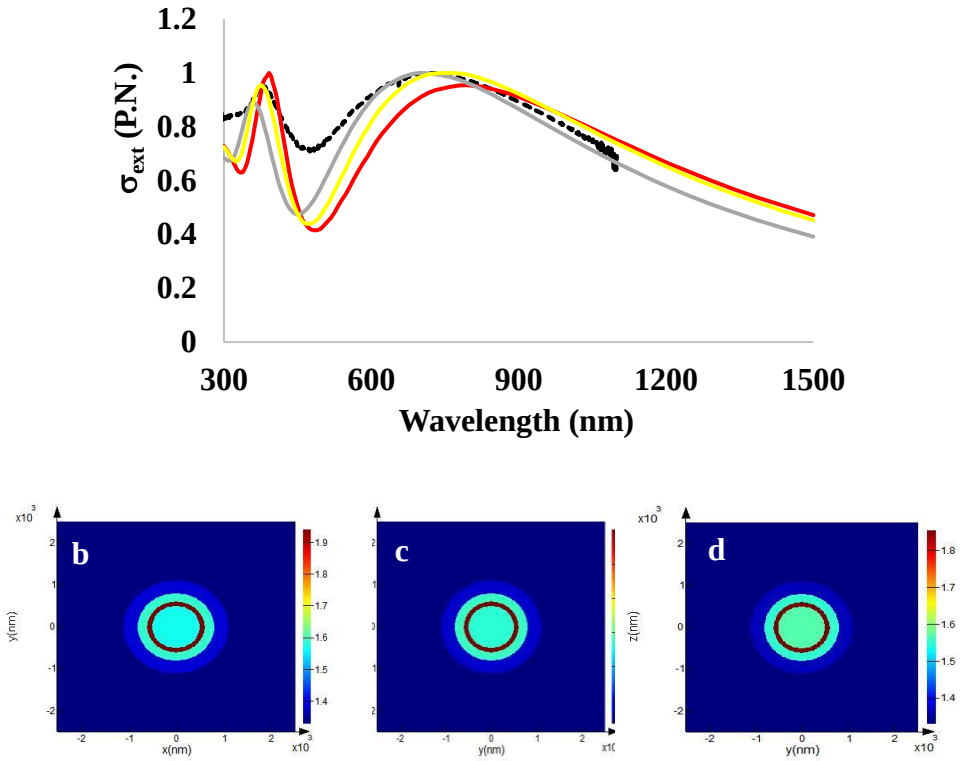

Figure 6.16 | Discretized gradient refractive index triple-shell model; triple-shell model having 3:2:1 (outer: middle: inner) thickness ratios with step-wise variations in refractive indices, where the refractive index of each shell layers are determined by Maxwell Garnett effective medium approximations; (**a**) FDTD simulations of σ_{ext} of the triple-shell model that corresponds to HPs having w = 120 m, l = 600 nm and N = 275 (**red**), N = 265 (**yellow**), N = 250 (**grey**). The perforated black line represents the spectroscopic measurement (A.U.) of HPs in aqueous suspension. Refractive index representation of the 3:2:1 triple-shell that corresponds to the (**b**) N = 275 (f_{outer} = 0.3 , f_{middle} = 0.55, f_{inner} = 0.90), (**c**) N = 265 (f_{outer} = 0.29 , f_{middle} = 0.53, f_{inner} = 0.87), (**d**) N = 250 (f_{outer} = 0.27 , f_{middle} = 0.50, f_{inner} = 0.82),), where f is the volume fraction of ZnO.

6.7.4.2 Spectral contributions

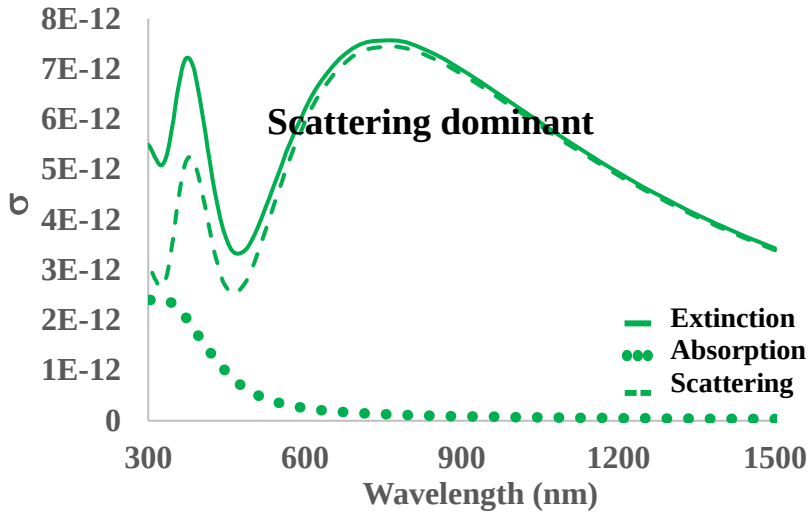

Figure 6.17 | Spectral contribution to σ_{ext} in a triple-shell model; contribution of σ_{abs} (dotted) and σ_{scat} (perforated) to the total σ_{ext} of a single triple-shell representation of HP (*N* = 265, ***w*** = 120 nm and ***l*** = 600 nm, 1:1:1).

Comment: Complex refractive index ($\tilde{n}$) of ZnO [383] (PV Lighthouse) was converted to complex dielectric function ($\tilde{\varepsilon}$),

$$\tilde{\varepsilon} = \varepsilon' + i\varepsilon''$$

$$\tilde{n} = n + ik$$

$$\varepsilon' = n^2 - k^2$$

$$\varepsilon'' = 2nk \qquad \text{Eq. 6.1}$$

to which Maxwell-Garnett EMA was applied [372] for each shell layers in the triple-shell model.

$$\overline{\varepsilon^{MG}} = \varepsilon_m \frac{\varepsilon_i + 2\varepsilon_m + 2f(\varepsilon_i - \varepsilon_m)}{\varepsilon_i + 2\varepsilon_m - f(\varepsilon_i - \varepsilon_m)}$$

Eq. 6.2

The Lumerical Solutions automatically converts to complex dielectric function to the complex refractive index.

6.7.5 Non-resonant scattering of model 'hedgehog' particle in air

6.7.5.1 Coupling-free behavior between M-HP with zero separation distance

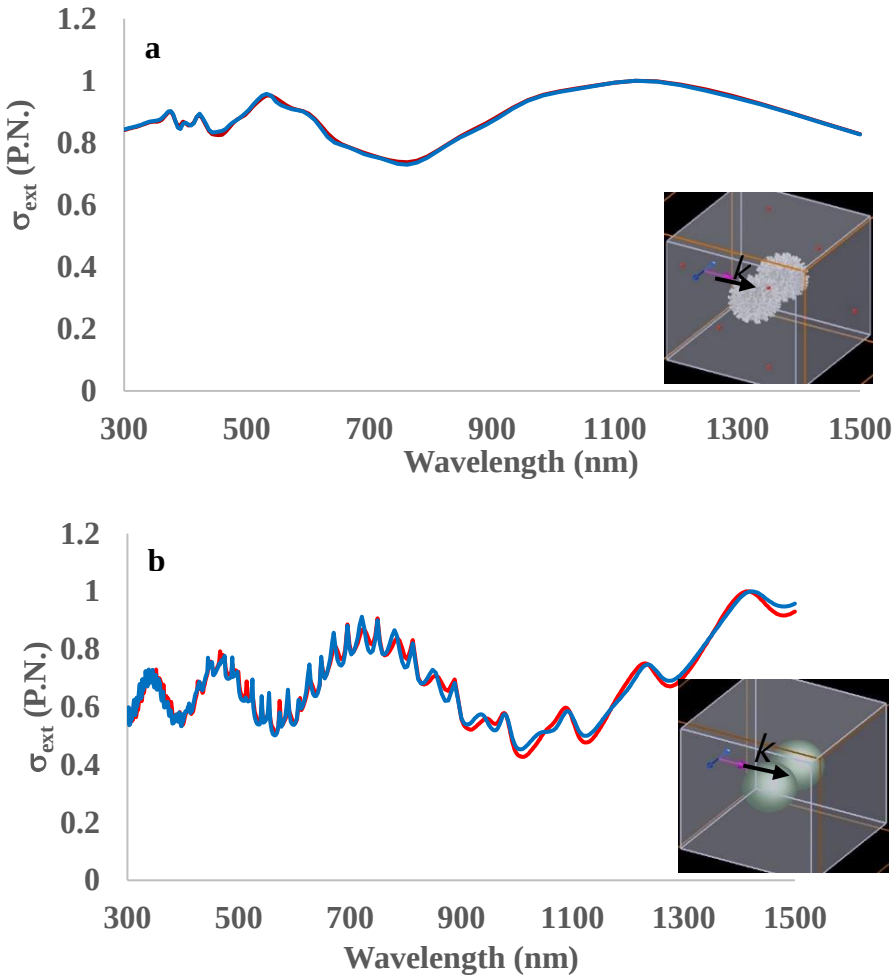

Figure 6.18 | σ_{ext} of two parallel particles aligned perpendicular to the incident TFSF plane wave (λ = 300 – 1500 nm); (**a**) Spectral overlap between the σ_{ext} of a single M-HP (red) and two M-HPs aligned perpendicular (blue) to the incident plane wave; (**b**) Spectral modulation between the σ_{ext} of a single PS μ-sphere (red) and two PS μ-spheres (r = 1.1 μm) aligned perpendicular (blue) to incident plane wave.

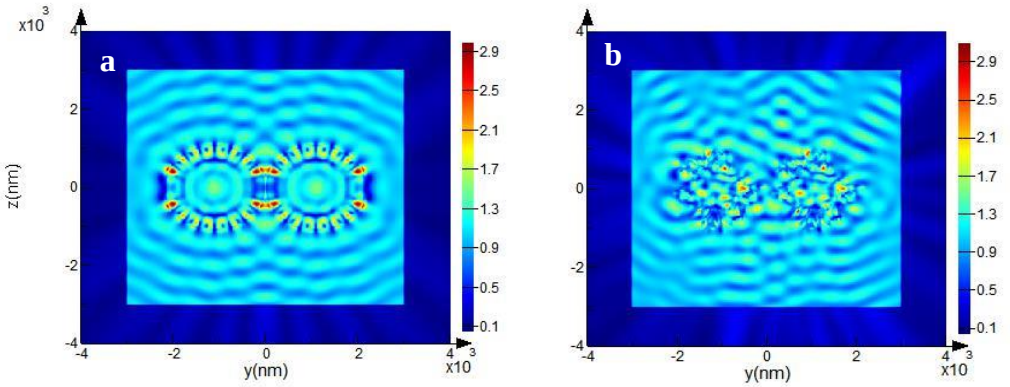

Figure 6.19 | Electric field (E-field) intensity distribution of two parallel particles (at zero separation distance, *s* = 0 nm) aligned perpendicular to the incident plane wave; (a) two PS μ-spheres (*r* = 1.1 μm) and (b) two M-HPs aligned perpendicular to the incident plane wave (*z*-polarized and propagating along *x*-direction, λ = 454 nm) at zero separation distance. E-field coupling is observed at the near-field between the PS μ-spheres, while couplig-free behavior is observed between the M-HPs.

6.7.6 Suppression of backscattering and enhanced forward scattering by a model 'hedgehog' in air

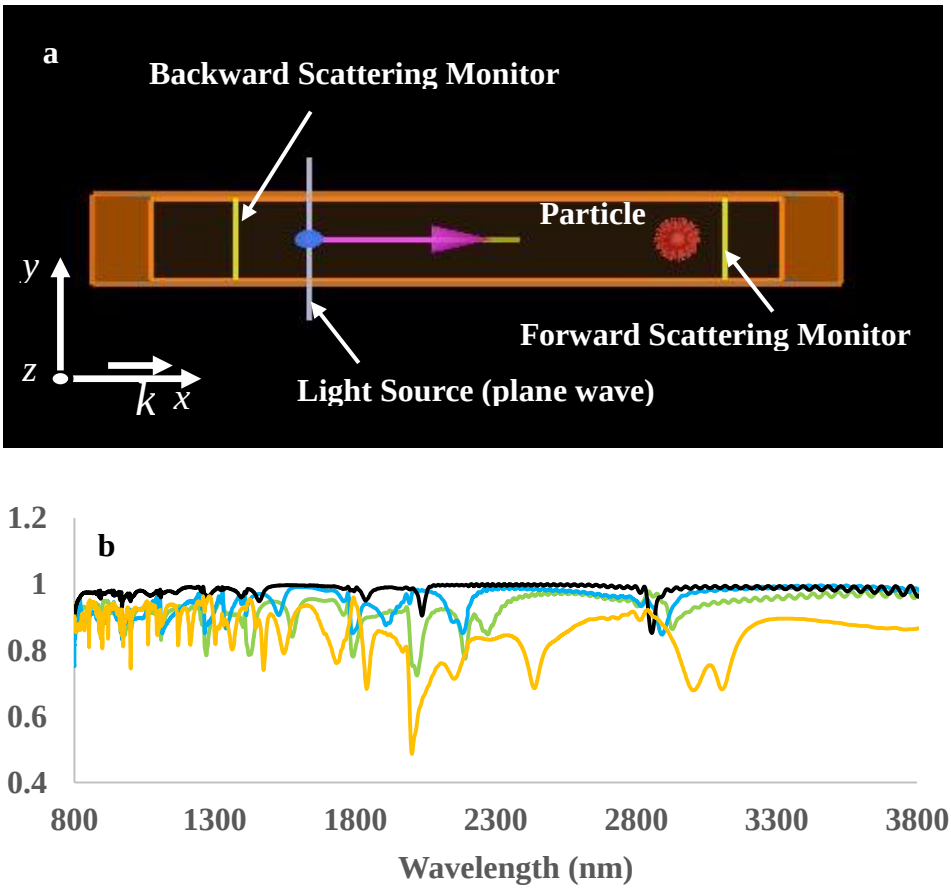

Figure 6.20 | Normalized power transmission; (a) FDTD simulation setup that includes monitors for power transmission behind the source plane wave for backscattering and behind the particle for forward scattering**; (b)** enhanced forward scattering exhibited by the HP (black) compared with PS and ZnO μ-sphere; PS μ-sphere (r = 1.1 μm, green), ZnO μ-sphere (r = 1.1 μm, orange) and triple-shell model (r = 1.1 μm, light blue)

Comment: Destructive interference in the backward scattering for simultaneous excitation of electric and magnetic dipole modes is explained as follows:

Scattering intensity, *I*, is expressed as follows[209,376]

$$I = \frac{1}{k^2 s^2}[|T_1(cos\theta)|^2 sin^2\varphi + |T_2(cos\theta)|^2 cos^2\varphi]$$

$$T_1(cos\theta) = \sum_{n=1}^{\infty} \frac{2n+1}{n(n+1)}[a_n \pi_n(cos\theta) + b_n \tau_n(cos\theta)]$$

$$T_2(cos\theta) = \sum_{n=1}^{\infty} \frac{2n+1}{n(n+1)}[a_n \tau_n(cos\theta) + b_n \pi_n(cos\theta)]$$

Eq. 6.3

, where a_n and b_n are Mie coefficients (n^{th} order electric and magnetic moments, respectively), π_n and τ_n are angular functions, θ and φ are polar and azimuthal angle, *k* is the wave number and *s* is the distance between the scattering center and the observation point.

The angular functions takes the form of associated Legendre functions,

$$\pi_n(cos\theta) = \frac{P_n^1(cos\theta)}{sin\theta}$$

$$\tau_n(cos\theta) = \frac{dP_n^1(cos\theta)}{d\theta}$$

Eq. 6.4

, and has the opposite parities with respect to $cos\theta$,

$$\pi_n(-cos\theta) = (-1)^{n+1}\pi_n(cos\theta)$$

$$\tau_n(-cos\theta) = (-1)^n \tau_n(cos\theta)$$

Eq. 6.5

Hence, in the case of simultaneous excitation of dipole modes only, destructive interference occurs in the backward direction, $\theta = 180^o$. When $a_n = b_n$ (equal magnitude electric and magnetic dipole), zero backscattering occurs, known as first kerker condition [384].

6.7.7 Enhanced forward scattering by model 'hedgehog' in air

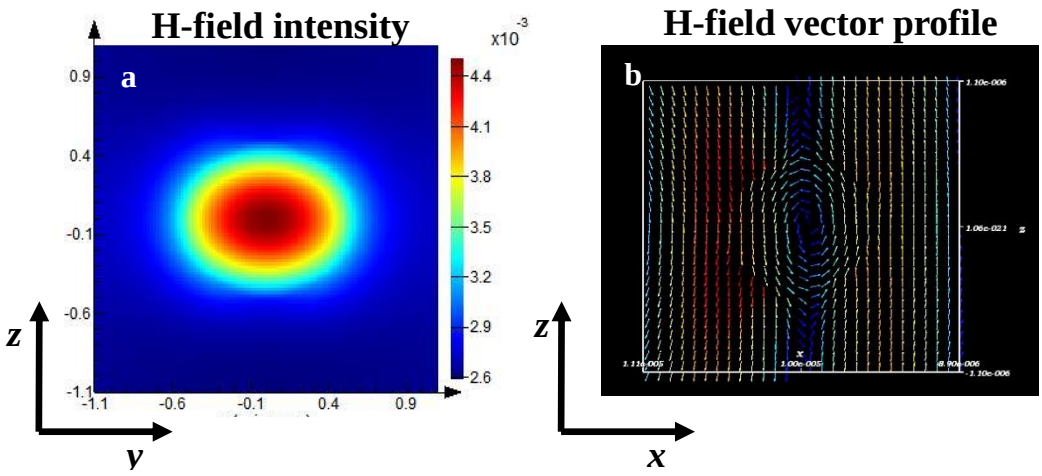

Figure 6.21 | Near-field profile in the PS μ-sphere of *r* = .5 μm, representing the core of the HP; H-field (**a**) intensity and (**b**) vector profile, irradiated with plane wave (*z*-polarized and propagating along the *x*-direction) of λ = 2323 nm.

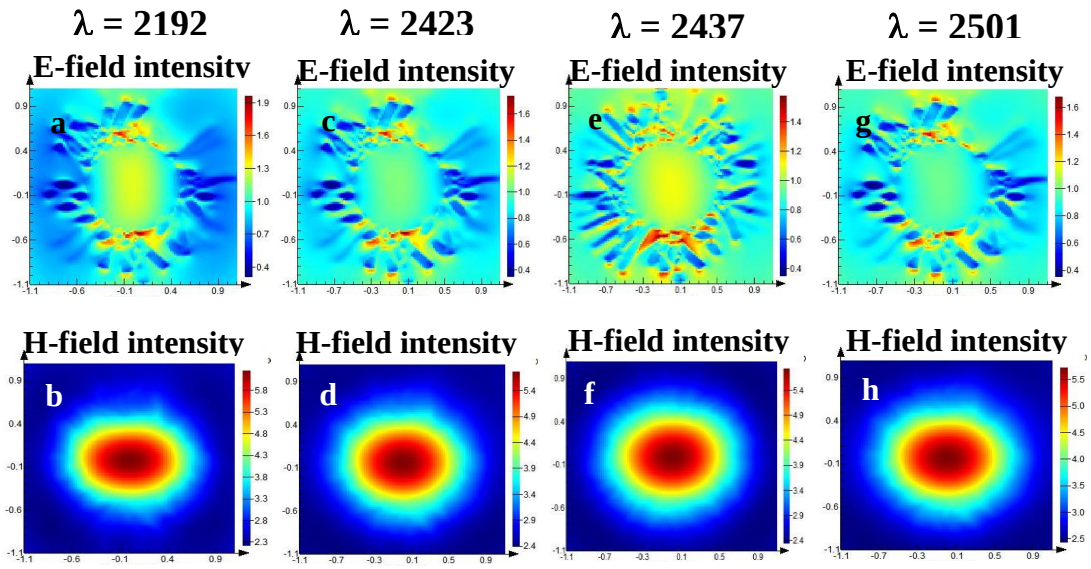

Figure 6.22 | Near-field profile in the M-HP showing co-excitation of ED and MD modes across the spectrum in Region 1 (2075 < λ < 2690); (**a, c, e, g**) E-field intensity and (**b**, **d**, **f**, **h**) H-field intensity profile at λ = 2192 nm, 2434 nm, 2437 nm, 2501 nm, respectively.

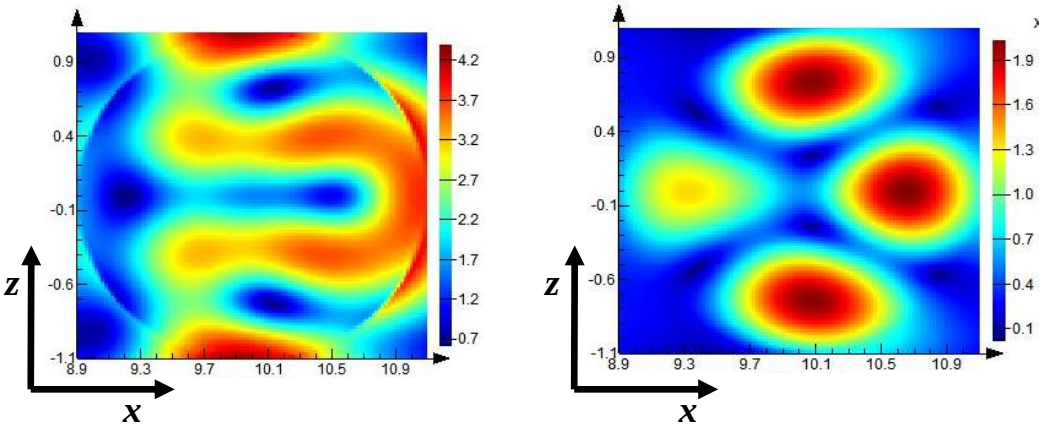

Figure 6.23 | Near-field intensity profiles in the PS μ-sphere of equivalent diameter to the HP (*r* = 1.1 μm) ; (**a**) E-field and (**b**) H-field intensity profile showing excitation of EQ mode, , irradiated with plane wave (*z*-polarized and propagating along the *x*-direction) of λ = 2192 nm.

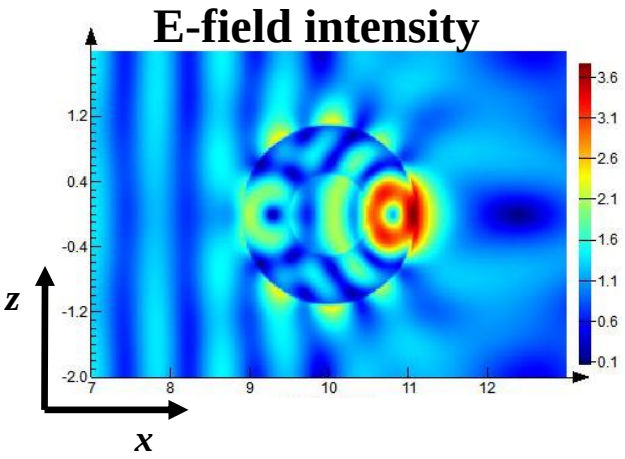

Figure 6.24 | Near-field profile in the PS-ZnO core-shell (core *r* = .5 μm, shell thickness *t* = .6 μm) showing excitation of higher order modes, irradiated with plane wave, λ = 1575 nm

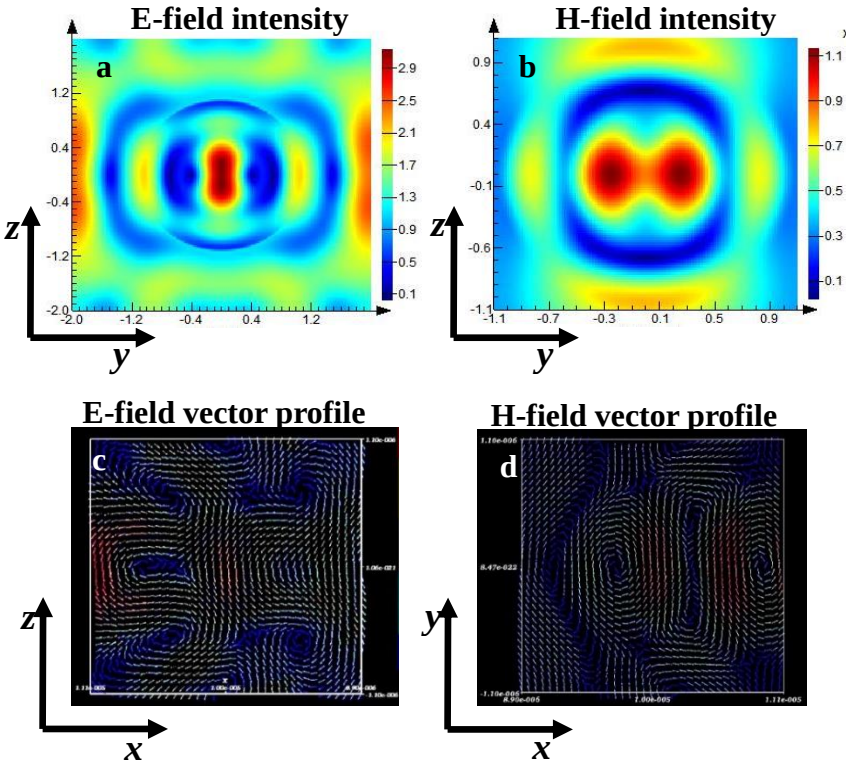

Figure 6.25 | Near-field profile in the PS μ-sphere of equivalent diameter to HP (*r* = 1.1 μm) showing excitation of magnetic octupole (MO) mode when irradiated with plane wave of λ = 1575 nm (z-polarized, propagating along x-direction); (**a**) E-field intensity, (**b**) H-field intensity, (**c**) E-field vector, (**d**) H-field vector profiles

Chapter VII

Conclusion and Future Directions in Biomedical Applications

Imparting high degree of interfacial corrugation affects its fundamental properties and processes due to changes in physical and chemical configurations. For example, surface roughness alters mass transport[385], catalysis[386] , adsorption[387], gelation behavior[388], deformation mechanics[389], cell adhesion[390], etc. Examples of fundamentally new properties due to surface roughness on particles are already present in nano-colloids, exemplified by markedly different optical and biological properties such as Raman scattering[391,392] and permeation across the cell membranes[393]. While these findings already envelops

significance of surface roughness, the effects of the nano-scale topography on numerous other properties remains a dynamic and exciting field that requires further progress.

Micro-scale dispersions have been realized from many materials: polymers, metals or metal oxides etc., and, typically, micro-colloids have smooth surfaces [394–398] with some variety of shapes. The smooth particles are much less heterogeneous and are easier to describe by a variety of models [399–402]. Despite numerous techniques to modify the colloidal surfaces so as to impart nano-scale topography, the degree of roughness is negligible in comparison to the core size. For instance, roughness amplitude imparted by polymer brushes is typically around 40 - 50nm[403–407]. The task of creating high corrugation in a controllable manner is much more amenable with nano-colloids due to closeness in size scales of macromolecules and nanoparticles.

Creating diverse types of highly reproducible and controllable micro-scale "rough" particles whose corrugation amplitude compares to the core dimension should enrich experimental platforms to investigate large variety of properties and processes. Furthermore, microparticles with high degree of nano-scale corrugation represents a case of integration of micro-/nano-scale regimes into hierarchical particles. Such allows one to take advantage of both worlds of material properties, including the quantum effects. Currently, there are only few examples of highly corrugated micro-colloidal dispersion, for example, catalytic hollow nickel microsphere decorated with carbon nanotubes[408]. Current uses in

diverse areas of processes and products, both in industry and scientific endeavors, of microparticles is as prevalent, if not more, as nanoparticles, hence provides additional incentives.

Solubility refers to particulate frameworks of various phases such as solid, liquid and gaseous substances to homogeneously form solutions in the solvent. Similar to particle dispersion stability, solubility of molecular compounds is directly tied to its intended performances. For example, bioavailability of therapeutic compounds depends on its solubility, amongst other factors (dissolution velocity, permeability, etc.[409]). The drug solubility is also desired for its appropriate therapeutic assessment at the early design and development stages, during which elimination of false positives is critical to reduce the attrition rate responsible for astronomical cost of the drug development process. However, a large portion (>40%) of potential therapeutic compounds identified during the screening processes, termed new chemical entities (NCEs) are water insoluble, or poorly soluble [410], and requires volatile organic solvents that may pose health risks. Techniques developed to enhance solubility includes physical modifications such as size miniaturization [411] and its embedment in hydrophilic matrix [412–414], chemical modifications into salt forms [415,416] and other assorted methods such as supercritical fluid processing and hydrotrophy [417,418].

The solubility enhancement achieved by the aforementioned processes, despite being highly successful, comes with limitations such as procedural complexities and the need to engineer the molecular or the carrier platform that

captures both the compound and solvent chemistries. The ‘hedgehog’ particles may represent as a novel drug carrier platform with unprecedented ability to disperse in all types of solvents irrespective of its chemical properties. A hydrophobic drug compounds may be easily loaded onto the ‘hedgehog’ particles through hydrophobic interaction in aqueous environment, yet remain being dispersed. Its applications may be envisioned in various orally administered drugs targeting the exterior epithelial linings, such as throat sprays, without the need for dispersion in toxic organic solvents. The particle components may be substituted with biocompatible moieties such as dextran cores.

Such anomalous dispersion character of the HPs can be employed to a wide variety of industrial processes and products. One can envision its use in a solution of pesticides (insecticide, bactericides, herbicides, fungicides, etc.). Pesticide compounds are generally hydrophobic and requires organic solvents to formulate its solution such ethanol and DMSO [419] causing environmental toxicities and ecological disturbances, thereby leading to serious health risks [420]. In fact, pesticide spills and accidents happen each year, including occurrences in manufacturing plants [421].

Deviations of electromagnetic responses from the analytical Mie theory[422], both near- and far-field, due to particles having rough surfaces have been well documented in previous studies [377,378,423]. Numerous numerical methods had also been developed to account for the surface roughness[424–430]. The great accomplishments notwithstanding, a robust modeling approach that is inclusive of

wide size ranges and material properties accompanied by experimental diversity may further deepen our understanding of the ties between the surface roughness and optical properties. In particular, accurate prediction of EM responses of all dielectric "rough" μ-particles in the Mie scattering regime is expected have a broad impact on a wide range of disciplines; majority of the particles found in nature have some form of interfacial corrugations, including biological entities such as cells[431,432] and atmospheric/cosmic dusts[433–436]. For example, accurate description of aerial aerosols using the M-HP approach will enable better characterization of electromagnetic radiation through the atmosphere and better assessment of their climatic impact and health effects [381,437,438]. Its utility may span to precise characterization of biological entities that uses light scattering such as flow cytometry[382].

Lastly, applications to other facets of health sciences can be envisioned due to its interfacial topography. HPs may find its way as an efficient platform for capture and concentration of some of the deadliest pathogens, such as the filovirus types. The most recent Ebola epidemic in western Africa posed an immense danger to the many. Although a world-wide pandemic caused by the Ebola virus (EBV) in 2014, or a similar pathogen, may seem less likely now, it is still in the realm of possibilities. Ignoring such possibility may result in catastrophic consequences. Ebola virus (EBV) is a highly aggressive virus causing lethal hemorrhagic fevers. Due to its capacity for rapid transmission to, and expansion in, the human

population–with mortality rates as high as 90% [439–441] for certain serotypes–there is a limitation on the hosts' behalf to develop acquired immunity.

In the face of potential epidemic disaster, prophylactic screenings in the form of early EBV detection prior to the symptomatic onset is in dire need to prevent/arrest infectious propagation amongst the human population. It is after the clinical symptoms that the bodily fluids impose infectious risks – severity of the symptoms and the concentration of EBV in blood is correlated. In the United States, current prophylactic measures include 21-day quarantine for suspected/possible hosts, despite early treatment being paramount measures for survival. Unfortunately, widespread and dependable prophylactic screenings prior to the onset of symptoms are yet to be available which further adds infective mobility and lethality to the hosts. Early screening with well-established and highly sensitive PCR assays using blood or plasma samples are not reliable. In the asymptomatic early stages of the disease progression, the initial site of EBV incubation relies mostly in organ tissues and therefore the virion concentration in the blood is miniscule [442,443].

It is important to note that appropriate virus concentration is required for reliable assays and definitive conclusions. The HPs feature spiky topography with significantly large and "sticky" (to the biological moieties) interfacial area on which for filo-type pathogens to entangle and anchor. Furthermore, colloidal interaction may be further engineered in the presence of the captured virus to induce visible optical effects, thereby potentially circumventing the use of PCR assays.

Together, the HPs may provide a highly mobile, cheap and readily accessible diagnostic platform for the detection of deadly pathogens.

Bibliography

1. Umbanhowar, P. B., Prasad, V. & Weitz, D. a. Monodisperse emulsion generation via drop break off in a coflowing stream. *Langmuir* **16,** 347–351 (2000).
2. Zakhidov, a. a. Carbon Structures with Three-Dimensional Periodicity at Optical Wavelengths. *Science (80-.).* **282,** 897–901 (1998).
3. Caminade, A.-M. & Turrin, C.-O. Dendrimers for drug delivery. *J. Mater. Chem. B* **2,** 4055 (2014).
4. Ma, W. *et al.* Attomolar DNA detection with chiral nanorod assemblies. *Nat. Commun.* **4,** 2689 (2013).
5. Xia, Y. *et al.* Self-assembly of self-limiting monodisperse supraparticles from polydisperse nanoparticles. *Nat. Nanotechnol.* **6,** 580–587 (2011).
6. Pazos-Pérez, N., Rodríguez-González, B., Hilgendorff, M., Giersig, M. & Liz-Marzán, L. M. Gold encapsulation of star-shaped FePt nanoparticles. *J. Mater. Chem.* **20,** 61 (2010).
7. Mirzaei, J., Reznikov, M. & Hegmann, T. Quantum dots as liquid crystal dopants. *J. Mater. Chem.* **22,** 22350 (2012).
8. Tang, Z. Y., Kotov, N. A. & Giersig, M. Spontaneous organization of single CdTe nanoparticles into luminescent nanowires. *Science (80-.).* **297,** 237–240 (2002).
9. Tang, Z., Zhang, Z., Wang, Y., Glotzer, S. C. & Kotov, N. A. Self-Assembly of CdTe Nanocrystals into Free-Floating Sheets. *Science (80-.).* **314,** 274–278 (2006).
10. Sanna, V., Pala, N. & Sechi, M. Targeted therapy using nanotechnology: Focus on cancer. *Int. J. Nanomedicine* **9,** 467–483 (2014).
11. McGuffie, M. J. *et al.* Zinc oxide nanoparticle suspensions and layer-by-layer

coatings inhibit staphylococcal growth. *Nanomedicine Nanotechnology, Biol. Med.* **12,** 33–42 (2016).

12. Roh, K., Martin, D. C. & Lahann, J. Biphasic Janus particles with nanoscale anisotropy. *Nat. Mater.* **4,** 759–763 (2005).
13. Ma, X., Liu, J., Liang, C., Gong, X. & Che, R. A facile phase transformation method for the preparation of 3D flower-like β-Ni(OH)2/GO/CNTs composite with excellent supercapacitor performance. *J. Mater. Chem. A* **2,** 12692–12696 (2014).
14. Kim, J. W. *et al.* Synthesis of Monodisperse Bi-Compartmentalized Amphiphilic Janus Microparticles for Tailored Assembly at the Oil-Water Interface. *Angew. Chemie - Int. Ed.* **55,** 4509–4513 (2016).
15. Lim, M. P. A., Lee, W. L., Widjaja, E. & Loo, S. C. J. One-step fabrication of core–shell structured alginate–PLGA/PLLA microparticles as a novel drug delivery system for water soluble drugs. *Biomater. Sci.* **1,** 486 (2013).
16. Hwangbo, K.-H., Kim, M. R., Lee, C.-S. & Cho, K. Y. Facile fabrication of uniform golf-ball-shaped microparticles from various polymers. *Soft Matter* **7,** 10874 (2011).
17. Maeda, K., Onoe, H., Takinoue, M. & Takeuchi, S. Controlled synthesis of 3D multi-compartmental particles with centrifuge-based microdroplet formation from a multi-barrelled capillary. *Adv. Mater.* **24,** 1340–1346 (2012).
18. Sudhir, B. & Kumar, S. Existence of a new force in colloidal systems — Hydrophobic attraction between macroscopic surfaces. *Resonance* **7,** 67–81 (2002).
19. Butt, H.-J., Graf, K. & Kappl, M. Physics and chemistry of interfaces. xii, 361 p. (2003). at <http://mirlyn.lib.umich.edu/Record/004933058 CN - QD 506 .B98 2003>
20. Israelachvili, J. N. Intermolecular and surface forces. xxx, 674 p. (2011). at <http://mirlyn.lib.umich.edu/Record/011052001 CN - QD461 .I87 2011>
21. Van Oss, C. J., Chaudhury, M. K. & Good, R. J. Interfacial Lifshitz-van der Waals and polar interactions in macroscopic systems. *Chem. Rev.* **88,** 927–941 (1988).

22. Parsegian, A. V & Ninham, B. W. Application of the Lifshitz theory to the calculation of Van der Waals forces across thin lipid films. *Nature* **224,** 1197–1198 (1969).
23. Prieve, D. C. & Russel, W. B. Simplified predictions of Hamaker constants from Lifshitz theory. *J. Colloid Interface Sci.* **125,** 1–13 (1988).
24. Bergström, L. Hamaker constants of inorganic materials. *Adv. Colloid Interface Sci.* **70,** 125–169 (1997).
25. Horn, R. G. & Israelachvili, J. N. Direct measurement of structural forces between two surfaces in a nonpolar liquid. *J. Chem. Phys.* **75,** 1400 (1981).
26. Kim, H. Y. & Kent, P. R. C. Van der Waals forces: Accurate calculation and assessment of approximate methods in dielectric nanocolloids up to 16 nm. *J. Chem. Phys.* **131,** 1–6 (2009).
27. Kim, H. Y., Sofo, J. O., Velegol, D., Cole, M. W. & Lucas, A. a. Van der waals dispersion forces between dielectric nanoclusters. *Langmuir* **23,** 1735–1740 (2007).
28. E. J. W., V. & J.Th.G., O. Theory of the Stability of Lyophobic Colloids. *Symp. Stabliity Colloid. Dispersions* 631–636 (1946). doi:10.1038/162315b0
29. Tadros, T. General Principles of Colloid Stability and the Role of Surface Forces. *Colloid Stab. Role Surf. Forces - Part I* **1,** 1–22 (2011).
30. Chapter 1. Electrical double layer around a charged colloidal particle in an electrolyte solution. *Theory of Colloid and Interfacial Electric Phenomena* **Volume 12,** 1–38 (2006).
31. Daiguji, H. Ion transport in nanofluidic channels. *Chem. Soc. Rev.* **39,** 901–911 (2010).
32. Tadros, T. in *Encyclopedia of Colloid and Interface Science SE - 76* (ed. Tadros, T.) 363 (Springer Berlin Heidelberg, 2013). doi:10.1007/978-3-642-20665-8_76
33. Ohshima, H. Surface Charge Density/Surface Potential Relationship for a Spherical Colloidal Particle in a Salt-Free Medium. *J. Colloid Interface Sci.* **247,** 18–23 (2002).
34. Xu, Z. & Yoon, R.-H. A study of hydrophobic coagulation. *J. Colloid Interface*

Sci. **134,** 427–434 (1990).

35. Xu, Z. & Yoon, R.-H. The role of hydrophobia interactions in coagulation. *J. Colloid Interface Sci.* **132,** 532–541 (1989).
36. Smit, B., Hilbers, P. A. J., Esselink, K., Rupert, L. A. M., Van Os, N. M., & Schlijper, A. G. Computer Simulationd of a water/oil interface in presence of micelles. *Nature* **348,** 624–625 (1990).
37. Tanford, C. The hydrophobic effect: formation of micelles and biological membranes. ix, 233 p. (1980). at <http://mirlyn.lib.umich.edu/Record/000032108 CN - QH601 .T361 1979 CN - QH601 T361 1979>
38. Spolar, R. S., Ha, J. H. & Record, M. T. Hydrophobic effect in protein folding and other noncovalent processes involving proteins. *Proc. Natl. Acad. Sci.* **86,** 8382–8385 (1989).
39. Harvey, E. newton *et al.* Bubble formation in animals. I Physical factors. *J. Cell. Comp. Physiol.* **24,** 1–22 (1944).
40. Preuss, M. & Butt, H.-J. Direct Measurement of Particle−Bubble Interactions in Aqueous Electrolyte: Dependence on Surfactant. *Langmuir* **14,** 3164–3174 (1998).
41. Claesson, P. M., Blom, C. E., Herder, P. C. & Ninham, B. W. Interactions between water—stable hydrophobic Langmuir—Blodgett monolayers on mica. *J. Colloid Interface Sci.* **114,** 234–242 (1986).
42. Israelachvili, J. N. & Pashley, R. . Measurement of the hydrophobic interaction between two hydrophobic surfaces in aqueous electrolyte solutions. *J. Colloid Interface Sci.* **98,** 500–514 (1984).
43. Luzar, A., Svetina, S. & Zeks, B. The contribution of hydrogen bonds to the surface tension of water. *Chem. Phys. Lett.* **96,** 485–490 (1983).
44. Pratt, L. R. & Chandler, D. Theory of the hydrophobic effect. *J. Chem. Phys.* **67,** 3683 (1977).
45. Marcelja, S., Mitchell, D. J., Ninham, B. W. & Sculley, M. J. Role of solvent structure in solution theory. *J. Chem. Soc. Faraday Trans. 2 Mol. Chem. Phys.* **73,** 630–648 (1977).

46. Christenson, H. K. *Non-Dlvo Forces Between Surfaces -Solvation, Hydration and Capillary Effects. Journal of Dispersion Science and Technology* **9,** (1988).
47. Claesson, P. M. & Christenson, H. K. Very long range attractive forces between uncharged hydrocarbon and fluorocarbon surfaces in water. *J. Phys. Chem.* **92,** 1650–1655 (1988).
48. Ishida, N., Sakamoto, M., Miyahara, M. & Higashitani, K. Attraction between hydrophobic surfaces with and without gas phase. *Langmuir* **16,** 5681–5687 (2000).
49. Ishida, N., Inoue, T., Miyahara, M. & Higashitani, K. Nano bubbles on a hydrophobic surface in water observed by tapping-mode atomic force microscopy. *Langmuir* **16,** 6377–6380 (2000).
50. Stillinger, F. H. Structure in Aqueous Solutions of Nonpolar Solutes from the Standpoint of Scaled-Particle Theory. *J. Solution Chem.* **2,** 141–158 (1973).
51. Stillinger, F. H. Liquid—Vapor Interface Potential for Water. *J. Chem. Phys.* **47,** 4431 (1967).
52. Lee, C.-Y., McCammon, J. A. & Rossky, P. J. The structure of liquid water at an extended hydrophobic surface. *J. Chem. Phys.* **80,** 4448 (1984).
53. Israelachvili, J. & Pashley, R. The hydrophobic interaction is long range, decaying exponentially with distance. *Nature* **300,** 341–342 (1982).
54. Rabinovich, Y. I. & Yoon, R.-H. Use of atomic force microscope for the measurements of hydrophobic forces. *Colloids Surfaces A Physicochem. Eng. Asp.* **93,** 263–273 (1994).
55. Yoon, R.-H. & Ravishankar, S. A. Long-Range Hydrophobic Forces between Mica Surfaces in Dodecylammonium Chloride Solutions in the Presence of Dodecanol. *J. Colloid Interface Sci.* **179,** 391–402 (1996).
56. Israelachvili, J. N. & Adams, G. E. Measurement of forces between two mica surfaces in aqueous electrolyte solutions in the range 0?100 nm. *J. Chem. Soc. Faraday Trans. 1* **74,** 975 (1978).
57. Yoon, R.-H. & Ravishankar, S. A. Application of Extended DLVO Theory: III. Effect of Octanol on the Long-Range Hydrophobic Forces between

Dodecylamine-Coated Mica Surfaces. *J. Colloid Interface Sci.* **166,** 215–224 (1994).

58. Rabinovich, Y. I. & Yoon, R.-H. Use of Atomic Force Microscope for the Measurements of Hydrophobic Forces between Silanated Silica Plate and Glass Sphere. *Langmuir* **10,** 1903–1909 (1994).
59. Churaev, N. . & Derjaguin, B. . Inclusion of structural forces in the theory of stability of colloids and films. *J. Colloid Interface Sci.* **103,** 542–553 (1985).
60. Christenson, H. K. & Claesson, P. M. Direct measurements of the force between hydrophobic surfaces in water. *Adv. Colloid Interface Sci.* **91,** 391–436 (2001).
61. Yoon, R.-H. & Ravishankar, S. A. Long-Range Hydrophobic Forces between Mica Surfaces in Alkaline Dodecylammonium Chloride Solutions. *J. Colloid Interface Sci.* **179,** 403–411 (1996).
62. Yoon, R.-H., Flinn, D. H. & Rabinovich, Y. I. Hydrophobic interactions between dissimilar surfaces. *J. Colloid Interface Sci.* **185,** 363–370 (1997).
63. Fitch, R. M. in (ed. Fitch, R. M. B. T.-P. C.) 6–47 (Academic Press, 1997). doi:http://dx.doi.org/10.1016/B978-012257745-1/50004-3
64. Kawakatsu, T., Kikuchi, Y. & Nakajima, M. Regular-sized cell creation in microchannel emulsification by visual microprocessing method. *J. Am. Oil Chem. Soc.* **74,** 317–321 (1997).
65. Thorsen, T., Roberts, R. W., Arnold, F. H. & Quake, S. R. Dynamic pattern formation in a vesicle-generating microfluidic device. *Phys. Rev. Lett.* **86,** 4163–4166 (2001).
66. Garstecki, P., Fuerstman, M. J., Stone, H. A. & Whitesides, G. M. Formation of droplets and bubbles in a microfluidic T-junction—scaling and mechanism of break-up. *Lab Chip* **6,** 437 (2006).
67. Anna, S. L., Bontoux, N. & Stone, H. a. Formation of dispersions using ‘flow focusing’ in microchannels. *Appl. Phys. Lett.* **82,** 364–366 (2003).
68. Gañán-Calvo, A. Generation of Steady Liquid Microthreads and Micron-Sized Monodisperse Sprays in Gas Streams. *Phys. Rev. Lett.* **80,** 285–288 (1998).
69. Jeong, W. J. *et al.* Continuous fabrication of biocatalyst immobilized

microparticles using photopolymerization and immiscible liquids in microfluidic systems. *Langmuir* **21,** 3738–3741 (2005).

70. Dendukuri, D. & Doyle, P. S. The synthesis and assembly of polymeric microparticles using microfluidics. *Adv. Mater.* **21,** 4071–4086 (2009).
71. Sugiura, S., Nakajima, M., Tong, J., Nabetani, H. & Seki, M. Preparation of Monodispersed Solid Lipid Microspheres Using a Microchannel Emulsification Technique. *J. Colloid Interface Sci.* **227,** 95–103 (2000).
72. Sugiura, S., Nakajima, M., Itou, H. & Seki, M. Synthesis of polymeric microspheres with narrow size distributions employing microchannel emulsification. *Macromol. Rapid Commun.* **22,** 773–778 (2001).
73. Nisisako, T., Torii, T. & Higuchi, T. Novel microreactors for functional polymer beads. *Chem. Eng. J.* **101,** 23–29 (2004).
74. Sugiura, S. *et al.* Size control of calcium alginate beads containing living cells using micro-nozzle array. *Biomaterials* **26,** 3327–3331 (2005).
75. Tan, W. H. & Takeuchi, S. Monodisperse alginate hydrogel microbeads for cell encapsulation. *Adv. Mater.* **19,** 2696–2701 (2007).
76. Kim, K. & Kim, D. High-performance liquid chromatography separation characteristics of molecular-imprinted poly(methacrylic acid) microparticles prepared by suspension polymerization. *J. Appl. Polym. Sci.* **96,** 200–212 (2005).
77. Vignali, D. A. A. Multiplexed particle-based flow cytometric assays. *J. Immunol. Methods* **243,** 243–255 (2000).
78. JIANG, W., GUPTA, R., DESHPANDE, M. & SCHWENDEMAN, S. Biodegradable poly(lactic-co-glycolic acid) microparticles for injectable delivery of vaccine antigens. *Adv. Drug Deliv. Rev.* **57,** 391–410 (2005).
79. Mathiowitz, E. *et al.* Biologically erodable microspheres as potential oral drug delivery systems. *Nature* **386,** 410–414 (1997).
80. Saralidze, K., Koole, L. H. & Knetsch, M. L. W. Polymeric Microspheres for Medical Applications. *Materials (Basel).* **3,** 3537–3564 (2010).
81. Bock, N., Dargaville, T. R., Kirby, G. T. S., Hutmacher, D. W. & Woodruff, M. A. Growth Factor-Loaded Microparticles for Tissue Engineering: The Discrepancies

of *In Vitro* Characterization Assays. *Tissue Eng. Part C Methods* **22,** ten.tec.2015.0222 (2015).

82. Kohane, D. S. & Langer, R. Polymeric biomaterials in tissue engineering. *Pediatr. Res.* **63,** 487–491 (2008).
83. Silva, G. A., Ducheyne, P. & Reis, R. L. Materials in particulate form for tissue engineering. 1. Basic concepts. *J. Tissue Eng. Regen. Med.* **1,** 4–24 (2007).
84. Silva, G. a, Coutinho, O. P., Ducheyne, P. & Reis, R. L. Materials in particulate form for tissue engineering. 2. Applications in bone. *J. Tissue Eng. Regen. Med.* **1,** 97–109 (2007).
85. Oliveira, M. B. & Mano, J. F. Polymer-based microparticles in tissue engineering and regenerative medicine. *Biotechnol. Prog.* **27,** 897–912 (2011).
86. Scott, D. L., Clark, C. W., Tooley, P. W., Carras, M. M. & Maas, J. L. The use of biomagnetic separation to recover DNA suitable for PCR from Claviceps species. *Lett. Appl. Microbiol.* **31,** 95–9 (2000).
87. Trefilov, A. *et al.* A microscale method of protein extraction from bacteria: Interaction of Escherichia coli with cationic microparticles. *J. Biotechnol.* **207,** 21–29 (2015).
88. Elaissari, A. Reactive Polymer Based Colloids for Biomedical Applications. *Macromol. Symp.* **229,** 47–55 (2005).
89. Asua, J. M. & service), S. (Online. Polymeric Dispersions: Principles and Applications. *Proceedings of the NATO Advanced Study Institute on Recent Advances in Polymeric Dispersions, Elizondo, Spain, June 23-July 5, 1996* XIX, 565 p. (1997). at <http://dx.doi.org/10.1007/978-94-011-5512-0>
90. Lovell, P. A. & El-Aasser, M. S. Emulsion polymerization and emulsion polymers. xxiv, 801 p. (1997). at <http://mirlyn.lib.umich.edu/Record/003161615 CN - QD 281 .P6 E4631 1997>
91. Tobing, S. D. & Klein, A. Molecular parameters and their relation to the adhesive performance of emulsion acrylic pressure-sensitive adhesives. II. Effect of crosslinking. *J. Appl. Polym. Sci.* **79,** 2558–2564 (2001).
92. Yablonovitch, E. Inhibited spontaneous emission in solid-state physics and

electronics. *Phys. Rev. Lett.* **58,** 2059–2062 (1987).

93. John, S. Strong localization of photons in certain disordered dielectric superlattices. *Phys. Rev. Lett.* **58,** 2486–2489 (1987).
94. Norris, D. J. Photonic crystals. A view of the future. *Nat. Mater.* **6,** 177–178 (2007).
95. Blanco, a *et al.* Large-scale synthesis of a silicon photonic crystal with a complete three-dimensional bandgap near 1.5 micrometres. *Nature* **405,** 437–40 (2000).
96. Yurii A. Vlasov James C. Sturm & David J. Norris, X.-Z. B. On-chip natural assembly of silicon photonic bandgap crystals. *Nature* **414,** 289–293 (2001).
97. Gil, S. C., Seo, Y. G., Kim, S., Shin, J. & Lee, W. High-speed fabrication of 3-dimensional colloidal photonic crystal films by slide coating of polymer microspheres with continuous feeding of colloidal suspension. *Thin Solid Films* **518,** 5731–5736 (2010).
98. Kim, S.-H., Lee, S. Y., Yang, S.-M. & Yi, G.-R. Self-assembled colloidal structures for photonics. *NPG Asia Mater.* **3,** 25–33 (2011).
99. Zhang, J., Sun, Z. & Yang, B. Self-assembly of photonic crystals from polymer colloids. *Curr. Opin. Colloid Interface Sci.* **14,** 103–114 (2009).
100. García-Santamaría, F. *et al.* Nanorobotic manipulation of microspheres for on-chip diamond architectures. *Adv. Mater.* **14,** 1144–1147 (2002).
101. Hynninen, A.-P., Thijssen, J. H. J., Vermolen, E. C. M., Dijkstra, M. & van Blaaderen, A. Self-assembly route for photonic crystals with a bandgap in the visible region. *Nat. Mater.* **6,** 202–205 (2007).
102. Kotov, N. A. *et al.* Inverted Colloidal Crystals as Three-Dimensional Cell Scaffolds. *Langmuir* **20,** 7887–7892 (2004).
103. Cuddihy, M. J. & Kotov, N. a. Poly(lactic-co-glycolic acid) bone scaffolds with inverted colloidal crystal geometry. *Tissue Eng. Part A* **14,** 1639–1649 (2008).
104. Lee, J., Shanbhag, S. & Kotov, N. a. Inverted colloidal crystals as three-dimensional microenvironments for cellular co-cultures. *J. Mater. Chem.* **16,** 3558 (2006).

105. Lee, J., Cuddihy, M. J., Cater, G. M. & Kotov, N. a. Engineering liver tissue spheroids with inverted colloidal crystal scaffolds. *Biomaterials* **30,** 4687–94 (2009).
106. Shanbhag, S., Wang, S. & Kotov, N. a. Cell distribution profiles in three-dimensional scaffolds with inverted-colloidal-crystal geometry: Modeling and experimental investigations. *Small* **1,** 1208–1214 (2005).
107. Nichols, J. E. *et al.* In vitro analog of human bone marrow from 3D scaffolds with biomimetic inverted colloidal crystal geometry. *Biomaterials* **30,** 1071–9 (2009).
108. Cuddihy, M. J., Wang, Y., Machi, C., Bahng, J. H. & Kotov, N. A. Replication of Bone Marrow Differentiation Niche: Comparative Evaluation of Different Three-Dimensional Matrices. *Small* **9,** 1008–1015 (2013).
109. Cui, J. Zinc oxide nanowires. *Mater. Charact.* **64,** 43–52 (2012).
110. Kind, H., Yan, H., Messer, B., Law, M. & Yang, P. Nanowire ultraviolet photodetectors and optical switches. *Adv. Mater.* **14,** 158–160 (2002).
111. Reynolds, D. C. *et al.* Time-resolved photoluminescence lifetime measurements of the Γ[sub 5] and Γ[sub 6] free excitons in ZnO. *J. Appl. Phys.* **88,** 2152 (2000).
112. Özgür, Ü. *et al.* A comprehensive review of ZnO materials and devices. *J. Appl. Phys.* **98,** 1–103 (2005).
113. Kayanuma, Y. Quantum-size effects of interacting electrons and holes in semiconductor microcrystals with spherical shape. *Phys. Rev. B* **38,** 9797–9805 (1988).
114. Wegscheider, W. *et al.* Lasing from excitons in quantum wires. *Phys. Rev. Lett.* **71,** 4071–4074 (1993).
115. Cao, H. *et al.* Spatial confinement of laser light in active random media. *Phys. Rev. Lett.* **84,** 5584–5587 (2000).
116. Bagnall, D. M. *et al.* Optically pumped lasing of ZnO at room temperature. *Appl. Phys. Lett.* **70,** 2230 (1997).
117. Yu, P. *et al.* Room-temperature gain spectra and lasing in microcrystalline ZnO thin films. *J. Cryst. Growth* **184-185,** 601–604 (1998).
118. Johnson, J. C. *et al.* Single nanowire lasers. *J. Phys. Chem. B* **105,** 11387–11390

(2001).

119. Yang, P., Yan, H. & Mao, S. Controlled growth of ZnO nanowires and their optical properties. *Adv. Funct. Mater.* 323–331 (2002). doi:10.1002/1616-3028(20020517)12:5<323::AID-ADFM323>3.0.CO;2-G

120. Law, M., Greene, L. E., Johnson, J. C., Saykally, R. & Yang, P. Nanowire dye-sensitized solar cells. *Nat. Mater.* **4,** 455–459 (2005).

121. Zhang, M.-L. *et al.* High efficiency solar cell based on ZnO nanowire array prepared by different growth methods. *RSC Adv.* **4,** 10462 (2014).

122. Hwang, J. O. *et al.* Vertical ZnO nanowires/graphene hybrids for transparent and flexible field emission. *J. Mater. Chem.* **21,** 3432–3437 (2011).

123. Zhao, Q. *et al.* 2D planar field emission devices based on individual ZnO nanowires. *Solid State Commun.* **151,** 1650–1653 (2011).

124. Kwon, S.-S. *et al.* Piezoelectric Effect on the Electronic Transport Characteristics of ZnO Nanowire Field-Effect Transistors on Bent Flexible Substrates. *Adv. Mater.* **20,** 4557–4562 (2008).

125. Wang, X. *et al.* Piezoelectric field effect transistor and nanoforce sensor based on a single ZnO nanowire. *Nano Lett.* **6,** 2768–2772 (2006).

126. Gao, Z. *et al.* Effects of piezoelectric potential on the transport characteristics of metal-ZnO nanowire-metal field effect transistor. *J. Appl. Phys.* **105,** 113707 (2009).

127. Li, L. *et al.* Hydrothermal synthesis and gas sensing properties of single-crystalline ultralong ZnO nanowires. *Appl. Phys. A* **98,** 635–641 (2009).

128. Fulati, A. *et al.* An intracellular glucose biosensor based on nanoflake ZnO. *Sensors Actuators B Chem.* **150,** 673–680 (2010).

129. Kumar, S. G. & Rao, K. S. R. K. Zinc oxide based photocatalysis: tailoring surface-bulk structure and related interfacial charge carrier dynamics for better environmental applications. *RSC Adv.* **5,** 3306–3351 (2015).

130. Kandavelu, V., Kastien, H. & Ravindranathan Thampi, K. Photocatalytic degradation of isothiazolin-3-ones in water and emulsion paints containing nanocrystalline TiO2 and ZnO catalysts. *Appl. Catal. B Environ.* **48,** 101–111

(2004).

131. Percherancier, J. P., Chapelon, R. & Pouyet, B. Semiconductor-sensitized photodegradation of pesticides in water: the case of carbetamide. *J. Photochem. Photobiol. A Chem.* **87,** 261–266 (1995).
132. Amine, A., Sehili, T., Pilichowski, J. & Boule, P. Photocatalytic degradation of 2-phenylphenol on TiO 2 and ZnO in aqueous suspensions. *J. Photochem. Photobiol. A Chem.* **141,** 231–239 (2001).
133. Li, Y. *et al.* Comparison of dye photodegradation and its coupling with light-to-electricity conversion over TiO2 and ZnO. *Langmuir* **26,** 591–597 (2010).
134. Chen, C. C. Degradation pathways of ethyl violet by photocatalytic reaction with ZnO dispersions. *J. Mol. Catal. A Chem.* **264,** 82–92 (2007).
135. Gouvêa, C. a *et al.* Semiconductor-assisted photocatalytic degradation of reactive dyes in aqueous solution. *Chemosphere* **40,** 433–440 (2000).
136. Schmitt, M. Synthesis and testing of ZnO nanoparticles for photo-initiation: experimental observation of two different non-migration initiators for bulk polymerization. *Nanoscale* 9532–9544 (2015). doi:10.1039/C5NR00850F
137. Wu, X.-F. & Neumann, H. Zinc-Catalyzed Organic Synthesis: C□C, C□N, C□O Bond Formation Reactions. *Adv. Synth. Catal.* **354,** 3141–3160 (2012).
138. Zou, X., Fan, H., Tian, Y. & Yan, S. Synthesis of Cu2O/ZnO hetero-nanorod arrays with enhanced visible light-driven photocatalytic activity. *CrystEngComm* **16,** 1149 (2014).
139. Rahman, Q. I., Ahmad, M., Misra, S. K. & Lohani, M. B. Hexagonal ZnO nanorods assembled flowers for photocatalytic dye degradation: Growth, structural and optical properties. *Superlattices Microstruct.* **64,** 495–506 (2013).
140. Tong, Y., Cheng, J., Liu, Y. & Siu, G. G. Enhanced photocatalytic performance of ZnO hierarchical nanostructures synthesized via a two-temperature aqueous solution route. *Scr. Mater.* **60,** 1093–1096 (2009).
141. Baruah, S., Jaisai, M., Imani, R., Nazhad, M. M. & Dutta, J. Photocatalytic paper using zinc oxide nanorods. *Sci. Technol. Adv. Mater.* **11,** 055002 (2010).
142. Jeon, E. H. *et al.* Comparative study of photocatalytic activities of hydrothermally

grown ZnO nanorod on Si(001) wafer and FTO glass substrates. *Nanoscale Res. Lett.* **10,** 361 (2015).

143. Wan, Q., Wang, T. H. & Zhao, J. C. Enhanced photocatalytic activity of ZnO nanotetrapods. *Appl. Phys. Lett.* **87,** 2013–2016 (2005).
144. Chen, Y. L. *et al.* ZnO nanorod optical disk photocatalytic reactor for photodegradation of methyl orange. *Opt. Express* **21,** 7240–9 (2013).
145. Ozgür, M., Hofstetter, D. & Morkoç, H. ZnO Devices and Applications: A Review of Current Status and Future Prospects. *Proc. IEEE* **98,** 1255–1268 (2010).
146. Yi, G.-C., Wang, C. & Park, W. Il. ZnO nanorods: synthesis, characterization and applications. *Semicond. Sci. Technol.* **20,** S22–S34 (2005).
147. Zhang, Y., Ram, M. K., Stefanakos, E. K. & Goswami, D. Y. Synthesis, Characterization, and Applications of ZnO Nanowires. *J. Nanomater.* **2012,** 1–22 (2012).
148. Petersen, E. W., Likovich, E. M., Russell, K. J. & Narayanamurti, V. Growth of ZnO nanowires catalyzed by size-dependent melting of Au nanoparticles. *Nanotechnology* **20,** 405603 (2009).
149. Protasova, L. N. *et al.* ZnO based nanowires grown by chemical vapour deposition for selective hydrogenation of acetylene alcohols. *Catal. Sci. Technol.* **1,** 768 (2011).
150. Ashraf, S. *et al.* MOCVD of Vertically Aligned ZnO Nanowires Using Bidentate Ether Adducts of Dimethylzinc. *Chem. Vap. Depos.* **17,** 45–53 (2011).
151. Wang, L. *et al.* Synthesis of well-aligned ZnO nanowires by simple physical vapor deposition on c -oriented ZnO thin films without catalysts or additives. *Appl. Phys. Lett.* **86,** 2–4 (2005).
152. Wang, J. S. *et al.* Catalyst-free highly vertically aligned ZnO nanoneedle arrays grown by plasma-assisted molecular beam epitaxy. *Appl. Phys. A* **97,** 553–557 (2009).
153. Tien, L. C., Pearton, S. J., Norton, D. P. & Ren, F. Synthesis and microstructure of vertically aligned ZnO nanowires grown by high-pressure-assisted pulsed-laser deposition. *J. Mater. Sci.* **43,** 6925–6932 (2008).

154. Kitamura, K., Yatsui, T., Ohtsu, M. & Yi, G.-C. Fabrication of vertically aligned ultrafine ZnO nanorods using metal-organic vapor phase epitaxy with a two-temperature growth method. *Nanotechnology* **19,** 175305 (2008).
155. Suh, D. I., Byeon, C. C. & Lee, C. L. Synthesis and optical characterization of vertically grown ZnO nanowires in high crystallinity through vapor-liquid-solid growth mechanism. *Appl. Surf. Sci.* **257,** 1454–1456 (2010).
156. Huang, M. H. *et al.* Catalytic growth of zinc oxide nanowires by vapor transport. *Adv. Mater.* **13,** 113–116 (2001).
157. Liu, B. & Zeng, H. C. Hydrothermal synthesis of ZnO nanorods in the diameter regime of 50 nm. *J. Am. Chem. Soc.* **125,** 4430–4431 (2003).
158. Dutta, J. Hydrothermal growth of ZnO nanostructures. *Sci. Technol. Adv. Mater.* **10,** 013001 (2009).
159. Baruah, S., Mahmood, M. A., Myint, M. T. Z., Bora, T. & Dutta, J. Enhanced visible light photocatalysis through fast crystallization of zinc oxide nanorods. *Beilstein J. Nanotechnol.* **1,** 14–20 (2010).
160. Xu, S., Lao, C., Weintraub, B. & Wang, Z. L. Density-controlled growth of aligned ZnO nanowire arrays by seedless chemical approach on smooth surfaces. *J. Mater. Res.* **23,** 2072–2077 (2008).
161. Caruso, F. Nanoengineering of particle surfaces. *Adv. Mater.* **13,** 11–22 (2001).
162. Oyama, H. T., Sprycha, R., Xie, Y., Partch, R. E. & Matijević, E. Coating of uniform inorganic particles with polymers, I. *Journal of Colloid and Interface Science* **160,** 298–303 (1993).
163. Sprycha, R., Zelenev, A., Matijevib, E. & Corporation, S. C. Characterization of polymer-coated silica particles by microelectrophoresis CH2C1 CH2Z CH2C1 Z : Polymerizat Na. **700,** 693–700 (1995).
164. Partch, R., Gangolli, G.S., Matijevic, E., Cai, W., Arajs, S. Conducting Polymer Composites. *J. Colloid Interface Sci.* 27–35 (1991).
165. Huang, C.-L. & Matijevic, E. Coating of uniform inorganic particles with polymers: III. Polypyrrole on different metal oxides. *J. Mater. Res.* **10,** 1327–1336 (2011).

166. Marinakos, S. M. *et al.* Template Synthesis of One-Dimensional Au , Au-Poly (pyrrole), and Poly (pyrrole) Nanoparticle Arrays crystals synthesized by Bawendi ' s group , 1 Mirkin and and the closest-packed surface-confined monolayers of structures have revealed electronic and. *Science (80-.).* **1,** 1214–1219 (1998).

167. Marinakos, S. M., Shultz, D. A. & Feldheim, D. L. Gold Nanoparticles as Templates for the Synthesis of Hollow Nanometer-Sized Conductive Polymer Capsules. *Adv. Mater.* **11,** 34–37 (1999).

168. Marinakos, S. M. *et al.* Gold particles as templates for the synthesis of hollow polymer capsules. Control of capsule dimensions and guest encapsulation. *J. Am. Chem. Soc.* **121,** 8518–8522 (1999).

169. Ottewill, R. H., Schofield, a. B., Waters, J. a. & Williams, N. S. J. Preparation of core-shell polymer colloid particles by encapsulation. *Colloid Polym. Sci.* **275,** 274–283 (1997).

170. Hergeth, W., Steinau, U., Bittrich, H., Schmutzler, K. & Wartewig, S. Submicron particles with thin polymer shells. **90,** 82–90 (1991).

171. Quaroni, L. & Chumanov, G. Preparation of polymer-coated functionalized silver nanoparticles [9]. *J. Am. Chem. Soc.* **121,** 10642–10643 (1999).

172. Sukhorukov, G. B. *et al.* Layer-by-layer self assembly of polyelectrolytes on colloidal particles. *Colloids Surfaces a-Physicochemical Eng. Asp.* **137,** 253–266 (1998).

173. Caruso, F., Donath, E., Mo, H. & Möhwald, H. Influence of Polyelectrolyte Multilayer Coatings on Förster Resonance Energy Transfer between 6-Carboxyfluorescein and Rhodamine B-Labeled Particles in Aqueous Solution. *J. Phys. Chem. B* **102,** 2011–2016 (1998).

174. Caruso, F., Lichtenfeld, H., Donath, E. & Möhwald, H. Investigation of Electrostatic Interactions in Polyelectrolyte Multilayer Films: Binding of Anionic Fluorescent Probes to Layers Assembled onto Colloids. *Macromolecules* **32,** 2317–2328 (1999).

175. Caruso, F., Schuler, C. & Kurth, D. G. Core-shell particles and hollow shells

containing metallo-supramolecular components. *Chem. Mater.* **11,** 3394–3399 (1999).

176. Caruso, F. Hollow capsule processing through colloidal templating and self-assembly. *Chemistry* **6,** 413–9 (2000).
177. Philipse, A. P., Bruggen, M. P. B. Van & Pathmamanoharan, C. Magnetic Silica Dispersions: Preparation and Stability of Surface-Modified Silica Particles with a Magnetic Core. *Langmuir* 92–99 (1994). doi:10.1021/la00013a014
178. Giersig, M., Ung, T., Liz-Marzhn, L. M. & Mulvaney, P. Direct Observation of Chemical Reactions in Silica-Coated Gold and Silver Nanoparticles. *Adv. Mater. Commun.* **9,** 570–575 (1997).
179. Bruggen, M. Van. Preparation and properties of colloidal core-shell rods with adjustable aspect ratios. *Langmuir* **7463,** 2245–2255 (1998).
180. Hall, S. R., Davis, S. a. & Mann, S. Cocondensation of organosilica hybrid shells on nanoparticle templates: a direct synthetic route to functionalized core-shell colloids. *Langmuir* **16,** 1454–1456 (2000).
181. Ung, T., Liz-Marzán, L. M. & Mulvaney, P. Redox Catalysis Using Ag @ SiO 2 Colloids. *J. Phys. Chem. B* **103,** 6770–6773 (1999).
182. Ung, T. & Liz-marza, L. M. Controlled Method for Silica Coating of Silver Colloids . Influence of Coating on the Rate of Chemical Reactions. *Langmuir* **14,** 3740–3748 (1998).
183. Correa-Duarte, M. a, Giersig, M. & Liz-Marzán, L. M. Stabilization of CdS semiconductor nanoparticles against photodegradation by a silica coating procedure. *Chem. Phys. Lett.* **286,** 497–501 (1998).
184. Ohmori, M. & Matijević, E. Preparation and properties of uniform coated colloidal particles. VII. Silica on hematite. *J. Colloid Interface Sci.* **150,** 594–598 (1992).
185. Ohmori, M. & Matijević, E. Preparation and properties of uniform coated inorganic colloidal particles. *Journal of Colloid and Interface Science* **160,** 288–292 (1993).
186. Kawahashi, N. & Matijevic, E. Preparation of Hollow Spherical Particles of

Yttrium Compounds. *J. Colloid Interface Sci.* **143,** 103–110 (1991).

187. Liz-Marzán, L. M., Giersig, M. & Mulvaney, P. Synthesis of Nanosized Gold-Silica Core-Shell Particles. *Langmuir* **12,** 4329–4335 (1996).
188. Caruso, F. & Möhwald, H. Preparation and characterization of ordered nanoparticle and polymer composite multilayers on colloids. *Langmuir* **15,** 8276–8281 (1999).
189. Caruso, F., Lichtenfeld, H., Giersig, M. & Mohwald, H. Electrostatic self-assembly of silica nanoparticle-polyelectrolyte multilayers on polystyrene latex particles [4]. *J. Am. Chem. Soc.* **120,** 8523–8524 (1998).
190. Bridging, C. P. Preparation of Novel Core – Shell Nanocomposite Particles by. *Ceramics* **44,** 140–144 (1998).
191. Keller, S. W., Johnson, S. a., Brigham, E. S., Yonemoto, E. H. & Mallouk, T. E. Photoinduced Charge Separation in Multilayer Thin Films Grown by Sequential Adsorption of Polyelectrolytes. *J. Am. Chem. Soc.* **117,** 12879–12880 (1995).
192. Lvov, Y., Ariga, K., Onda, M., Ichinose, I. & Kunitake, T. Alternate Assembly of Ordered Multilayers of SiO 2 and Other Nanoparticles and Polyions. *Langmuir* **13,** 6195–6203 (1997).
193. Oldenburg, S. ., Averitt, R. ., Westcott, S. . & Halas, N. . Nanoengineering of optical resonances. *Chem. Phys. Lett.* **288,** 243–247 (1998).
194. Rogach, A. *et al.* Nano- and microengineering: Three-dimensional colloidal photonic crystals prepared from submicrometer-sized polystyrene latex spheres pre-coated with luminescent polyelectrolyte/nanocrystal shells. *Adv. Mater.* **12,** 333–337 (2000).
195. Caruso, F., Susha, A. S., Giersig, M. & Möhwald, H. Magnetic Core-Shell Particles : Preparation of Magnetite Multilayers on Polymer Latex Microspheres. *Adv. Mater.* **11,** 950–953 (1999).
196. Vereda, F., Morales, M. del P., Rodríguez-González, B., Vicente, J. de & Hidalgo-Alvarez, R. Control of surface morphology and internal structure in magnetite microparticles: from smooth single crystals to rough polycrystals. *CrystEngComm* **15,** 5236 (2013).

197. Ahmed, W., Stefan Kooij, E., van Silfhout, A. & Poelsema, B. Controlling the morphology of multi-branched gold nanoparticles. *Nanotechnology* **21,** 125605 (2010).
198. Barbosa, S. *et al.* Tuning Size and Sensing Properties in Colloidal Gold Nanostars. *Langmuir* **26,** 14943–14950 (2010).
199. Yang, M. *et al.* SERS-Active Gold Lace Nanoshells with Built-in Hotspots. *Nano Lett.* **10,** 4013–4019 (2010).
200. Suresh, L. & Walz, J. Y. Effect of Surface Roughness on the Interaction Energy between a Colloidal Sphere and a Flat Plate. *J. Colloid Interface Sci.* **183,** 199–213 (1996).
201. Chew, N. Y. K., Tang, P., Chan, H. K. & Raper, J. a. How much particle surface corrugation is sufficient to improve aerosol performance of powders? *Pharm. Res.* **22,** 148–152 (2005).
202. Hulst, H. C. van de. Light scattering by small particles. 470 p. (1957). at <http://mirlyn.lib.umich.edu/Record/001480676 CN - QC 431 .H926>
203. BORN, M. A. X. & WOLF, E. in (Pergamon, 1980). doi:http://dx.doi.org/10.1016/B978-0-08-026482-0.50008-6
204. Lecler, S. Etude de la diffusion de la lumière par des particules sub-microniques. **33,** (Université Louis Pasteur, 2005).
205. Seinfeld, J. H. & Pandis, S. N. Atmospheric chemistry and physics: from air pollution to climate change. xxviii, 1203 p. (2006). at <http://mirlyn.lib.umich.edu/Record/007265755 CN - QC 879.6 .S45 2006>
206. Zubko, E., Shkuratov, Y., Hart, M., Eversole, J. & Videen, G. Backscattering and negative polarization of agglomerate particles. *Opt. Lett.* **28,** 1504–1506 (2003).
207. Tarcea, N. Microcapsule Sizing by Elastic Light Scattering Mineral Investigation by in situ Raman Spectroscopy. (Bayerischen Julius-Maximilians-Universität Würzburg, 2004).
208. García-Cámara, B. On Light Scattering by nanoparticles with conventional and non-conventioanl optical properties. **9,** (Universidad de Cantabria, 2010).
209. Bohren, C. F. & Huffman, D. R. Absorption and scattering of light by small

particles. xiv, 530 p. (1983). at <http://mirlyn.lib.umich.edu/Record/000469939 CN - QC882 .B631 1983>

210. Shifrin, K. S. & Zolotov, I. G. Remark about the notation used for calculating the electromagnetic field scattered by a spherical particle. *Appl. Opt.* **32,** 5397–5398 (1993).
211. Love, A. E. H. The Scattering of Electric Waves by a Dielectric Sphere. *Proc. London Math. Soc.* 308–321 (1899).
212. B. Maheu , Gérard Gréhan, G. G. Generalized Lorenz-Mie theory : first exact values and comparisons with the localized approximation. *Appl. Opt.* **26,** 23–25 (1987).
213. Li, Y. *et al.* Giant resonant light forces in microspherical photonics. *Light Sci. Appl.* **2,** e64 (2013).
214. Sbanski, O., Roman, V. E., Kiefer, W. & Popp, J. Elastic light scattering from single microparticles on a femtosecond time scale. *J. Opt. Soc. Am. A. Opt. Image Sci. Vis.* **17,** 313–9 (2000).
215. Schulte, J. & Schweiger, G. Inelastic scattering on spherical microparticles with inclusions. **18,** 117–123 (2001).
216. Serpenguzel, A., Arnold, S., Griffel, G. & Lock, J. A. Enhanced coupling to microsphere resonances with optical fibers. *J. Opt. Soc. Am. B-Optical Phys.* **14,** 790–795 (1997).
217. Chandler, W. L., Yeung, W. & Tait, J. F. A new microparticle size calibration standard for use in measuring smaller microparticles using a new flow cytometer. *J. Thromb. Haemost.* **9,** 1216–1224 (2011).
218. Hergert, W., Wriedt, T. & service), S. (Online. The Mie Theory Basics and Applications. (2012). at <http://dx.doi.org/10.1007/978-3-642-28738-1>
219. Ge, J. M., Su, J., Fu, Q., Ackerman, T. P. & Huang, J. P. Dust aerosol forward scattering effects on ground-based aerosol optical depth retrievals. *J. Quant. Spectrosc. Radiat. Transf.* **112,** 310–319 (2011).
220. Fu, Q., Thorsen, T. J., Su, J., Ge, J. M. & Huang, J. P. Test of Mie-based single-scattering properties of non-spherical dust aerosols in radiative flux calculations.

J. Quant. Spectrosc. Radiat. Transf. **110,** 1640–1653 (2009).

221. Dayou, J., Chang, J. H. W., Sentian, J. & service), S. (Online. Ground-Based Aerosol Optical Depth Measurement Using Sunphotometers. VI, 62 p. 21 illus., 10 illus. in color (2014). at <http://dx.doi.org/10.1007/978-981-287-101-5>
222. Chamaillard, K., Jennings, S. G., Kleefeld, C., Ceburnis, D. & Yoon, Y. J. Light backscattering and scattering by nonspherical sea-salt aerosols. *J. Quant. Spectrosc. Radiat. Transf.* **79-80,** 577–597 (2003).
223. Pinnick, R. G., Rosen, J. M. & Hofmann, D. J. Measured light-scattering properties of individual aerosol particles compared to mie scattering theory. *Appl. Opt.* **12,** 37–41 (1973).
224. Kahnert, M., Nousiainen, T. & Räisänen, P. Mie simulations as an error source in mineral aerosol radiative forcing calculations. *Q. J. R. Meteorol. Soc.* **133,** 299–307 (2007).
225. Facts, C. American Cancer Society: Cancer Facts and Figures 2015. (2015). doi:10.3322/caac.21254
226. Hodgson, J. ADMET-turning chemicals into drugs. *Nat. Biotechnol.* **19,** 722–726 (2001).
227. Albushra, Y. Prevention and Management of High Dose Methotrexate Toxicity. *J. Cancer Sci. Ther.* **05,** 106–112 (2013).
228. Pabla, N. & Dong, Z. Cisplatin nephrotoxicity: mechanisms and renoprotective strategies. *Kidney Int.* **73,** 994–1007 (2008).
229. Chatterjee, K., Zhang, J., Honbo, N. & Karliner, J. S. Doxorubicin cardiomyopathy. *Cardiology* **115,** 155–162 (2010).
230. Azambuja, E., Fleck, J. F., Batista, R. G. & Menna Barreto, S. S. Bleomycin lung toxicity: who are the patients with increased risk? *Pulm Pharmacol Ther* **18,** 363–366 (2005).
231. Bolten, B. M. & Degregorio, T. FROM THE ANALYST ' S COUCH Trends in development cycles FROM THE ANALYST ' S COUCH Market indicators. *Discovery* **1,** 1–2 (2002).
232. Zegers, M. M. P., O'Brien, L. E., Yu, W., Datta, A. & Mostov, K. E.

Epithelial polarity and tubulogenesis in vitro. *Trends Cell Biol.* **13,** 169–176 (2003).

233. Petersen, O. W., Rønnov-Jessen, L., Howlett, A. R. & Bissell, M. J. Interaction with basement membrane serves to rapidly distinguish growth and differentiation pattern of normal and malignant human breast epithelial cells. *Proc. Natl. Acad. Sci. U. S. A.* **89,** 9064–9068 (1992).
234. Alford, D. & Taylor-Papadimitriou, J. Cell adhesion molecules in the normal and cancerous mammary gland. *J. Mammary Gland Biol. Neoplasia* **1,** 207–18 (1996).
235. Kim, J. Bin, Stein, R. & O'Hare, M. J. Three-dimensional in vitro tissue culture models of breast cancer-- a review. *Breast Cancer Res. Treat.* **85,** 281–291 (2004).
236. Smalley, K. S. M., Lioni, M. & Herlyn, M. Life isn't flat: taking cancer biology to the next dimension. *In Vitro Cell. Dev. Biol. Anim.* **42,** 242–247 (2006).
237. Roskelley, C. D. & Bissell, M. J. Dynamic reciprocity revisited: a continuous, bidirectional flow of information between cells and the extracellular matrix regulates mammary epithelial cell function. *Biochem. Cell Biol.* **73,** 391–397 (1994).
238. Abbott, A. Biology ' s new dimension. *Nature* **424,** 870–872 (2003).
239. Grinnell, F. Fibroblast biology in three-dimensional collagen matrices. *Trends Cell Biol.* **13,** 264–269 (2003).
240. Webb, D. J. & Horwitz, A. F. New dimensions in cell migration. *Nat. Cell Biol.* **5,** 690–692 (2003).
241. Cukierman, E., Pankov, R. & Yamada, K. M. Cell interactions with three-dimensional matrices. *Curr. Opin. Cell Biol.* **14,** 633–639 (2002).
242. Tollman, P., Guy, P., Altshuler, J., Flanagan, A. & Steiner, M. A Revolution in R&D. How Genomics and Genetics Are Tranforming the Biopharmaceutical Industry. *Bost. Consult. Gr.* (2001).
243. Wilding, I. R. & Bell, J. A. Improved early clinical development through human microdosing studies. *Drug Discov. Today* **10,** 890–4 (2005).
244. Zhang, Y., Wang, S., Eghtedari, M., Motamedi, M. & Kotov, N. A. Inverted-Colloidal-Crystal Hydrogel Matrices as Three-Dimensional Cell Scaffolds. *Adv.*

Funct. Mater. **15,** 725–731 (2005).

245. Cho, K., Wang, X., Nie, S., Chen, Z. G. & Shin, D. M. Therapeutic nanoparticles for drug delivery in cancer. *Clin. Cancer Res.* **14,** 1310–6 (2008).
246. Quevedo, E., Steinbacher, J. & Mcquade, D. T. Interfacial Polymerization within a Simplified Microfluidic Device: Capturing Capsules Scheme 1. Schematic of Fluidic Device. *J. Am. Chem. Soc* **127,** 10498–10499 (2005).
247. Drury, J. L. & Mooney, D. J. Hydrogels for tissue engineering: Scaffold design variables and applications. *Biomaterials* **24,** 4337–4351 (2003).
248. van Wachem, P. B. *et al.* Adhesion of cultured human endothelial cells onto methacrylate polymers with varying surface wettability and charge. *Biomaterials* **8,** 323–328 (1987).
249. Rosso, F. *et al.* New polyelectrolyte hydrogels for biomedical applications. *Mater. Sci. Eng. C* **23,** 371–376 (2003).
250. Lipdon, J., Minett, W. & Tighe, B. J. Cellular interactions with synthetic polymer surfaces in culture. *Biomaterials* **6,** 396–402 (1985).
251. Hooper, H. H., Baker, J. P., Blanch, H. W. & Prausnitz, J. M. Swelling equilibria for positively ionized polyacrylamide hydrogels. *Macromolecules* **23,** 1096–1104 (1990).
252. TANAKA, T., NISHIO, I., SUN, S.-T. & UENO-NISHIO, S. Collapse of Gels in an Electric Field. *Science (80-.).* **218,** 467–469 (1982).
253. Mullarney, M. P., Seery, T. a P. & Weiss, R. a. Drug diffusion in hydrophobically modified N,N-dimethylacrylamide hydrogels. *Polymer (Guildf).* **47,** 3845–3855 (2006).
254. Sperling, R. a & Parak, W. J. Surface modification, functionalization and bioconjugation of colloidal inorganic nanoparticles. *Philos. Trans. A. Math. Phys. Eng. Sci.* **368,** 1333–1383 (2010).
255. Feng, L. *et al.* Super-hydrophobic surfaces: From natural to artificial. *Adv. Mater.* **14,** 1857–1860 (2002).
256. Lafuma, A. & Quéré, D. Superhydrophobic states. *Nat. Mater.* **2,** 457–460 (2003).
257. Parker, a R. & Lawrence, C. R. Water capture by a desert beetle. *Nature* **414,**

33–34 (2001).

258. Yang, B. P. *et al.* Controlled Growth of ZnO Nanowires and Their Optical Properties **. 323–331 (2002).

259. Kim, S. H., Abbaspourrad, A. & Weitz, D. a. Amphiphilic crescent-moon-shaped microparticles formed by selective adsorption of colloids. *J. Am. Chem. Soc.* **133,** 5516–5524 (2011).

260. Walther, A. & Mu, A. H. E. Janus Particles : Synthesis , Self-Assembly , Physical Properties , and Applications. *Chem. Rev.* **113,** 5194–5261 (2013).

261. Yan, J., Bloom, M., Bae, S. C., Luijten, E. & Granick, S. Linking synchronization to self-assembly using magnetic Janus colloids. *Nature* **491,** 578–81 (2012).

262. Papadopoulos, P., Mammen, L., Deng, X., Vollmer, D. & Butt, H. How superhydrophobicity breaks down. *Proc. Natl. Acad. Sci. U. S. A.* **110,** 3254–3258 (2013).

263. Verho, T. *et al.* Mechanically Durable Superhydrophobic Surfaces. *Adv. Mater.* **23,** 673–678 (2011).

264. Wang, S. & Jiang, L. Definition of Superhydrophobic States. *Adv. Mater.* **19,** 3423–3424 (2007).

265. Quéré, D. Wetting and Roughness. *Annu. Rev. Mater. Res.* **38,** 71–99 (2008).

266. Whyman, G. & Bormashenko, E. How to make the cassie wetting state stable? *Langmuir* **27,** 8171–8176 (2011).

267. Tyrrell, J. W. G. & Attard, P. Images of nanobubbles on hydrophobic surfaces and their interactions. *SOCAR Proc.* **2011,** 75–79 (2011).

268. Mao, M., Zhang, J., Yoon, R. H. & Ducker, W. A. Is there a thin film of air at the interface between water and smooth hydrophobic solids? *Langmuir* **20,** 1843–1849 (2004).

269. Martines, E. *et al.* Air-trapping on biocompatible nanopatterns. *Langmuir* **22,** 11230–3 (2006).

270. Poetes, R., Holtzmann, K., Franze, K. & Steiner, U. Metastable underwater superhydrophobicity. *Phys. Rev. Lett.* **105,** 1–4 (2010).

271. Tang, Z. Spontaneous Organization of Single CdTe Nanoparticles into

Luminescent Nanowires. *Science (80-.).* **297,** 237–240 (2002).

272. Dong, A. G., Chen, J., Vora, P. M., Kikkawa, J. M. & Murray, C. B. Binary nanocrystal superlattice membranes self-assembled at the liquid-air interface. *Nature* **466,** 474–477 (2010).
273. Takahashi, M. Zeta potential of microbubbles in aqueous solutions: electrical properties of the gas-water interface. *J. Phys. Chem. B* **109,** 21858–21864 (2005).
274. Graciaa, A., Morel, G., Saulner, P., Lachaise, J. & Schechter, R. S. The zeta-potential of gas-bubbles. *J. Colloid Interface Sci.* **172,** 131–136 (1995).
275. Beattie, J. K., Djerdjev, A. N. & Warr, G. G. The surface of neat water is basic. *Faraday Discuss.* **141,** 31–39 (2009).
276. Beattie, J. K. & Djerdjev, A. M. The pristine oil/water interface: surfactant-free hydroxide-charged emulsions. *Angew. Chem. Int. Ed.* **43,** 3568–3571 (2004).
277. Huang, R. X., Carney, R. P., Stellacci, F. & Lau, B. L. T. Colloidal stability of self-assembled mono layer-coated gold nanoparticles: the effects of surface compositional and structural heterogeneity. *Langmuir* **29,** 11560–11566 (2013).
278. Saltzman, W. M. & Torchilin, V. Drug Delivery Systems. (2008).
279. Zhou, H. Self-assembly mechanism of spiky magnetoplasmonic supraparticles. *Adv. Funct. Mater.* **24,** 1439–1448 (2014).
280. Hollingsworth, A., Leunissen, M., Irvine, W., Chaikin, P. & van Blaaderen, A. Charged colloids in low polar solvents. *Bull. Am. Phys. Soc.* **53,** (2008).
281. Li, Q. C. *et al.* Fabrication of ZnO Nanorods and Nanotubes in Aqueous Solutions. *Chem. Mater.* **17,** 1001–1006 (2005).
282. Ma, T., Guo, M., Zhang, M., Zhang, Y. & Wang, X. Density-controlled hydrothermal growth of well-aligned ZnO nanorod arrays. *Nanotechnology* **18,** 035605 (2007).
283. Sun, H. *et al.* Position and density control in hydrothermal growth of ZnO nanorod arrays through pre-formed micro/nanodots. *Nanotechnology* **19,** 395602 (2008).
284. Wu, W., Hu, G., Cui, S., Zhou, Y. & Wu, H. Epitaxy of vertical ZnO nanorod arrays on highly (001)-oriented ZnO seed monolayer by a hydrothermal route.

Cryst. Growth Des. **8,** 4014–4020 (2008).

285. Hou, X., Zhou, F., Yu, B. & Liu, W. Superhydrophobic zinc oxide surface by differential etching and hydrophobic modification. *Mater. Sci. Eng. A* **452–453,** 732–736 (2007).
286. Kornherr, A. *et al.* Molecular dynamics simulations of the adsorption of industrial relevant silane molecules at a zinc oxide surface. *J. Chem. Phys.* **119,** 9719 (2003).
287. Petoral, R. M., Yazdi, G. R., Lloyd Spetz, A., Yakimova, R. & Uvdal, K. Organosilane-functionalized wide band gap semiconductor surfaces. *Appl. Phys. Lett.* **90,** 223904 (2007).
288. Zeng, J. *et al.* Octadecyltrimethoxysilane functionalized ZnO nanorods as a novel coating for solid-phase microextraction with strong hydrophobic surface. *Analyst* **137,** 4295 (2012).
289. Feng, X. & Jiang, L. Design and creation of superwetting/antiwetting surfaces. *Adv. Mater.* **18,** 3063–3078 (2006).
290. Yang, C., Dabros, T., Li, D., Czarnecki, J. & Masliyah, J. H. Measurement of the Zeta Potential of Gas Bubbles in Aqueous Solutions by Microelectrophoresis Method. *J. Colloid Interface Sci.* **243,** 128–135 (2001).
291. Patankar, N. A. Transition between superhydrophobic states on rough surfaces. *Langmuir* **20,** 7097–102 (2004).
292. Tsori, Y. Discontinuous liquid rise in capillaries with varying cross-sections. *Langmuir* **22,** 8860–8863 (2006).
293. Xiu, Y., Zhu, L., Hess, D. W. & Wong, C. P. Hierarchical silicon etched structures for controlled hydrophobicity/ superhydrophobicity. *Nano Lett.* **7,** 3388–3393 (2007).
294. Allen, C. G. *et al.* Surface modification of zno using triethoxysilane-based molecules. *Langmuir* **24,** 13393–13398 (2008).
295. Everett, D. H. *Colloid Science*. **4,** (The Royal Society of Chemistry, 1983).
296. Hackley, V. A., Somasundaran, P. & Lewis, J. A. Polymers in particulate systems: properties and applications. vi, 367 p. (2002). at

<http://mirlyn.lib.umich.edu/Record/003589411 CN - QD 382 .W3 P651 2002>

297. Lambourne, R. & Strivens, T. A. Paint and surface coatings: theory and practice. xii, 784 p. (1999). at <http://mirlyn.lib.umich.edu/Record/004021719 CN - TP 935 .P241 1999>

298. Ring, T. A. Fundamentals of ceramic powder processing and synthesis. xxii, 961 p. (1996). at <http://mirlyn.lib.umich.edu/Record/003080728 CN - TP 815 .R561 1996>

299. Romero-Cano, M. S., Martín-Rodríguez, A. & de las Nieves, F. J. Electrosteric Stabilization of Polymer Colloids with Different Functionality. *Langmuir* **17,** 3505–3511 (2001).

300. Vincent, B. The van der Waals attraction between colloid particles having adsorbed layers. II. Calculation of interaction curves. *J. Colloid Interface Sci.* **42,** 270–285 (1973).

301. Shanbhag, S. & Kotov, N. A. On the Origin of a Permanent Dipole Moment in Nanocrystals with a Cubic Crystal Lattice : Effects of Truncation , Stabilizers , and Medium for CdS Tetrahedral Homologues. 12211–12217 (2006).

302. Yang, M., Sun, K. & Kotov, N. a. Formation and assembly-disassembly processes of ZnO hexagonal pyramids driven by dipolar and excluded volume interactions. *J. Am. Chem. Soc.* **132,** 1860–1872 (2010).

303. Tadmor, R. The London-van der Waals interaction energy between objects of various geometries. *J. Phys. Condens. Matter* **13,** L195 (2001).

304. Lefèvre, G. & Jolivet, a. Calculation of Hamaker constants applied to the deposition of metallic oxide particles at high temperature. *Proc. Int. Conf. Heat Exch. Fouling an Clean. VIII* **2009,** 120–124 (2009).

305. Rahaman, M. N. Ceramic processing. 473 p. (2007). at <http://mirlyn.lib.umich.edu/Record/005293518 CN - TP 807 .R2781 2007>

306. Hamaker, H. C. The London—van der Waals attraction between spherical particles. *Physica* **4,** 1058–1072 (1937).

307. Purcell, E. M. & Pennypacker, C. R. Scattering and Absorption of Light by Nonspherical Dielectric Grains. *Astrophys. J.* **186,** 705 (1973).

308. Nijboer, B. R. A. & Renne, M. Microscopic derivation of 1macroscopic van der waals forces. *Chem. Phys. Lett.* **1,** 317–320 (1967).
309. Verdult, M. W. J. A Microscopic Approach to Van-der-Waals Interactions between Nanoclusters: the Coupled Dipole Method. *Thesis* (2010).
310. Goodwin, J. W. in *Colloids and Interfaces with Surfactants and Polymers – An Introduction* 61–93 (John Wiley & Sons, Ltd, 2004). doi:10.1002/0470093919.ch3
311. Hemmerle, A. *et al.* Controlling interactions in supported bilayers from weak electrostatic repulsion to high osmotic pressure. *Proc. Natl. Acad. Sci. U. S. A.* **109,** 19938–42 (2012).
312. Chang, H.-C., Yossifon, G. & Demekhin, E. A. Nanoscale Electrokinetics and Microvortices: How Microhydrodynamics Affects Nanofluidic Ion Flux. *Annu. Rev. Fluid Mech.* **44,** 401–426 (2012).
313. Kim, D., Posner, J. D. & Santiago, J. G. High flow rate per power electroosmotic pumping using low ion density solvents. *Sensors Actuators, A Phys.* **141,** 201–212 (2008).
314. Wang, C., Wang, L., Zhu, X., Wang, Y. & Xue, J. Low-voltage electroosmotic pumps fabricated from track-etched polymer membranes. *Lab Chip* **12,** 1710–1716 (2012).
315. Hogg, R., Healy, T. W. & Fuerstenau, D. W. Mutual coagulation of colloidal dispersions. *Trans. Faraday Soc.* **62,** 1638 (1966).
316. Mishchuk, N. The role of hydrophobicity and dissolved gases in non-equilibrium surface phenomena. *Colloids Surfaces A Physicochem. Eng. Asp.* **267,** 139–152 (2005).
317. Mishchuk, N. *et al.* Influence of Dissolved Gas on van der Waals Forces between Bubbles and Particles. *Analysis* **106,** 689–696 (2002).
318. Mishchuk, N., Ralston, J. & Fornasiero, D. Influence of very small bubbles on particle/bubble heterocoagulation. *J. Colloid Interface Sci.* **301,** 168–75 (2006).
319. Mishchuk, N. A. The model of hydrophobic attraction in the framework of classical DLVO forces. *Adv. Colloid Interface Sci.* **168,** 149–166 (2011).

320. Kim, K.-M. *et al.* Colloidal behaviors of ZnO nanoparticles in various aqueous media. *Toxicol. Environ. Health Sci.* **4,** 121–131 (2012).
321. Rabinovich, Y. I. & Derjaguin, B. V. Interaction of hydrophobized filaments in aqueous electrolyte solutions. *Colloids and Surfaces* **30,** 243–251 (1988).
322. Boinovich, L. B. The forces determining the stability of thin wetting films of solutions with nonpolar solvent. *Adv. Colloid Interface Sci.* **37,** 177–193 (1992).
323. Meurk, A., Luckham, P. F. & Bergström, L. Direct Measurement of Repulsive and Attractive van der Waals Forces Between Inorganic Materials. *Langmuir* **13,** 3896–3899 (1997).
324. Tabor, R. F., Manica, R., Chan, D. Y. C., Grieser, F. & Dagastine, R. R. Repulsive van der Waals Forces in Soft Matter: Why Bubbles Do Not Stick to Walls. *Phys. Rev. Lett.* **106,** 064501 (2011).
325. French, R. H. Origins and Applications of London Dispersion Forces and Hamaker Constants in Ceramics. *J. Am. Ceram. Soc.* **83,** 2117–2146 (2000).
326. Song, S. & Lopez-Valdivieso, a. Computational Studies on Interaction between Air Bubbles and Hydrophobic Mineral Particles Covered by Nonpolar Oil. *J. Colloid Interface Sci.* **212,** 42–48 (1999).
327. Zhang, N., Yu, X., Hu, J., Xue, F. & Ding, E. Synthesis of silver nanoparticle-coated poly(styrene-co-sulfonic acid) hybrid materials and their application in surface-enhanced Raman scattering (SERS) tags. *RSC Adv.* **3,** 13740–13747 (2013).
328. Tabor, R. F., Grieser, F., Dagastine, R. R. & Chan, D. Y. C. Measurement and analysis of forces in bubble and droplet systems using AFM. *J. Colloid Interface Sci.* **371,** 1–14 (2012).
329. Drummond, C. J. & Chan, D. Y. C. van der Waals Interaction, Surface Free Energies, and Contact Angles: Dispersive Polymers and Liquids. *Langmuir* **7463,** 3890–3895 (1997).
330. Biesheuvel, P. M. Evidence for charge regulation in the sedimentation of charged colloids. *J. Phys. Condens. Matter* **16,** L499–L504 (2004).
331. van Zwol, P. J., Palasantzas, G. & DeHosson, J. T. M. Weak dispersive forces

between glass and gold macroscopic surfaces in alcohols. *Phys. Rev. E* **79,** 041605 (2009).

332. Moriyoshi, T., Ishii, T., Tamai, Y. & Tado, M. Static dielectric constants of water + ethanol and water + 2-methyl-2-propanol mixtures from 0.1 to 300 MPa at 298.15 K. *J. Chem. Eng. Data* **35,** 17–20 (1990).
333. Logtenberg, E. H. . & Stein, H. N. Zeta potential and coagulation of ZnO in Alcohols. *Colloids and Surfaces* **17,** 305–312 (1986).
334. Yin, G., Zheng, Z., Wang, H. & Du, Q. Slightly surface-functionalized polystyrene microspheres prepared via Pickering emulsion polymerization using for electrophoretic displays. *J. Colloid Interface Sci.* **361,** 456–64 (2011).
335. Sastry, N. V & Valand, M. K. Dielectric constants, refractive indexes and polarizations for 1-Alcohol +Heptane mixtures at 298.15 and 308.15 K. *Berichte der Bunsengesellschaft für Phys. Chemie* **101,** 243–250 (1997).
336. Briscoe, W. H. & Horn, R. G. Direct measurement of surface forces due to charging of solids immersed in a nonpolar liquid. *Langmuir* **18,** 3945–3956 (2002).
337. Stappers, L., Zhang, L., Van der Biest, O. & Fransaer, J. The effect of electrolyte conductivity on electrophoretic deposition. *J. Colloid Interface Sci.* **328,** 436–446 (2008).
338. Ebaadi, S. H. Van der Waals interaction between surfactant-coated and bare colloidal particles. *Colloids and Surfaces* **2,** 155–168 (1981).
339. Ederth, T. Computation of Lifshitz- van der Waals Forces between Alkylthiol Monolayers on Gold Films. *Langmuir* **17,** 3329–3340 (2001).
340. Roth, C. M., Neal, B. L. & Lenhoff, a M. Van der Waals interactions involving proteins. *Biophys. J.* **70,** 977–87 (1996).
341. Kim, T., Lee, K., Gong, M. S. & Joo, S. W. Control of gold nanoparticle aggregates by manipulation of interparticle interaction. *Langmuir* **21,** 9524–9528 (2005).
342. Zhang, H. *et al.* Influence of interparticle electrostatic repulsion in the initial stage of aqueous semiconductor nanocrystal growth. *J. Phys. Chem. C* **112,** 1885–1889

(2008).

343. Zhang, Tang, Kotov, N. A. & Glotzer, S. C. Simulations and Analysis of Self-Assembly of CdTe Nanoparticles into Wires and Sheets. *Nano Lett.* **7,** 1670–1675 (2007).

344. Koppenol, W. H., Rush, J. D., Mills, J. D. & Margoliash, E. The dipole moment of cytochrome c. *Mol. Biol. Evol.* **8 ,** 545–558 (1991).

345. Yaroslavov, A. A. *et al.* What is the effective charge of TGA-stabilized CdTe nanocolloids? *J. Am. Chem. Soc.* **127,** 7322–7323 (2005).

346. Makino, K. & Ohshima, H. Electrophoretic mobility of a colloidal particle with constant surface charge density. *Langmuir* **26,** 18016–18019 (2010).

347. Qin, B., Zhao, Z., Song, R., Shanbhag, S. & Tang, Z. A temperature-driven reversible phase transfer of 2-(diethylamino) ethanethiol-stabilized CdTe nanoparticles. *Angew. Chemie - Int. Ed.* **47,** 9875–9878 (2008).

348. Hwang, Y. J., Hong, S. H., Lee, S. G., Cho, M. H. & Shin, D. M. Surface characteristics of photoaligned polyimide film interfacial reacted with bromine or ethanethiol. *Ultramicroscopy* **108,** 1266–1272 (2008).

349. Wei, J. Heterogeneous Electron Transfer of Supramolecular Assemblies. *Ph.D. Thesis* **1,** (University of Pittsburgh, 2005).

350. Park, J. Il *et al.* Terminal supraparticle assemblies from similarly charged protein molecules and nanoparticles. *Nat. Commun.* **5,** 3593 (2014).

351. Morrison, I. D. & Ross, S. Colloidal dispersions: suspensions, emulsions, and foams. xxvii, 616 p. (2002). at <http://mirlyn.lib.umich.edu/Record/004243222 CN - QD 549 .M6871 2002>

352. Sinyagin, A. Y., Belov, A., Tang, Z. & Kotov, N. A. Monte Carlo computer simulation of chain formation from nanoparticles. *J. Phys. Chem. B* **110,** 7500–7507 (2006).

353. Stubenrauch, C., Rojas, O. J., Schlarmann, J. & Claesson, P. M. Interactions between nonpolar surfaces coated with the nonionic surfactant hexaoxyethylene dodecyl ether C 12E 6 and the origin of surface charges at the air/water interface. *Langmuir* **20,** 4977–4988 (2004).

354. Mizuno, T., Namiki, A. & Tsuzuki, S. A Novel Filter Rating Method Using Less Than 30-nm Gold Nanoparticle and Protective Ligand. **22,** 452–461 (2009).
355. Zhang, H. & Wang, D. Controlling the growth of charged-nanoparticle chains through interparticle electrostatic repulsion. *Angew. Chemie - Int. Ed.* **47,** 3984–3987 (2008).
356. Gregory, J. Interaction of unequal double layers at constant charge. *J. Colloid Interface Sci.* **51,** 44–51 (1975).
357. Jahani, S. & Jacob, Z. All-dielectric metamaterials. *Nat. Nanotechnol.* **11,** 23–36 (2016).
358. Boardman, A. D. & Zayats, A. V. Nonlinear plasmonics. *Handb. Surf. Sci.* **4,** 329–347 (2014).
359. Fan, X., Zheng, W. & Singh, D. J. Light scattering and surface plasmons on small spherical particles. *Light Sci. Appl.* **3,** e179 (2014).
360. Fu, Y. H., Kuznetsov, A. I., Miroshnichenko, A. E., Yu, Y. F. & Luk'yanchuk, B. Directional visible light scattering by silicon nanoparticles. *Nat. Commun.* **4,** 1527 (2013).
361. Liu, W., Miroshnichenko, A. E., Neshev, D. N. & Kivshar, Y. S. Broadband unidirectional scattering by magneto-electric core-shell nanoparticles. *ACS Nano* **6,** 5489–5497 (2012).
362. Person, S. *et al.* Demonstration of zero optical backscattering from single nanoparticles. *Nano Lett.* **13,** 1806–1809 (2013).
363. Li, Y. *et al.* Broadband zero-backward and near-zero-forward scattering by metallo-dielectric core-shell nanoparticles. *Sci. Rep.* **5,** 12491 (2015).
364. Novotny, L. & van Hulst, N. Antennas for light. *Nat. Photonics* **5,** 83–90 (2011).
365. Atwater, H. A. & Polman, A. Plasmonics for improved photovoltaic devices. *Nat. Mater.* **9,** 865–865 (2010).
366. Sundararajan, S. P., Grady, N. K., Mirin, N. & Halas, N. J. Nanoparticle-lnduced enhancement and suppression of photocurrent in a silicon photodiode. *Nano Lett.* **8,** 624–630 (2008).
367. Curto, A. G. *et al.* Unidirectional Emission of a Quantum Dot Coupled to a

Nanoantenna. *Science (80-.).* **329,** 930–933 (2010).

368. Bahng, J. H. *et al.* Anomalous dispersions of ‘hedgehog’ particles. *Nature* **517,** 596–599 (2014).
369. Li, C., Kattawar, G. W. & Yang, P. Effects of surface roughness on light scattering by small particles. *J. Quant. Spectrosc. Radiat. Transf.* **89,** 123–131 (2004).
370. Evlyukhin, A. B. *et al.* Demonstration of magnetic dipole resonances of dielectric nanospheres in the visible region. *Nano Lett.* **12,** 3749–3755 (2012).
371. Garnett, J. C. M. Colours in Metal Glasses and in Metallic Films. *Philos. Trans. R. Soc. London A Math. Phys. Eng. Sci.* **203,** 385–420 (1904).
372. Niklasson, G. a, Granqvist, C. G. & Hunderi, O. Effective medium models for the optical properties of inhomogeneous materials. *Appl. Opt.* **20,** 26–30 (1981).
373. Chýlek, P. Partial-wave resonances and the ripple structure in the Mie normalized extinction cross section. *J. Opt. Soc. Am* **66,** 1975–1977 (1976).
374. Chýlek, P., Kiehl, J. T. & Ko, M. K. W. Narrow resonance structure in the Mie scattering characteristics. *Appl. Opt.* **17,** 3019–3021 (1978).
375. Khudiyev, T., Huseyinoglu, E. & Bayindir, M. Non-resonant Mie scattering: emergent optical properties of core-shell polymer nanowires. *Sci. Rep.* **4,** 4607 (2014).
376. Liu, W. *et al.* Ultra-directional forward scattering by individual core-shell nanoparticles. *Opt. Express* **22,** 16178–16187 (2014).
377. Wang, H. & Halas, N. J. Mesoscopic au ‘meatball’ particles. *Adv. Mater.* **20,** 820–825 (2008).
378. Wang, H. *et al.* Controlled texturing modifies the surface topography and plasmonic properties of Au nanoshells. *J. Phys. Chem. B* **109,** 11083–11087 (2005).
379. Wang, T., Zheng, N., Xin, J. & Ma, Z. Integrating millimeter wave radar with a monocular vision sensor for on-road obstacle detection applications. *Sensors* **11,** 8992–9008 (2011).
380. Tonouchi, M. Cutting-edge terahertz technology. *Nat. Photonics* **1,** 97–105 (2007).

381. Ghan, S. J. & Schwartz, S. E. Aerosol properties and processes: A path from field and laboratory measurements to global climate models. *Bull. Am. Meteorol. Soc.* **88,** 1059–1083 (2007).
382. Kerker, M. Elastic and Inelastic Light Scattering in Flow Cytometry. *Cytometry* **4,** 1–10 (1983).
383. No Title. *Unpubl. data* (2012).
384. Kerker, M., Wang, D.-S. & Giles, C. L. Electromagnetic scattering by magnetic spheres. *J. Opt. Soc. Am.* **73,** 765 (1983).
385. Zhang, Z., Detch, J. & Metiu, H. Surface roughness in thin-film growth: The effect of mass transport between layers. *Phys. Rev. B* **48,** 4972–4975 (1993).
386. Smith, M. A. *et al.* Surface roughness effects in the catalytic behavior of vanadia supported on SBA-15. *J. Catal.* **312,** 170–178 (2014).
387. Rechendorff, K., Hovgaard, M. B., Foss, M., Zhdanov, V. P. & Besenbacher, F. Enhancement of Protein Adsorption Induced by Surface Roughness. 10885–10888 (2006).
388. Mizoue, T., Tokita, M., Honjo, H., Barraza, H. J. & Katsuragi, H. in (eds. Tokita, M. & Nishinari, K.) 63–67 (Springer Berlin Heidelberg, 2009). doi:10.1007/978-3-642-00865-8_9
389. Bhushan, B. Contact mechanics of rough surfaces in tribology: multiple asperity contact. *Tribol. Lett.* **4,** 1–35 (1998).
390. Biazar, E., Heidari, M., Asefnejad, A. & Montazeri, N. The relationship between cellular adhesion and surface roughness in polystyrene modified by microwave plasma radiation. *Int. J. Nanomedicine* **6,** 631–639 (2011).
391. Bakr, O. M., Wunsch, B. H. & Stellacci, F. High-yield synthesis of multi-branched urchin-like gold nanoparticles. *Chem. Mater.* **18,** 3297–3301 (2006).
392. Sun, X. & Li, Y. Colloidal Carbon Spheres and Their Core/Shell Structures with Noble-Metal Nanoparticles. *Angew. Chemie Int. Ed.* **43,** 597–601 (2004).
393. Verma, A. *et al.* Surface-structure-regulated cell-membrane penetration by monolayer-protected nanoparticles. *Nat. Mater.* **7,** 588–595 (2008).
394. Song, J. S., Tronc, F. & Winnik, M. a. Two-stage dispersion polymerization

toward monodisperse, controlled micrometer-sized copolymer particles. *J. Am. Chem. Soc.* **126,** 6562–6563 (2004).

395. Shen, Z.-R., Wang, J.-G., Sun, P.-C., Ding, D.-T. & Chen, T.-H. Fabrication of lanthanide oxide microspheres and hollow spheres by thermolysis of pre-molding lanthanide coordination compounds. *Chem. Commun.* 1742 (2009). doi:10.1039/b820096c
396. Meseguer, F. *et al.* Silicon colloids: A new enabling nanomaterial. *J. Appl. Phys.* **109,** (2011).
397. Bai, M.-Y., Cheng, Y.-J., Wickline, S. a & Xia, Y. Colloidal hollow spheres of conducting polymers with smooth surface and uniform, controllable sizes. *Small* **5,** 1747–52 (2009).
398. Kim, S. H., Lee, S. Y. & Yang, S. M. Janus microspheres for a highly flexible and impregnable waterrepelling interface. *Angew. Chemie - Int. Ed.* **49,** 2535–2538 (2010).
399. Asakura, S. & Oosawa, F. Interaction between particles suspended in solutions of macromolecules. *Journal of Polymer Science* **33,** 183–192 (1958).
400. Verma, R., Crocker, J., Lubensky, T. & Yodh, a. Entropic Colloidal Interactions in Concentrated DNA Solutions. *Phys. Rev. Lett.* **81,** 4004–4007 (1998).
401. Ohshima, Y. *et al.* Direct Measurement of Infinitesimal Depletion Force in a Colloid-Polymer Mixture by Laser Radiation Pressure. *Phys. Rev. Lett.* **78,** 3963–3966 (1997).
402. Vrij, a. Polymers at Interfaces and the Interactions in Colloidal Dispersions. *Pure Appl. Chem.* **48,** 471–483 (1976).
403. Zhao, B., Brittain, W. J., Zhou, W. & Cheng, S. Z. D. AFM study of tethered polystyrene-b-poly(methyl methacrylate) and polystyrene-b-poly(methyl acrylate) brushes on flat silicate substrates. *Macromolecules* **33,** 8821–8827 (2000).
404. Edmondson, S., Osborne, V. L. & Huck, W. T. S. Polymer brushes via surface-initiated polymerizations. *Chem. Soc. Rev.* **33,** 14–22 (2004).
405. Ma, H., Hyun, J., Stiller, P. & Chilkoti, A. 'Non-Fouling' Oligo(ethylene glycol)-Functionalized Polymer Brushes Synthesized by Surface-Initiated Atom Transfer

Radical Polymerization. *Adv. Mater.* **16,** 338–341 (2004).

406. Zhao, B., Brittain, W. J., Zhou, W. & Cheng, S. Z. D. Nanopattern formation from tethered PS-b-PMMA brushes upon treatment with selective solvents [19]. *J. Am. Chem. Soc.* **122,** 2407–2408 (2000).
407. Lemieux, M. *et al.* Reorganization of binary polymer brushes: Reversible switching of surface microstructures and nanomechanical properties. *Macromolecules* **36,** 7244–7255 (2003).
408. Han, M., Zhang, W., Gao, C., Liang, Y. & Xu, Z. Hollow nickel microspheres covered with oriented carbon nanotubes and its magnetic property. *Carbon N. Y.* **44,** 211–215 (2006).
409. Amidon, G. L., Lennernäs, H., Shah, V. P. & Crison, J. R. A Theoretical Basis for a Biopharmaceutic Drug Classification: The Correlation of in Vitro Drug Product Dissolution and in Vivo Bioavailability. *Pharmaceutical Research: An Official Journal of the American Association of Pharmaceutical Scientists* **12,** 413–420 (1995).
410. Lipinski, C. A. Drug-like properties and the causes of poor solubility and poor permeability. *J. Pharmacol. Toxicol. Methods* **44,** 235–249 (2000).
411. Yalkowsky, S. H. & Myrdal, P. B. in *Encyclopedia of Pharmaceutical Technology, Third Edition* **null,** 3311–3333 SE – (Taylor & Francis, 2013).
412. Gupta, P., Kakumanu, V. K. & Bansal, A. K. Stability and solubility of celecoxib-PVP amorphous dispersions: A molecular perspective. *Pharm. Res.* **21,** 1762–1769 (2004).
413. Abdul-Fattah, A. M. & Bhargava, H. N. Preparation and in vitro evaluation of solid dispersions of halofantrine. *Int. J. Pharm.* **235,** 17–33 (2002).
414. Sinha, S. *et al.* Solid dispersion as an approach for bioavailability enhancement of poorly water-soluble drug ritonavir. *AAPS PharmSciTech* **11,** 518–27 (2010).
415. Savjani, K. T., Gajjar, A. K. & Savjani, J. K. Drug solubility: importance and enhancement techniques. *ISRN Pharm.* **2012,** 195727 (2012).
416. Parve, B., Shinde, P., Rawat, S., Rathod, S. & Waghmode, G. Solubility enhancement techniques: a review. *World J. Pharm. Pharm. Sci.* **3,** 23,400–422

(2014).

417. Rasool, A. A., Hussain, A. A. & Dittert, L. W. Solubility enhancement of some water-insoluble drugs in the presence of nicotinamide and related compounds. *J. Pharm. Sci.* **80,** 387–393 (1991).

418. Pathak, P., Meziani, M. J. & Sun, Y.-P. Supercritical fluid technology for enhanced drug delivery. *Expert Opin. Drug Deliv.* **2,** 747–761 (2005).

419. El Jay, a. Effects of Organic Solvents and Solvent-Atrazine Interactions on Two Algae ,. *Arch. environemental Contam. Toxicol.* **31,** 84–90 (1996).

420. Aktar, M. W., Sengupta, D. & Chowdhury, A. Impact of pesticides use in agriculture: their benefits and hazards. *Interdiscip. Toxicol.* **2,** 1–12 (2009).

421. Wang, P. & Keller, A. A. Partitioning of hydrophobic pesticides within a soil-water-anionic surfactant system. *Water Res.* **43,** 706–714 (2009).

422. G.A. Shah, M. S. V. Scattering by Rough Cylindrical Particles. *Nature* **235,** 115–116 (1972).

423. Wang, H., Fu, K., Drezek, R. A. & Halas, N. J. Light scattering from spherical plasmonic nanoantennas: Effects of nanoscale roughness. *Appl. Phys. B Lasers Opt.* **84,** 191–195 (2006).

424. Peltoniemi, J. I., Lumme, K., Muinonen, K. & Irvine, W. M. Scattering of light by stochastically rough particles. *Appl. Opt.* **28,** 4088–95 (1989).

425. Schuerman, D. W. & service), S. (Online. Light Scattering by Irregularly Shaped Particles. (1980). at <http://dx.doi.org/10.1007/978-1-4684-3704-1>

426. Kiehl, J. T., Ko, M. W., Mugnai, A. & Chýlek, P. in (ed. Schuerman, D. W.) 135–140 (Springer US, 1980). doi:10.1007/978-1-4684-3704-1_16

427. Bahar, E., Chakrabarti, S. & Fitzwater, M. a. Extinction cross sections and albedos for particles with very rough surfaces. *Appl. Opt.* **25,** 2530 (1986).

428. Mukai, S., Mukai, T., Giese, R. H., Weiss, K. & Zerull, R. H. Scattering of radiation by a large particle with a random rough surface. *moon planets* **26,** 197–208 (1982).

429. Perrin, J.-M. & Lamy, P. L. Light Scattering by Large Particles. *Opt. Acta Int. J. Opt.* **33,** 1001–1022 (1986).

430. O'Donnell, K. A. High-order perturbation theory for light scattering from a rough metal surface. *J. Opt. Soc. Am. A. Opt. Image Sci. Vis.* **18,** 1507–18 (2001).
431. D Antonio, P., Lasalvia, M., Perna, G. & Capozzi, V. Scale-independent roughness value of cell membranes studied by means of AFM technique. *Biochim. Biophys. Acta - Biomembr.* **1818,** 3141–3148 (2012).
432. Hoek, E. M. V, Bhattacharjee, S. & Elimelech, M. Effect of membrane surface roughness on colloid-membrane DLVO interactions. *Langmuir* **19,** 4836–4847 (2003).
433. Kolokolova, L., Das, H. S., Dubovik, O., Lapyonok, T. & Yang, P. Polarization of cosmic dust simulated with the rough spheroid model. *Planet. Space Sci.* **116,** 30–38 (2015).
434. Woodward, X., Kostinski, A., China, S., Mazzoleni, C. & Cantrell, W. Characterization of Dust Particles' 3D Shape and Roughness with Nanometer Resolution. *Aerosol Sci. Technol.* **49,** 229–238 (2015).
435. Evan, A. T., Flamant, C., Fiedler, S. & Doherty, O. An analysis of aeolian dust in climate models. *Geophys. Res. Lett.* **41,** 5996–6001 (2014).
436. Lurton, T. *et al.* Light scattering at small angles by atmospheric irregular particles: Modelling and laboratory measurements. *Atmos. Meas. Tech.* **7,** 931–939 (2014).
437. Poschl, U. Atmospheric aerosols: Composition, transformation, climate and health effects. *Angew. Chemie - Int. Ed.* **44,** 7520–7540 (2005).
438. Zaveri, R. A., Barnard, J. C., Easter, R. C., Riemer, N. & West, M. Particle-resolved simulation of aerosol size, composition, mixing state, and the associated optical and cloud condensation nuclei activation properties in an evolving urban plume. *J. Geophys. Res. Atmos.* **115,** 1–19 (2010).
439. Peters, C. J. *et al.* Filoviruses as emerging pathogens. *Semin. Virol.* **5,** 147–154 (1994).
440. Sullivan, N., Yang, Z. & Nabel, G. J. Ebola Virus Pathogenesis : Implications for Vaccines and Therapies MINIREVIEW Ebola Virus Pathogenesis : Implications for Vaccines and Therapies. *J. Virol.* **77,** 9733–9737 (2003).
441. Manicassamy, B., Wang, J., Jiang, H. & Rong, L. Comprehensive Analysis of

Ebola Virus GP1 in Viral Entry Comprehensive Analysis of Ebola Virus GP1 in Viral Entry. *J. Virol.* **79,** 4793–4805 (2005).

442. Niedrig, M. *et al.* First International Quality Assurance Study on the Rapid Detection of Viral Agents of Bioterrorism First International Quality Assurance Study on the Rapid Detection of Viral Agents of Bioterrorism. **42,** 1753–1755 (2004).

443. Panning, M. *et al.* Diagnostic reverse-transcription polymerase chain reaction kit for filoviruses based on the strain collections of all European biosafety level 4 laboratories. *J. Infect. Dis.* **196 Suppl ,** S199–204 (2007).